Direct and semi-direct aerosol effects on the southern African regional climate during the austral winter season

Fiona Tummon

Thesis Presented for the Degree of
DOCTOR OF PHILOSOPHY

March 2011

Acknowledgements

There are a great many people to thank for all the help, support, patience and encouragement that I've needed during the past three years. Firstly, I am deeply indebted to Fabien Solmon for his thorough and insightful supervision, for always being ready to answer my innumerable questions, no matter how mundane and for keeping a sense of humour throughout it all. I am also extremely grateful to Mark Tadross and Bruce Hewitson for their guidance, endless stream of interesting ideas and their invaluable criticism along the way. The enthusiasm of all three of my supervisors and their passion for their work is contagious and the immense depth of their knowledge has been of great inspiration.

Secondly, this thesis would never have been possible without the financial support of a CNRS bourse BDI-PED and, for the final months, the IDAF project. A big thank you is also due to CSAG and the LA for financing my trips between Cape Town and Toulouse (and especially for allowing me to experience an endless summer for almost two years).

Being split between two continents has been far from easy, but everyone from CSAG and the LA have always welcoming, willing to help and made the past three years a terrific experience. Special thanks to Cathy Liousse for her commitment, enthusiasm and all the informative discussions along the way, as well as to Robert Rosset for his continuous supply of useful articles. A very big thank you is also due to all the IT staff at the CHPC and CSAG in Cape Town, especially Jeremy Main and Chris Jack, for helping me through the somewhat painful process of installing RegCM. Also, to the IT staff at the LA in Toulouse, an enormous thank you – for always being ready to come to the rescue with a smile on their faces and taking the time to fix whatever problem there was, no matter how small.

Finally, for their continuous support, encouragement and always believing in me even when I didn't, I thank my fabulous family (mom, dad and Oisin) and my friends, old and new, who've been there for the journey: Susanna, Steffi, Daniel, Eric-Michel, Héloise, Rebecca, Justin, Michaela, Erwan, Laurie, Vivija and Gosia, amongst the many others. The past three years would quite simply not have been the same had it not been for the kindness, care, willingness to listen and the weekend adventures shared with these people. Merci vraiment beaucoup!!

Abstract

The regional climate model RegCM3 is used to investigate the direct and semi-direct aerosol effects on the southern African climate during the austral winter season (June-September). The sensitivity of simulated aerosol-climate effects to different biomass burning inventories, boundary conditions and sea surface temperature (SST) feedbacks is tested to assess the range of uncertainty associated with these parameters. Sensitivity to both boundary forcing and SST feedbacks appears to be negligible, while the aerosol radiative forcing (RF) is found to vary approximately linearly in response to aerosol emissions (varying by up to a factor of two in response to the factor of two difference between emissions inventories). In all cases the surface RF is negative, while the top-to-atmosphere RF is negative over most of the domain but positive over high-albedo savannah regions where aerosol loading is concentrated. Although the magnitude of simulated RF varies depending on the biomass burning emissions inventory used, all simulations show similar aerosol-climate impacts. Surface temperature decreases over most of the subcontinent, a signal which acts to reduce model bias over the western half of the region. The absorbing nature of the simulated aerosol burden results in heating at altitude, which, in combination with the surface cooling, serves to increase stability in the lower atmosphere over most of the subcontinent. In the middle troposphere, however, this warming induces an elevated heat-pump effect in the equatorial regions between approximately 8°N and 5°S. This enhances convection, precipitation as well as soil moisture and effectively acts to spin-up the hydrological cycle in the tropics. An investigation of the interannual variability of seasonal average aerosol impacts shows that significant difference in variability is apparent only in the main biomass burning regions, where aerosol loading is highest. The seasonal average precipitation changes varies more from year to year than aerosol-induced surface temperature changes, likely as a result of the greater variability associated with convective processes controlling precipitation in the regions affected. In contrast, despite there being significant differences between synoptic conditions, there is little synoptic-scale variability of aerosol-climate impacts. This suggests that, at least on the synoptic-scale, the atmospheric aerosol loading is more sensitive to the magnitude of emissions than any other control.

Résumé

Le modèle climatique régional RegCM3 est utilisépour examiner les effets direct et semi-direct des aérosols sur le climat du sud de l'Afrique pendant l'hiver austral (juin-septembre). La sensibilité des effets simulés aux différents inventaires d'émissions de combustion de biomasse et aux différentes conditions aux limites est evaluer, afin d'estimer l'incertitude associée à ces paramètres. La sensibilité aux conditions aux limites derivées de réanalyses est modeste, mais le forçage radiatif des aérosols varie linéairement en réponse au différents inventaires testées jusqu'à un facteur deux. Le forçage radiatif est toujours négatif, alors que le forçage radiatif au sommet de l'atmosphère est negatif sur la plupart du domaine sauf au-dessus les régions de savane ou le contenu atmosphérique d'aérosols est élevée. Même si la magnitude du forçage radiatif varie, les simulations pour la période présente montrent des impacts climatiques comparables. La température de surface diminue sur la plupart de la région, ce signale qui réduit le biais du modèle sur l'ouest du sous-continent. L'échauffement en altitude est lié à la charge d'aérosols absorbants et cela, en combinaison avec la réduction de température en surface, mène à la stabilisation de la basse atmosphère. Toutefois, dans la moyenne troposphère de la zone équatoriale (entre 8°N et 5°S) cet échauffement à pour résultat un effet de 'pompe à chaleur en altitude'. Cet effet augmente la convection, les précipitations et l'humidité du sol, en accélérant le cycle hydrologique dans cette région. Une étude de la variabilité interannuelle des effets climatiques des aérosols montre que les changements des précipitations en moyenne saisonnière sont plus variables d'un an à l'autre que les changements de température de surface. Par contre, malgré des différences significatives entre les conditions synoptiques, la variabilité synoptique des impacts climatiques des aérosols est faible.

Abbreviations

AAO – Antarctic Oscillation

AEJ-N – African Easterly Jet - Northern branch

AEJ-S – African Easterly Jet - Southern branch

AERONET – Aerosol Robotic Network

AMMA – African Monsoon Multidisciplinary Analyses

AOD – Aerosol Optical Depth

BATS – Biosphere-Atmosphere Transfer Scheme

BC – Black Carbon

CCM – Community Climate Model

CCN – Cloud Condensation Nuclei

CLWP – Cloud Liquid Water Path

CMAP – CPC Merged Analysis of Precipitation

CPC – Climate Prediction Centre

CRU – Climate Research Unit (of the University of East Anglia)

DEBITS – Deposition of Biogeochemically Important Species (umbrella project of IGAC)

DJF – December/January/February

ECMWF – European Centre for Medium-range Weather Forecasting

ENSO – El Niño Southern Oscillation

ERA40 – ECMWF 40-year Reanalysis

GCM – Global Climate Model

GFED – Global Fire Emissions Database

GLCC – Global Land Cover Characterisation

GPCP – Global Precipitation Climatology Project

GPH – Geopotential Height

ICTP – International Centre for Theoretical Physics

IDAF – IGAC DEBITS Africa

IGAC – International Global Atmospheric Chemistry

IN – Ice Nuclei

IPCC – International Panel for Climate Change

ITCZ – Inter-Tropical Convergence Zone

JJA – June/July/August

JJAS – June/July/August/September

LW – Longwave

MAM – March/April/May

MBL – Marine Boundary Layer

MISR – Multi-angle Imaging Spectro-Radiometer

MIT – Massachusetts Institute of Technology

MM4 – Mesoscale Model version 4

MM5 – Mesoscale Model version 5

MODIS – Moderate Resolution Imaging Spectrometer

NAO – North Atlantic Oscillation

NCAR – National Centre for Atmospheric Research

NCEP-II – National Centre for Environmental Prediction reanalysis product version 2

NDVI – Normalised Difference Vegetation Index

NOAA – National Ocean Atmosphere Administration

OC – Organic Carbon

PBL – Planetary Boundary Layer

RCM – Regional Climate Model

RegCM – Regional Climate Model

RF – Radiative Forcing

RH – Relative Humidity

RMSD – Root-Mean-Square Difference

SON – September/October/November

SSA – Single Scattering Albedo

SST – Sea Surface Temperature

SW – Shortwave

TOA – Top Of Atmosphere

TOMS – Total Ozone Monitoring System

TRMM – Tropical Rainfall Monitoring Mission

USGS – United States Geological Surveys

ZAB – Zaire Air Boundary

Contents

Chapter 3: Dynamical downscaling – Regional Climate Model III

Chapter 4: Climatic impacts of southern African aerosol – short-term focus on biomass burning 2001-2006

CHAPTER 1

Why aerosols? Why southern Africa?

1.1 Motivation from a global perspective

Aerosols affect the earth system in a multitude of ways, by influencing the radiative budget, atmospheric chemistry processes, ecosystem functioning and even human health. Aerosol impacts on the earth-atmosphere energy budget affect global and regional climate by redistributing heat within the atmosphere and influencing atmospheric stability, affecting regional circulation patterns and the hydrological cycle [*Chylek and Coakley,* 1974; *Martin et al.,* 1990; *Dockery et al.,* 1994; *Garstang et al.,* 1998; *Lohmann and Feichter*, 2005; *Solomon et al.,* 2007; *Ramanathan and Carmichael*, 2008].

Light-coloured aerosols, such as sulphate particles, tend to scatter incoming radiation, cooling both the atmosphere and surface by reflecting radiation that would normally have entered the earth system [*Chylek and Coakley,* 1974; *Arimoto,* 2001; *Sinha et al.,* 2003; *Huang et al.*, 2007]. On the other hand, dark-coloured aerosols have a somewhat more complex impact, serving both to reflect and absorb incoming radiation. Absorption by these aerosol locally warms the atmosphere but simultaneously also contributes to surface cooling through the conventional 'surface dimming' effect [*Kaufman et al.,* 2002; *Giorgi et al.,* 2003; *Kinne et al.,* 2003; *Ramanathan and Carmichael,* 2008]. Aerosol-induced warming at altitude may serve to decrease cloud cover (termed 'cloud burning') and exacerbate the positive, warming effect by locally reducing relative humidity [e.g. *Ackerman et al.,* 2000; *Koren et al.*, 2004]. In other cases, however, the warming at altitude may also serve to enhance cloud cover particularly if humidity is high and the absorbing aerosol layer lies above a low-level cloud deck [e.g. *Johnson et al.*, 2004; *Brioude et al.,* 2009; *Perlwitz and Miller*, 2010]. Whether resulting in a positive or negtive radiative forcing, this warming at altitude and the consequent impacts on cloud cover are known as the semi-direct aerosol effects.

In addition, aerosols also indirectly affect the earth's energy budget by acting as cloud and ice condensation nuclei [*Twomey*, 1974; *Kaufman et al.,* 2002; *Lohmann and Feichter*, 2005]. Increasing the aerosol loading generally tends to decrease average cloud and ice droplet size, thus resulting in increased cloud albedo and thickness [*Twomey,* 1974], as well as an increase in cloud lifetime [*Albrecht,* 1989], and, depending on the cloud type, also possible delays in precipitation onset and possible increases in precipitation intensity [*Kaufman et al.,* 2002; *Lohmann and Feichter*, 2005]. Finally, and not to be forgotten, aerosols have numerous non-climatic impacts. They affect regional ecosystems through deposition of micronutrients as well as through the formation of acid rain [e.g.*OECD*, 1977; *Garstang et al.,* 1998; *Piketh et al*., 2000; *Tyson and Gatebe*, 2001; *Billmark et al*., 2005] and also significantly impact human health, particularly in urban areas [e.g. *Dockery et al.,* 1994; *Forsberg et al.,* 2005; *Liu et al.,* 2009].

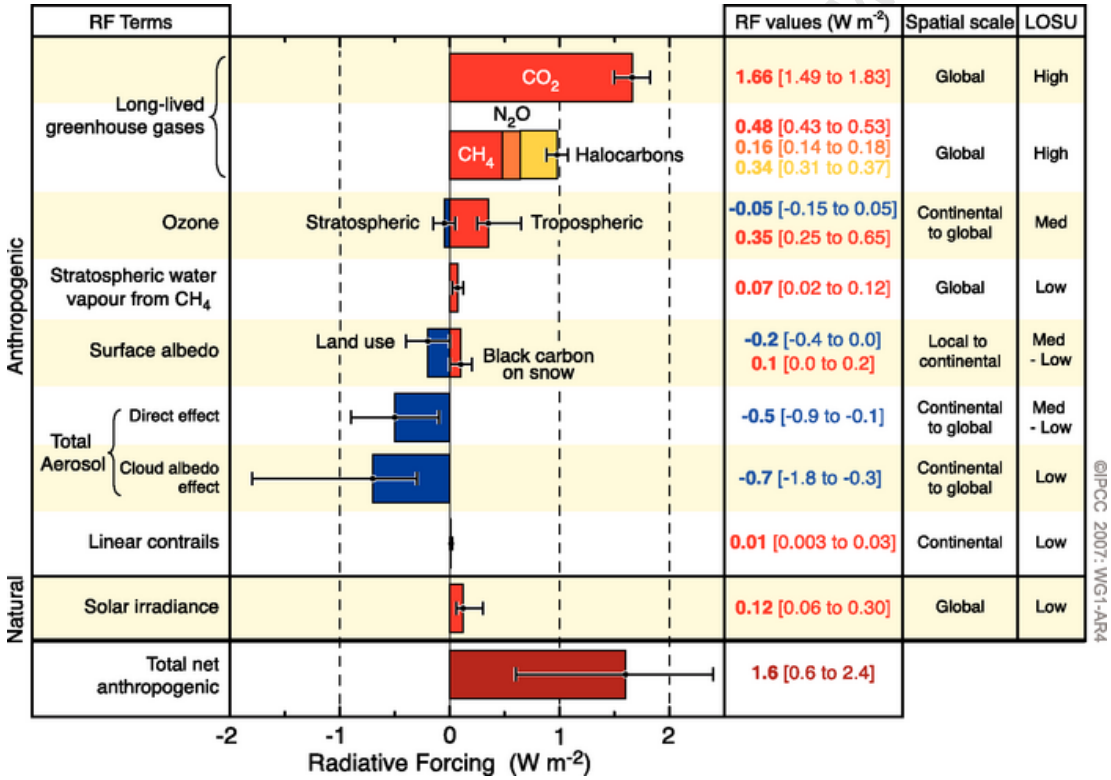

Figure 1.1: Radiative forcing estimates of various components of the earth system, as well as the scale at which they dominate and the level of scientific understanding (LOSU) associated with each process [*extracted from the IPCC AR4 report*, 2007].

The relatively short atmospheric lifetime of aerosols leads to highly heterogeneous distributions through space and time. Partly as a result of this large variability and also because of uncertainty regarding their optical properties, the magnitude of the global aerosol radiative forcing remains highly uncertain [*Pilewskie et al.,* 2003; *Kinne et al.,* 2003; *Solomon*

et al., 2007]. The most recent International Panel on Climate Change (IPCC) report [2007] suggests that aerosol are likely to have a negative radiative forcing (thus cooling effect) comparable in magnitude to the warming effect of carbon dioxide (CO_2). The uncertainty associated with these estimates is, however, of similar magnitude to the estimates themselves and scientific understanding of these processes is still relatively low (see the well-known IPCC radiative forcing chart in fig. 1.1). At the regional scale, uncertainty in terms of aerosol radiative forcing and associated climate impacts is even greater.

Over the past two decades, awareness of the importance of aerosols on the climate system has grown and a large number and variety of models have been developed as means to estimate aerosol radiative forcing and their impact on climate, ecosystems and human health. In addition, a large number of earth-observing satellite missions have been launched and a wealth of aerosol-related observational data has become available over the past decade. Because of the enormous complexity of aerosol-related processes, some of which are still being discovered, measuring and simulating the aerosol impact on climate is a non-trivial task, no matter what scale is considered: global, regional or local. Models, thoroughly validated with observations are, at present, one of the best-available tools to further our understanding of aerosol impacts and to make better estimations of their radiative effect on the global energy budget.

1.2 Motivation at the regional level

At the regional scale aerosol radiative forcing may be as large or even greater than that of greenhouse gases [e.g. *Keil and Haywood,* 2003; *Kinne et al.,* 2003]. Over southern Africa, however, the radiative impacts of aerosol and particularly their climatic impacts have been relatively poorly studied. This is especially important for Africa, which has been targeted as one of the most vulnerable regions to global change [*Solomon et al.*, 2007]. Specific, regional-level information is of particular importance in developing regions such as southern Africa, where vulnerability to climate variability is high and the ability to cope and adapt to climatic changes is relatively low. It is thus vital that climate variability and the influence of the regional atmospheric aerosol burden over the subcontinent is better understood and more accurately quantified.

Southern Africa provides the ideal test bed for aerosol-climate studies. Its unique geographical location, climate and biophysical attributes mean that the region is influenced by virtually all aerosol types. The atmospheric aerosol loading is affected by strong seasonal biomass burning [*Piketh et al.,* 1999b; *Tyson and Gatebe,* 2001; *Swap et al.,* 2003], mineral dust production [*Prospero et al.,* 2002], anthropogenic emissions [*Zunckel*, 1999; *Terblanche et al.,* 2000] as well as marine aerosol [*Piketh et al.,* 1999a]. Moreover, since most of

southern African lies in the subtropics, below the descending branch of the Hadley Cell, high pressures and subsidence dominate atmospheric circulation patterns for much of the year [*Tyson et al.,* 1996a; *Privette and Roy,* 2005]. As a result of the high degree of atmospheric stability and anticyclonic circulation patterns associated with these conditions, the regional aerosol burden recirculates and accumulates below expansive stable layers that may stretch over 30° latitude in extent [*Cosijn and Tyson,* 1996; *Tyson et al.,* 1996a,b]. This is particularly the case during the dry, austral winter season when biomass burning and dust aerosol concentrations are highest. As a consequence of the extensive recirculation, atmospheric aerosol lifetimes over southern Africa are longer than most other regions [*Liousse et al.,* 1996; *Tyson et al.*, 1996b] and the regional aerosol loading is likely to strongly affect the radiative balance over much of the subcontinent [*Garstang et al.,* 1996; *Swap et al.,* 2002a,b; *Reason et al.,* 2006].

Figure 1.2: Map of southern Africa and its component countries, with inset showing its situation relative to the rest of Africa. Depending on the definition, Tanzania may be included as East Africa rather than southern Africa.

In addition, the southern African region also has an important impact on the global atmosphere, with aerosol and trace gases from the region being transported and affecting the atmosphere and climate well beyond the subcontinent [e.g. *Fishman et al.,* 1991; *Sturman et al.*, 1997; *Pak et al.*, 2003]. As an example, evidence suggests that the transport of iron-rich mineral dust aerosol to the southwest Indian Ocean supports the very high biological activity

observed in this area. This activity is associated with a large uptake of carbon dioxide and the region serves as an important carbon sink and is significant in terms of the global carbon budget, and possibly even global climate [*Tyson and Gatebe,* 2001].

In an effort to better understand southern African aerosols and their impacts over the region two large, multi-disciplinary field campaigns were carried out in 1992 and 2000. These experiments aimed to characterise the regional atmospheric aerosol and trace gas composition as well as to investigate their sources, transport, physical and chemical transformation, their eventual deposition and their eventual influence on regional ecosystems and climate [*Swap et al*., 2002a,b]. A number of smaller, more local experiments and field campaigns have also taken place throughout the region over the past few decades, contributing to our working knowledge of the region and its atmospheric chemistry [e.g. *Kirkman et al*., 2000; *Jayaratne and Verma*, 2001; *Martins et al*., 2007]. A relatively small number of modelling studies concentrating on southern Africa have also been performed, ranging from global studies with some focus on the region [e.g. *Takemura et al.,* 2002; *Abel et al.,* 2005; *Kinne et al.,* 2006], through to regional climate investigations [e.g. *Joubert et al.,* 1996, 1999; *Tadross et al.,* 2005] and studies of local radiative transfer budgets [e.g. *Bergstrom et al.,* 2003; *Jury and Whitehall,* 2009].

1.3 Why regional climate modelling?

The climate model era dawned in the late 1970s with the development of global atmospheric models, which were typically run at very coarse resolutions ranging between 5°-7.5°. The need for resolving processes occurring at sub-grid-scale resolution led to the evolution, in the late 1980s, of limited-area models for climate applications. This work was pioneered by Dickinson et al. [1989] and Giorgi [1990], and is essentially based on the idea that a low-resolution global model or gridded observational dataset can be used as lateral boundary forcing for a high-resolution regional model focusing on a specific area of interest (see fig. 1.3 for an idealised depiction of this concept).

Over the years, both global and regional climate models have continued to develop in parallel, as our understanding of the earth system has improved and computing resources have advanced. The current generation of global climate models (GCMs) can run at resolutions as high as up to 50km (some even up to 20km, but with considerable changes to model physics) and most have been coupled to ocean and sea-ice models (AOGCMs), as well as to dynamic vegetation, hydrological and aerosol-chemistry models. The complexity of these models, however, means that simulating at such high resolutions over the long multi-century periods necessary for climate studies is not computationally feasible, and, at present, global models are typically still run at resolutions ranging from ~125-400km. This is

particularly true for global chemistry-climate models, which are extremely computationally intensive and which are generally still run at even lower resolutions (e.g. at ~2ºx 2.5º latitude by longitude).

Regional climate models (RCMs), which are currently run at resolutions varying anywhere between less than 10 to 80km, therefore continue to provide higher spatial information than GCMs [*Vannitsem and Chome*, 2005; *Solomon et al.,* 2007]. The fine-scale resolution of topography, land-use characteristics and vegetation structure means that RCMS are better able to resolve the local effects these features have on weather and climate more accurately than the current generations of GCMs [*Christensen et al.,* 1997; *Joubert et al.,* 1999; *Giorgi et al.,* 2006]. This high resolution is particularly important for the simulation of aerosol processes, which, as mentioned, are highly heterogeneous in space and time [*Simmons et al.*, 2004].

Figure 1.3: A schematic representation of the horizontal and vertical resolution typical of a regional climate model (RCM).

Over the past two decades RCMs have been widely applied in various studies around the globe. Most studies have concentrated on the northern hemisphere, where, traditionally, the technical capacity for carrying out these studies has been focused. Compared to other regions, relatively few regional modelling studies have been carried out over Africa and a large part of this work has focused on the West African Monsoon region [e.g. *Afiesimama et*

al., 2006; *Konare et al*., 2008]. Although some regional climate modelling investigations have been carried out over the southern African region [e.g. *Joubert et al.,* 1999; *Hudson and Jones,* 2002a; *Tadross et al.,* 2005, 2006], no studies have yet examined the aerosol-climate impacts over the subcontinent using a coupled regional climate-chemistry model. In addition, very few modelling studies have concentrated on climate change scenarios for southern Africa [e.g. *Hudson and Jones,* 2002b]. Investigating the impact of climate change, and the likely feedbacks of aerosol forcing on this signal, is essential for the southern African region given its vulnerability and relatively low level capacity for mitigation and adaptation [*Solomon et al.,* 2007]. To date, only a very limited number of studies have investigated these impacts.

1.4 Goals and aims of this study

The primary goal of this work is to investigate the direct and semi-direct radiative effects of aerosols on the southern African regional climate. For this purpose, the regional climate model RegCM3, which includes a basic land surface model as well as aerosol-chemistry and mineral dust emission modules, is used. We concentrate on the direct and semi-direct radiative effect of aerosols, since these aspects of aerosol forcing are more completely understood over Africa, at least in terms of the physical nature of such processes, and are thus better formulated in RegCM3. In addition, we focus on the dry austral winter season, since during these months very little precipitation occurs over southern Africa and the indirect aerosol effect is likely to be of little consequence to the regional atmosphere [*Swap et al.,* 2003].

Within this context, the initial step is to validate RegCM3 and its aerosol chemistry module over the southern African region and in particular to assess the degree of uncertainty associated with the parameterisation of certain aerosol processes, such as emission and deposition. Thereafter, the second step is to explore the seasonal average climatic impacts of the atmospheric aerosol burden and to investigate the degree of variability between simulated impacts when using different biomass burning aerosol emissions inventories and different boundary forcing conditions. This is especially important given the high degree of uncertainty still associated with such emissions estimates (ranging up to a factor of two [e.g. *Korontzi et al.,* 2004; *Liousse et al.,* 2010]. Finally, the last step is to evaluate the variability of the various aerosol-climate impacts at different time scales, ranging from the interannual to the synoptic. The possible temporal variability of aerosol-climate impacts is a feature little explored in the literature, but one that is of considerable importance given the multitude of time scales over which aerosol processes act.

To summarise, the main objectives of this work are identified as:

- evaluating the internal variability within RegCM3 and determining the model

sensitivity to various parameters associated with the online aerosol module;

- assessing the ability of RegCM3 to reproduce southern African regional climate and especially seasonal atmospheric aerosol characteristics;
- investigating the simulated direct and semi-direct aerosol effects on the regional climate during the austral winter and to explore the sensitivity of model simulated aerosol-climate impacts in response to various aerosol emissions inventories and a forced sea surface temperature-feedback; and
- investigating the aerosol-climate impacts at different time scales, ranging from the interannual to the synoptic scale.

This thesis has been developed into five sections to respond to these aims. Chapter two provides a general overview of the literature relevant to this study, including a description of the southern African region, various aerosol processes and the wide range of observations used for model validation. Chapter three includes a description of the regional climate model used, as well as results from a number of sensitivity tests that were carried out to assess model sensitivity over southern Africa. On the basis of these results the best model configuration over the southern African region was chosen. Chapter four is based on work carried out for the article 'Simulation of the direct and semi-direct aerosol effects on the southern Africa regional climate during the biomass burning season', recently published in the Journal of Geophysical Research [*Tummon et al.*, 2010]. This chapter focuses on the climatic impact of biomass burning aerosol during the southern hemisphere winter season over the 2001-2006 period. Chapter five extends this work, covering a 20-year period, specifically aimed at investigating the variability of aerosol impacts at different scales, from the interannual through to the synoptic, as well as to further explore the uncertainty resulting from another, decadal-average emissions inventory. Finally, a summary of the most relevant results as well as perspectives on the investigations carried out completes this work in the final section, chapter six.

CHAPTER 2

Background and introduction

2.1 Southern Africa: A regional description

2.1.1 Regional climate and mean circulation patterns

Southern Africa is a diverse and dynamic region in terms of many aspects: culturally, politically, ecologically and climatologically. Landscapes contrast widely, varying from poor to wealthy, stable to fluctuating and rich and fertile to dry and barren. Because of this variety, the subcontinent provides a unique and challenging environment in which to investigate the multitude of components that make up the regional coupled atmosphere-ocean system.

Geographically speaking, southern Africa is most frequently described as the region south of approximately 10ºS [*Tyson and Preston-Whyte*, 2000]. Much of the subcontinent lies on an elevated plateau at altitudes well in excess of 1000m, while the coastal margins are narrow, particularly in the south and southeast. Vegetation coverage essentially follows the north-south precipitation gradient, with the northern, wetter parts being dominated by broad-leafed, deciduous woodlands and dry forests. This progressively transitions into semi-arid, fine-leafed savannahs and grasslands that extend through most of the southern, drier parts of the region [*Privette et al.*, 2004; *Shugart et al.*, 2004]. To the very southwest, where semi-arid to arid conditions prevail, vegetation cover is sparse and shrubland or semi-desert vegetation dominate [*Privette and Roy*, 2005].

Most of southern African is situated in the subtropics, experiencing warm, dry winters and hot, humid summers. The regional atmospheric circulation is dominated by the semi-permanent high-pressure systems that constitute the general circulation of the southern hemisphere in this zone (see fig. 2.1.1). Except for at the surface, circulation patterns are anticyclonic for much of the year, the result of subsidence associated with the descending branch of the southern Hadley Cell [*Tyson and Preston-Whyte,* 2000; *Reason et al.,* 2006]. These

circulation patterns are most frequent during the austral winter, from May through September, when the southern hemisphere Hadley Cell moves northwards and land surface temperatures are cooler. During this season the Inter-Tropical Convergence Zone (ITCZ), associated with the convergence of the northern and southern Hadley Cells is situated in the northern hemisphere.

As the year progresses and the surface warms, the southern Hadley Cell and ITCZ migrate southwards. This signals the beginning of the rainy season for most of southern Africa in October and November. On average, the ITCZ extends to about 15-17ºS, although this may vary by several degrees latitude from year to year [*Torrance,* 1972]. In some years it is situated further north than average, near 10-12ºS, and during these seasons southern African rainfall tends to be below normal since the comparatively dry south-easterly trades that form the southerly branch of the ITCZ dominate regional circulation patterns. In other years, the ITCZ strays unusually far south, sometimes reaching as far as 20ºS, bringing with it anomalously moist air and heavy rain to these regions [*McHugh and Rogers,* 2001]. Outside of the summer season rainfall may occur sporadically, but generally contributes relatively little to annual precipitation totals [*Tyson and Preston*-Whyte, 2000; Shugart *et al.*, 2004].

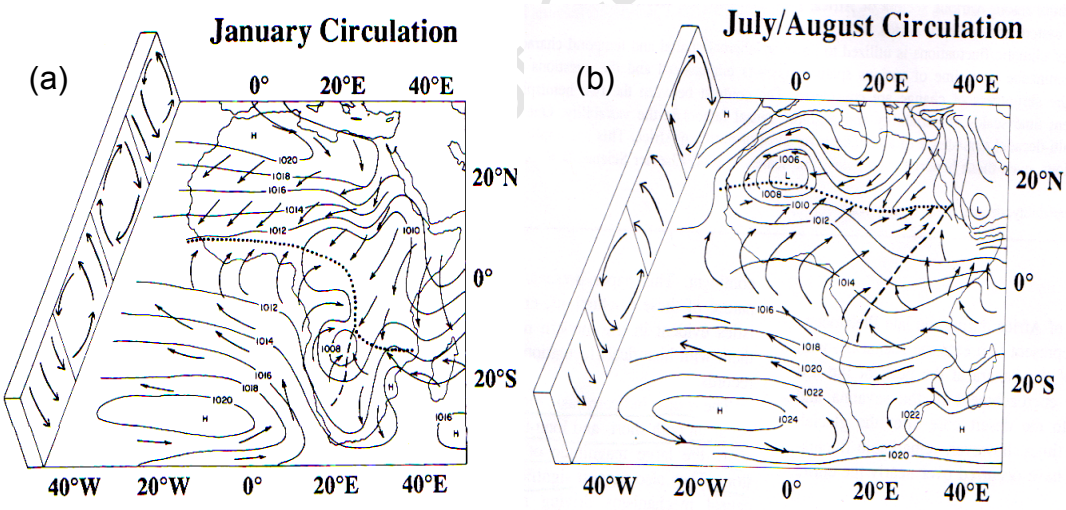

Figure 2.1.1: (a) Summer and (b) winter average sea-level pressure (contours) and winds (vectors) over Africa. The stippled (dashed) line indicates the climatological location of the Inter-Tropical Convergence Zone (Zaire Air Boundary). Average vertical circulation patterns are presented on the left of each figure. [*Following Nicholson and Grist, 2003*].

A secondary convergence feature, the Zaire Air Boundary (ZAB; alternatively known as the Congo Air Boundary) originating from the South Atlantic, also influences circulation and precipitation patterns, particularly over the western half of the subcontinent [*Tyson and*

Preston-Whyte, 2000; *McHugh and Rogers*, 2001]. The ZAB affects southern Africa largely only in the austral summer when it extends from southwest to northeast traversing the subcontinent at similar latitudes to the ITCZ and eventually converging with this feature over eastern central Africa [*Tyson and Preston-Whyte*, 2000; see fig. 2.1.1]. As this air stream moves eastward over the Congo basin and flows toward the higher elevations of eastern Africa it cools adiabatically and brings abundant rainfall to these regions [*Torrance*, 1972; *Nicholson*, 1996]. The seasonal average position of the ITCZ and ZAB in both the southern hemisphere summer (January) and winter (July/August) seasons can be seen in figure 2.1.1(a) and (b) respectively.

Anticyclonic circulation returns to dominate the regional atmosphere as the rainy season comes to an end in March and April and the ITCZ begins its migration back towards the northern hemisphere. As the land surface cools and dries a surface temperature gradient is established between the semi-arid southern parts of the subcontinent and the sub-humid, perennially vegetated regions further north. From August onwards this temperature gradient induces a seasonal jet system, the southern branch of the African Easterly Jet (AEJ-S), which is usually persistent through until December [*Nicholson and Grist,* 2003]. Over the continent this jet has a well-defined core centred near 5º south at an altitude of approximately 700hPa, but over the adjacent Atlantic Ocean, the AEJ-S is situated closer to the equator and is neither as persistent nor as strong as over land. During the late summer (January to March) the jet degenerates as the ITCZ shifts back into the southern hemisphere and the precipitation it produces over the southern semi-arid regions reduces the strong surface temperature gradient that contributes to the formation of this jet [*Nicholson and Grist,* 2003].

The south-western-most tip of the subcontinent is the only region that does not experience a summer rainfall regime. Closer to the mid-latitudes than the tropics, this small portion of southern Africa receives maximum precipitation in the austral winter when the westerlies that dominate the temperate southern hemisphere regions strengthen and expand equatorward [*Cosijn and Tyson*, 1996; *Shugart et al.*, 2004]. Rainfall is significant from July through to November, when the mid-latitude jet stream, a core feature of the westerly circulation patterns, reaches its most northerly position centred near 25°S [*Garstang et al.*, 1996; *Tyson and Preston-Whyte*, 2000]. Similar to the AEJ-S, this jet stream is maintained by a strong meridional temperature gradient, but on this occasion one that exists in the mid- and upper troposphere.

Circulation patterns over the adjacent Atlantic and Indian Oceans are more consistent than over land, with anticyclonic conditions prevalent throughout the year. Although these systems undergo seasonal intensification and shift both in terms of latitude and longitude from season to season, they effectively remain a strong feature of the high-pressure systems that dominate the subtropical belt [*Tyson and Preston-Whyte,* 2000]. On the daily scale, the

Atlantic high may ridge east and south of the continent, sometimes leading to the 'budding' off of a separate high that then migrates eastward to the Indian Ocean. These ridging anticyclones strongly affect the weather of the subcontinent, particularly during the austral summer when the ocean high-pressures are most intense [*Tyson and Preston-Whyte,* 2000].

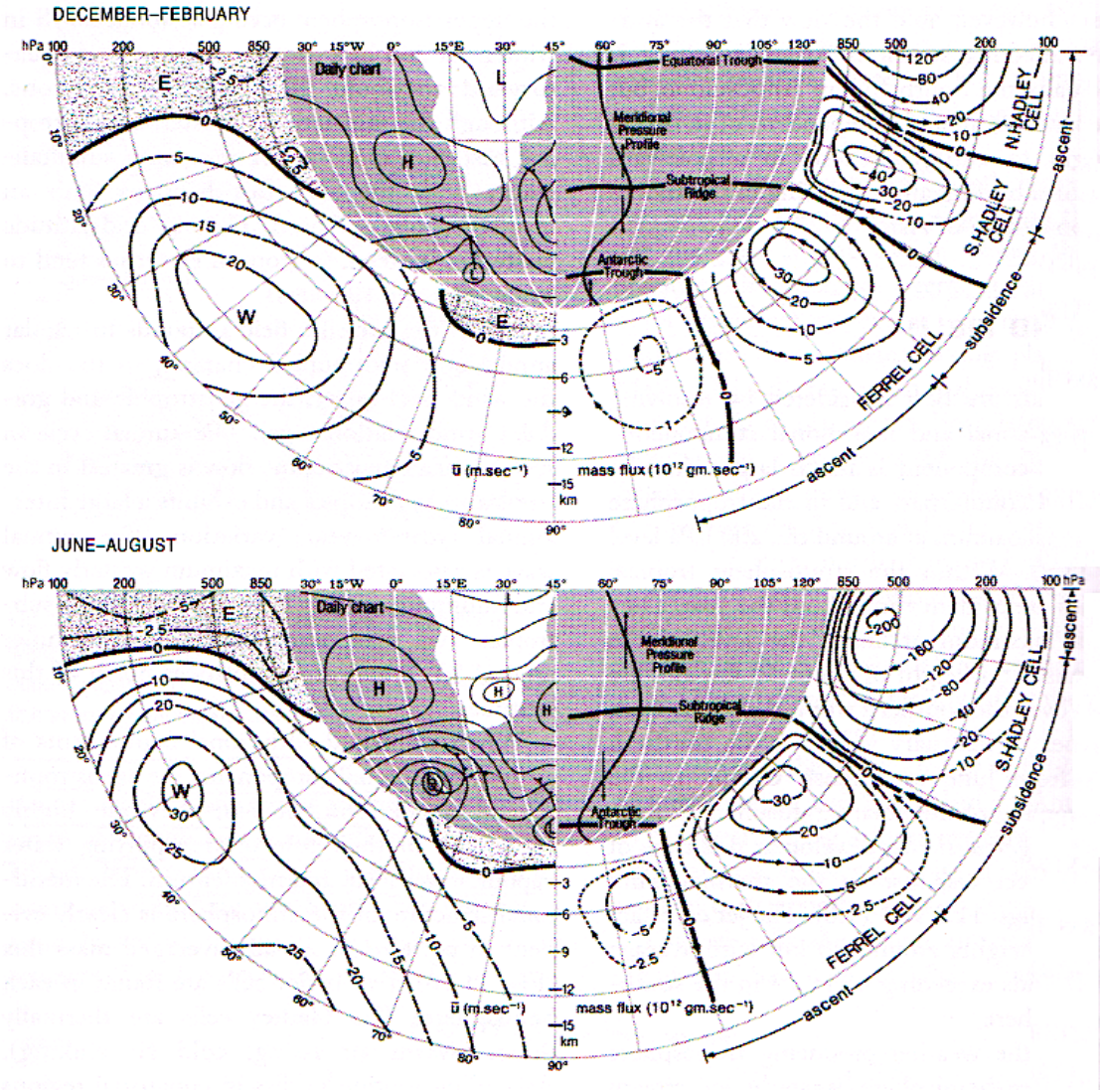

Figure 2.1.2: Mean austral summer (a; December to February) and winter (b; June to August) zonal wind (left sections) and mass flux (right sections). Areas where easterly zonal winds dominate are stippled grey (left sections) and dotted lines indicate mass flux contours less than 10^{12}gm.s^{-1} (right sections). [*Following Tyson and Preston-Whyte, 2000*].

A number of the above-mentioned features are also evident in fig. 2.1.2, which shows the mean summer (December-February) and winter (June-August) zonal wind (left) and mass flux (right) profiles of the Southern Hemisphere. Seasonal average surface pressure (left) and meridional pressure profiles (right) are also shown in this figure. The latitudinal position of the

southern Hadley cell and the climatological region of subsidence (stretching over much of southern Africa, especially in winter) are clear. The position of the mid-latitude westerly jet is also evident near 200hPa during both seasons, as are the semi-permanent high pressure systems over the Atlantic and Indian Oceans.

2.1.2 Absolutely stable layers

The predominance of anticyclonic circulation and large-scale subsidence over southern Africa results in clear, dry conditions and adiabatic warming occurs throughout much of the regional atmosphere [*Tyson and Gatebe*, 2001; *Kirkman et al.,* 2000]. The clear conditions mean that during the day the rate of incoming solar radiation is high, while at night significant cooling can occur. This, in combination with the adiabatic warming that occurs, creates the potential for a very a stable atmospheric thermodynamic structure, ideal for the generation of absolutely stable layers throughout the troposphere [*Tyson et al.,* 1996].

Absolutely stable layers are defined as regions where the environmental lapse rate is less than the saturated adiabatic lapse rate [*Tyson et al.,* 1996]. At any one time, up to four such layers may be present simultaneously over southern Africa [*Tyson et al.,* 1996; *Tyson and Gatebe*, 2001]. These layers confine both horizontal transport and vertical diffusion of aerosols and trace gases (including water vapour) over the entire subcontinent and lead to an accumulation of both anthropogenic and biogenic products in the regional atmosphere [*Tyson et al.*, 1996; *Freiman and Tyson*, 2000; *Tyson and Gatebe*, 2001; *Freiman et al.,* 2002]. The longevity and ubiquity of these features is unique to southern Africa, and they are of considerable consequence, particularly in terms of regional atmospheric chemistry [*Swap et al.*, 2002a,b].

The lowest of these absolutely stable layers occurs at approximately 850hPa, and is associated with the top of the mixing layer over the narrow coastal regions. This layer does not exist over the central plateau region since the plateau is, for the most part, higher in altitude than this level [*Cosijn and Tyson*, 1996]. In addition to anticyclone-associated subsidence, the development of the 850hPa absolutely stable layer is also affected by ocean-atmosphere heat fluxes, topographical influences, as well as sea breezes [*Freiman and Tyson*, 2000]. The second absolutely stable layer, which forms near 700hPa, occurs over the entire southern African region and is associated with the top of the mixing layer over much of the central plateau [*Kirkman et al.*, 2000]. Both of these lower layers are frequently disrupted by the passage of low-pressure systems, which promote vertical mixing of aerosols and trace gases up to the 500hPa level. On average these low-pressure systems pass every six to seven days [*Preston-Whyte and Tyson*, 2000; *Tyson et al.*, 1996].

The third absolutely stable layer forms preferentially at 500hPa and is the most persistent, being present on approximately 78% of the days of the year and at times for as long as up to 40 consecutive days [*Cosijn and Tyson*, 1996; *Tyson et al.*, 1996; *Piketh et al.*, 1999a; *Freiman and Tyson*, 2000; *Freiman and Piketh*, 2003]. Due to its enormous spatial extent (often covering up to 30º latitude) and the dense haze that is often trapped below this layer, it is commonly referred to as the 'African haze layer' [*Tyson et al., 1996*; *Garstang et al.*, 1996]. Above this layer the air is remarkably clear, with aerosol number concentrations dropping by at least two orders of magnitude from between 3000-10000/cm^3 in the haze layer to between 10-90/cm^3 above it [*Tyson and D'Abreton*, 1998]. The fourth and highest level occurs at approximately 300hPa in the upper troposphere and is of greater relevance to the vertical and horizontal transport of ozone than to aerosols and trace gases [*Tyson et al.,* 1996].

Somewhat surprisingly, absolutely stable layers are common even in the wet summer season on no-rain days, occurring on over 70% of all days over South Africa [*Cosijn and Tyson,* 1996]. Only deep convection or unstable barotropic easterly disturbances occurring during the rainy season cause a break down of the stable layers at all four levels simultaneously. These processes induce extensive vertical mixing and also enhance aerosol transport out of the region [*Cosijn and Tyson*, 1996; *Garstang et al.*, 1996; *Freiman et al.,* 2002]. Equatorward of 15°S the stable layers rise in altitude and ultimately disappear in the convective region of the ITCZ [*Garstang et al.*, 1996].

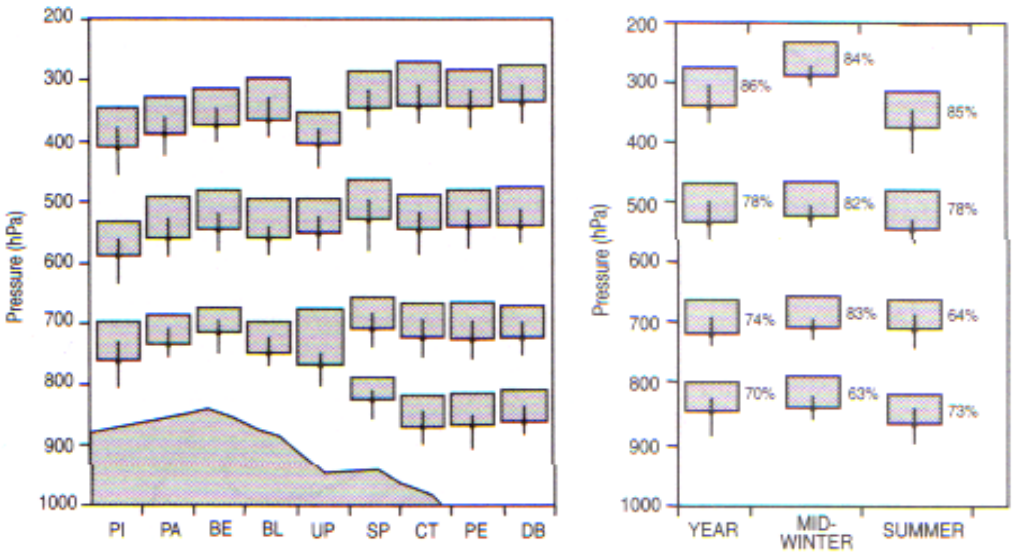

Figure 2.1.3: The occurrence of absolutely stable layers on no-rain days over South Africa averaged over the seven-year period 1986-1992 from a total of 2925 radiosonde ascents at (a) nine different stations and (b) averaged over different periods of the year (% occurrence). The depth of each layer is indicated by the vertical extent of each box and vertical lines give the standard deviation of base height. PI denotes Pietersberg, PA Pretoria, BE Bethlehem, BL Bloemfontein, UP Uppington, SP Springbok, CT Cape Town, PE Port Elizabeth and DB Durban. [*Following Cosijn and Tyson, 1996*].

The average position and frequency of occurrence of the four absolutely stable layers is shown in fig. 2.1.3 for nine stations in South Africa where radiosonde measurements were taken from 1986-1992. The altitude of all four (three) layers over the coastal (plateau) stations is clear (fig. 2.1.3(a)), as is the very high frequency of occurrence throughout the year (fig. 2.1.3(b)). Also presented are the average vertical depth and variability of base height of each level (vertical lines extending from the bottom of each box).

On occasion, absolutely stable layers may merge for one or several days, causing the aerosols trapped below these layers to mix. For example, merging of the 700 and 500hPa layers has been found to occur as frequently as 35 and 25% of the time in summer and winter respectively [*Freiman and Tyson*, 2000]. Alternatively, if a particular layer is not present, aerosols are also vertically mixed up to the next stable layer [*Freiman et al.*, 2002]. In general, all the stable layers are relatively shallow features, seldom exceeding 1km in depth [*Cosijn and Tyson*, 1996]. Interestingly, despite large differences in synoptic conditions and their respective aerosol accumulation mechanisms, the vertical structure of the southern African lower troposphere remains remarkably similar, with all major absolutely stable layers present in similar vertical positions and extending over similar regions horizontally [*Stein et al.*, 2003].

2.1.3 Recirculation over southern Africa

The dominant anticyclonic circulation patterns also result in a significant amount of recirculation of air, at local, regional and subcontinental scales [*Tyson et al.*, 1996; *Piketh et al.*, 1999b; *Tyson and Gatebe*, 2001]. Recirculation can be defined as the recycling of air, or transport that returns an air parcel to its point of origin from the opposite direction to which it left, having rotated or recurved in cyclonic or anticyclonic circulation systems [*Tyson and Gatebe*, 2001; *Torres et al.*, 2002]. On average over the year, approximately 54% of all air is recirculated at least once over the subcontinent before exiting to either the Atlantic or Indian Ocean. Recirculation is induced by either stationary continental high pressure systems, which occur on average 40% of the year (maximum in July (70%) and minimum in January, (15%)), or with the passage of transient ridging anticyclones, which commonly follow in the path of mid-latitude low-pressure systems [*Tyson et al.,* 1996; *Piketh et al.*, 1999a; *Torres et al.*, 2002].

Recirculation also occurs, although to a lesser degree, from the Atlantic and Indian Oceans back towards the subcontinent. The air thus returns containing marine aerosol, which may have become incorporated into the air parcel during transport [*Garstang et al.*, 1996; *Tyson and D'Abreton*, 1998; *Piketh et al.*, 1999a; *Eck et al., 2003*]. Recirculation back towards the subcontinent is biased towards the west coast, where, at 15°E, approximately 35% of air

recirculates back towards the east. In contrast, over the east coast, at 35ºE only 13% of air recirculates back towards the continent [*Garstang et al.*, 1996].

The atmospheric lifetime of a particular aerosol species depends largely on its physical and chemical properties, as well as its place, time and height of release. As a consequence of the high degree of recirculation, aerosol residence times over southern Africa are considerably longer compared to most other regions [*Tyson et al.*, 1996; *Liousse et al.,* 1996]. The climatological mean recirculation period over southern Africa is approximately 7-10 days, however, on occasion air has been found to recirculate over the subcontinent as long as 20 days. Recirculation thus maintains high aerosol loads over the region [*Swap and Tyson*, 1999], particularly during winter, when there is little humidity or precipitation [*Tyson et al.*, 1996; *Tyson and D'Abreton*, 1998; *Piketh et al.*, 1999a]. Importantly, the maintenance of cloud-free conditions and high-levels of insolation associated with the prevalent anticyclonic circulation patterns also enhance heterogeneous photochemical transformations of airborne species [*Swap et al.*, 2003].

2.1.4 Aerosol plumes exiting the subcontinent

Despite the high degree of recirculation and the long atmospheric lifetime of aerosols over the southern African subcontinent, a significant quantity of aerosol are transported offshore from the region to the adjacent Atlantic and Indian Oceans in large plumes before deposition occurs [*Tyson and D'Abreton*, 1998; *Piketh et al.*, 1999a]. In fact, little material is deposited during transport over the continent, with aerosol concentrations in the plumes remaining fairly constant from the regional interior through to the coastal areas [*Tyson and D'Abreton*, 1998].

The location of the two major exit pathways depends on the relative position of the semi-permanent anticyclone over the subcontinent, but is generally restricted to south of approximately 10°S [*Tyson et al.*, 1998; *Tyson and D'Abreton*, 1998]. The plumes vary in depth and form depending on the prevalent synoptic conditions, but always lie above the marine boundary layers of both oceans, which occur between the surface and approximately 1.5km above sea level around most of the southern African coast [*Tyson and D'Abreton*, 1998]. The plumes are complex in structure, simultaneously being made up of in- and out-flowing air streams, which may either lie very close to each other or be separated by hundreds of kilometres [*Tyson and D'Abreton*, 1998].

Approximately 75% of all southern African air exits via the Indian Ocean plume, which can reach almost 1000km in width [*Tyson and D'Abreton*, 1998; *Piketh et al.*, 1999a; see fig. 2.1.4]. This plume is a major feature not only of the regional atmosphere but also of the southern hemisphere. It transports an estimated 45 million tons of aerosol each year and

plays a significant role in large-scale, inter-regional aerosol transport [*Tyson and Gatebe*, 2001]. The air and particulate matter it contains is frequently transported to Amsterdam Island [*Moody et al.*, 1991] and, on occasion even as far as Australia and New Zealand [*Sturman et al.*, 1997; *Pak et al.,* 2003]. The Indian Ocean plume exits the subcontinent with its core situated near 31°S at an altitude of approximately 750hPa [*Piketh et al.*, 1999a]. As the air moves offshore and eastwards, it rises, reaching up to 450hPa, before re-descending to near the surface over the central Indian Ocean at approximately 70°E [*Tyson and Gatebe*, 2001; *Torres et al.*, 2002]. Deposition into the southern Indian Ocean occurs throughout transport by gravitational settling and precipitation processes. The plume occurs most frequently in winter (72% of all days from May-August), whilst occurring only 33% of all days in summer (November-February) [*Tyson and D'Abreton*, 1998].

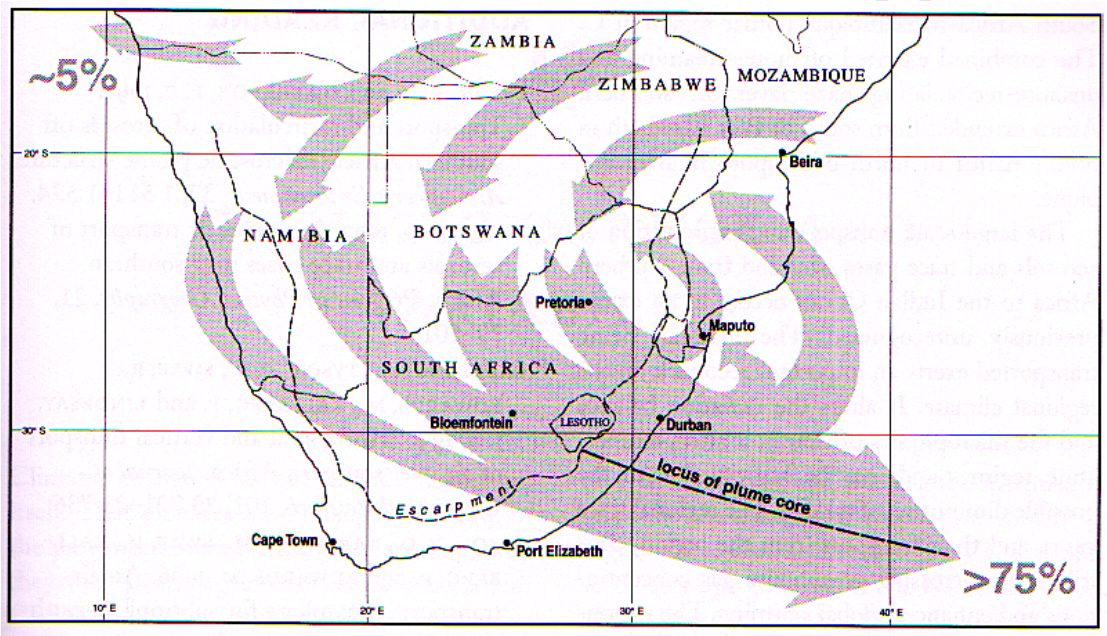

Figure 2.1.4: Generalised atmospheric transport pathways over southern Africa, including the large Indian Ocean and smaller Atlantic Ocean plumes and recirculatory structures. [*Following Tyson and Preston-Whyte, 2000*].

Although the frequency of occurrence of air transport towards the Indian Ocean does not vary significantly from year to year, there appear to be significant differences in the plume structure and position from year to year as a result of the different circulation patterns typical of wet and dry conditions [*Garstang et al.*, 1996]. A clearly defined Indian Ocean plume was visible during the SAFARI-92 experiment (a dry year), whilst during SAFARI-2000 (a wet year) the plume was considerably more diffuse. It is likely that diminished strength of the mid-latitude westerlies and the increased recirculation that occurs during dry years contribute to

these differences [*Garstang et al.*, 1996; *Swap et al.*, 2003; more about the SAFARI campaigns in section 2.3].

A series of events leads up to Indian Ocean outflow events. Initially, a high pressure anticyclonic system or col region forms over the subcontinent during which aerosols accumulate over the region [*Stein et al.,* 2003], then the passage of low pressure system travelling in the westerlies induces offshore flow and the atmosphere is effectively cleansed as unpolluted marine air is advected over the region and the aerosol-laden air exits the subcontinent towards the Indian Ocean. Aerosols are also rained out if precipitation occurs in association with the cold front.

As a result of the asymmetrical situation of the semi-permanent continental anticyclone over southern Africa, a considerably smaller percentage of aerosol get transported offshore to the Atlantic Ocean [*Tyson and Gatebe*, 2001; again see fig. 2.1.4]. The Atlantic Ocean plume occurs under two different synoptic situations. Firstly, if a quasi-stationary easterly wave is present over the subcontinent, aerosol material is transported to the equatorial Atlantic from the coast of Angola [*Swap et al.*, 1996; *Torres et al.*, 2002]. Or, secondly, if a transient ridging high passes over the region, air gets transported out to the southern Atlantic Ocean off the coast of Namibia [*Kirkman et al.*, 2000]. Direct transport to the equatorial Atlantic Ocean occurs almost exclusively in summer [*Freiman and Piketh*, 2003], when easterly waves and ridging anticyclones are most frequent. In both cases, as air moves off the coast and westwards it subsides rapidly as a result of the equatorward geostrophic flow along the eastern margin of the South Atlantic anticyclone. As a result, most aerosols are deposited to the surface before reaching the meridian of 10°W. The flux of aerosols exiting to this region has been estimated at approximately 29 million tons per year [*Tyson and Gatebe*, 2001].

2.1.5 Southern African climate variability

Southern Africa is characterised by a high degree of interannual and interdecadal climate variability, especially in the western regions [*Tyson* 1986; *Mason and Jury*, 1997*; Tyson and Gatebe*, 2001; *Hudson and Jones*, 2002a]. Interannual variability is dominated largely by sea surface temperature (SST) variability [*Entekhabi and Nicholson*, 1988; *Mason* 1997; *Jury et al.*, 1996; *Rocha and Simmonds* 1997a,b; *Todd and Washington*, 2004; *Washington and Preston*, 2006] and the El-Niño Southern Oscillation (ENSO), which affects the southeastern parts of the subcontinent and East Africa most strongly [*Janowiak*, 1988; *Ropelewski and Halpert,* 1996; *Reason*, 2002; *Jury et al.*, 2004].

In terms of SSTs Mason [1990] showed, that at least over South Africa, SSTs in the South Atlantic explained the greatest amount of variance in rainfall throughout the year, while

variability in southwest Indian Ocean SSTs, which is statistically independent of ENSO, has also been found to influence southern African rainfall variability significantly [*Washington and Preston*, 2006]. These latter authors found that an enhanced poleward SST gradient in the southwest Indian Ocean is associated with extreme dry years, whilst a weakened gradient is associated with some extreme wet years [*Washington and Preston*, 2006].

In terms of the ENSO, El Niños (La Niñas) generally induce warm and dry (cool and wet) conditions over much of southeastern Africa. In East Africa the reverse is true, with El Niños (La Niñas) being linked with flooding (drought) [*Janowiak*, 1988; *Ogallo*, 1988; *Kiladis and Diaz,* 1989; *Ropelewski and Halpert,* 1996]. The ENSO signal is thought to be communicated from the tropics to the extra-tropics through SST changes, particularly from the Indian Ocean [*Nicholson and Kim*, 1997; *Richard et al.,* 2001], as well as through the atmosphere, as an 'atmospheric bridge' [*Richard et al.,* 2000; *Richard et al.,* 2001]. This results in a lag between the observed timing of ENSO impacts in the tropics and mid-latitudes. As a consequence of the circulation changes induced around the globe, the subtropical westerly jets shift equatorward (poleward) and tend to intensify during El Niño (La Niña) events [e.g. *Horrell and Wallace*, 1981; *Sinclair et al.*, 1997]. Warm and cool ENSO events occur with a periodicity of between three to seven years, peaking around three to four years [*Janowiak*, 1988; *Ropelewski and Halpert*, 1996; *Tyson and Gatebe,* 2001].

Interannual variability over southern African has also been linked with the North Atlantic Oscillation (NAO) [*Rogers*, 1984; *McHugh and Rogers*, 2001; *Jury*, 2009]. During positive NAO phases the Icelandic low-pressure system deepens, while the high-pressure over the Azores region to the south strengthens [*Hurrell*, 1995]. The NAO has a mean period of between 7.3-8 years and has been observed in rainfall patterns [*Jury,* 2009], air pressure fields as well as upper-level zonal winds [*Hurrell*, 1995]. The NAO is exhibited through five elongated bands of alternating zonal wind anomalies extending from the Arctic to equatorial Africa [*McHugh and Rogers*, 2001]. When the NAO is positive (negative) the most southerly band exhibits anomalous westerly (easterly) flow and divergence (convergence) occurs over southeastern Africa and the region experiences anomalously wet (dry) summers [*McHugh and Rogers*, 2001; Jury, 2009]. These shifts in zonal winds appear to be related to movement of the ITCZ, which shifts southward (northward) when the NAO is positive (negative) [*McHugh and Rogers*, 2001].

The Antarctic Oscillation (AAO), alternatively known as the Southern Annular Mode (SAM), is essentially the southern hemisphere equivalent of the Northern Annular Mode (NAM), to which the NAO is closely related. Positive AAO phases are associated with a stronger pressure gradient between mid- and high-latitudes, resulting in a strengthening of the westerlies as well as anomalously warm temperatures in the mid-latitudes but unusually cool temperatures over the Antarctic [*Thompson and Wallace,* 2000*; Thompson and Solomon,*

2002; *Reason and Roualt,* 2005]. The negative phase is associated with the reverse conditions. The AAO has been found to contribute significantly to climate variability over southern Africa, particularly the most southern reaches of the subcontinent, which are most affected by the mid-latitude westerlies and the low pressure systems transported in the upper-level jet stream associated with these winds [*Reason and Roualt,* 2005; *Reason et al.,* 2006].

Southern Africa is also subject to interdecadal variability, which has been observed with a quasi-periodicity in the range of 16-20 years, peaking at 18.6 years [*Nicholson*, 1986]. This oscillation has been observed in the precipitation and temperature signals of the summer rainfall region of South Africa [*Keen*, 1971], river runoff [*Abbott and Dyer*, 1976], tree rings [*Tyson*, 1978], as well as in sea surface temperatures around the southern African subcontinent [*Mason*, 1990]. This decadal-scale climate variability appears to be strongly linked to changes in circulation patterns, however, the cause of this modulation remains uncertain [*Tyson and Preston-Whyte*, 2000]. The oscillation varies between positive and negative phases during which the large-scale circulation fields vary substantially [*Harrison, 1988; Tyson and Preston-Whyte*, 2000]. During wet (dry) years the tropical easterlies strengthen (weaken) whilst the mid-latitude westerlies weaken (strengthen). North of 10°S little change in circulation is observed between wet to dry spells [*Garstang et al.*, 1996].

2.1.6 Observed temperature and precipitation trends

These interannual and interdecadal modulations of climate variability occur on top of background, long-term trends. In southern Africa trends in both surface temperature and precipitation have been observed over the past few decades. Observations of mean annual maximum temperatures indicate that they have steadily risen over much of southern Africa, with maximum temperatures over the central interior having increased by as much as 2°C per century since 1900. In contrast, the southern and southeastern parts of South Africa have been observed to have cooled by nearly 1°C over the same period [*Tyson et al.,* 1998]. In terms of precipitation, little systematic change over the last century has been observed over much of southern Africa. Only over the central tropical region, which includes western Angola, have rainfall increases of over 10% per century (since 1900) been observed [*Tyson and Preston-Whyte*, 2000]. Despite there being little long-term trend in annual rainfall amounts, Mason et al. [1999] reported an increase of the most extreme type of daily precipitation over South Africa, while Usman and Reason [2004] found a similar increase in the frequency of heavy rainfall events over the 1979-2002 period for the southern African region in general.

2.1.7 Future climate projections

Recent regional projections suggest that southern Africa may warm by between 2-6°C by 2100, with winter minimum temperatures expected to increase most significantly over the central regions [*Tyson and Gatebe*, 2001; *Hudson and Jones*, 2002b; *Solomon et al., 2007*]. Warming is projected to be less significant in the equatorial and coastal regions; however, the estimated temperature changes over the entire region exceed one sigma level of natural temperature variability [*Hulme et al.,* 2001; *Solomon et al., 2007*].

Precipitation projections are considerably more uncertain, but simulations suggest that over most of southern Africa rainfall is likely to become more intense and dry spells longer, trends which, as just described, have already begun to be observed [*Tyson and Gatebe*, 2001; *Hudson and Jones*, 2002b; *Reason et al.,* 2006; *Solomon et al., 2007*]. Summer rainfall is projected to decrease over the central western tropical and subtropical regions, with reductions of up to 2mm/day, translating into decreases of 20-30% [*Hudson and Jones,* 2002a,b]. It appears that increased subsidence in this region, indicated by a strengthening of both the South Atlantic and South Indian anticyclones, contributes to this precipitation signal [*Hudson and Jones,* 2002b]. In concert with the projected decreases in summer rainfall, the increased warming also means decreased cloud cover, increased rates of potential evapotranspiration and a resultant reduction in soil moisture [*Hudson and Jones*, 2002b; *Balling*, 2005]. It has thus been suggested that there will likely be an increase in the frequency, intensity and magnitude of droughts in Africa [*Balling*, 2005].

In contrast, the eastern equatorial areas are expected to become wetter, with more intense precipitation events (but little change in the number of rain days) [*Giorgi et al.,* 2001; *Hudson and Jones,* 2002a,b; *Hewitson and Crane,* 2006]. Under warmer atmospheric conditions specific humidity generally increases, particularly in the equatorial regions, and this is likely to enhance moisture convergence and precipitation in this region [*Hudson and Jones,* 2002b]. Similarly, winter rainfall is also likely to increase slightly, although this is of little physical consequence since very little precipitation occurs over most of southern Africa during this season [*Giorgi and Francisco*, 2000; *Giorgi et al.,* 2001; *Hudson and Jones*, 2002b; *Hewitson and Crane,* 2006]. Over the south-western region, projections indicate a reverse trend, with winter rainfall likely to decrease, a signal that is likely to be of significant consequence since this area receives most rainfall in winter [*Tyson and Gatebe*, 2001; *Hudson and Jones*, 2002b; *Hewitson and Crane,* 2006].

2.2 Atmospheric aerosol

Atmospheric particulate material originates from a wide variety of sources, both natural and anthropogenic, and the physical and chemical properties of these particles vary extremely widely. Technically, the term aerosol is used to describe any suspension of solid or liquid particles in a gas [*Seinfeld and Pandis*, 2006]. Aerosols are either emitted directly into the atmosphere (primary aerosol) or form through gas-to-particle conversion processes (secondary aerosol). The huge variety and chemical nature of these sources means that tropospheric aerosols span over four orders of magnitude in size, with particles ranging from just a few nanometres (nm) to tens of micrometers (μm) in diameter [*Seinfeld and Pandis*, 2006].

Once airborne, aerosols may undergo changes in size and/or composition, through various processes such as the condensation or evaporation of gaseous species on to the particle, chemical reaction or coagulation with other particles, or by activation in the presence of water vapour to form cloud or fog droplets or ice particles. Eventually, all aerosols return to the earth's surface through either dry or wet deposition processes. Generally, tropospheric aerosols have relatively short atmospheric residence times, on the scale of several days up to a few weeks, and this factor, in addition to the highly heterogeneous nature of sources, leads to strongly non-uniform spatial and temporal distributions of aerosols around the globe [*Seinfeld and Pandis*, 2006]. The main aerosol sources and atmospheric processes are shown schematically in figure 2.2.1 and are further explained in the remainder of this section.

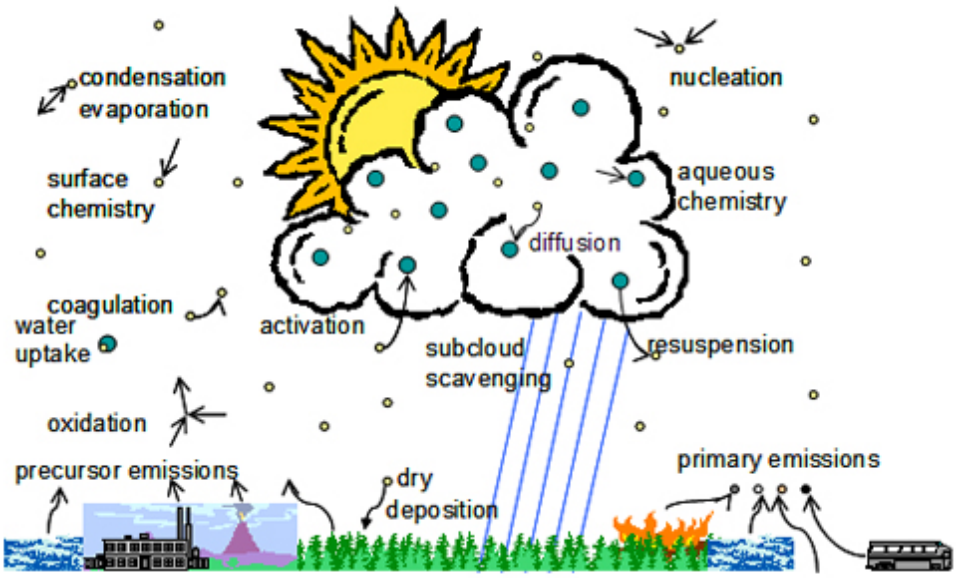

Figure 2.2.1: Schematic diagram representing the major aerosol sources, atmospheric processes and removal mechanisms.

2.2.1 Aerosol formation, particle growth and size distribution

The nature of the process through which aerosols are generated determines the physical and chemical properties of the particle produced. The smallest aerosols are produced through the condensation of gaseous species, which can occur either homogeneously just in the gaseous phase, or heterogeneously on to already existing particles. In all but the most pristine conditions, the large aerosol surface area present in the atmosphere provides a suitable substrate for heterogeneous nucleation, and in general this process tends to dominate [*Seinfeld and Pandis*, 2006]. Larger particles are mostly produced through direct emission into the atmosphere via physical mechanisms, such as wind erosion or from volcanoes, or by chemical mechanisms, such as fossil fuel combustion.

The particle size distribution is of vital importance to a number of processes, determining atmospheric lifetime, as well as the physical, chemical and radiative properties of the aerosol population. Generally, aerosols are divided into two size categories, those with diameters smaller than 2.5μm are usually referred to as 'fine' particulate matter, whilst those greater than 2.5μm in diameter are termed 'coarse' particles (see fig. 2.2.2). Fine and coarse material differ in terms of most aspects, originating from different sources, being transformed and removed through separate processes, as well as having different chemical, physical and optical properties [*Seinfeld and Pandis*, 2006].

Fine particles can further be divided into three modes, a *nucleation* mode comprising particles with diameters up to 10nm, an *Aitken* mode spanning the range from 10nm-100nm (0.1μm) and an *accumulation* mode including particles with diameters from 0.1-2.5μm (although only two of these modes are specified in fig. 2.2.2). The nucleation and Aitken modes make up by far the greatest proportion of aerosols in terms of number, but because of their very small size they make up only a negligibly small fraction of the total atmospheric aerosol mass loading. Accumulation mode aerosols, on the other hand, account for the greatest proportion of total particle surface area [*Sinha et al.*, 2003] as well as a significant fraction of the aerosol mass burden [*Seinfeld and Pandis*, 2006].

Nucleation mode aerosols form through either gas-to-particle condensation or photochemically, while Aitken particles can either be directly emitted as primary particles or generated through gas-to-particle condensation, similarly to nucleation mode particles. Concentrations of particles in these two smallest size modes are depleted primarily as a result of coagulation, as the particles aggregate to form larger, accumulation mode aerosol. The third fine mode, the accumulation mode, owes its name to the fact that both wet and dry aerosol removal processes are least efficient in this size range, resulting in the accumulation of these particles in the atmosphere. Consequently, this size mode generally has the longest

atmospheric lifetime [*Kirkman et al.*, 2000; *Jayaratne and Verma*, 2001; *Seinfeld and Pandis*, 2006].

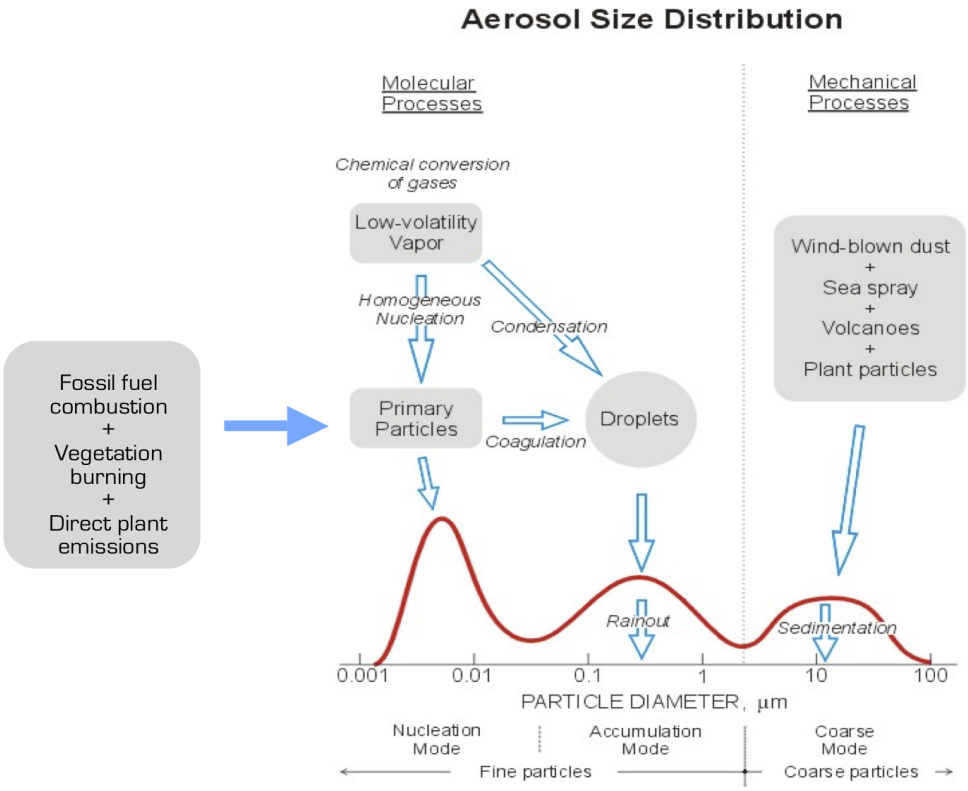

Figure 2.2.2: Schematic diagram of aerosol size distribution including the formation and deposition processes associated with each size mode. [*Adapted from Seinfeld and Pandis, 2006*].

As just mentioned, coarse mode particles form largely through mechanical processes, such as wind erosion, sea salt spray as well as from volcanoes and plants. Sedimentation velocities of these aerosols are high and they generally have relatively short atmospheric residence times compared to fine-mode aerosols. Nevertheless, the coarse mode, in combination with the accumulation mode, contributes practically all the aerosol mass because of the large particle sizes [*Kirkman et al.*, 2000; *Seinfeld and Pandis*, 2006]. Occasionally, an additional category, *giant nuclei,* may be used to describe aerosols with diameters in the size range from 10-20µm.

2.2.2 Aerosol sources

Broadly speaking there are essentially four types of aerosol, each associated with different sources and with different chemical and optical properties: (i) Industrial aerosol derives largely from fossil fuel combustion and other chemical processes occurring in populated

regions, (ii) biomass burning aerosol is produced by vegetative fires, mostly of savannahs and forests, (iii) mineral dust is swept up into the atmosphere by wind and (iv) marine aerosols, which originate from emissions of inorganic sea salt particles or from biological activity [*Dubovik et al.,* 2002]. For modelling purposes aerosol are often separated into those of anthropogenic or natural origin. However, in reality, it is difficult to distinguish between the two, since even individual particles are often mixtures of both natural and anthropogenic components [*Kaufman et al*., 2002].

2.2.2.1 Industrial aerosol

Since 1800 urban populations have continued to grow faster than the total population and the UN estimated that in the year 2000 almost 47% of the global population lived in cities [*Gurjar and Lelieveld*, 2005]. These densely populated urban centres emit significant quantities of aerosol, often resulting in regional air pollution and photochemical smog that consequently reduce air quality [*Molina and Molina*, 2005].

The main sources of industrial aerosol include fossil fuel combustion, coal refining, automobiles, chemical industries as well as ore smelting [*Pham et al.,* 1995]. In general, industrial aerosol particles are hygroscopic and fall into the fine mode category [*Kaufman et al*., 2002]. Unlike most other aerosol sources, industrial emissions fluctuate little throughout the year [*Piketh et al.,* 1999a,b; *Zunckel et al.,* 2000]. Changes in concentrations of gases and aerosols from these sources occur largely only as a result of varying meteorological conditions and seasonal changes in plant physiology, both of which affect oxidation rates, deposition, etc [*Zunckel et al.,* 2000].

Sulphur-containing compounds make up the largest proportion of industrial emissions, with estimates of global sulphur emissions varying from 92-103.6TgS/yr [*Cullis and Hirschler*, 1980; *Muller,* 1992, *Spiro et al*., 1992]. One of the most common of these species is sulphur dioxide (SO_2), which is produced through a wide variety of industrial activities as well as fossil fuel burning [*Taylor and Penner,* 1994; *Qian et al*., 2001]. Present anthropogenic SO_2 emissions are thought to be considerably greater than sulphur-containing gaseous emissions from natural sources, such as dimethyl sulphide (DMS) from marine phytoplankton [*Charlson et al.,* 1992].

Although more than 90% of industrial SO_2 is produced in the northern hemisphere [*Charlson et al.,* 1992], southern Africa, and more specifically South Africa, produces a very significant proportion of the southern hemisphere's fraction of the total (although relative to the global total this fraction remains small) [*Kirkman et al.,* 2000]. Because of the country's ample coal reserves (6^{th} largest in the world), nearly half, or approximately 24GW of Africa's total electricity needs are met by coal-fired power production that occurs in the South African Highveld region (between approximately 25.5°S, 27.5°E and 27°S, 30.5°E) [*Zunckel,* 1999;

Terblanche et al., 2000]. Industrial and energy production activities in this small region releases more than one million tonnes of SO_2 per year, or 94% of South Africa's total SO_2 emissions, as well as almost 86% of the countries scheduled particulate emissions [*Zunckel,* 1999; *Freiman and Piketh*, 2003]. The only other significant industrial source region in southern Africa is the Zambian copper mining belt, situated on the northern border between Zambia and the Democratic Republic of Congo, although in recent years copper production and associated emissions have decreased [*Freiman and Piketh*, 2003].

Oxidation of SO_2 to form sulphate (SO_4) aerosol can occur through either gaseous- or aqueous-phase processes, the rates of which are strongly seasonal since they depend to a large extent on ambient temperature and relative humidity [*Taylor and Penner,* 1994]. Over southern Africa aqueous-phase oxidation is favoured during the humid and warm summer season, while during the dry winter months more gaseous conversion tends to occur [*Zunckel,* 1999; *Piketh et al*. 1999b]. In fact, south of 20°S most of the fine-mode aerosol burden is made up of industrially derived sulphates [*Maenhaut et al.,* 1996; *Piketh et al*. 1999; *Liu et al.,* 2000]. From measurements at 23 sites on the South African Highveld from 1985-1990 SO_4 concentrations varied between 1-15µg/m^3, with a monthly mean of 4µg/m^3 [*Held et al*., 1994]. And, although concentrations decrease significantly away from the main source regions, SO_4 still makes up between 18-37% of the total aerosol loading, or as much as 89% of the fine-mode portion [*Piketh et al.,* 1999b].

The recirculation of sulphur-laden air from the South African Highveld is of considerable consequence for the surrounding countries, since direct transport of trace gas and aerosol loaded air occurs relatively frequently, most particularly in winter. Direct transport to Moçambique occurs about 33% of the time, whilst transport to Zimbabwe occurs 15% of all days of the year. Air is also transported to Botswana and Namibia, but to a lesser extent [*Freiman and Piketh,* 2003]. Air that does not recirculate over the subcontinent exits directly to the Indian Ocean, where an estimated 70% of sulphur is derived from South African industry [*Tyson and Gatebe,* 2001].

2.2.2.2 Carbonaceous aerosol

Although a large proportion of industrially emitted aerosol is made up of sulphurous material, a considerable fraction of anthropogenic aerosol released into the atmosphere is made up of carbonaceous matter. These particles mostly consist of oxidised organic material, the by-product of combustion processes [*Penner et al.,* 1993; *Penner et al.,* 1998; *Seinfeld and Pandis*, 2006]. The combustion processes may not, however, always be related to anthropogenic activity and a large fraction of carbonaceous aerosol are also derived from the burning of vegetation and other biological material. This section provides an insight to the main chemical and physical properties of carbonaceous particles in general, whether from

industrial or natural sources. The following section (2.2.2.3) concentrates particularly on biomass burning and describes related processes in greater detail.

Since most carbonaceous particles are produced through combustion processes they tend to be small, falling into the sub-micron size range (nucleation and Aitken modes) [*Penner et al.,* 1998]. As a result, these aerosols generally have relatively long average atmospheric lifetimes, ranging from 3-7 days [*Liousse et al.,* 1996]. Chemically, carbonaceous aerosol can essentially be separated into two distinct components: black carbon (BC) and organic carbon (OC) [*Penner et al.,* 1998; *Seinfeld and Pandis*, 2006]. Close to sources and in areas of new particle formation these two components are largely externally mixed (i.e. BC, OC and other components remain separate), however, further from source regions the particles mix with each other as well as other airborne species, forming heterogeneous, internally mixed compounds [*Liousse et al.,* 1996].

2.2.2.2.1 Black carbon

Black carbon (BC), alternatively known as soot, is made up largely of agglomerates of small spherules of pure carbonaceous material released directly into the atmosphere as a result of incomplete combustion [*Liousse et al.,* 1996]. BC formation depends strongly on the ratio of carbon to oxygen present in the mixture burned, as well as on temperature, with both lower oxygen concentrations and temperatures resulting in less complete combustion and more BC formation [*Bergstrom et al.,* 2002; *Seinfeld and Pandis*, 2006]. This has important consequences in practice, with flaming fires producing considerably less soot than smouldering phase burning.

Upon release, the small BC particles are spherical and generally cluster together to form straight or branched chain-like structures, which in turn collapse into dense aggregates forming visible soot particles a few micrometers in size. As they do so, whatever components were part of, or attached to the chains, become internally mixed into the particle [*Abel et al.,* 2003; *Posfai et al.*, 2003; *Seinfeld and Pandis*, 2006]. Thus, although black carbon consists largely of pure atomic carbon, particles also usually contain about 10% hydrogen and traces of other elements such as nitrogen, which are often derived from organic vapours absorbed on to the particle surface [*Seinfeld and Pandis*, 2006].

Pure black carbon particles tend to be mostly insoluble upon release, but mixing with other atmospheric compounds (as described above) may render the particle soluble [*Croft et al.,* 2005]. In most present climate models it is assumed that 80% of all BC is released in the hydrophobic state, and the remaining 20% is hydrophilic. After emission, the atmospheric conversion from insoluble to soluble is generally assumed to follow an exponential decay process [*Cooke et al.,* 1999; *Lohmann et al.,* 1999], but, in reality, such processes are more complex and depend on a number of physical processes that affect particle aging, such as

coagulation and various oxidative reactions that occur throughout the atmosphere [*Croft et al.,* 2005]. The solubility of BC particles is of considerable importance, both in terms of optical properties and in terms of deposition processes, since BC particles may double in size as relative humidity increases from 0 to 100% [*D'Almeida et al.,* 1991].

Because of the ubiquity of combustion processes, occurring in industrial regions as well as most vegetated areas, carbonaceous aerosols have significant worldwide distributions [*Liousse et al.,* 1996; *Bergstrom et al.,* 2002]. Global BC emissions have been estimated to range between 8-24.0Tg/yr [*Penner et al*., 1993; *Bond et al.,* 2004], with similar quantities released through fossil fuel and biomass burning [*Eck et al.,* 2003]. Bond et al. [2004] estimated that approximately 8Tg(C)/yr BC was emitted globally in 1996, with 42% of this total derived from open burning. In terms of atmospheric loading, BC concentrations range from 5-20ng/m^3 over the remote open oceans, to 0.2-2µg/m^3 in rural areas and up to 1.5-20µg/m^3 in the major source regions [Clarke, 1989; *Liousse et al.,* 1996].

2.2.2.2.2 Organic carbon

Organic carbon (OC) is generated through combustion of fossil fuels and biogenic material, as well as being directly emitted from living vegetation. OC aerosols can either be emitted directly (primary OC) or form in situ in the atmosphere through the condensation of low-volatility organic gases (secondary OC). The ratio of primary to secondary OC at release depends on the source and is further influenced by meteorology, as well as by diurnal and seasonal variability in emissions [*Seinfeld and Pandis*, 2006]. Globally, it appears that secondary OC aerosol contribute a large fraction of total OC concentrations, particularly in summer when vegetation is most active [*Crosier et al*., 2007]. Estimates of total global emissions of primary OC material range from 17-77Tg/yr, with approximately 75% of this coming from open burning, while fossil fuel combustion is estimated to contribute only 7% of the total [*Bond et al.,* 2004]. Estimated atmospheric OC concentrations range from approximately 0.5µg(C)/m^3 over remote marine regions, to 3.5µg(C)/m^3 in rural areas [*Stevens et al*., 1984] and up to 5-20µg(C)/m^3 in polluted regions [*Wolff et al.,* 1991]. The largest proportion of organic compounds occurs in the Aitken mode, with radii between 0.1-10µm [*McMurry and Zhang*, 1989].

Estimates of secondary OC emissions are technically challenging to obtain, largely since most OC compounds vary significantly in terms of chemical volatility (i.e. they can be present in both gaseous and solid phases thus blurring the distinction between primary and secondary OC), but also because there is such a high diversity of OC-containing compounds.

2.2.2.3 Biomass burning

By far the greatest proportion of southern African carbonaceous aerosol originates from biomass burning. Although natural fire played a vital role in the history of life on the

subcontinent, in present times the majority (~70-90%) of vegetative burning is the result of anthropogenic-related activity [*Crutzen and Andreae*, 1990; *Scholes and Andreae,* 2000; *Hao et al.,* 2005; *Reissel*, 2007]. Burning is used as a tool for various purposes, including for energy production (burning of fuelwood, charcoal and dung for heating and cooking), shifting cultivation, land management, as well as to clear land in savannah and forested regions [*Crutzen and Andreae*, 1990; *Liousse et al.,* 1996; *Delmas et al*., 1999; *Hao et al.,* 2005; *Reissel*, 2007]. Current estimates of total global biomass burning aerosol emissions (40-150Tg/yr) suggest that biomass burning is almost as great a source of particulate matter as anthropogenic sulphate emissions [*Crutzen and Andreae*, 1990]. Of the biomass burning sources, savannah and forest fires appear to be the largest, with estimates of fine-mode particle emissions from savannah fires alone estimated between 11-18Tg/yr [*Le Canut et al.,* 1996; *Liousse et al.,* 1996; *Scholes and Andreae,* 2000; *Alleaume et al.,* 2005].

Since most biological material is made of carbon, hydrogen and oxygen in a ratio of approximately 1:2:1 and since the majority of oxygen and hydrogen are consumed during combustion, the greatest proportion of particulate material originating from biomass consists almost solely of carbonaceous material [*Cachier et al.,* 1995; *Helas and Pienaar,* 1996; *Andreae et al.,* 1998; *Andreae and Merlet*, 2001]. The chemical and optical properties of the emitted particles vary widely depending on the proportions of different carbon compounds in the fuel, oxygen availability, the vegetation type and on the nature of the combustion itself [*Cachier et al*., 1995; *Helas and Pienaar,* 1996; *Turn et al.,* 1997; *Andreae and Merlet*, 2001; *Seinfeld and Pandis*, 2006]. Micronutrients such as nitrogen, sulphur, phosphorus and potassium generally make up only very small percentages of emissions since they are generally present only in very small quantities in the vegetative material itself [*Helas and Pienaar,* 1996; *Liousse et al.,* 1996].

An important distinction is made between two phases of burning: flaming and smouldering. Burning in the flaming phase is more efficient and the products generated tend to be more fully oxidised (e.g. CO_2). In contrast, burning in the smouldering phase is not as complete and less-oxidised products, such as CO, are produced [*Korontzi et al.,* 2004]. Variability of combustion completeness is usually quite marked within the biomass burning season since vegetation moisture content is generally high early in the season, while later, towards the end of the season most material has dried considerably and thus burns more readily [*Hoffa et al.,* 1999; *Korontzi et al.*, 2004]. In addition, the burning phase may also vary between different vegetation types. Forest fires are characterised by a short flaming stage, which is followed by a longer smouldering phase during which the thick wood not completely consumed in the flaming stage emits considerably more particulate matter. In comparison, grass fires tend to burn rapidly and completely, emitting considerably lower quantities of aerosol since little or no smouldering phase occurs [*Kaufman et al.,* 2002]. Observations of savannah fires suggest that BC comprises between 10-30% of particulate emissions in the smouldering phase

[*Liousse et al*., 1996; *Andreae and Merlet,* 2001; *Swap et al.,* 2003], however, a much smaller percentage (~3%) of BC is emitted during the flaming phase [*Liousse et al.,* 1996; *Ward et al.,* 1996; *Moosmuller et al.,* 2007].

The burning phase is not only of importance to the aerosol chemical composition but also plays a role in determining the size of emitted particles, with smouldering fires producing larger particles than flaming ones. The size of the particles released also, however, depends on several other factors such as the fuel characteristics, ambient temperature as well as relative humidity [*Dubovik et al.,* 2002]. Near sources biomass burning smoke is dominated by accumulation mode aerosols [*Dubovik et al.,* 2002], with particles ranging in size from 0.1-0.03μm [*Jayaratne and Verma,* 2001; *Sinha et al.,* 2003]. Because of their small size, biomass burning aerosol can easily be transported over long distances, and smoke plumes generally tend to cover extensive areas, potentially affecting regional radiative balances significantly [*Le Canut et al.,* 1996; *Moosmuller et al.,* 2007].

After release into the atmosphere, biomass burning particles rapidly undergo physical and chemical conversion and size distributions change significantly within the first hour after release [*Hobbs et al*., 2003; *Posfai et al.,* 2003; *Sinha et al*., 2003; *Swap et al.,* 2003]. Transformations occur through a variety of processes, including gas-to-particle condensation of volatile organic compounds as well as through coagulation [*Reid et al*., 1998; *Gong et al.,* 2003; *Hobbs et al*., 2003; *Yokelson et al.,* 2003; *Hao et al.,* 2005]. Observations have shown that aerosol mass concentrations may increase by 20-45% through aging, with an estimated 50-75% of this increase the result of gas-to-particle condensation of volatile organic gases [*Reid et al.,* 1998]. The aerosol population also changes as a result of deposition processes and during the first hour the large, chain-like aggregates of BC that may be present in fresh smoke, are usually deposited through gravitational settling [*Ross et al.,* 2003]. Over southern Africa it was shown that after approximately one to two hours, chemical and optical properties remain relatively stable [*Swap et al.,* 2003].

Despite OC making up the greater fraction of biomass burning aerosol, biomass burning particles are generally less hygroscopic than industrial aerosol. At the relative humidities typical over southern Africa (80-85%) only 10-20% of biomass burning aerosol associated with atmospheric moisture, while under the same conditions approximately 50% of industrial pollution aerosols have been found to be associated with water [*Kaufman et al.,* 2002]. It is only in the supersaturation conditions typically found in convective clouds that a greater proportion (between 30-100%) of particles emitted from savannah fires may act as cloud condensation nuclei (CCN) [*Terblanche et al.,* 2000; *Sinha et al.,* 2003]. However, since the bulk of biomass burning occurs in the dry season these supersaturation conditions are generally not met over most of southern Africa during the austral winter season.

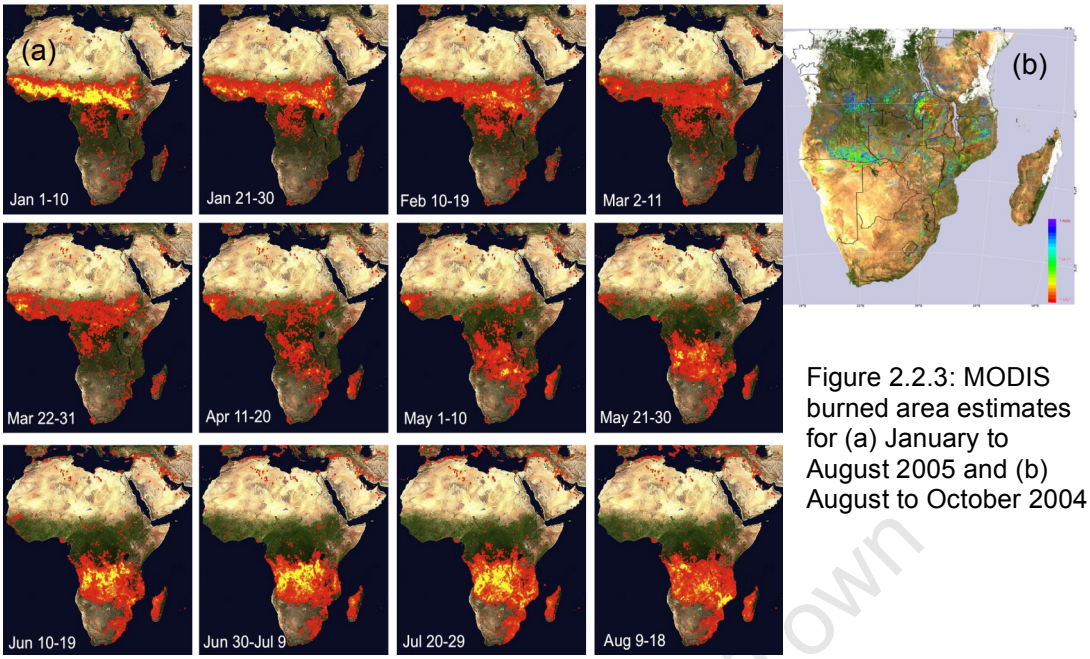

Figure 2.2.3: MODIS burned area estimates for (a) January to August 2005 and (b) August to October 2004.

The southern African biomass burning season starts in early June and progresses from northwest to southeast during the dry, austral winter, coming to an end in October or November as the rainy season begins [*Andreae et al.*, 1996; *Liousse et al.,* 1996; *Maenhaut et al,* 1996; *Scholes et al.,* 1996; *Freiman and Piketh,* 2003; *Korontzi,* 2005]. The clear seasonality of fire on the African continent can clearly be seen in fig. 2.2.3(a), as well as more specifically over southern Africa in fig 2.2.3(b). As the dry season progresses, vegetation either dies (annual grasslands) or becomes dormant (e.g. deciduous trees), shedding their leaves and thus providing considerable amounts of fine, easily-combustible, dry material [*Scholes*, 1997; *Frost*, 1999]. As a consequence, fires that occur later in the dry season tend to be more intense as more dry fuel is available, and because the warmer, more windy conditions allow fires to spread more easily [*Roy et al.,* 2005].

The highest frequency of burning in southern African occurs between 10-20°S [*Swap et al.,* 1996; *Piketh et al,* 1999a; *Tyson and Gatebe,* 2001]. Approximately 31% of the total burned area occurs in the Democratic Republic of Congo, followed by Angola (28%), with the rest occurring largely in Zambia, Zimbabwe, Moçambique and South Africa [*Maenhaut et al.,* 1996; *Kirkman et al.,* 2000; *Swap et al.,* 2003]. Less than 1% of all southern African burning occurs in Namibia because of the sparse vegetation coverage in this country [*Swap et al.,* 2003].

Biomass burning in southern Africa has also been found to exhibit a strong diurnal cycle, which may vary somewhat depending on the vegetation type burned [*Giglio*, 2007; *Roberts et al.,* 2008; *Ellicott et al.,* 2009]. Minimum burning generally occurs between midnight and 7am local time, whilst burning peaks around 2pm local time, as fires are ignited in the late morning and early afternoon. Burning in grassland fires also tends to last longer (5-8 hours) compared to fires in woodland areas (2-4 hours), likely because of the increased proportion of fine, dry material present in grassland regions [*Roberts et al.,* 2008]. Little or no diurnal AOD cycle (on the order of 5-10% only) has been observed outside of the main biomass burning regions since the atmospheric aerosol loading is more strongly influenced by transport controlled by synoptic atmospheric conditions than diurnal fire cycles [*Myhre et al*., 2003; *Swap et al*., 2003].

2.2.2.4 Mineral dust aerosol

Although in terms of global aerosol number concentrations industrial and biomass burning aerosol make up the largest proportion because of their small size, in terms of atmospheric aerosol mass, the largest fraction is derived from mineral dust emissions [*Tegen and Fung,* 1994, 1995; *Tegen et al.,* 1996; *Prospero et al*., 2002; *Tegen et al.,* 2002; Tanré et al., 2003]. In general, dust plumes have been found to be larger, more persistent and to occur more frequently than those associated with either industrial or biomass aerosol [*Husar et al.,* 1997]. Actual estimates of global dust emissions and atmospheric burden remain, however, highly uncertain, mainly because of the complexity of processes that lead to their emission [*Seinfeld and Pandis*, 2006]. Estimates of total global annual emission range by up to a factor of five, from 1000 to over 5000Tg/yr [*Schutz*, 1980, *Duce et al.,* 1991; *Alfaro et al.,* 2000]. Uncertainty regarding the total atmospheric mineral dust burden is similarly large, ranging from 8 to 36Tg, or by a factor of four [*Zender et al*., 2004].

The main process generating mineral dust aerosol is wind acting on dry, bare soils, lifting particles into the atmosphere. The quantity of mineral dust becoming airborne depends on several factors, including wind velocity, soil moisture content, soil composition as well as the degree of surface disturbance [*Alfaro et al.,* 1998; *Alfaro et al.,* 2000; *Prospero et al.,* 2002; *Bryant,* 2003]. Because of the enormous variability of these factors, dust particles range in size from several tens of nanometres to tens of microns or larger [*Woodward and Roberts*, 2000; *Satheesh and Moorthy*, 2005].

In general, dust aerosols have a bimodal size distribution structure, with coarse particles (diameters >2.5μm) dominating [*Dubovik et al.,* 2002]. Near the source, sand particles up to several hundred micrometers in size may be present, but, because of their size, these particles settle quickly and do not make up a large proportion of the tropospheric dust loading [*Prospero et al.,* 2002]. These large particles do, however, play an important role in the production of finer dust particles through saltation, grinding and impaction processes [*Gillette*

et al., 1998; *Bryant et al.,* 2007]. As the large, airborne sand particles fall back towards the surface they bombard and shatter large particles into smaller particles, ejecting these smaller ones into the atmosphere [*Gillette et al.,* 1998]. In addition, fluvial and chemical weathering processes have also been found to be efficient at producing small particles (<10μm in diameter) [*Pye*, 1989].

Generally, the greater the distance from source the smaller the average particle size [*Woodward and Roberts,* 2000], and, a few hundred kilometres from most dust sources small particles dominate the size distribution, with the mass median diameter dropping well below 10μm [*Prospero et al.,* 2002]. Of particular importance to global atmospheric chemistry and the earth's radiative balance are dust aerosols with diameters smaller than 5μm. These particles, on average, have atmospheric lifetimes of up to two weeks and can be transported extensive distances (well over 5000km on occasion) [*Miller and Tegen,* 1999; *Woodward and Roberts,* 2000; *Arimoto*, 2001; *Seinfeld and Pandis*, 2006]. For example, Saharan dust is routinely observed over the Caribbean, while Asian dust plumes are frequently detected over the North Pacific and at times even over the west coast of North America [*Seinfeld and Pandis*, 2006]. Long-range dust dispersal can only occur, however, if the aerosol are lifted and detrained above the boundary layer where they are subsequently transported by free tropospheric winds [*Zhang et al.,* 2009b]. Near source regions dry deposition is the dominant mechanism of dust removal, since little precipitation generally occurs [*Zhao et al.,* 2003]. However, further away from these regions wet deposition becomes more and more important. Chemically, mineral dust is composed mainly of quartz, clays, gypsum, calcite and various iron oxides. The physical, chemical and optical properties of dust aerosol depend on the relative abundance of these minerals. As a result of their mineral nature, electron microscope images of dust particles have revealed that they are almost exclusively irregular in shape [*Gao and Anderson*, 2001]. This morphological and chemical complexity is, however, currently impractical to include in model calculations and as a first order approximation all dust particles are usually assumed to be spheroids [*Yang et al.,* 2007].

Interestingly, nearly all major dust source regions occur in the northern hemisphere (e.g. the Sahara in North Africa, the Taklamakan in Mongolia, etc), and the southern hemisphere is largely devoid of dust activity on the same kind of scale [*Miller and Tegen*, 1999; *Woodwards and Roberts*, 2000; Prospero *et al.,* 2002]. Although relatively small compared to their northern hemisphere counterparts, southern African dust sources are still significant in terms of the global budget and certainly play an important role in regional atmospheric processes and ecosystem functioning [*Garstang et al.*, 1998].

A study of TOMS satellite imagery has shown that the most active dust sources in southern Africa are either associated with or situated near topographic lows, where thick layers of sediment deposited during previous periods of flooding have become exposed to physical

and chemical weathering processes [*Washington et al.,* 2003]. In addition, as a general rule, most dust is emitted from regions where annual rainfall is low, typically between 100-200mm/yr [*Prospero et al.,* 2002]. The largest dust source on the subcontinent is the flat saltpan of Etosha (situated near 16ºE, 18ºS in northern Namibia), which fits these criteria exactly, being situated in a topographical low within a semi-arid region [*Prospero et al.,* 2002]. Although the pan itself is small, between 5000-6000km^2 in size, there are a number of other ephemeral lakes and swamps surrounding the pan, and observations suggest that the region is in fact the 7th largest dust source in the world [*Washington et al.,* 2003]. Additionally, a massive number of indigenous people, approximately 25% of Namibia's population, were moved just north of the pans to form a "native homeland", Ovamboland [*Prospero et al.,* 2002]. The agricultural and land clearing practices in this area have considerably degraded the land surface, thus likely also contributing to the significant dust emissions from the region [*Prospero et al.,* 2002; *Bryant,* 2003]. A second large dust source, the Makgadikgadi pans, occurs in Botswana (near 21ºS, 26ºE, southwest of the world-renowned Okavango Delta). Not only do these pans constitute the largest of their kind in the world, covering nearly 22,000km^2, but they have been estimated to be the 9th largest dust source in the world [*Prospero et al.,* 2002; *Bryant et al.,* 2007].

Further mineral dust emissions originate from a large number of small but persistent point sources that occur along the southern African west coast [*Privette and Roy,* 2005; *Eckard and Kuring,* 2005]. Space-shuttle imagery from a three-year period has been used to identify over 250 dust plumes extending over the Atlantic Ocean from this region. These plumes are generally too small and occur too low in the atmosphere to be identified with traditional remote sensing products (e.g. TOMS, which does not detect in the lowest 1km of the atmosphere; see section 2.3.2.2 for a full description of the TOMS product) [*Eckard and Kuring,* 2005]. These point sources are associated with fluvial landforms such as dry riverbeds and saltpans and they are recharged on shorter timescales than most of the world's major dust sources, with new supplies of sediment being transported in the regional rivers, which flood whenever high rainfall occurs on the Namibian highlands. Because the landscape is so barren the floods pick up and carry very high sediment loads, which quickly become available for deflation once the flood has passed (typically the rivers flow for only a few days) [*Eckard and Kuring,* 2005].

Dust activity in southern Africa occurs year round but peak emission occurs simultaneously with maximum biomass burning during the winter season from August to October when soils are dry and surface wind speeds are maximum [*Prospero et al.,* 2002; *Bryant et al.,* 2007].

2.2.2.5 Marine aerosol

Marine aerosol is composed largely of sea salt particles as well as various biogenic particles that are released by marine organisms [*Kaufman et al*., 2002]. Most coarse salt particles are emitted from bursting sea foam, with greater emission occurring in windy conditions. Sea salt makes up an estimated 30-75% of all natural aerosols, and approximately 1000-10,000Tg are produced per year [*Winter and Chylek,* 1997]. Despite the high rate of emissions, aerosol optical depth over remote oceanic regions generally doesn't exceed 0.15 (at 440nm), largely because marine aerosol, like dust, is mainly made up of large, coarse mode particles, which are quickly re-deposited to the ocean surface [*Dubovik et al.* 2002]. Despite this, measurements at two sites along the west coast in South Africa showed that marine aerosol made up a large proportion of the aerosol loading, varying between 51 and 69% between summer and winter respectively. Over the inland plateau though, marine aerosol concentrations are well over an order of magnitude lower [*Piketh et al.,* 1999a,b].

2.2.3 Aerosol deposition

After a certain period in the atmosphere, during which they are likely to have undergone several physical and chemical changes, aerosols are ultimately removed from the atmosphere through wet and dry deposition processes. The relative importance of these processes depends on a number of factors, including the physico-chemical properties of the species being removed, prevailing atmospheric conditions as well as the land surface type and terrain upon which deposition occurs [*Seinfeld and Pandis*, 2006].

2.2.3.1 Dry deposition

Dry deposition can essentially be defined as the deposition of a particulate species in the absence of precipitation [*Seinfeld and Pandis*, 2006]. This process is generally considered to occur via three steps. Firstly, particles are transported through the atmospheric surface layer by turbulent diffusion to a thin layer directly above the deposition surface. Secondly, Brownian transport of the species occurs across this layer of air (the quasi-laminar sub-layer), and, finally, the species is deposited onto the surface itself.

The deposition flux is generally calculated as a function of the local concentration at some reference height above the surface and the deposition velocity of the species of interest. Higher dry deposition rates can be expected in unstable atmospheric conditions and over surfaces with greater roughness length (i.e. more variable surfaces, such as forests compared to short grasses) [*Seinfeld and Pandis*, 2006]. For this reason, dry deposition has a strong diurnal cycle over land but generally not over water. For dry deposition of particulate matter, particle size is the strongest factor determining deposition rate, since gravitational settling plays a vital role, especially for larger species [*Seinfeld and Pandis*, 2006].

Despite the theoretical simplicity of dry deposition processes, directly measuring the rate of dry deposition is considerably more challenging than measuring wet deposition. A number of different methods have been developed over the years, but these techniques are generally very costly, requiring both extensive instrumentation and technical resources [*Clarke et al.*, 1997]. As a result of this cost, relatively few dry deposition observational studies have been carried out over southern Africa [*Zunckel et al.*, 1999] and most studies focused on the deposition of sulphur-containing compounds in South Africa [e.g. *Piketh et al.,* 1999; *Zunckel et al.,* 2000].

2.2.3.2 Wet deposition

Wet deposition can be defined as the processes through which material is removed from the atmosphere by precipitation hydrometeors (cloud, fog or rain droplets, hail and snow). The term *rainout* usually refers to particle capture within clouds (in-cloud scavenging), whilst *washout* refers to below-cloud scavenging by falling precipitation droplets. Wet deposition is considerably more complex than dry deposition since phenomena occur on widely varying physical scales, ranging from the microphysical to synoptic and involves interactions between components in different physical phases [*Seinfeld and Pandis,* 2006].

Similarly to dry deposition, wet removal can be considered as a three-step process. Firstly, the aerosol species is brought into the presence of condensed water, then it is scavenged by a precipitation hydrometeor, a process that occurs either within or below the cloud. Inside clouds, aerosols are incorporated into cloud or rain droplets through nucleation scavenging, the growth of CCN or by interstitial aerosol collection by existing cloud droplets. Finally, as the hydrometeor falls through the atmosphere below the cloud it either collides with airborne particles or sweeps them up through inertial impaction or interception processes [*Seinfeld and Pandis*, 2006]. Importantly, and to further complicate matters, nearly all wet deposition processes are reversible and chemical conversion may occur at any time between the point of particle capture by hydrometeors and eventual deposition at the ground surface. For example, aerosols may get scavenged below a cloud by precipitation droplets, but if these droplets evaporate before reaching the surface the aerosol may be re-released into the atmosphere, possibly having undergone chemical or physical transformations [*Seinfeld and Pandis*, 2006].

Aerosol rain- and wash-out are highly effective removal processes. For example, aerosol measurements taken over the South African Highveld in January 1999 showed that after three days of no rainfall accumulation aerosol concentrations were up to four times higher than after two days of widespread thunderstorms [*Ross et al.*, 2003].

2.2.4 Aerosol optical properties

Aerosol chemical composition and size distribution determine, to a large extent, their optical properties [*Myhre et al.,* 2008]. The temporal and spatial variability of aerosol optical properties are still not well understood since they depend on a large number of microphysical properties such as morphology (which includes particle size), chemical composition and dielectric characteristics [*Yang et al*., 2000, *Mishchenko et al.,* 2003; *Kalashnikova and Sokolik*, 2004]. These properties may vary significantly between, and even within, aerosol types, as well as with relative humidity [*Haywood et al.,* 1997; *Smirnov et al.,* 2002; *Myhre et al.,* 2004]. Microphysical properties also change with time as aging processes such as coagulation, precipitation scavenging, in-cloud chemical conversion and gas-to-particle conversion act upon the aerosol population [*Smirnov et al.,* 2002].

In a modelling framework, three aerosol optical properties need to be known in order to solve the radiative transfer equation and estimate the aerosol effect on atmospheric radiation. These three properties are (i) aerosol optical thickness, (ii) phase function and (iii) the single scattering albedo [*Smirnov et al.,* 2002]. The sign of aerosol radiative forcing, positive or negative (resulting in heating or cooling of the earth-atmosphere system, respectively), depends on the single scattering albedo, whilst the aerosol phase function and optical thickness determine the magnitude of this forcing.

2.2.4.1 Aerosol optical depth

Aerosol optical depth (AOD) gives an indication of the atmospheric aerosol burden, with high AOD values indicative of high aerosol loading. It can be determined from column aerosol mass, using assumed or measured aerosol size distributions and aerosol scattering and absorption cross-sections. The scattering and absorption cross-sections vary with humidity, thus it is important to take this factor into account in calculations [*Penner et al.,* 2002; *Pilinis et al.,* 1995]. AOD is the most commonly monitored aerosol optical property, given the relative ease of measuring this property (see section 2.3 for more details).

2.2.4.2 Phase function

All atmospheric aerosol scatter light to some extent in different directions. The phase function effectively describes how much light is scattered in each direction, (i.e. the angular dependence of light scattering). The asymmetry parameter is derived from the phase function, and is defined as the average of the cosine of the scattering angle [*Seinfeld and Pandis*, 2006]. A positive (negative) asymmetry parameter indicates that the aerosol particle scatters more light in the forward (backward) direction.

2.2.4.3 Single scattering albedo

Single scattering albedo (SSA) is essentially a measure of the ratio of scattering to total extinction (scattering plus absorption) of a particular aerosol species. It depends on two aerosol properties: chemical composition and size distribution, and also varies, to some degree, with wavelength [*Dubovik et al.,* 2002; Seinfeld and Pandis, 2006]. The SSA parameter is vital for determining the direct aerosol effect on climate, since it effectively controls the sign of radiative forcing, whether positive or negative (as the percentage of absorption increases or decreases) [*Dubovik et al.,* 2002; *Seinfeld and Pandis*, 2006; *Leahy et al.,* 2007]. For example, a modelling study by Hansen et al. [1997] found that decreasing the SSA of desert dust by just 0.1 from 0.95 to 0.85, would change the global dust forcing from significant cooling to significant heating.

SSA is, however, one of the most uncertain parameters in present aerosol radiation models [*Kaufman et al*., 1997], largely because it is one of the most challenging to measure [*Heltzenberg et al*., 1997]. A large degree of uncertainty derives from the fact that the mixing state of BC aerosol and its different optical properties remain relatively unknown [*Fuller et al*., 1999; *Bond and Bergstrom*, 2006; *Bond et al*., 2006]. Additional uncertainty is also associated with the optical properties of OC aerosol, with some indications that these aerosols may be more absorbing than initially assumed [*Andreae and Gelencser*, 2006; *Lukacs et al*., 2007].

2.2.5 Aerosol-radiation-climate interactions

Uncertainty surrounding aerosol optical properties plays a significant role in limiting our understanding of aerosol radiative forcing, changes to the earth's radiative balance and current quantitative estimates of anthropogenic climate change [*Dubovik et al.,* 2000; *Kinne et al.,* 2003; *Pilewski et al.,* 2003; *Solomon et al., 2007*]. At present, we lack knowledge regarding both macrophysical (sources, sinks and loading) as well as microphysical (composition, size distribution, chemistry) aerosol properties [*Dubovik et al.,* 2000; *Solomon et al., 2007*]. In addition, there is even greater uncertainty regarding the interaction of aerosols with clouds, and their numerous possible feedbacks on the climate system [*Lohmann and Feichter,* 2005; *Solomon et al., 2007*].

For comparison, the radiative forcing due to the increase of greenhouse gases since the pre-industrial period is known relatively precisely to be 2.45+/-0.37W/m^2 [*Solomon et al., 2007*]. However, the radiative forcing due to just the direct aerosol effect is estimated at -0.5 W/m^2, but with an uncertainty of a factor of at least two [*Hobbs et al.,* 1997; *Myhre et al.,* 2003; *Schulz et al.,* 2006; *Solomon et al., 2007*]. Similarly, the radiative forcing of the indirect aerosol effect has been roughly estimated to be between -0.5 to -2W/m^2, but this estimate is associated with an even larger uncertainty of a factor of three [*Menon et al.,* 2002; *Myhre et*

al., 2003; *Solomon et al., 2007*]. It is largely because of the uncertainties in aerosol-cloud feedbacks that the range of increase in global mean temperature in response to a doubling of CO_2 varies between 1.5 and 4.5°K [*Solomon et al., 2007*]. What is perhaps most important to note, is that at present emission levels, the negative radiative forcing induced by industrial and biomass burning aerosols is estimated to be large enough to offset a large proportion of the current greenhouse gas-induced warming [*Kaufman et al.,* 1991; *Penner et al.,* 1992; *Solomon et al., 2007*; see fig. 1.1].

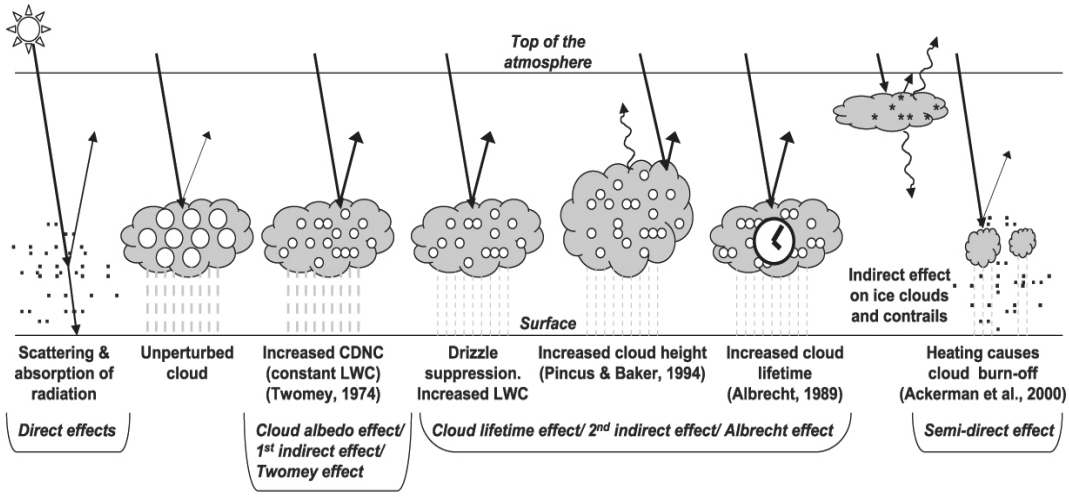

Figure 2.2.4: Schematic diagram of the radiative effects of aerosol (direct, semi-direct and indirect). [*Following Solomon et al., 2007*].

Compared to most greenhouse gases, which have long atmospheric lifetimes (up to 100's of years), aerosols have relatively short lifetimes, generally approximately only a week [*Kaufman et al.,* 2002; *Andreae,* 1996]. This results in greenhouse gases being relatively homogeneously distributed around the globe, whilst tropospheric aerosols have strongly heterogeneous spatial and temporal distributions. The resultant climate forcing by aerosols is highly regionalised [*Andreae,* 1996; *Penner et al.,* 2002; *Kaufman et al.,* 2002], whilst the positive forcing resulting from greenhouse gases is almost equally distributed between the hemispheres and varies only as a function of latitude [*Taylor and Penner,* 1994]. In addition, in comparison to greenhouse gases which act only on outgoing longwave radiation, aerosols affect both sides of the earth's radiative balance equation, affecting long- and short-wave radiation depending on their composition and size [*Andreae,* 1996]. The various aerosol-radiation-cloud interactions are shown schematically in figure 2.2.4 and are further discussed in the following three sub-sections.

2.2.5.1 The direct aerosol effect

The direct aerosol effect describes the interaction of aerosols with in- and out-going radiation of all wavelengths. The magnitude of radiative forcing at a particular time and location depends on the abundance and optical properties of the aerosol present, the wavelength of incident radiation as well as on the surface albedo [*Arimoto,* 2001; *Bergstrom et al.,* 2002; *Myhre et al,* 2008]. Direct radiative forcing can be defined as the difference in net radiative flux between a case with aerosol present and one where aerosols are not, and it is generally measured either at the top-of-the-atmosphere (TOA) or at the surface [*Seinfeld and Pandis*, 2006]. At the TOA the effects of absorption and scattering are subtractive, whilst at the surface these effects are additive [*Collins et al,* 2002]. If only purely scattering aerosols are present, the TOA and surface radiative forcing are approximately equal. However, if absorbing aerosols, such as mineral dust or black carbon are present, the surface forcing can be a factor of two to three times greater than at the TOA. This occurs because incoming radiation is not only scattered back toward space, but the aerosol also absorb some of the radiation that would normally have reached the surface [*Seinfeld and Pandis*, 2006].

The vertical distribution of an absorbing aerosol layer relative to clouds, if present, is vital in terms of their radiative impact on climate, since absorbing particles can absorb up to three times more shortwave radiation when situated above clouds rather than in cloud-free conditions [*Johnson et al.,* 2004]. This may result in a positive TOA radiative forcing since the aerosols absorb a large proportion of the multiply-scattered shortwave radiation that would otherwise have been reflected out of the earth system by the clouds [*Kaufman et al.,* 2002; *Takemura et al.,* 2002]. Over low albedo surfaces, for example over dark oceans (albedo ~6%), aerosol absorption needs to be as high as 15% of AOD to result in a positive TOA forcing. This proportion decreases, however, with increasing surface albedo, where absorption of 10% of AOD over land (albedo ~20%) and absorption of just 5% of AOD above boundary layer clouds is necessary to result in a positive TOA radiative forcing [*Kaufman et al*., 2002]. In contrast, if situated below a cloud layer, the absorbing aerosol layer will have a negative TOA forcing [*Takemura et al.,* 2002].

Aerosols may also interact with outgoing longwave radiation, further affecting the TOA balance. This effect is usually small though, since aerosol opacity tends to decrease significantly at longer wavelengths and because aerosols are mostly concentrated in the lower troposphere, where the atmospheric temperature which governs emissions, is largely the same as that of the surface [*Charlson et al.,* 1992]. Only for coarse mineral dust aerosol does this effect become important, since these particles are large enough to interact with outgoing infrared radiation [*Torres et al.,* 2002].

The uncertainty associated with estimates of direct aerosol radiative forcing remains high (ranging from -0.9 to -0.1W/m²; see figure 1.1.1), largely because uncertainty associated with

global aerosol optical properties and because of the differences between estimates from global models and observations (the latter tending to have larger negative forcing) [*Schulz et al.,* 2006; *Solomon et al.,* 2007]. Significant differences also exist between models, and are likely, at least in part, due to simulated differences in absorption between internally- and externally-mixed aerosols [*Myhre,* 2009].

2.2.5.2 The semi-direct aerosol effect

As already mentioned, dark-coloured, absorbing aerosols have a two-fold effect on climate, both scattering and absorbing incoming radiation. Warming occurs in the aerosol layer as a consequence of this absorption, and this in turn may affect ambient relative humidity, cloud cover and possibly even convection. This is termed the semi-direct effect. Depending on the relative position of the aerosol layer compared to clouds and the type of clouds present (if any) this effect may exert a positive or negative TOA radiative forcing [e.g. *Ackerman et al.,* 2000; *Kaufman et al.,* 2002; *Giorgi et al.,* 2003; *Huang et al.,* 2007; *Brioude,* 2009; *Perlwitz and Miller,* 2010].

A modelling study by Ackerman et al. [2000] using data collected during the 1999 INDOEX field campaign showed that even at low AODs the semi-direct effect could be of importance. The study was carried out off the west coast of India, a region of cool subtropical ocean where the well-mixed marine boundary layer is often topped by stratocumulus cloud. Under aerosol-free conditions convection in these regions is driven by downdrafts that are generated by radiative cooling from the cloud tops. The presence of a strongly absorbing aerosol haze (AOD of 0.2, single-scattering albedo of 0.88) was found to cause heating that was sufficient to offset the longwave cooling enough so as to suppress convective mixing, thus cutting the cloud layer off from its moisture source (the ocean surface) and dissipating the cloud. Averaged over daytime, the INDOEX hazes were found to reduce cloud cover by between 25-40%, and the trade cumulus cleared earlier in the day [*Ackerman et al.,* 2000]. Long-term satellite observations over Europe and China also show evidence for a reduction in planetary albedo as a result of the presence of absorbing aerosols in winter [*Kruger and Grabl*, 2002; *Kruger et al*., 2004].

Recent studies suggest that the semi-direct aerosol effect does not always result in positive radiative forcing [e.g. *Johnson et al*., 2004; *Brioude et al*., 2009]. In certain situations, particularly when the aerosol loading results in enhanced moisture convergence, specific humidity increases may exceed the temperature effect on relative humidity, increasing cloud cover and inducing a negative radiative forcing [*Perlwitz and Miller*, 2010].

Conventional indirect effects (more about these in the next section) oppose the cloud-burning effect of strongly absorbing aerosols, hence the net aerosol effect depends on the meteorological conditions as well as on the optical and chemical properties of both the

aerosol haze and cloud droplets. GCM simulations suggest that on a global-scale the increased cloud albedo and lifetime dominate over the semi-direct cloud-burning effect, which only occurs in regions where highly polluted air lies above low-level clouds [*Ackerman et al.,* 2000; *Lohmann and Feichter*, 2005].

2.2.5.3 The indirect aerosol effect

In practical terms nearly every cloud droplet requires an aerosol particle to condense upon and without these particles few clouds would form at all. The size, concentration and composition of CCN and ice nuclei (IN) play a large part in determining cloud properties as well as their evolution and possible development of precipitation [*Kaufman et al*., 2002]. Estimates of the radiative forcing of the two components of the indirect aerosol effect (the first and second effects, as will be explained below) suggest that they are of similar magnitude and both negative [see fig. 1.1.1; *Solomon et al., 2007*].

The first indirect effect, as proposed by Twomey [1974], results from an increased number of CCN increasing cloud droplet concentrations and droplet surface area and thus increasing shortwave cloud albedo. This process, however, reaches a critical threshold, above which any increase in CCN concentration will not result in more droplets being formed, since there is competition between droplets for the available water vapour. This threshold depends on a variety of factors, including cloud dynamics, aerosol size distribution and chemical properties, as well as the amount of moisture available in the ambient atmosphere - the larger and more hygroscopic the particle, the greater its ability to attract moisture [*Kaufman et al*., 2002]. Besides for the cloud droplet surface area, cloud reflectance also depends on several other factors as well, including cloud optical thickness (which in turn depends on the amount of water/ice present) as well as the single-scattering albedo and asymmetry parameter (the amount of energy scattered forwards) of the cloud droplets [*Noone,* 2001].

In terms of the effect on longwave radiation, the impact of increased cloud droplet concentrations on longwave absorption is considerably less, nearly negligible, at least for tropospheric clouds. This is because tropospheric clouds are generally almost totally optically thick at infrared wavelengths to begin with, so any change in reflectivity does little to increase this further [*Charlson et al.,* 1992]. The effect of aerosols on optically-thin, cirrus clouds may, however, be important, but the magnitude of these effects is not yet known [*Lohmann and Feichter*, 2005].

The second indirect effect is induced when smaller cloud droplets decrease precipitation efficiency, resulting in increased cloud liquid water content, fractional cloud-cover and cloud lifetime [*Albrecht*, 1989; *Pincus and Baker*, 1994]. Similarly to the first indirect effect, the second indirect effect produces a negative radiative forcing, cooling the earth-atmosphere system. For example, a modelling study indicated that increasing the droplet size of just

marine stratus clouds by 30% would result in a global mean decrease of shortwave radiative forcing of 2W/m^2 [*Charlson et al.,* 1992]. It is also important to note that the inhibition of precipitation development and the consequent alteration to the amount and vertical distribution of water and heat may further modify the hydrological cycle and affect radiative balance in more complex ways [*Charlson et al.,* 1992; *Lohmann and Feichter,* 2005; *Solomon et al., 2007*].

Indeed, satellite data over Australian and Canadian pollution plumes and Indonesian smoke plumes have shown that cloud droplets are smaller not only at the cloud base in such aerosol-polluted regions, but that droplet size does not increase as the cloud develops in vertical extension [*Lohmann and Feichter*, 2005]. This may cause a delay or indeed a complete inhibition of precipitation. Other observations in polluted deep convective clouds have also shown that the small cloud droplets did not collide efficiently to form raindrops, and freezing was delayed until the cloud reached temperatures of -37ºC, resulting in the production of super-cooled water [*Kaufman et al*., 2002].

As just described, if freezing is delayed because of high aerosol loading, convection can, conversely, be enhanced. This occurs predominantly only in deep convective clouds with warm bases, where the increased number of smaller particles delays precipitation and the condensates may ascend to super-cooled levels instead of raining out earlier in the warm liquid phase. When the condensates do form ice hydrometeors, they release latent heat aloft and then reabsorb the same amount of heat when they fall and melt at lower levels. More heat is thus transported upward and a greater amount of static energy is converted and released as kinetic energy, thus potentially invigorating convection, leading to more precipitation and deeper depletion of static instability [*Lohmann and Feichter,* 2005]. In shallow or short-lived clouds the reduction of cloud droplet size appears to lead only to a decrease of precipitation, through the processes already described.

Moisture that is not precipitated out because of aerosol-induced precipitation suppression may also be advected and accumulated in regions downstream, where rainfall may in fact be increased at a later time. The enhanced and delayed release of latent heat may lead to an enhancement (as just described) or redistribution of convection, low-level moisture convergence and precipitation, potentially influencing regional circulation patterns as well [*Noone,* 2001; *Lohmann and Feichter,* 2005]. The existence of just a few super-micron CCN particles can, however, significantly reduce the second indirect effect and bring about precipitation as would occur in a relatively clean atmosphere [*Kaufman et al*., 2002].

Finally, a positive feedback exists between aerosols decreasing precipitation and aerosol concentrations. Less precipitation means fewer aerosols are removed from the atmosphere

by wet deposition, which results in longer aerosol lifetime and yet more aerosol present, which can further affect cloud cover and precipitation [*Lohmann and Feichter,* 2005].

2.2.6 Other aerosol impacts

Atmospheric aerosols also have notable non-climatic effects. For example, in urban areas where aerosol concentrations can reach very high concentrations, they may have significant detrimental effects on human health [*Dockery et al.,* 1994; *Torres et al.,* 2002; *Forsberg et al.,* 2005]. Submicrometer (<1µm) aerosol particles can easily be inhaled and pose certain health hazards depending on their concentrations, chemical composition and time of exposure. Hazards range from respiratory irritation and small decreases in the level of lung function all the way to mortality [*Gong et al.,* 2003]. Aerosols also contribute to the formation of photochemical smog, which is a considerable threat to both human and ecosystem health [*Pham et al.,* 1995]. Natural ecosystems are also affected by aerosol deposition processes, with the problem of acidic rainfall having been observed since the 1950's [*OECD,* 1977; *Cowling*, 1982].

In addition, aerosols are of considerable importance in terms of the biogeochemical cycling in various ecosystems around the world [*Torres et al.,* 2002], which in turn may have climatic feedbacks through, for example, increased carbon dioxide take-up by oceanic phytoplankton [e.g. *Martin et al*., 1990]. Biogeochemical cycles in southern Africa are affected by the regional aerosol loading, which is composed mainly of biomass burning material, mineral dust, anthropogenic particles as well as marine aerosols [*Piketh et al.,* 1999; *Billmark et al.,* 2005]. The particulate material recirculated around the subcontinent contains many compounds that are essential to growth in both the terrestrial and marine biospheres [*Tyson and Gatebe,* 2001; *Bryant,* 2003]. For example, a study over the Okavango Delta in Botswana showed that an estimated 250 000 tons of aerosol material are deposited over the region per year, the equivalent of roughly 0.57kg/ha per day of anticyclonic circulation. As a consequence, nearly 52% of the total required phosphate and 30% of required nitrate is provided through the deposition of atmospheric aerosol alone [*Garstang et al.,* 1998].

Similarly, aerosol deposition that occurs from the large aerosol plume that exits the subcontinent near 31°S appears to be a significant source of iron to parts of the South Indian Ocean, a major global CO_2 sink area [*Tyson and Gatebe,* 2001]. There is strong evidence to suggest that the aerosols deposited from the southern African plume provide enough soluble iron to support the high biological activity characteristic of this region. Measurements between 60-85ºE have shown that during episodes of peak atmospheric aerosol transport up to 0.99µg/m^2 of fine aerosol iron were deposited per day, with such deposition estimated to occur on at least 100 days per year [*Piketh et al.,* 2000].

2.3 Aerosol observations

The highly heterogeneous nature of aerosol concentrations means that long-term global-scale observation of these particles is difficult. In situ measurements, whether ground- or aircraft-based, have traditionally been regarded as the most reliable, however, because of their limited spatial coverage (and nearly always temporal coverage as well), they are inappropriate for global monitoring of aerosol properties and processes. These types of measurements also generally don't characterise the aerosol characteristics of the total atmospheric column, a feature that is particularly important for model validation [*Dubovik et al.,* 2002].

Since the dawn of the satellite era, remote sensing techniques have provided a non-intrusive and global means of measuring aerosol characteristics at relatively high temporal scales. These observations, however, require the extraction of the aerosol contribution from the measured signal, a process that generally depends on the parameterisation of a number of surface and atmospheric properties [*Dubovik et al.,* 2002]. These assumptions are usually made at a global scale and thus may not be accurate for all regions during all seasons. As a result, considerable uncertainty is still associated with satellite-based measurements. However, at present, satellite-based measurements of aerosol properties are certainly useful in terms of their near-continuous global coverage, although their accuracy remains to be refined, particularly in terms of their ability to measure in the vertical [*Kaufman et al.,* 1997; *King et al.,* 1999].

In situ, ground-based and airborne studies are still an essential means to directly obtain highly accurate observations, which can be used both to validate and further improve remote sensing products. A combination of in situ and remote sensing observations is therefore necessary to deepen our understanding of atmospheric aerosol processes as well as to improve estimates of their radiative forcing on both regional and global scales. The following two sections provide brief descriptions of the regional field campaigns carried out in southern Africa over the past two decades and the global aerosol remote sensing products, which have been used for validation purposes throughout this work.

2.3.1 Field campaigns in southern Africa

Few large field campaigns were carried out in southern Africa prior to 1992, largely because of the significant financial costs associated with such experiments and to a certain extent because the technical knowledge and equipment necessary was generally not available on the subcontinent. Much of this changed, however, in the early 1990's when interest in the region was sparked by the realisation that Africa was a significant pollution source, in terms of both trace gases and aerosols.

2.3.1.1 SAFARI-1992

Using satellite observations Fishman et al. [1991] noted very high ozone and trace gas concentrations over the eastern tropical South Atlantic Ocean during the austral spring season, from August to October. Results pointed to this peak being related to biomass burning activities occurring on the African continent. In order to investigate this feature further, and in an attempt to understand the sources of the observed pollution better, the South Tropical Atlantic Regional Experiment (STARE) was launched in 1992 [*Andreae et al.,* 1996]. The project was carried out in two parts, with the Southern African Fire-Atmosphere Research Initiative-92 (SAFARI-92), based over the African continent, and the Transport and Atmospheric Chemistry near the Equator-Atlantic (TRACE-A) campaign [*Fishman et al.,* 1996] concentrated largely over the south tropical Atlantic Ocean.

SAFARI-92 was the first large, international and inter-disciplinary field campaign to be carried out in southern Africa and involved research groups from atmospheric chemistry, meteorology, climatology, biogeochemistry, fire ecology, soil science, microbiology and forestry. Ground-based experiments were carried out in concert with complementary aircraft and remote sensing observations during the austral spring season of 1992, from late September to early October [*Andreae et al*., 1996; *Lindesay et al.,* 1996]. A very strong El Niño event occurred prior to and during the campaign and this strongly affected the entire southern African region. Much of the subcontinent experienced drought conditions [*Janowiak*, 1993; *Trenberth*, 1997] and anomalously strong anticyclonic circulation occurred during the winter and spring of 1992 [*Stein et al.,* 2003]. Approximately 55% of the 45 days of the SAFARI-92 campaign were dominated by these conditions and virtually no rainfall was recorded during the entire experiment period [*Garstang et al*., 1996; *Maenhaut et al*., 1996]. The abnormally dry conditions also resulted in significantly lower than normal vegetation growth. The Normalised Difference Vegetation Index (NDVI), an indicator of vegetation cover, was up to 80% below normal during the September to November period of 1992 over much of Moçambique, eastern South Africa and Zimbabwe and it was estimated that biomass burning emissions were up to 30% lower than usual because of the drought conditions [*Lindesay et al*., 1996; *Anyamba et al*., 2003].

The stability induced by anticyclonic conditions further resulted in strong stratification of the regional atmosphere on nearly all days, with maximum aerosol concentrations found below the layer present at ~700hPa [*Kirkman et al.,* 1998]. The smoke and haze which dominated these stratified layers was found to originate from the northern parts of the subcontinent, although the exact location and extent of sources as well as the mechanisms dominating transport patterns were not completely elucidated by results from the campaign [*Swap et al.,* 2003]. In addition to biomass burning, other sources of aerosol and trace gases were found to impact the southern African region, particularly industrial material, which was found to

comprise approximately 30% of the total fine particulate burden south of 20ºS [*Maenhaut et al*., 1996].

2.3.1.2 SA'ARI-1994

The Southern African Atmospheric Research Initiative (SA'ARI-94; SAFARI without the fire) was carried out in late May 1994 as an extension of the SAFARI-92 experiment. The experiment aimed to characterise the southern African aerosol loading outside of the main biomass burning season [*Kirkman et al*., 2000]. However, results from various measurements showed that pyrogenic material was already present in most samples and that large-scale biomass burning had likely already started in the northern parts of the subcontinent. Biomass burning aerosols were found to originate from both local sources (the local population using biofuels such as wood and charcoal for cooking and heating) as well as from more distant sources, such as the southern DRC, northern Angola and Zambia, where the biomass burning season had already begun. Nevertheless, comparison between SA'ARI-94 and SAFARI-92 data showed significant differences since aerosol concentrations were considerably lower than measured during the main austral winter burning season. Biomass burning was found to be the most significant contributor to the seasonality of aerosol concentrations, making up the greatest proportion of the total burden in the southern African troposphere north of approximately 20°S. In the southern regions of the subcontinent the aerosol loading was also lower than observed during winter, and the atmospheric burden was dominated by industrial aerosol rather than biomass burning particulates [*Kirkman et al.,* 1998].

2.3.1.3 SAFARI-2000

In order to more fully investigate the questions remaining after the SAFARI-92 and SA'ARI-94 campaigns, the Southern African Regional Science Initiative (SAFARI-2000) was carried out from March 1999 to March 2001, through one wet season and two dry seasons. The largest of any campaign in southern Africa to date, it brought together scientists from 18 different countries and a wide field of disciplines [*Otter et al.,* 2002; *Swap et al*., 2002a,b; *Swap et al*., 2003; *Privette and Roy*, 2005].

The majority of the SAFARI-2000 campaign was carried out in abnormally wet conditions, with ENSO being in the La Niña phase for most of the year 2000 [*Roy et al*., 2001]. These conditions were amplified by above-normal sea surface temperatures (SSTs) in both the south-western Indian and southern Atlantic Oceans which also strongly affected the southern African region [*Bell et al*., 2000; *Anyamba et al*., 2002]. Above-average rainfall and high vegetation rates were recorded south of 15°S during the wet season experiment, with NDVI values exceeding the long-term mean by between 20-100% in the south east [*Anyamba et al*., 2003; *Swap et al.,* 2003; *Privette et al.,* 2004; *Shugart et al*., 2004]. These conditions continued into the dry season, resulting in abnormally high rates of biomass burning,

particularly in Botswana, southern Zimbabwe and Moçambique [*Swap et al.,* 2003; *Shugart et al*., 2004; *Privette and Roy*, 2005]. Furthermore, the above-normal rainfall increased the extent of vegetation coverage and burning into more southern regions, which are more sensitive to fluctuations in precipitation and which do not usually burn [*Anyamba et al*., 2003].

Unusual synoptic conditions prevailed during much of the dry season campaign, with a higher than usual frequency of westerly waves and a poleward shift of the tropical easterly wave belt [*Stein et al*., 2003; *Swap et al*., 2003]. Atmospheric circulation patterns generally lacked strong synoptic organisation and the high-pressure systems, if present, tended to be weak. Col regions were more frequent during SAFARI-2000, and acted as the dominant aerosol accumulation mechanism rather than strong anticyclonic conditions, which dominated during the SAFARI-92 campaign [*Annegarn et al.,* 2002; *Stein et al.,* 2003]. As a result of the unusual atmospheric conditions recirculation and air mass build-up was considerably reduced compared to those prevailing during SAFARI-92, and more offshore transport towards the southwest Indian Ocean was observed [*Annegarn et al*., 2002; *Stein et al*., 2003; *Swap et al*., 2003]. The large plume of aerosol haze exiting the subcontinent was observed to extend up to almost 20° in latitude, transporting large amounts of smoke-laden air from the subtropics towards the mid-latitudes. This phenomenon was later termed the 'River of Smoke' [*Annegarn et al*., 2002].

Consistent with the increased biomass burning, aerosol optical depth (AOD) was higher than average during much of the 2000 dry season campaign [*Campbell et al*., 2003]. Highest monthly average AOD (0.89) was observed during September at Mongu, Zambia, a site dominated by biomass burning aerosol since it is situated near the main source regions [*Eck et al.,* 2003; *Swap et al*., 2003]. A strong north-south AOD gradient occurred during the early part of the season, with AOD values at more southerly sites, such as Skukuza, South Africa and Inhaca Island, Moçambique, typically less than 50% of those observed at Mongu. This gradient was in part due to dispersion and deposition that occurred during southward transport [*Eck et al*., 2003; *Queface*, 2003], but also due to the amount of biomass burned locally, which is primarily a function of the north-south gradient in rainfall and vegetation production and is considerably lower in the southern regions [*Scholes et al.,* 1996; *Justice et al.,* 1996; *Eck et al.,* 2001].

Aerosol size distributions measured within the aged regional haze during SAFARI-2000 were found to have three mass modes, centred between 0.2-0.4μm, at ~1μm and ~2μm. Size distributions in fresh smoke plumes were somewhat similar, but bimodal, with peak mass modes at 0.2-0.3μm and 2μm. Aitken and accumulation-size particles were found in extreme concentrations only in fresh smoke plumes. As a result of their small size, these particles provide a large surface area for gaseous condensation to occur and the average diameter of

these aerosol was found to rapidly grow, with fine Aitken and accumulation mode particles generally not evident in the regional haze [*Formenti et al*., 2003].

Southern African aerosol and trace gases were also observed to influence the regional atmosphere of Australia, where aircraft measurements were also made during the SAFARI-2000 period [*Pak et al*., 2003]. Elevated ozone and ethane concentrations within air masses situated between 2-4km were found to have originated from southern African, following approximately 7-10 days transport [*Pak*, 2000; *Pak et al.,* 2003].

2.3.1.4 IGAC DEBITS AFrica (IDAF)

As part of the International Global Atmospheric Chemistry (IGAC) DEposition of BIogeochemically imporTant Species (DEBITS) program an Africa-wide network of measurement sites was established under the umbrella of the IDAF (IDAF DEBITS AFrica) project. Passive sampling techniques are used to obtain monthly average trace gas concentrations at several stations around the continent, four of which are situated in southern Africa and pertinent to this study. Three of the four sites are located in South Africa, at Amersfoort (on the industrial Highveld), Louis Trichardt (a rural site) and Cape Point (in a nature reserve, but near the large city of Cape Town). The fourth site is a remote rural station situated at Okakuejo, Namibia. Measurements at these sites have been carried out for over 10 years (since 1998) and provide an extremely useful database of long-term observations over the continent [*Martins et al*., 2007].

Seasonal cycles of sulphur dioxide (SO_2) concentrations indicate that maximum concentrations are observed during the dry season at all four sites. The stable meteorological conditions experienced in the dry season (winter for the Amersfoort, Louis Trichardt and Okakuejo sites but summer for Cape Point) are likely the main factor contributing to this seasonality. At Amersfoort, the site most influenced by industrial and power plant emissions, this is likely compounded by increased energy production during the cool winter months [*Tyson and Gatebe,* 2001*; Martins et al.,* 2007]. Monthly average SO_2 concentrations ranged from a minimum of 0.2ppb observed at the two rural sites, Louis Trichardt and Okakuejo, to a maximum of up to 6.3ppb observed at Amersfoort [*Martins et a*l., 2007].

2.3.2 Remote sensing observations

Satellite observations provide the only practical means to continuously measure aerosol properties globally, helping to reduce the significant uncertainty surrounding global estimates of global aerosol radiative forcing [*Heineman and Fischer*, 2000]. This is particularly true over the oceanic regions where very few surface-based monitoring sites exist.

Various aerosol optical properties can be measured from space, such as optical depth, particle size distribution as well as aerosol type [*Heineman and Fischer*, 2000]. Aerosol detections are most accurate when aerosol loading is high, since, in clean atmospheric conditions the absolute magnitude of the aerosol retrieval becomes comparable to the magnitude of the error associated with the measurement itself, and aerosol retrievals are not as accurate. In fact, it has been suggested that most of the aerosol radiative forcing may occur within the noise level of most remote sensing instruments [*Remer et al.,* 2002]. This is particularly the case in remote regions, where although concentrations are generally very low, and the transport of aerosol from a distant source (e.g. an industrial region or desert) may easily double the aerosol loading above background levels, thus doubling the radiative forcing, but still remaining within the instrument noise levels [*Heineman and Fischer*, 2000].

Further uncertainty is associated with aerosol remote sensing measurements as a result of the simplified assumptions made in the aerosol retrieval algorithms regarding aerosol optical properties. Assumptions are also made in terms of the vertical distributions of aerosol, a factor which may considerably impact observations [*Kaufman et al.,* 1997]. For example, the presence of a layer of absorbing aerosols or undetected clouds can significantly affect retrievals, resulting in an over- or under-estimation of aerosol optical depth by a factor of two or more [*Quijano et al.*, 2000]. Nearly all aerosol retrieval algorithms also assume spherical particle shape [*Penner et al.*, 2002] – an assumption, which holds for most aerosol types, such as biomass burning, marine and industrial, but not necessarily for mineral dust aerosol. In addition, one of the largest sources of uncertainty in aerosol optical depth retrieval is associated with the cloud-screening algorithms, with differences in optical depth of up to 0.1 or greater, depending on the system used [*Mishchenko et al.*, 1999].

2.3.2.1 The Aerosol Robotic Network (AERONET)

The AErosol RObotic NETwork (AERONET) comprises a worldwide system of ground-based, optical monitoring sites [*Holben et al.*, 1998]. The project was initiated by NASA in the late 1990's and has since been expanded by federation with several non-NASA institutions to incorporate over 200 sites around the globe [*Dubovik et al.*, 2000]. Calibrated sun-sky multi-wavelength radiometers measure aerosol optical depth directly at all stations, and a number of other parameters, including single scattering albedo, aerosol size distribution, refractive index and asymmetry factor are later derived through inversion algorithms [*Dubovik et al.*, 2000].

For optical depths greater than 0.5 the AERONET observations are accurate to 0.03, however, at lower optical depths, particularly below 0.2, the absolute instrument error becomes comparable to the actual AOD measurement and uncertainty is on the order of 5-10% [*Dubovik et al.*, 2002]. This is partly because at low AOD the relative contribution of gaseous absorption and molecular scattering becomes similar to the contribution by aerosol.

In addition, a number of other factors introduce error at all optical depths, including assumptions made in the cloud-screening algorithm (which eliminates any measurement for influenced by clouds, effectively resulting in a systematic under-representation of cloudy conditions), uncertainty in terms of calibration error as well as changes in atmospheric pressure and total ozone amount (for which a climatology is used) [*Dubovik et al*., 2002; *Eck et al.*, 2003].

Furthermore, it is also assumed that all aerosols are homogeneous, spherical particles. This assumption does not hold in the presence of either mineral dust aerosol (which are largely non-spherical) or mixed particles (e.g. an absorbing black carbon core coated with scattering organic carbon) [*Dubovik et al.*, 2002]. Mie scattering theory, which is used in the AERONET AOD retrieval algorithm, may thus not be appropriate in cases when either non-spherical or mixed particles are present. The AERONET retrieval algorithm also doesn't take into account the detailed vertical distribution of aerosols and how this may vary over time, although simulations have shown that errors associated with assumed vertical aerosol distributions in the AERONET measurements tend to be small [*Dubovik et al*., 2000].

2.3.2.2 Total Ozone Monitoring System (TOMS)

Total Ozone Monitoring System (TOMS) instruments were launched on two polar-orbiting satellites, initially onboard the Nimbus-7, in orbit from 1979-1992, and then later on the Earth Probe from 1996-2001 [*Torres et al*., 2002; *Kinne et al*., 2003]. Although not originally intended for monitoring aerosols, the measurements taken in the near UV channels (where weak or no ozone absorption occurs) were found to be useful for the retrieval of aerosol properties [*Torres et al*., 2002; *Kinne et al*., 2003]. The main advantage of TOMS observations is that at near UV wavelengths surface reflectivity is minimal, thus continuous observations over all surfaces can be taken. In addition, there is large sensitivity to the absorbtivity of aerosol types, allowing differentiation between absorbing and scattering aerosols [*Torres et al*., 2002], however, it is not possible to make an objective distinction between the types of absorbing or scattering aerosol [*Prospero et al.*, 2002].

Similar to all other remote sensing instruments, measurements cannot be taken in cloudy conditions, except if the aerosol layer lies above the clouds [*Prospero et al.*, 2002]. Unfortunately, the low resolution of TOMS observations (~50x50km) makes it difficult to avoid cloud contamination, which can have a significant impact on the retrieval of absorbing aerosol in particular [*Kinne et al*., 2003]. Also, the TOMS instrument does not detect aerosol in the lowest 500-1000m of the atmosphere [*Torres et al.,* 1998], perhaps an important drawback, especially in source regions where high aerosol concentrations are situated in the lowest layers of the atmosphere.

Comparison of TOMS and MODIS (see section 2.3.2.4 below) AOD observations suggest that TOMS averages are higher over both dust source and biomass burning regions [*Kinne et al.*, 2003], whilst comparison with AERONET observations over southern Africa have shown that TOMS data agree reasonably well with AERONET, usually within 30% of the ground-based AERONET observations [*Torres et al*., 2002].

2.3.2.3 Multi-angle Imaging Spectro-Radiometer (MISR)

The MISR instrument was launched into orbit aboard the TERRA satellite in December 1999 [*Diner et al.*, 2001]. Imagery is collected at four different wavelengths (446, 558, 672 and 866nm) and at various resolutions from 275m to 1.1km. The narrow swath width of the instrument allows for high-resolution imaging, but prevents continuous global coverage, the main disadvantage of this instrument [*Ichoku et al.*, 2003].

Ground-based observations from the SAFARI-2000 campaign were used to verify and validate the MISR aerosol retrieval algorithm. Close agreement was shown between AERONET measurements and the MISR estimates, and the aerosol retrievals of the instrument were found to be accurate to well within the pre-mission estimates [*Diner et al.*, 2001]. However, compared to MODIS (see following section, 2.3.2.4), MISR observations were found to be less accurate, possibly because of the reduced temporal coverage of this product [*Swap et al*., 2003].

2.3.2.4 MODerate resolution Imaging Spectrometer

Two MODIS instruments are currently in orbit on separate NASA satellites [*Ichoku et al.*, 2003; *Hao et al.,* 2005]. The first instrument was launched simultaneously with MISR onboard the TERRA satellite in December 1999, whilst the second was launched with the AQUA satellite in 2001. Both satellites are sun-synchronous, in near-polar orbits at an altitude of 705km, providing almost complete global coverage daily because of their large swath width (~2300km). TERRA crosses the equator twice daily at 10:30am and 10:30pm local time, while AQUA also passes twice daily, but at 1:30am and 1:30pm local time [*Hao et al.*, 2005]. 36 spectral bands are measured, ranging from 0.405-14.385nm and all aerosol parameters are retrieved at 1km resolution and then aggregated to a global grid of 10km resolution at daily, weekly and monthly time scales [*Ichoku et al.*, 2003].

Different retrieval algorithms are used over land and ocean because of the different surface reflective properties. AOD is calculated at 470, 550 and 660nm over land, whilst it is calculated at 550, 660, 870, 1200, 1600 and 2100nm over the oceans. Distinction between small and large aerosol size categories and measurements of effective radius are made only over the oceans, where AOD retrievals at longer wavelengths permit this [*Ichoku et al*., 2003]. Cloud screening is carried out at 1km resolution, thus allowing superior filtering than the previous satellite observations of TOMS and AVHRR [*Kinne et al.*, 2003].

Similarly to MISR, the MODIS instrument was validated with ground-based observations from the SAFARI-2000 campaign. For low aerosol optical depths (less than 0.6 at 470nm) the MODIS retrievals agree well with those of AERONET [*Ichoku et al.*, 2003]. At higher wavelengths and with increasing AOD, however, MODIS values were significantly lower (by up to 40-50%) than those derived from a network of 38 hand-held sunphotometer observations and the AERONET ground-stations [*Ichoku et al.*, 2003; *Schmid et al.,* 2003; *Hao et al.*, 2005]. This underestimation was largely attributed to the application of a constant single scattering albedo value of 0.90 [*Ichoku et al.*, 2003], which was found to best suit observations over the eastern United States and Brazil rather than southern Africa [*Chu et al.*, 2002]. Observations from the SAFARI-2000 campaign indicated instead that an SSA value of 0.88 (at 470nm) would perhaps be more representative of the regional atmospheric loading during this season [*Dubovik et al.*, 2000; *Ichoku et al.,* 2003]. The MODIS observations have since been re-processed using a more appropriate SSA value, improving accuracy compared to ground-based observations [*Swap et al.,* 2003; *Remer et al.,* 2005].

2.4 Regional climate modelling

This section provides a brief introduction to the concept of regional climate modelling, particularly the caveats and assumptions that need to be borne in mind in regards to studies carried out with these models. A short description of some of the most relevant studies is also provided, although the most pertinent results are presented in later chapters where appropriate.

2.4.1 A brief introduction to regional climate models

Regional climate models (RCMs) continue to serve as a practical means to provide higher resolution information than global climate models (GCMs) [*Vannitsem and Chome*, 2005; *IPCC,* 2007]. The high-resolution information provided by these models is particularly necessary for the accurate representation of the highly heterogeneous nature of atmospheric aerosol processes in aerosol-climate studies [*Simmons et al.*, 2004]. However, a number of assumptions and caveats need to be acknowledged when performing regional modelling studies.

Firstly, the ability of an RCM to reproduce climate depends to a large extent on the realism of the lateral boundary conditions used to force the model [e.g. *Pan et al.,* 2001]. Any insufficiency or error in the observational or GCM boundary forcing is carried through into the RCM, which will not necessarily improve this signal [*Meadows and Hoffman,* 2003]. Secondly, a balance needs to be found between the degree of lateral boundary forcing and the freedom

of the internal model dynamics [*Giorgi et al.,* 1993]. The boundary forcing essentially provides the large-scale synoptic structure of the atmosphere upon which the RCM embeds high-resolution circulation patterns, which are induced by local forcings such as topography. The model domain thus needs to be chosen carefully so that the major features forcing regional climate are included so that the RCM remains consistent with the boundary forcing, but also so that enough freedom is given so that the model can produce its own meso-scale information [*Seth and Giorgi,* 1998; *Giorgi and Mearns,* 1999]. Essentially, the larger the domain, the more the model tends to diverge from the boundary forcing and the greater the internal model error [*Jones et al.,* 1995; *Seth and Giorgi,* 1998]. Internal error also tends to be greater when synoptic-scale circulation exerts less control over the regional climate, for example during summer in a convectively active region [*Christensen et al.,* 1997; *Giorgi and Bi,* 2000]. Furthermore, the ratio between the resolution of the driving fields and the RCM needs to be taken into consideration - a large difference between the two may result in numerical problems within the regional model [*Christensen et al.,* 1998].

In addition, the nesting of an RCM is typically one-way, that is, there is no dynamic feedback between the boundary forcing and the model, and any feedback from the regional to the global scale is thus not taken into account [*Giorgi and Mearns,* 1999]. In terms of making future climate projections, not only is this feature an issue, but further uncertainty is added to the system through the GCM boundary conditions used and because it is assumed that the physics describing the present climate and any parameterisations made in relation to these processes will hold under future climate conditions. Unfortunately, at present there is no way to get around this assumption, and it simply remains to be borne in mind when considering future climate scenarios.

Furthermore, the inclusion of aerosols in regional models also requires the treatment of the species included at the lateral boundaries. Usually, aerosols are assumed to transported out of the domain if flow is in that direction but, in contrast, no aerosol are transported into the domain if circulation patterns suggest air movement in this direction [e.g. *Solmon et al.,* 2006]. Sud et al. [2009], however, showed that, at least for their domain (over West African and India) this assumption led to somewhat different aerosol-climate feedbacks than those exhibited in simulations where aerosol were transported into the domain from the exterior.

Despite the caveats associated with regional modelling a large body of work has shown that RCMs indeed provide improved regional information compared to GCMs [*Mearns et al.,* 1995] RCMs have thus been widely used as a dynamical a downscaling tool to understand regional climate processes and variability [e.g. *Pal and Eltahir*, 2003; *Abiodun et al*., 2007], regional climate change [e.g. *Giorgi et al.*, 2004; *Im et al*., 2008] as well as to investigate the impacts of external forcing on various regions [e.g. *Jenkins*, 1997].

2.4.2 Regional climate modelling studies over Africa

Although RCMs have been widely applied, relatively few studies have focused specifically on Africa, particularly on the southern parts of the continent. This is in large part due to the computationally expensive nature of regional climate modelling, since until relatively recently most southern African research groups have not had access to the necessary technology or infrastructure [*Hudson and Jones,* 2002a]. Although regional climate modelling remains in its infancy within the region, a certain number of studies have been carried out over the past decade and a half. For example, Joubert et al. [1999] used the Australian model, DARLAM, in a process-based study to investigate the summer climate of southern Africa, while more recently, Tadross et al. [2006] used MM5 to detail elements of the diurnal cycle over the subcontinent. Kgatuke et al. [2008] investigated the internal model variability of the regional climate model version 3 (RegCM3, the model used in this study) specifically over South Africa whereas Sylla et al. [2009] used the same model to study the climate over the entire African continent, specifically investigating the impact of using new, high-resolution reanalysis data as boundary forcing. Hudson and Jones [2002b] carried out one of the very few dynamical downscaling studies to produce future climate projections for the 2071-2100 period using the HadRM3H model.

Besides for having been used in the two above-mentioned studies focusing on Africa, RegCM3 has also been more widely used to simulate climate of other regions of the world. Of particular interest are those studies investigating the aerosol impacts on regional climate, which to date have been carried out over Asia [e.g. *Qian et al.*, 2001; *Giorgi et al.*, 2003], South America [e.g. *Zhang et al.*, 2008; *Zhang et al.,* 2009a], West Africa [e.g. *Afiesimama et al.,* 2006; *Konare et al.,* 2008; *Solmon et al.,* 2008; *Zhang et al.,* 2009b] and Europe [e.g. *Solmon et al.,* 2006].

In general, relatively fewer aerosol modelling studies have been carried out at the regional level over climatic time scales, in large part because these models are more complex and their development begun somewhat later than regional atmosphere-only models. To date, no regional climate modelling study investigating the aerosol radiative impacts on climate over southern Africa has been carried out.

CHAPTER 3

Dynamical downscaling: Regional Climate Model III

3.1 RegCM3 dynamics and physics description

3.1.1 A little history:

The original version of RegCM was developed in the late 1980's, based on the dynamical core of the NCAR-Pennsylvania State University Mesoscale Model 4 [MM4; *Dickinson et al*., 1989; *Giorgi*, 1989]. This first generation version included the CCM1 (Community Climate Model) radiative transfer scheme, the BATS (Biosphere-Atmosphere Transfer Scheme) for surface processes, a medium-resolution local planetary boundary scheme, the explicit moisture scheme of Hsie et al. [1984] and a Kuo-type cumulus convection scheme [*Anthes*, 1977].

The model physics and numerical schemes were later updated in the early 1990's to include a split-explicit time integration scheme, an updated version of the CCM radiative transfer scheme (version 2), the non-local boundary layer scheme of Holtslag et al. [1990], a newer version of the surface scheme [BATS1e; *Dickinson et al*., 1993] as well as another convective scheme option, the Grell [1993] mass flux cloud scheme [*Giorgi et al*., 1993].

A third generation version of the model (RegCM3, used in this work) was released in the mid-2000's with a number of updates. Again, the radiative transfer scheme was changed, this time to the newer CCM3 scheme [*Kiehl et al.,* 1996], a large-scale cloud and precipitation scheme [*Pal et al*., 2000] was adapted and a new ocean surface flux parameterisation was included [*Zeng et al*., 1998] as well as an additional convection scheme [*Emanuel*, 1991; *Emanuel and Zivkovic-Rothman*, 1999]. Furthermore, a mosaic-type parameterisation was added in order to account for sub-grid-scale heterogeneity in topography and land-use [*Giorgi et al*., 2003] while the explicit moisture scheme [*Hsie et al.,* 1984] was simplified, in the interests of computational efficiency.

3.1.2 RegCM3 physics

RegCM3 is a hydrostatic, primitive equation model with compressibility and sigma vertical coordinates. The sigma levels are not evenly spaced in the vertical, with seven layers in the lowest 1.5km of the atmosphere and the remaining levels distributed throughout the rest of the atmosphere. Sigma levels follow the terrain but become progressively flatter towards the top of the atmosphere (see fig. 3.1.1). An Arakawa-Lamb B-staggering technique is used in the horizontal, with scalar variables (temperature, specific humidity, etc) being described at the centre of each grid box, while the velocity vectors (u- and v-wind components) are specified at the grid point corners.

Four different options are available for the numerical treatment of the lateral boundaries, including a time-dependent scheme, linear relaxation, a sponge formulation and exponential

relaxation. The exponential formulation ensures a stronger control by the boundary conditions than the linear relaxation scheme, and results in a smoother transition toward the domain interior [*Giorgi et al.,* 1993]. This is particularly the case for the wind fields, where the linear formulation does not provide a good transition from boundary to model interior. Giorgi et al [1993] found that a buffer zone of only three points was too small for relatively large domains, thus the model default is a buffer zone of six grid points.

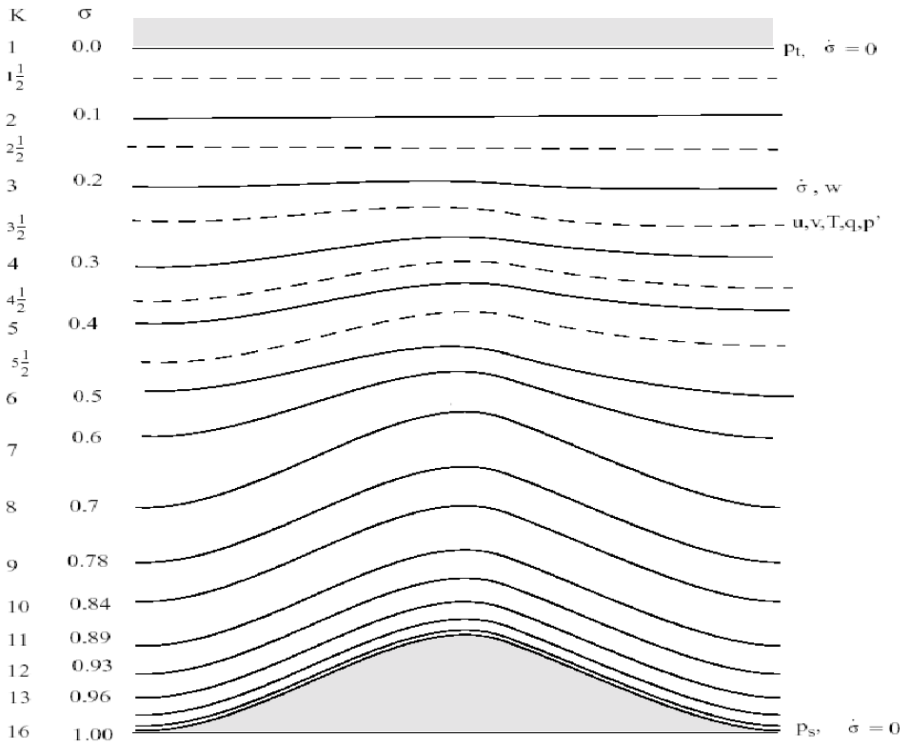

Figure 3.1.1: Schematic representation of the model vertical structure (example for 16 vertical levels). Solid lines represent the full-sigma levels while the dashed lines indicate the half-sigma levels. [*Following Elguindi et al., 2007*].

Further details regarding the core dynamic equations used in RegCM3, and their numerical discretisation are described by Grell et al. [1994], while a simplified explanation of these equations can be found in Elguindi et al. [2007].

3.1.2.1 Radiative transfer scheme

RegCM3 uses the CCM3 radiative transfer scheme [*Kiehl et al.,* 1996], which follows the delta-Eddington approximation, including 18 discrete spectral intervals from 0.2-4.5μm and taking into account the effects of O_3, H_2O, CO_2 and O_2. The parameterisation of Slingo [1989] is used to describe cloud scattering and absorption, through which cloud liquid water content and effective drop radius are determined by three droplet optical properties: extinction optical depth, single scattering albedo and the asymmetry parameter. Clouds are assumed to be as

thick as the model layer in which they occur, with different cloud water content values being specified for low- and mid-level clouds. Fractional cloud cover is calculated such that the total cloud cover extending from the cloud-base to -top is a function of horizontal grid-point spacing, assuming random overlap.

3.1.2.2 Land surface model

RegCM3 incorporates the BATS1e land surface model off Dickinson et al. [1993]. The BATS1e model includes up to five surface layers: a vegetated layer, a snow layer (if present), a surface soil layer, a root zone layer and a deep soil layer. A generalised version of the force-restore method of Deardoff [1978] is used to describe temperatures in each of the soil layers, whilst the temperatures in the vegetation canopy and canopy foliage are calculated diagnostically through an energy balance equation. A standard surface drag coefficient formulation based on surface-layer similarity theory is used to calculate momentum, sensible heat and water vapour fluxes. The drag coefficient is in turn estimated using the specified surface roughness length and model-calculated atmospheric stability in the surface layer.

The soil hydrological cycle is described by a number of equations, which take into account the effects of precipitation, evapotranspiration, snowmelt, surface runoff, soil infiltration and water exchange between soil layers. Precipitation is assumed to fall as snow if the temperature in the lowest atmospheric level drops below 271°K. Snow depth is then calculated from the total snowfall, snowmelt and sublimation processes. The surface evapotranspiration rate depends on the availability of soil water.

Twenty vegetation types are included in the BATS1e scheme and modifications by Giorgi et al. [2003] allow for sub-grid variability of land cover and topography, a feature which was found to greatly improve the simulated hydrological cycle in mountainous regions [*Giorgi et al.,* 2003]. Land cover is specified using the Global Land Cover Characterisation (GLCC) version 2 dataset, provided by the U.S. Geological Survey (USGS) Earth Resources Observation System Data Centre [*Loveland et al.,* 2000]. More details regarding the BATS1e model can be found in Dickinson et al. [1993].

Sea surface temperatures (SSTs) in RegCM3 are prescribed, thus no two-way interaction between atmosphere and ocean is possible in the current version of the model [*Pal et al.,* 2007].

3.1.2.3 Planetary boundary layer scheme

The non-local boundary layer scheme of Holtslag et al. [1990] adopted in RegCM3 takes into account the counter-gradient fluxes that result from large-scale eddies in a well-mixed, unstable atmosphere. The scheme is based on a non-local diffusion concept, where the counter-gradient term describes the non-local transport resulting from dry convection. The

formulation is used to estimate the eddy diffusivity, taking turbulent convective and friction velocities into account, as well as planetary boundary layer (PBL) height and the Monin-Obhukov length. The PBL height is calculated using the computed wind components, virtual temperature, gravity and bulk Richardson number. Further description of the equations describing this scheme in RegCM3 can again be found in Elguindi et al. [2007] and a more detailed discussion of the scheme in Holtslag et al. [1990].

3.1.2.4 Large-scale precipitation scheme

Non-convective clouds and precipitation are handled in RegCM3 by the SUB-grid EXplicit (SUBEX) moisture scheme [*Pal et al.,* 2000]. This scheme calculates the autoconversion of cloud water to rain water as well as accretion, evaporation and cloud fraction at each grid point. In terms of model calculations, the SUBEX scheme is called after the convective scheme. This means that some of the large-scale precipitation produced through the SUBEX scheme may result from moisture transported aloft but not rained out by the convective scheme [*Davis et al.,* 2009].

3.1.2.5 Convective parameterisation schemes

Four convective schemes are available in RegCM3: (1) modified-Kuo [*Anthes*, 1977], (2), MIT-Emanuel [*Emanuel*, 1991; *Emanuel and Zivkovic-Rothman*, 1999], (3) Grell with Arakawa-Schubert closure [*Grell et al.*, 1994] and (4) Grell with Fritsch-Chappell closure [*Grell et al.*, 1994; *Fritsch and Chappell*, 1980].

3.1.2.5.1 The Modified-Kuo scheme

The modified-Kuo scheme uses a moisture convergence term, *M*, to determine at which point convection is activated. When the atmosphere is convectively unstable and *M* exceeds a critical threshold, convective activity is initiated. Part of this moisture convergence moistens the atmosphere whilst the rest is converted into precipitation. The fraction of moisture remaining in the atmosphere depends on the relative humidity (RH), with precipitation occurring only if RH is greater than 0.5 (or 50%).

The moisture convergence term only includes the advective tendencies for water vapour, but the effects of evapotranspiration are indirectly taken into account through this scheme since evapotranspiration from the previous time-step moistens the lower atmosphere (thus the more evapotranspiration, the more moisture is converted into precipitation, assuming the atmospheric column is unstable). Latent heat of condensation is distributed from cloud top to bottom by a function which preferentially allocates maximum heating to the upper portion of the cloud, whilst numerical point storms are eliminated through a horizontal diffusion term.

3.1.2.5.2 The MIT-Emanuel scheme

Convective activity in the MIT-Emanuel scheme is activated when the level of neutral buoyancy occurs above the cloud-base level. Air is lifted between the cloud base and level of neutral buoyancy and a fraction of the moisture it contains is condensed into precipitation, while the remaining moisture forms the cloud. This scheme assumes that cloud mixing is episodic and non-homogeneous, with convective fluxes occurring through idealised sub-cloud-scale up- and down-drafts. The cloud is assumed to mix with its environment as air parcels ascend or descend to their respective levels of neutral buoyancy within the cloud. The entrainment and detrainment rates depend on the local vertical buoyancy gradients within the clouds, whilst the fraction of the total cloud base mass flux that detrains is proportional to the undiluted buoyancy rate of change with altitude.

The MIT-Emanuel scheme also includes an auto-conversion parameter, which is temperature dependent, thus allowing ice-processes to be crudely accounted for. Precipitation is added to a single, hydrostatic, unsaturated downdraft that transports heat and water.

3.1.2.5.3 The Grell scheme

The Grell scheme considers convective clouds as a closed system comprising an up- and downdraft. No mixing occurs between these circulations or with the environment, except at the top and bottom of the cloud, thus mass flux is constant with height. The downdraft mass flux (m_o) depends on the updraft mass flux (m_b) according to the following relation:

$$m_o = (\beta I_1/I_2)*m_b$$

Where I_1 is the normalised condensation occurring in the updraft, I_2 is the normalised evaporation occurring in the downdraft and β is the fraction of updraft condensation that re-evaporates in the downdraft (this value depends in turn on the wind shear). The levels at which the up- and down-drafts originate are given by the levels of maximum and minimum moist static energy, respectively. Convection is activated when a lifted parcel attains moist convection. The values of m_o and m_b are calculated differently depending on the closure assumption adopted.

Two closure assumptions are available for the Grell scheme: Arakawa-Schubert [*Anthes*, 1977] and Fritsch-Chappell [*Fritsch and Chappell*, 1980]. Essentially, the Arakawa-Schubert scheme assumes that convective clouds stabilise the environment as fast as non-convective processes destabilise it. Thus, this closure assumption relates convective fluxes and precipitation to tendencies in the state of the atmosphere. The Fritsch-Chappell assumption on the other hand, relates convective fluxes to the degree of instability in the atmosphere, and basically assumes that available buoyant energy is removed over a given time scale. This closure assumption has been widely implemented in a number of other GCMs and RCMs.

3.2 Internal model variability

Because of the non-linear nature of the atmosphere, models describing this system are inherently non-linear and thus sensitive to any perturbations. This is particularly the case for global climate models (GCMs), since they are initialised only once and then simulate the atmosphere according to a prescribed set of dynamics. Such model systems may become strongly divergent after a matter of only a few days of simulation, if initialised using slightly different conditions [*Shukla*, 1998; *Robertson et al.*, 2004]. In regional climate models (RCMs) this level of divergence is limited to a certain degree by the use of lateral boundary forcing fields and, at least at the large scale, RCM climatologies generally do not differ significantly from the forcing fields applied [Giorgi and Bi, 2000]. An RCM system is, however, not completely free of non-linearities and will exhibit a certain level of internal variability depending on the model physics and dynamics. It is vital to assess the degree of this variability since it can affect, and possibly even mask, physically forced signals reproduced by the model [*Giorgi and Bi*, 2000]. Divergence between simulations is also of interest because of possible errors in the observations used for initial conditions, and lateral boundary forcing in the case of RCM simulations [*Shukla*, 1998].

3.2.1 Experiment setup

In order to investigate the internal variability within RegCM3 an ensemble of seven simulations is carried out. Each ensemble member is initialised from a different consecutive day starting from 1st January 2001 through 7th January 2001 and run until the end of December 2002 (although for analysis purposes the first month is ignored as spin-up). All other model parameters are kept constant between simulations and no other perturbations are introduced (e.g. through the lateral boundary forcing). The simulations are run over a domain covering the region from 18ºN-43ºS and 4ºW-60ºE. This domain was decided upon after several tests investigating the model sensitivity to domain size and situation (see appendix A.1). Results from these tests showed that the model representation of the southern African regional climate over this domain is sufficiently accurate and provided the best performance in terms of computational efficiency.

All simulations are carried out using the NCAR-NCEP-II reanalysis product [*Kanamitsu et al.,* 2002] and National Ocean and Atmosphere Administration's (NOAA) Optimum Interpolated sea surface temperature (OISST) product [*Reynolds et al.,* 2002] as lateral boundary forcing. A horizontal grid resolution of 60km is used. Although RegCM3 can be used at resolutions of up to 10km (but not beyond this because it is hydrostatic), the fairly coarse resolution of 60km is chosen for several reasons. Firstly, the focus of this work is on the climate-scale, thus relatively long-term simulations of several years are necessary. These lengthy simulations require considerable computational time, particularly given the use of the online aerosol

module. Similarly, the domain chosen for most of the simulations carried out in this work is relatively large. And, finally, the aerosol emissions inventories used, as well as most of the observational datasets used for validation purposes, are available at similar or lower resolutions. The use of a 60km horizontal resolution thus provides the best compromise between these factors.

All simulations are run using the Grell convective parameterisation scheme with the Fritsch-Chappell closure assumption. Sensitivity tests assessing all four convective schemes available in RegCM3 showed that this parameterisation performed best overall, particularly in terms of surface temperature and precipitation (see Appendix A.2). The domain simulated is divided into six sub-regions so as to facilitate the investigation of this analysis (see figure A.2.1).

The deviation from the ensemble mean (treated as the baseline) is quantified using two, slightly different measures: the root-mean-square deviation (RMSD) and the average difference (BIAS). The RMSD is calculated according to the following relation:

$$RMSD = \sqrt{\sum \frac{(Ti - Tb)^2}{N}}$$

where for a particular variable T_i and T_b are the values for the i^{th} simulation and ensemble mean (baseline) respectively, at a particular time-step, and N the number of grid points for a given region. The corresponding BIAS is calculated as follows:

$$BIAS = \sum \frac{Ti - Tb}{N}$$

The RMSD compounds the deviations at all individual points regardless of their sign (and therefore is always positive), whilst the BIAS gives an estimate of the systematic deviation in a particular direction (positive or negative).

3.2.2 Root-mean-square difference (RMSD)

The daily average RMSD for surface temperature and precipitation is shown in figures 3.2.1(a) and (b) respectively. Although the total annual cycle was investigated only the austral winter (JJA) and summer (DJF) seasons are presented, since results from the intermediary spring and autumn seasons are similar.

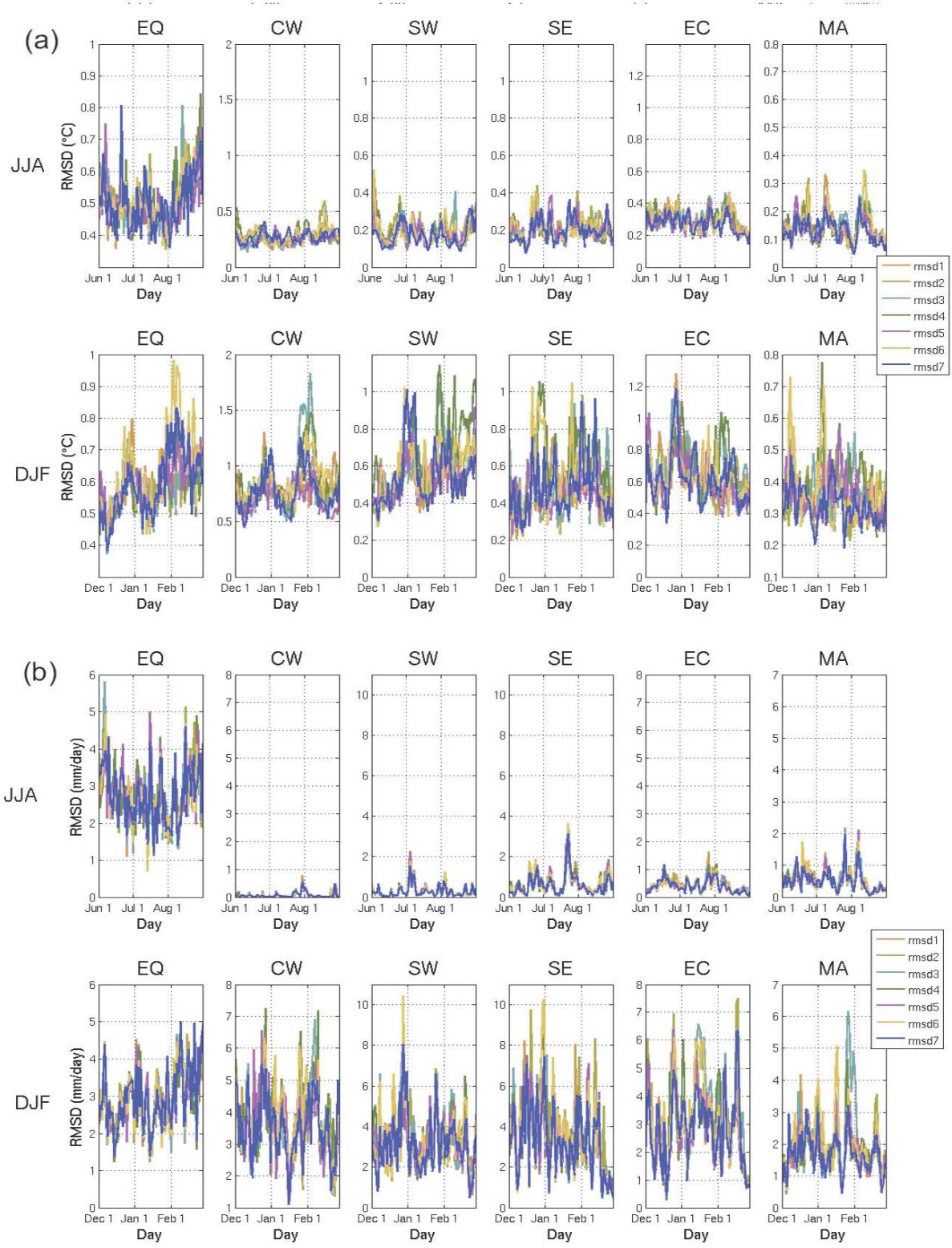

Figure 3.2.1: Daily average Root-Mean-Square Difference (RMSD) of all ensemble members for (a) temperature (in °C) and (b) precipitation (in mm/day). The austral winter (JJA) and summer (DJF) seasons are shown in the top and bottom rows of each plot, respectively. Note the different y-axis ranges for each sub-region.

It is clear that for both surface temperature and precipitation the RMSD is considerably greater during summer (DJF) than in winter (JJA). The only exception is the equatorial sub-region (EQ), where the RMSD remains relatively constant throughout the year. The non-linear nature of mesoscale convective processes induces a greater degree of internal model variability, resulting in higher RMSD. Therefore, during the seasons when convection is most prevalent (DJF over most of southern African, but throughout the year in the equatorial sub-region) RMSD is higher. Conversely, when little or no convective precipitation occurs (JJA for most sub-regions), the RMSD is much lower since there is inherently less internal variability. Also notable is the fact that the RMSD for precipitation is higher in all six sub-regions than that for surface temperature. Again, this is somewhat as expected, since at the daily time-scale, precipitation tends to be considerably more variable than surface temperature.

Perhaps of more importance, however, is the fact that in terms of the actual magnitude of surface temperature and precipitation there is no significant difference between any of the ensemble members, or between any of the ensemble members and the ensemble mean. All ensemble members deviate from the ensemble mean to a certain extent but all members appear to deviate to a very similar degree in all sub-regions and all seasons. Thus, although RegCM3 exhibits a certain degree of internal model variability, it seems to be relatively stable and there is little divergence between simulations started with different initial conditions.

3.2.3 Bias

In order to investigate whether there is any systematic bias between ensemble members and the ensemble mean, the daily average bias of surface temperature and precipitation for all six sub-regions is shown in figures 3.2.2(a) and (b), respectively. As for the RMSD only the results for the austral winter (JJA) and summer (DJF) season are shown, since the intermediary seasons again show similar results.

In both winter and summer no systematic model bias is observed in any sub-region, with the bias oscillating around zero in all cases. Similarly to RMSD, the bias is greater in the austral summer season (DJF) in the five extra-tropical regions, whilst it remains relatively constant throughout the year in the tropics (EQ sub-region). Again, these results imply that greater internal model variability is apparent when convective processes dominate. In JJA, large-scale processes are of greater importance for most of the domain (except in the EQ sub-region), and thus the lateral boundary forcing exerts greater control on the model solution and less internal variability is observed.

As for the RMSD, the bias in terms of precipitation is greater than that for surface temperature, indicating that there are greater differences between individual ensemble members and the ensemble mean for this variable. Again, this is somewhat as expected,

since there is greater variability in precipitation processes compared to those associated with surface temperature.

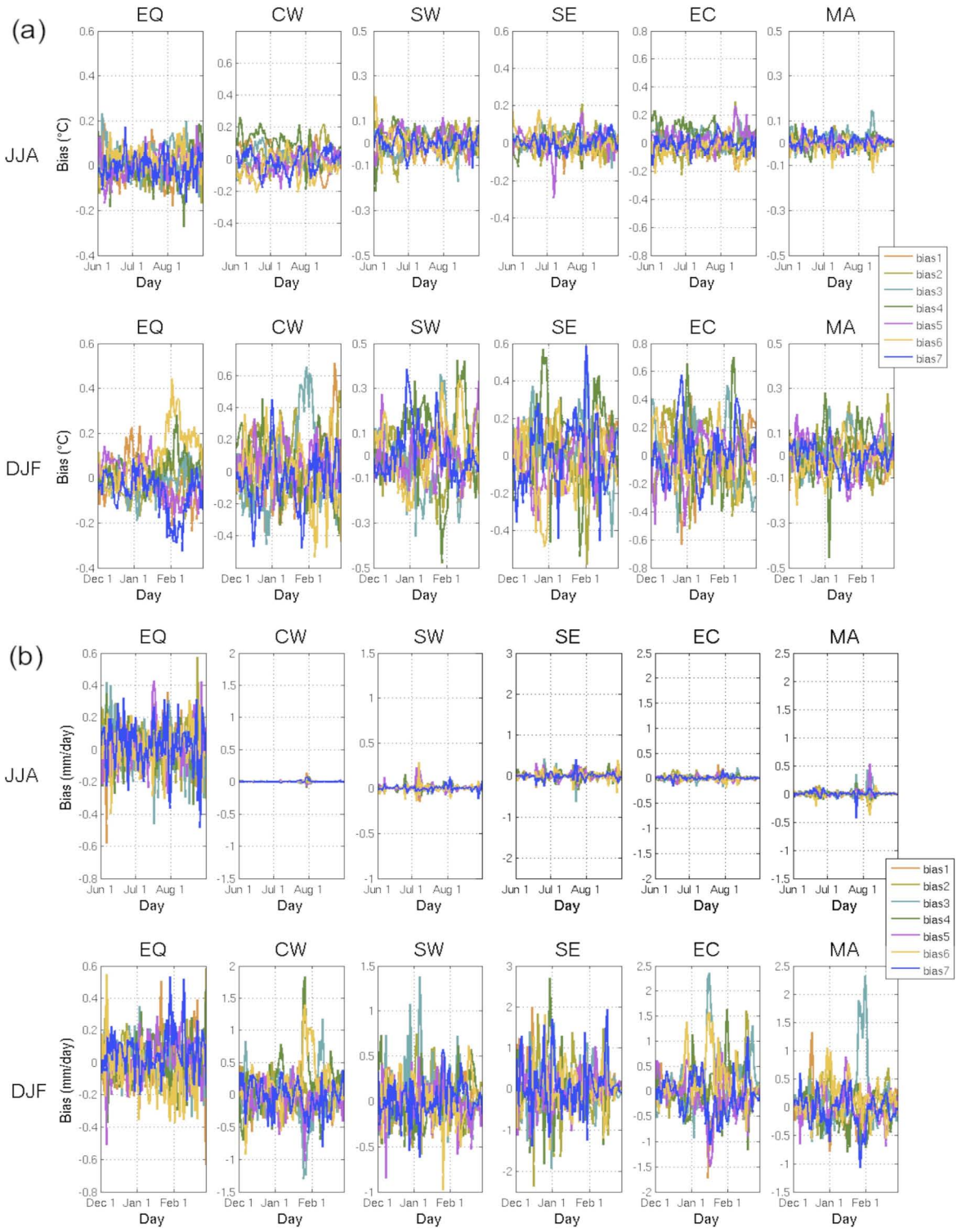

Figure 3.2.13: Daily average bias compared to the ensemble mean for each of the seven ensemble members, for (a) temperature (in °C) and (b) precipitation (in mm/day). The austral winter (JJA) and summer (DJF) seasons are shown in top and bottom rows of each plot, respectively.

Anthes et al. [1989] and Giorgi and Bates [1989] found similar results over different domains, with internal model error growing for the first 24-48 hours of simulation, but then levelling off and varying around an asymptotic value when dynamical equilibrium between the external boundary forcing and the internal model solution is reached. Thus, although RegCM3 does show a certain inherent amount of internal model variability, a priori it should not strongly affect the physically forced model signal, for example, from an aerosol perturbation. This lends confidence to the use of RegCM3 as a tool to represent the southern African regional climate and to accurately estimate the physical forcing mechanisms active over the subcontinent.

3.3 The RegCM3 aerosol module

3.3.1 Aerosol chemistry

RegCM3 includes a basic online aerosol-chemistry module describing three aerosol tracer species: black carbon (BC), organic carbon (OC) and sulphate (SO_4) as well as one gaseous species, sulphur dioxide (SO_2), effectively the main source of aerosol SO_4. The scheme describes horizontal and vertical transport through advection by atmospheric winds, turbulent diffusion and cumulus convection transport. It also characterises dry and wet removal processes as well as gaseous and aqueous chemical conversions [*Pal et al.,* 2007]. Wet deposition of aerosol by resolvable and sub-grid scale precipitation is parameterised as a function of the rate of conversion from cloud water to rain water and the hydrophilic nature of the aerosol considered following Giorgi and Chameides [1986]. Dry deposition is calculated using prescribed deposition velocities over land and water surfaces [*Pal et al.,* 2007] and no aerosol is transported into the domain from the exterior (i.e. the aerosol concentrations are fixed to zero at the boundaries) [*Solmon et al.,* 2006].

The carbonaceous aerosol scheme is based on the work of Chameides et al. [2002]. Both BC and OC are assumed to be primary aerosols, directly emitted into the atmosphere in hydrophobic and hydrophilic forms. Following Cooke et al. [1999], 80% of BC emissions are assumed to be in the hydrophobic form, whilst in the case of OC, 50% is assumed to be hydrophobic upon release. Aging from the hydrophobic to hydrophilic form occurs at a pseudo-first-order rate of $7.1 \times 10^{-6}.s^{-1}$ [*Cooke and Wilson*, 1996]. This assumption is a simplification that attempts to account for the wide variety of very complex processes that affect aerosol particles during transport. These aging processes are not yet totally understood and have only very recently been taken into account in the most advanced climate models. It is however, generally recognised that freshly emitted particles tend to be mostly hydrophobic, becoming more hydrophilic over time [*Cooke et al.*, 1999; *Posfai et al.,* 2003; *Croft et al.,* 2005].

The effect of hygroscopic growth on the extinction coefficient is parameterised as in Kasten [1969]. Both hydrophobic and hydrophilic forms of BC and OC are vertically mixed by convective clouds using the same vertical weighting factor as for sulphate, following Tan et al. [2002]. Only the hydrophilic component is removed through wet deposition (washout/rainout) processes. The dry deposition velocity for hydrophilic carbonaceous species is assumed to be 0.2cm.s^{-1} over water and 0.025m.s^{-1} over land, whilst for the hydrophobic form a value of 0.025m.s^{-1} is used over all surfaces [*Ganzeveld et al.,* 1998]. Wavelength dependent optical properties are prescribed for both BC and OC particles, with external mixing assumed for both species [*Solmon et al.,* 2006].

The RegCM3 sulphur scheme follows the work of Kasibhatla et al. [1997], with updates by Qian et al. [2001] and Tan et al. [2002]. The scheme takes between 7-10 days of simulation time to equilibrate with the meteorological forcing [*Qian et al.,* 2001]. Both sulphur compounds are directly released into the atmosphere, assuming that 97% of total emissions are in the form of gaseous sulphur dioxide (SO_2) and the remaining 3% made up of particulate sulphate (SO_4). The large majority of SO_4 is formed in the atmosphere, as SO_2 is oxidised to SO_4 by one of two pathways, either through gaseous conversion, by reaction with hydroxyl radical (OH), or through the aqueous phase, which involves the dissolution of SO_2 in cloud water to form HSO_3^- and SO_3 ions [*Qian et al.,* 2001]. These ions are subsequently oxidised by H_2O_2 if the pH is below 5 *[Kasibhatla et al.,* 1997], a reaction that depends largely on the available concentration of gaseous phase H_2O_2 [*Qian et al.,* 2001; *Huang et al.,* 2007]. Because oxidation of SO_2 by O_3 accounts for only 10% of all SO_2 oxidation it is not included in the simplified scheme [*Qian et al.,* 2001]. The parameterisation of Kiehl et al. [2000] is used to account for the hygroscopic growth of sulphate and its influence on the aerosol optical properties.

Aerosols are transported vertically within cumulus clouds by assuming that when cumulus convection is activated the tracer becomes mixed between the surface and the top of the cumulus cloud (i.e. the mixing ratio is constant between these levels) [*Tan et al.,* 2002]. This is, however, only a first order estimate of these transport processes and the present version of RegCM3 does not include a complete convective transport and scavenging parameterisation scheme for aerosols. As for BC and OC, wet removal of both SO_2 and SO_4 is based on the scheme of Giorgi and Chameides [1986]. The fraction of tracer dissolved into the cloud water is assumed to be one for SO_4 (i.e. it is completely soluble), while the equilibrium dissolution value is used for SO_2 (this depends on the liquid water content). A constant dry deposition velocity of 0.2cm.s^{-1} is assumed for SO_2 over all surfaces, while for SO_4 values of 0.3cm.s^{-1} and 0.8cm.s^{-1} are assumed over land and ocean respectively [*Qian et al.,* 2001]. More detailed descriptions of the chemistry scheme can be found in Solmon et al. [2006] and Huang et al. [2007].

3.3.2 The RegCM3 dust scheme

RegCM3 also contains an online dust scheme which calculates emission, transport and deposition of four particle size-bins, accounting for particles with diameters ranging from 0.01-20μm [*Zakey et al.,* 2006]. The emissions scheme is based on the work of Marticorena et al. [1995] and Alfaro and Gomes [2001]. Horizontal dust saltation and vertical dust fluxes are both taken into account in the dust emission term, which depends on a minimum threshold friction velocity. This threshold velocity is a non-linear function of the near-surface wind speed and in turn depends on the particle radius, soil moisture and texture as well as vegetation type [*Konare et al.,* 2008]. Upper soil moisture content is one of the most important factors in the dust production term and is initialised using a standard procedure, originally described by Giorgi and Bates [1989], through which the soil moisture depends simply on the vegetation type. Vertical transport through convective processes, turbulent boundary layer mixing, gravitational settling and below-cloud scavenging are all parameterised as well.

Overall, the RegCM3 dust and aerosol modules are relatively simplistic, with a considerable number of assumptions being made in both schemes. In addition, there is no microphysics scheme in this version of the model, thus aerosol-cloud interactions are not taken into account. Despite this, RegCM3 still serves as a useful tool to provide a first order assessment of the climatic impact of aerosols, particularly in view of other large sources of uncertainty in the aerosol framework (e.g. emissions estimates; see ensuing discussions). A community-wide effort is currently being made to improve both our understanding of aerosol related processes and their representation in climate models, including within RegCM.

3.3.3 Aerosol radiative properties

Direct aerosol radiative forcing in RegCM3 is calculated using the NCAR Community Climate Model (CCM3) radiative package [*Kiehl et al.,* 1996]. Three aerosol optical properties are specified in this scheme: extinction coefficient (how much radiation is absorbed at a particular wavelength), single scattering albedo and asymmetry parameters. In RegCM3 these three parameters vary depending on aerosol physical parameters, solar wavelength and the environmental relative humidity [*Solmon et al.,* 2006, *Solmon et al.,* 2008]. Mie theory [*Matzler*, 2002] is used to calculate the extinction coefficient of dry aerosols using prescribed refractive indices and characteristic lognormal size distributions (see tables 3.2.7 and 3.2.8 for the dry extinction coefficient and single scattering albedo, respectively, for the eight shortwave bands used in RegCM3).

Dust aerosol are assumed to be spherical, an assumption which has been found to be sufficient for climate modelling purposes [*Miller and Tegen,* 1998]. The optical parameters and the online model-calculated aerosol concentrations are then used to force the CCM3

radiation package [*Huang et al.,* 2007]. Sulphate and both hydrophobic and hydrophilic components of the OC aerosol have radiative properties that follow Kiehl and Briegleb [1993], except that hydrophobic OC is assumed not to take up any water [*Chameides et al.,* 2002].

The aerosol effects on longwave (thermal/infrared) radiation are not included in the version of RegCM3 used here. However, since the interactions of carbonaceous and sulphate particles with radiation decreases rapidly with increasing wavelength, this is not an unrealistic assumption, at least for these aerosol. In contrast, dust aerosol do have a significant impact on long wave (LW) radiation, largely because of their greater size [*Dufresne et al.,* 2002; *Slingo et al.,* 2006], but these effects are not taken into account in this study. Further investigation with the latest version of RegCM (RegCM4, released July 2010), which includes a LW parameterisation scheme, would certainly be of interest.

Tracer / ***Wavelength Band***	**BC_{hb}**	**BC_{hl}**	**OC_{hb}**	**OC_{hl}**	**$Dust_1$**	**$Dust_2$**	**$Dust_3$**	**$Dust_4$**
200-245nm	20.78	14.85	6.06	3.54	1.88	0.76	0.37	0.17
245-265nm	17.21	14.26	6.07	3.62	2.02	0.78	0.37	0.17
265-275nm	15.86	13.94	6.12	3.72	1.95	0.76	0.37	0.17
275-285nm	15.05	13.72	6.01	3.71	1.90	0.75	0.37	0.17
285-295nm	14.30	13.51	5.80	3.65	1.79	0.74	0.37	0.17
295-305nm	13.61	13.29	5.70	3.64	1.71	0.75	0.37	0.17
305-350nm	11.97	12.72	5.65	3.68	1.54	0.82	0.38	0.17
350-640nm	6.58	9.44	4.33	3.45	2.45	0.86	0.38	0.17
640-700nm	4.40	6.97	3.15	2.98	3.11	0.74	0.43	0.18

Table 3.2.7: RegCM3 dry extinction coefficient (in m^2/g) for hydrophobic (hb) and hydrophilic (hl) black carbon (BC) and organic carbon (OC) as well as for the four dust size-bins.

In addition, as already mentioned, only the direct and semi-direct effects are calculated in RegCM3, since there is no aerosol-microphysics coupling in the current version of the model. Over southern Africa during the dry season this does not, however, appear to be a completely unrealistic assumption. Swap et al. [2003] suggested that relative humidity and precipitation are so low in the austral winter that the indirect effects are essentially of little consequence, and the subcontinent is largely influenced by direct aerosol radiative forcing only. At this point, it is acknowledged that this assumption is indeed a limitation of this work, most notably in the convective equatorial regions where precipitation does occur year round. Given the large uncertainty still associated with the indirect aerosol effect [*Lohmann and Feichter,* 2005;

Solomon et al., 2007], and the fact that to date no other regional modelling study has investigated the aerosol radiative forcing over southern Africa. The focus of this work is rather on the better-parameterised and better-understood direct and semi-direct effects.

Tracer / *Wavelength Band*	BC_{hb}	BC_{hl}	OC_{hb}	OC_{hl}	$Dust_1$	$Dust_2$	$Dust_3$	$Dust_4$
200-245nm	0.245	0.461	0.917	0.879	0.643	0.552	0.538	0.543
245-265nm	0.210	0.449	0.924	0.883	0.678	0.569	0.536	0.542
265-275nm	0.195	0.444	0.929	0.892	0.673	0.560	0.539	0.542
275-285nm	0.186	0.441	0.931	0.896	0.663	0.553	0.540	0.542
285-295nm	0.177	0.437	0.933	0.900	0.681	0.574	0.543	0.541
295-305nm	0.169	0.434	0.938	0.905	0.680	0.585	0.542	0.541
305-350nm	0.149	0.424	0.940	0.908	0.727	0.687	0.586	0.546
350-640nm	0.071	0.359	0.953	0.934	0.947	0.882	0.808	0.705
640-700nm	0.038	0.296	0.955	0.950	0.896	0.892	0.864	0.758

Table 3.2.8: RegCM3 single scattering albedo (unitless) for hydrophobic (hb) and hydrophilic (hl) black carbon (BC) and organic carbon (OC) as well as for the four dust size-bins.

3.4 Aerosol module tests

3.4.1 Experiment description

Uncertainty in aerosol models derives largely from the numerous parameterisations that are necessary to simplify the complex chemical and physical interactions occurring in nature. In an effort to estimate, at least to some degree, some of the uncertainty within the relatively simple aerosol chemistry module of RegCM3, a number of sensitivity tests are carried out. All tests include the ten tracers available in RegCM3: hydrophobic and hydrophilic black and organic carbon species, sulphur dioxide, sulphate and dust (separated into four size bins). Emissions from both biomass burning and anthropogenic sources (industrial, vehicular, household emissions) are used. A summary of the tests is provided in table 3.4.1.

Experiment Name	Simulation Characteristics
LOWET	Reduced BC-hl and OC-hl solubility
NOWET	No wet deposition for all tracers
NODRY	No dry deposition for all tracers
DECR	Decreased aerosol injection height

Table 3.4.1: Simulation characteristics of the five aerosol sensitivity tests carried out. BC-hl and OC-hl are hydrophilic black and organic carbon respectively.

Two tests investigating the role of the parameterisation of aerosol deposition are performed, one with no dry deposition (NODRY) and one with no wet deposition (NOWET). The dry and wet deposition rates used in these tests are shown in table 3.4.2. A final test is performed to examine the role of biomass burning injection height on the model solution. Injection height is decreased, effectively meaning that more aerosol are released lower in the atmosphere (see table 3.4.3 for the relative proportions emitted into the lowest four model levels). Injection of biomass burning aerosol into the free troposphere has not been observed over Africa [*Labonne et al.,* 2007], therefore no test is carried out assuming deep-injection.

	CTRL	**NOWET**	**NODRY**
BC-hb	0.05	0.00	0.05
BC-hl	0.80	0.00	0.80
OC-hb	0.05	0.00	0.05
OC-hl	0.80	0.00	0.80
SO2	0.20	0.00	0.20
SO4	0.80	0.00	0.80
Dust 1	0.30	0.00	0.30
Dust 2	0.40	0.00	0.40
Dust 3	0.50	0.00	0.50
Dust 4	0.60	0.00	0.60

Table 3.4.2: Fraction of each tracer removed during wet deposition for the deposition experiments: Control (CTRL), no wet deposition test (NOWET) and no dry deposition (NODRY).

All tests are carried out covering the period January 2001 to December 2002, and over the same domain as described in the previous section (see section 3.2.1). Similarly, the NCEP-II reanalysis data in combination with the NOAA OISST data are again used as lateral boundary forcing.

Experiment Name	**% per model level (approximate height in metres)**			
	1 (~35m)	*2 (~35-150m)*	*3 (~150-300m)*	*4 (~300-550m)*
CTRL	20	30	40	10
DECR	50	30	10	10

Table 3.4.3: Percentage of biomass burning emissions released per model level (with approximate level heights shown in parentheses) for the control (CTRL) and decreased injection height (DECR) tests.

3.4.2 Aerosol optical depth comparison

3.4.2.1 Temporal comparison

The sensitivity of simulated aerosol optical depth (AOD) to the various deposition and emission parameters tested is presented for the two southern African AERONET sites (see section 2.3.2.1 for a full description) for which long-term observations are available (see fig. 3.4.3(a) for the location of these sites). The first of these sites, Mongu (15.5ºS, 29.1ºE), is situated in a region covered by Miombo forest in western Zambia, and is relatively close to major biomass burning sources. The second, Skukuza (25.0ºS, 31.6ºE), is situated almost 10º further south in the dry savannah regions of northeast South Africa. Skukuza is at greater distance from the main southern African biomass burning regions but is still affected by the long distance transport of these emissions to the site. Skukuza is also influenced by smaller, local biomass burning sources, which dominate later in the year [*Liousse et al.,* 1996; *Maenhaut et al,* 1996; *Scholes et al.,* 1996; *Freiman and Piketh,* 2003] and, depending on meteorological conditions, by industrial aerosol from the South African Highveld region as well [*Salma et al.,* 1997; *Campbell et al*., 2003]. Simulated AOD is also compared to two satellite AOD products, MISR (see section 2.3.2.3) and MODIS (see section 2.3.2.4).

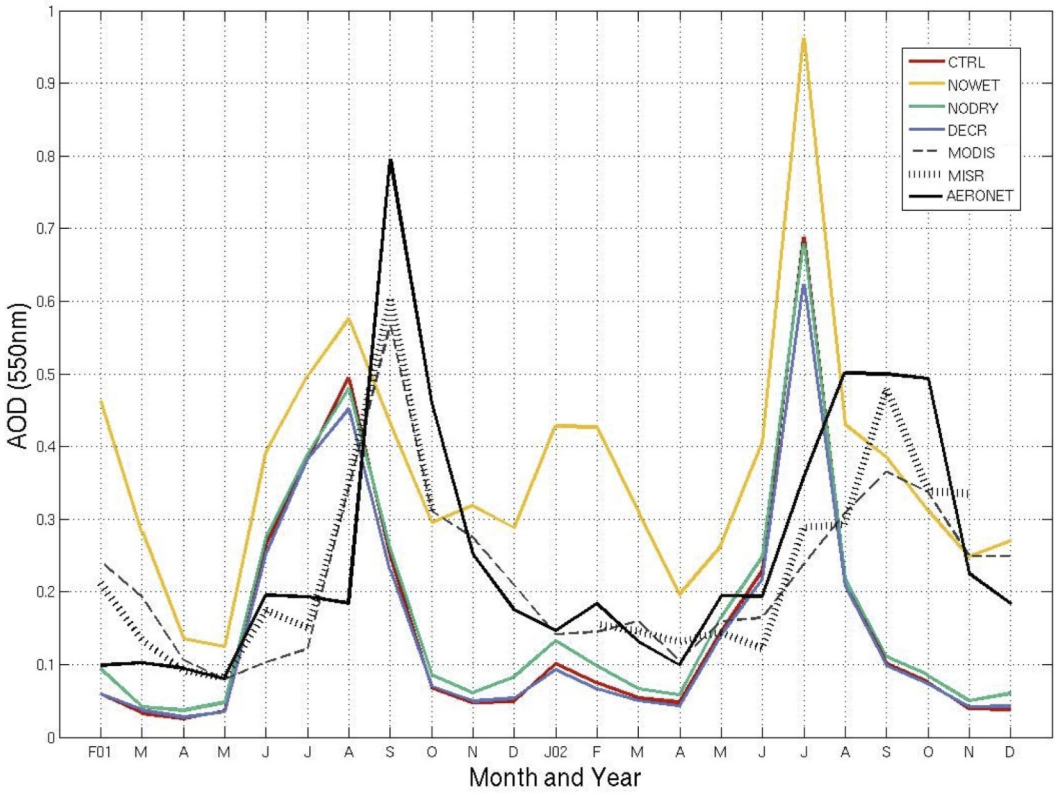

Figure 3.4.1: Aerosol Optical Depth (AOD) for AERONET, all model sensitivity tests, as well as the MODIS and MISR satellite products at Mongu, Zambia.

At both Mongu (fig. 3.4.1) and Skukuza (fig. 3.4.2) the RegCM3 CTRL simulation reproduces the AERONET measured AOD relatively well. For the period simulated (2001-2002) the magnitude of AOD appears to be accurately represented. In terms of the timing of maximum AOD, however, the model exhibits a systematic early bias, reproducing maximum AOD up to two months in advance of the AERONET and satellite observations. This bias is most likely related to the biomass burning emissions inventory used, since the emission inventory used suggests that emissions peak in July or August depending on the region. A more complete discussion of this, and related features, is provided in chapter four, where simulations using these data are validated in greater depth over a longer time period. In the context of the tests carried out here it suffices rather to compare the results between tests in order to assess the model sensitivity to the parameterisation of aerosol deposition and emission.

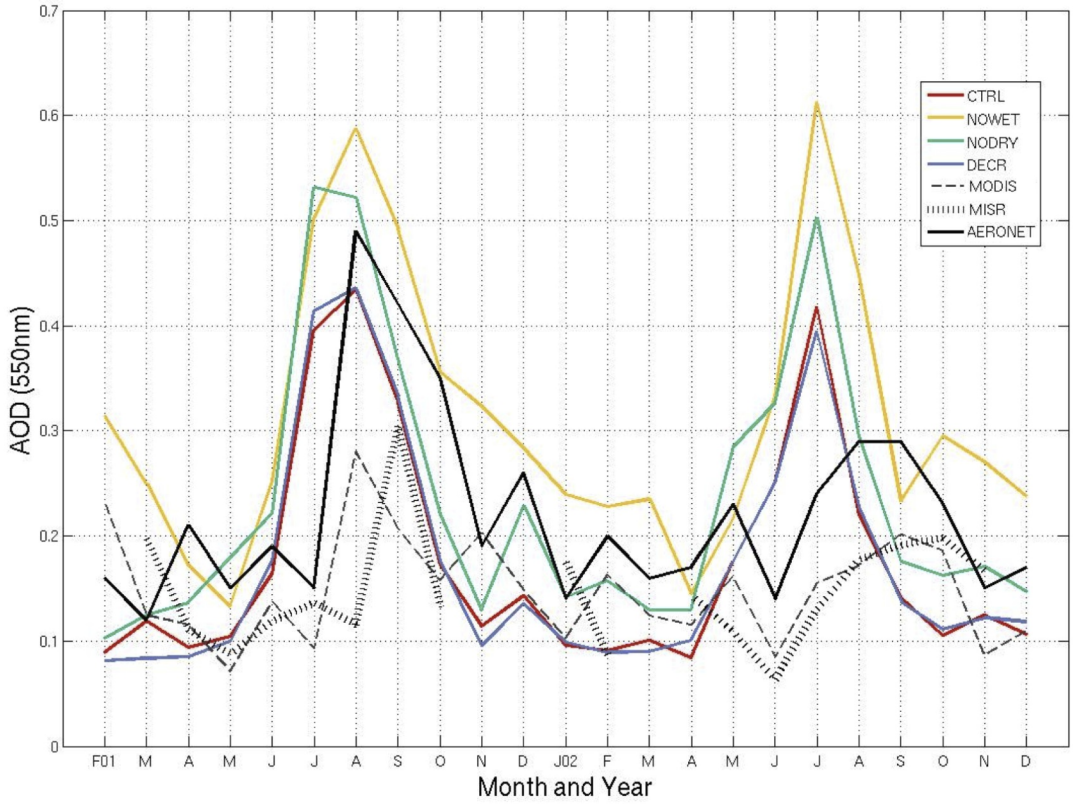

Figure 3.4.2: Aerosol Optical Depth (AOD) for AERONET, all RegCM3 sensitivity tests, as well as the MODIS and MISR satellite observations at Skukuza, South Africa.

There is no significant difference between the CTRL test and the NODRY test at Mongu (see table 3.4.4), indicating that at this site there is little sensitivity to the parameters used to describe dry deposition. A similar signal is observed at Skukuza, although there is a slightly greater difference between these tests than at Mongu, with simulated AOD being up to 0.1 higher in the NODRY test (these differences are not significant however; see table 3.4.4).

This suggests: (i) that dry deposition is of greater importance in this region (which seems logical, since this region is drier than the region around Mongu) and (ii) that a greater degree of error is introduced at Skukuza because of uncertainty regarding the parameters used to represent dry deposition processes.

In terms of biomass burning emissions injection height there is also no significant difference between the CTRL and DECR tests at either Mongu or Skukuza. Again, this indicates that there is little sensitivity to this factor and that uncertainty regarding this process likely has very little impact on simulated AOD, which in turn affects the estimated aerosol radiative forcing. This signal also suggests that boundary layer mixing in RegCM3 is effective, since it appears that even if released lower in the atmosphere the emitted aerosol quickly become mixed in the model boundary layer.

A significant difference in simulated AOD only becomes apparent when wet deposition is completely suppressed (see table 3.4.4). In the NOWET test AOD is greater throughout the year at both Mongu and Skukuza, particularly in the wet season (November to April) when this form of deposition plays a more dominant role. During this season AOD is up to four times greater than in the CTRL simulation at Mongu. It is important to note, however, that the NOWET simulation is a rather unrealistic case since it is certain that wet deposition does occur, it is only the parameterisation of this process that is uncertain. This test serves to provide an idea of the comparative role of wet deposition, which appears to be considerably more important than dry deposition. Therefore, greater uncertainty is attached to the parameterisation of wet deposition processes at the two AERONET sites investigated.

	Mongu, Zambia	Skukuza, South Africa
NOWET	$1.078e^{-4}$	$5.688e^{-4}$
NODRY	0.7856	0.1195
DECR	0.8736	0.9639

Table 3.4.4: p-values from two-tailed Student's t-tests comparing simulated AOD for the NOWET, NODRY and DECR tests to the CTRL test at Mongu, Zambia and Skukuza, South Africa (values highlighted in red if significant at the 95% level).

It is important to note that the differences between the three observational AOD products are significantly larger than those between the CTRL and NODRY and between the CTRL and DECR tests. Indeed, differences between the satellite and in-situ AERONET observations are as large, or indeed for some months, even larger than the difference between the CTRL simulation and the satellite observations. At Skukuza both the MODIS and MISR observations are significantly different from the AERONET measurements for the period simulated

(p=0.003 at both sites, at the 95% level using a Student's T-test). This indicates that the uncertainty associated with the parameterisation of aerosol deposition and emission processes falls well within the range of uncertainty still associated with various observational techniques.

3.4.2.2 Spatial comparison

In order to better capture the spatial variability of simulated AOD, model results are also compared to seasonal average daily composites of MODIS and MISR observations for June through August (see figure 3.4.3). These results again highlight certain features already mentioned in terms of model sensitivity to aerosol chemistry parameterisation:

- sensitivity to dry deposition parameters is relatively low, with dry deposition playing a relatively small role over most of southern Africa during the biomass burning season, as seen by comparing the CTRL (fig. 3.4.3(c)) and NODRY (fig. 3.4.3(d)) simulations. Dry deposition is largely determined by particle size, with smaller particles being less affected by this process than larger particles [*Seinfeld and Pandis,* 2006]. Given the size range of biomass burning particles, it is thus not very surprising that dry deposition plays a less significant role over the region in the burning season. This feature has been observed in previous modelling studies as well [e.g. *Liousse et al.,* 1996; *Cooke and Wilson,* 1996];
- despite it being the dry season, sensitivity to wet deposition is greater than dry deposition since complete suppression of wet deposition has a significant impact on the simulated AOD signal, with simulated AOD in the NOWET test (fig. 3.4.3(f)) reaching values well over 1 over a considerably larger area than shown in the CTRL simulation; and
- there appears to be almost no sensitivity to biomass burning injection height, with little difference between the CTRL and DECR (fig. 3.4.3(e)) simulations.

Although the magnitude of AOD is well simulated, it is clear that the region of maximum AOD is situated approximately 5º too far south compared to the satellite observations. This feature will be further discussed in section 4.2.3. Here it is relevant just to point out that the temporal and spatial mismatch between satellite observed and simulated AOD does not appear to be a result of error associated with aerosol deposition processes or biomass burning aerosol injection height, since similar errors are apparent in all tests. It is possible that errors exist in the MODIS and MISR observations, since there is considerable difference between the two seasonal average products shown (fig. 3.4.3(a) and (b), respectively), as well as between satellite estimates and AERONET (as discussed above in section 3.4.2.1). This error is, however, unlikely to account for all the difference observed between the model and the satellite measurements. At this point, it suffices to note that the spatial patterns of AOD simulated over southern Africa are of similar magnitude to those observed from the MODIS and MISR platforms as well as that measured at the two available AERONET sites.

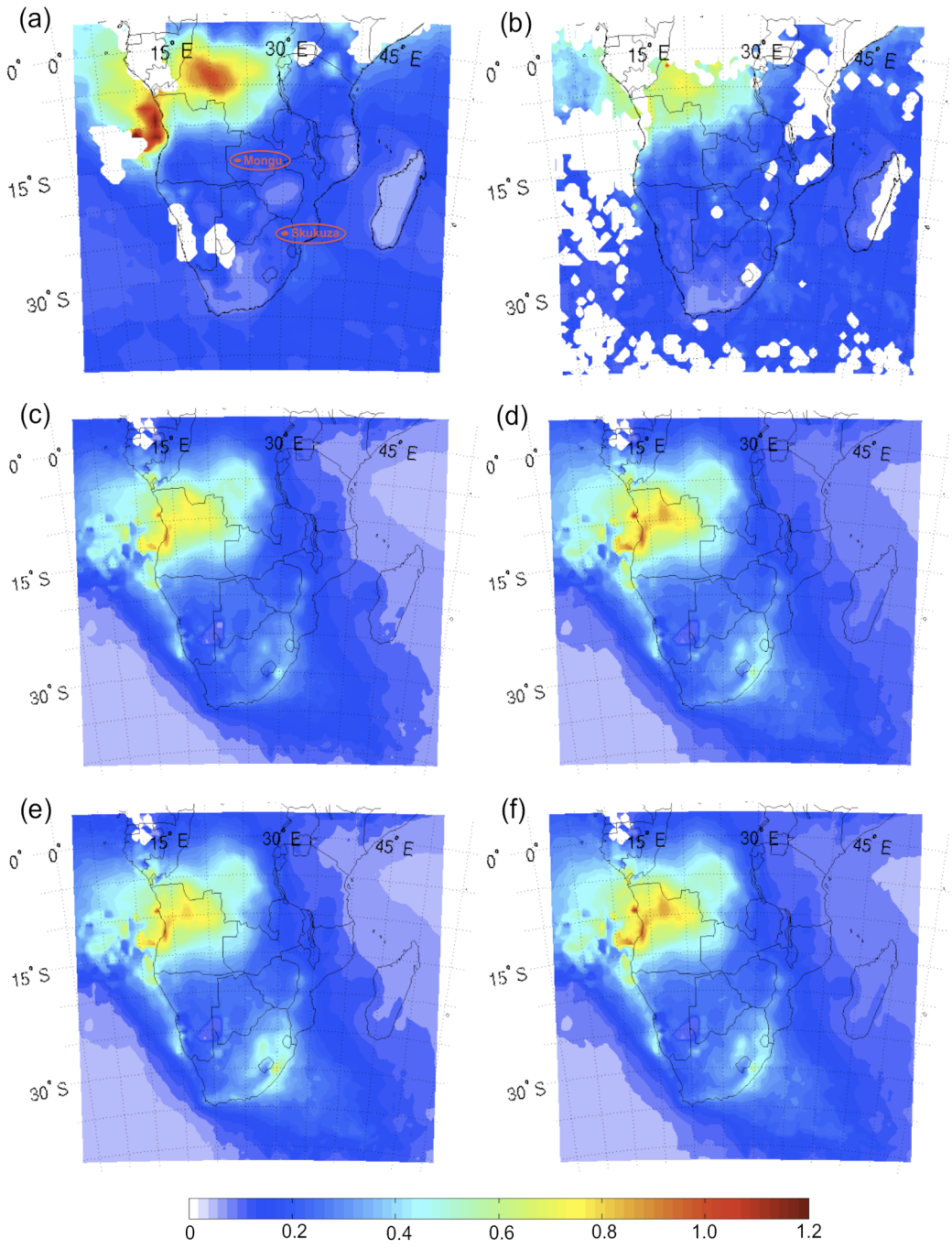

Figure 3.4.3: June-July-August (JJA) 2001 average aerosol optical depth for (a) MODIS, (b) MISR, (c) CTRL, (d) NODRY, (e) NOWET and (f) DECR. White areas in the MODIS and MISR plots ((a) and (b) respectively) are where no satellite observations were available. The two AERONET sites (Mongu, Zambia and Skukuza, South Africa) are shown in (a) to indicate their relative location.

3.4.3 Comparison with surface sulphur dioxide concentrations

This analysis focuses on the comparison of simulated sulphur dioxide (SO_2) concentrations with ground-based IDAF (see section 2.3.1.4 for a full description) sulphur dioxide observations. Results from only the CTRL and NODRY tests are shown, since the wet deposition of SO_2 emissions is not varied between tests and there is thus little difference between simulated column burdens of both SO_2 and SO_4 for the NOWET and DECR tests. At present, these IDAF SO_2 observations are the only such aerosol or trace gas concentration observations available over southern Africa for the period over which the sensitivity tests are run (2001-2002).

Highest surface SO_2 concentrations are measured at Amersfoort (3.4.4(a)), which is situated near the industrial South African Mpumalanga Highveld region, an area that produces a large proportion of South Africa's industrial aerosol emissions [*Terblanche et al.,* 2000]. Similar magnitude SO_2 concentrations are also observed at Louis Trichardt (fig. 3.4.4(b)), a rural site situated approximately 400km directly north of Amersfoort. The CTRL test simulated SO_2 concentrations agrees well with the available observations at Amersfoort approximately half the months for which observations are available. At Louis Trichardt, however, the model tends to overestimate surface SO_2 concentrations during almost all months. These differences may result from several factors:

- possibly the model simulates too much northward transport to the Louis Trichardt site; or
- SO_2 deposition is underestimated; or
- SO_2 emissions in the region are too high; or finally
- because too little chemical conversion to SO_4 is simulated.

It is difficult to accurately assess which factor is more important in the observed model bias at this point, particularly since no measurements of SO_4 concentrations are available for this site for the period simulated.

At Cape Point, a marine background site at some distance from the large metropolitan area of Cape Town, the signal is more mixed (fig. 3.4.4(c)). The model agrees relatively well with the observations in some months, but considerably overestimates SO_2 concentrations in others. The very low concentrations simulated for the winter months of 2002 (May through September) seem somewhat at odds with the concentrations simulated in the previous year's winter season, however, the observations that are available (only for August) show similarly low values. The model result therefore appears to be realistic despite being somewhat unusual, although the lack of observations makes it impossible to assess whether this is indeed the case. At Okakuejo, another rural site in northern Namibia, the model tends to

overestimate SO_2 concentrations throughout the year as at Louis Trichardt. Again, there are likely to be several factors responsible for the observed model bias (see the above discussion).

Of greater importance in the context of this study, however, is not the precise validation of the model (although indeed this is useful), but rather a comparison between the CTRL and NODRY sensitivity tests. At all four sites the surface SO_2 concentrations are higher in the NODRY test throughout the year (again see fig. 3.3.4). This is particularly the case during the summer months, indicating that this process plays a greater role during this season. This fits with theory and observations, which both indicate that dry deposition of SO_2 is an important process over southern Africa, especially in summer when the rate of incoming solar radiation and surface turbulence are greater [*Zunckel et al.,* 1996, 1999, 2000].

Similar to the AOD signal, there seems to be some inconsistency in terms of the timing of peak concentrations in the model, with the month of maximum simulated surface SO_2 concentration varying relatively inconsistently between the two years simulated at all four sites. The IDAF observations tend to hint at peak surface SO_2 concentrations in the austral winter season, a trend which has also been suggested by observational and modelling studies by Zunckel et al. [1999, 2000]. However, the measurements at all four sites are not continuous for the entire period simulated and it is thus not completely obvious when peak SO_2 concentrations occur at all four sites. It is interesting to note that despite the consistency of the industrial emissions used in the model monthly average SO_2 concentrations at Amersfoort and Louis Trichardt (the two sites most directly influenced by these emissions because of their proximity to the main source regions) vary considerably. This suggests that meteorological controls likely impact atmospheric sulphur concentrations more than the emissions themselves and that a large degree of the variability in simulated SO_2 concentrations is a result of simulated meteorological variability.

The discrepancy between the simulated and observed monthly average SO_2 concentrations is likely the result of several features. Firstly, it is unlikely that the model captures the local meteorological conditions (e.g. boundary layer height) at each site correctly, or that the simple sulphur chemistry module fully represents the complex processes contributing to atmospheric sulphur conversion and deposition at the local scale. It is also possible that certain seasonal effects linked to energy consumption (e.g. increased coal burning in winter) are not taken into account in the emissions inventory. This would have repercussions particularly for those sites influenced by urban emissions (e.g. Cape Point). Furthermore, since only one model grid box is compared to a single point observation site it is very important to regard these comparisons with considerable caution. The model may indeed be representative of the region, but may not match exactly with the precise site where measurements were taken.

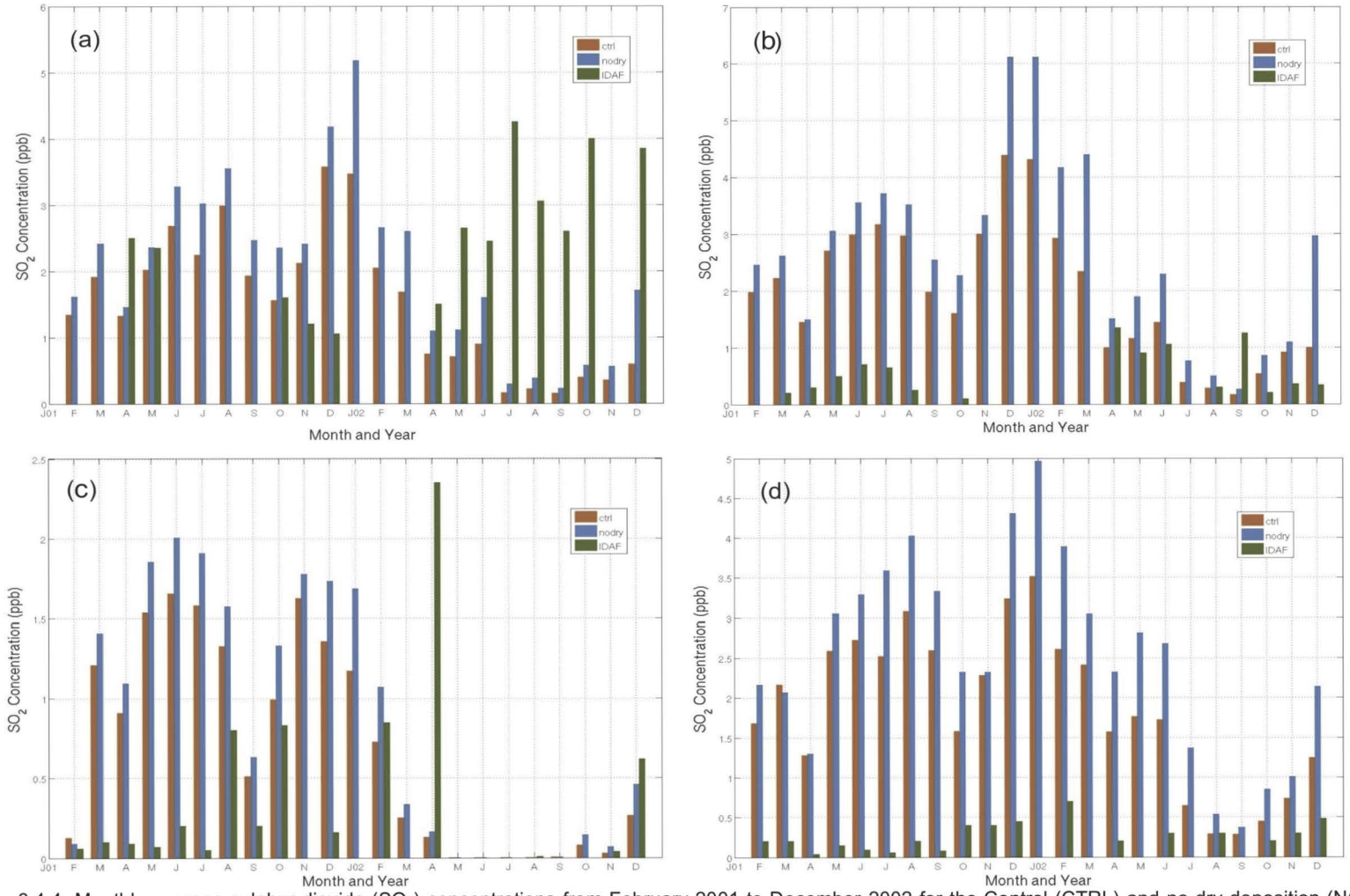

Figure 3.4.4: Monthly average sulphur dioxide (SO_2) concentrations from February 2001 to December 2002 for the Control (CTRL) and no dry deposition (NODRY) sensitivity tests and IDAF observations at (a) Amersfoort, South Africa, (b) Louis Trichardt, South Africa, (c) Cape Point, South Africa and (d) Okakeujo, Namibia. SO_2 concentrations are given in parts per billion (ppb).

3.4 Conclusions

A suite of tests is carried out to assess the internal variability of RegCM3 and to evaluate the model sensitivity to various parameters associated with aerosol emission and deposition.

Two measures are used to assess the internal variability within RegCM3 in an ensemble of seven simulations. No significant difference is found in either the root-mean-square difference or bias between any of the seven ensemble members for either surface temperature or precipitation. Internal variability is larger in the equatorial region and during the summer season (for the rest of the domain), when meso-scale convective processes dominate. It is thus assumed that although RegCM3 exhibits a certain degree of internal variability, this signal is not likely to strongly affect the model solution when perturbed, for example, by atmospheric aerosol.

Four test simulations are carried out to assess the sensitivity of RegCM3 to uncertainty associated with the parameterisations of aerosol emission and deposition processes. These include a control (CTRL) with standard parameters, a test suppressing wet deposition completely (NOWET), a test suppressing dry deposition (NODRY) and a test reducing the biomass burning aerosol injection height (DECR). Comparison of these tests with ground-based and satellite AOD observations as well as with in situ sulphur dioxide concentration measurements indicates several features:

- the CTRL simulation performs relatively well over the period simulated (February 2001 to December 2002), however maximum AOD is simulated approximately 5º too far south and tends to occur too early in the year compared to AERONET, MODIS and MISR;
- there appears to be relatively little sensitivity to the dry deposition rates used, since the NODRY test shows little difference from the CTRL simulation;
- wet deposition appears to play a more important role over southern Africa, since AOD and SO_2 concentrations are considerably higher in the NOWET simulation. Although rather unrealistic in terms of the aerosol parameters assessed, this test provides an idea of the relative importance of wet aerosol deposition and the effect this removal process has on the regional atmosphere;
- there seems to be very little sensitivity to aerosol injection height, with almost no discernible difference evident between the CTRL and DECR tests; and
- finally, comparison with ground-based observations of sulphur dioxide show that the model tends to overestimate surface concentrations in remote regions, but performs better at sites closer to sources.

Overall, compared to the available observations RegCM3 performs relatively well over southern Africa, particularly in terms of the meteorological variables investigated. Although plenty of room exists for the improvement of the simulated aerosol signal, the uncertainty exhibited by the model appears to fall within the range of error still associated with different observation techniques. Therefore, RegCM3 appears to be a quite adequate tool for a preliminary investigation of the direct and semi-direct aerosol impacts the southern African regional climate.

CHAPTER 4

Climatic impacts of southern African aerosol: Short-term focus on biomass burning 2001-2006

4.1 Experiment design

Biomass burning is the largest contributor to atmospheric aerosol loading over most of southern Africa during the austral winter season. This chapter focuses on an investigation of the direct and semi-direct radiative effects, particularly of biomass burning aerosols on the southern African regional climate for six winter seasons from 2001-2006. This chapter is based on an article recently published in the Journal of Geophysical Research [*Tummon et al.,* 2010].

4.1.1 Model domain and lateral boundary conditions

The domain simulated is the same as that used in the sensitivity tests of the previous chapter and covers the region from 18°N-43°S, 10°W-59°E. However, since the focus of this study is southern Africa, results are shown only for the region south of 5ºS.A horizontal grid point spacing of 60km is used, and the model includes 18 vertical levels extending to 25mb. Although a resolution of 60km is fairly coarse, the purpose of this study is to provide a first-order (in terms of large scale thermodynamics) quantitative estimate of the aerosol radiative impacts over southern Africa during the main biomass burning season. To this end, a large domain size as well as several years of simulation is necessary and it was thus decided to run with a slightly coarser horizontal resolution so as to reduce computational time. As for the simulations run for chapter three, the NCEP-II reanalysis [*Kanamitsu et al.,* 2002] is used for initial and boundary conditions, whilst NOAA OISST weekly averages [*Reynolds et al.,* 2002] are used as sea surface temperature (SST) forcing.

4.1.2 Ensemble simulation setup

Model simulated direct and semi-direct aerosol radiative effects are evaluated using two four-member ensembles. All simulations are run from April 2000 through December 2006, but only the six-year period from January 2001 to December 2006 is analysed (the first nine months are considered as spin-up period). The first set of simulations (CTRL) includes aerosols but takes no account of their radiative interactions (i.e. they are effectively inert tracers), whilst the second set of simulations (AERO) uses the same initial and boundary forcing but does include the calculation of aerosol radiative forcing. In both cases the BB-AMMA emissions (see section 4.1.3.1 below) are used to describe biomass burning emissions sources.

The four members of each ensemble are initiated from four consecutive days from 1-4 April 2000. A study by Giorgi and Bi [2000] investigating the internal model variability of RegCM3 found that there was little sensitivity to the magnitude or source of the perturbation. They compared the difference between simulations carried out with continuous perturbation of the lateral boundary conditions and simulations for which only the initial conditions were

perturbed. They found no significant difference in the level of internal model variability between the two experiments. It was thus considered sufficient just to start simulations from different days (i.e. varying initial conditions only) in order to initiate internal model variability. Similar results were also shown in over southern Africa in this work (see section 3.2).

4.1.3 Aerosol emissions and chemistry module parameters

4.1.3.1 The AMMA biomass burning inventory

The high spatial and temporal resolution BB-AMMA emissions inventory is used to describe the regional biomass burning aerosol sources. This inventory was developed by Liousse et al. [2010] in the context of the African Monsoon Multidisciplinary Analysis (AMMA) project. Biomass burning emissions are calculated using the SPOT-vegetation L3JRC burnt area product [*Tansey et al.,* 2007] in combination with the Global Land Cover (GLC) vegetation cover map and biomass density and burning efficiency estimates specific to Africa, as measured during the AMMA campaign [*Mieville et al.,* 2010]. The BB-AMMA inventory covers the period from April 2000 to March 2007 at a resolution of 0.5ºx0.5º and captures the daily and interannual variability of biomass burning emissions around the globe. Uncertainty associated with this database is estimated to be approximately 54% [*Liousse et al.,* 2010].

4.1.3.2 The GFEDv2 biomass burning inventory

The Global Fire Emissions Database version 2 (GFEDv2) inventory is used for an additional sensitivity test (see below, section 4.1.5.1). This inventory provides estimates of global monthly open biomass burning emissions at 1ºx1º resolution for the period 1997-2005. Emissions are calculated based on burned area data from TRMM-VIRS and ATSR (prior to 2001) and MODIS (post 2001) [*van der Werf et al.,* 2006]. The satellite-detected burned area estimates are used to drive the fire module of a biogeochemical model in which vegetative fuel load is calculated on a monthly basis. The model also calculates combustion completeness based on the fuel type and moisture conditions. These estimates are then combined together with emission factors to produce the final emissions product. The GFEDv2 inventory has been widely used in the literature [e.g. *Myhre et al.,* 2008; *Meyer et al.,* 2007; *Gloudemans et al.,* 2006; *Jain,* 2006]. Although a new version of the inventory, GFEDv3 [*van der Werf et al.,* 2010], has very recently been released at 0.5ºx0.5º resolution, these data have not been used in this work.

4.1.2.3 Aerosol and dust module setup

Emissions estimates of black carbon (BC) and organic carbon (OC) from the BB-AMMA inventory are used. As presented in section 3.3, wavelength dependent optical properties are prescribed for both BC and OC, and external mixing is assumed for both species. In terms of

dust emissions, four bin sizes are used (0.01-1.00μm, 1.00-2.50μm, 2.50-5.00μm, 5.00-20.00μm). All other aerosol parameters are as specified for the CTRL test in section 3.4.

Inflow/outflow boundary conditions are used in a configuration where no aerosol is advected into the domain from outside of the region, but aerosol can freely advect out when they reach the domain boundaries and flow is outward. These assumptions neglect the contribution of external sources to the regional aerosol budget. However, since we are concerned mainly with the impact of southern African biomass burning aerosol, it is useful to limit the impact of aerosol from other regions and can for the purposes of this study, be ignored. In addition the average winter circulation patterns over southern Africa are such that aerosol from source regions outside of the domain are not likely to be transported into it.

4.1.4 Internal model variability

In order to estimate the random internal model error the surface aerosol radiative forcing was spatially averaged over the region where aerosol optical depth (AOD) > 0.3 and compared between ensemble members. As an example, the surface shortwave (SW) forcing varies by 0.25W/m² and by 1.81W/m² within the CTRL and AERO ensembles, respectively. These values are significantly lower than the difference between ensemble means (40.39W/m²). This suggests that although internal variability does indeed exist within RegCM3 it does not appear to strongly impact or mask the aerosol forcing signal. The results for the other variables investigated show similar results and confirm those found in section 3.2.

4.1.5 Sensitivity tests

4.1.5.1 Testing biomass burning inventories

Uncertainty associated with biomass burning emissions estimates, which is currently estimated to be up to a factor of two, is greater than that associated with estimates of fossil fuel emissions [*Kasischke and Penner,* 2004; *Korontzi et al.,* 2005; *Solomon et al., 2007*; *Liousse et al.,* 2010]. Regionally, uncertainty in terms of biomass burning emissions may be even larger [*Ramanathan and Carmichael,* 2008; *Liousse et al.,* 2010; *Stropianna et al.,* 2010]. To investigate the sensitivity of simulated radiative forcing to different biomass burning estimates a single simulation using the GFEDv2 database [*van der Werf et al.,* 2006] is carried out. Since GFEDv2 emissions don't exist for the final year of simulation (2006), values from 2005 were used for 2006 as well.

4.1.5.2 Aerosol-sea surface temperature feedbacks

Aerosols have a strong cooling effect on the earth's surface through the 'surface dimming' effect [*Solomon et al.,* 2007; *Ramanathan and Carmichael,* 2008]. Over the continent, this impact is taken into account by the RegCM3 land surface model, however, over the oceans,

where observational SST forcing is used, no aerosol-surface feedback is accounted for. In order to investigate this aspect further, a third ensemble of four simulations is run exactly as for the AERO ensemble except that aerosol radiative forcing is included by artificially decreasing SST as a function of AOD. Current estimates of the impact of aerosol AOD on SST are variable and depend on the oceanic region studied [e.g. *Evan*, 2007; *Lau and Kim*, 2007; *Foltz and McPhaden*, 2008]. Here, a value of 0.8°C/unit AOD is used, a value established from studies using mixed-layer ocean models to simulate the impact of decreased radiative fluxes on SST in the North Atlantic dust outflow region [cf. *Yoshioka et al.,* 2007; *Evan,* 2007; *Martinez Avellaneda,* 2010).

4.2 Model validation

To have confidence in the simulated estimates of direct aerosol radiative forcing it is essential that the model simulates the basic state of the atmosphere and aerosol properties accurately. The following sections discuss validation of the model compared to various observational datasets, both in terms of climatic as well as aerosol-related features.

4.2.1 Surface air temperature

Model surface air temperature is compared to the CRU observational dataset [*Mitchell et al.,* 2004]. This dataset consists of monthly average surface air temperature (and precipitation and cloud cover) observations over land, gridded at 0.5ºx0.5º resolution. It is only possible to compare the initial two years of model output (2001-2002), since the CRU data cover the period from 1900 to 2002. In regions were observational data are sparse, most notably over Angola and the Democratic Republic of Congo, the CRU monthly mean surface temperature is expected to be accurate to within approximately 1ºC [*Jacob et al.,* 2007] and the dataset tends toward the climatology in these areas [*Mitchell et al.,* 2004].

For the austral winter season (JJAS) the model appears to simulate surface temperature relatively well (fig. 4.2.1(a), the CTRL ensemble mean bias compared to CRU). It is clear that RegCM3 exhibits a tendency to overestimate temperature over the western half of southern Africa west of approximately 30°E, whilst east of this meridian, temperature tends to be underestimated by a similar magnitude (approximately 1-3°C). Temperature bias may be a result of error in one or a combination of a number of factors, including cloud cover, radiation balance, precipitation, surface properties (such as surface albedo), surface energy fluxes and temperature advection [e.g. *Christensen et al.*, 1997; *Giorgi et al.,* 1998; *Tadross et al.,* 2006]. Since different factors contribute to varying degrees in different regions, it is difficult to unambiguously determine the cause of temperature bias. A more in-depth analysis of surface

processes, cloud cover and circulation patterns would likely provide a better indication of the source of this bias, however, this is beyond the scope of this study.

The inclusion of the aerosol forcing decreases the simulated temperature bias significantly (fig. 4.2.1(b)), with a large decrease in the positive bias over the western half of southern Africa and only a slight increase of the cold bias over the eastern half of the region. The significance of these results will be discussed further in section 4.4.1. However, it is important to note at this point, that typical values of RCM seasonal surface temperature bias range within ±4°C [e.g. *Giorgi et al.,* 1998*; Hudson and Jones,* 2002b; *Tadross et al.,* 2006; *Sylla et al.,* 2009], thus our simulation biases fall within the range of results obtained using other state-of-the-art regional models.

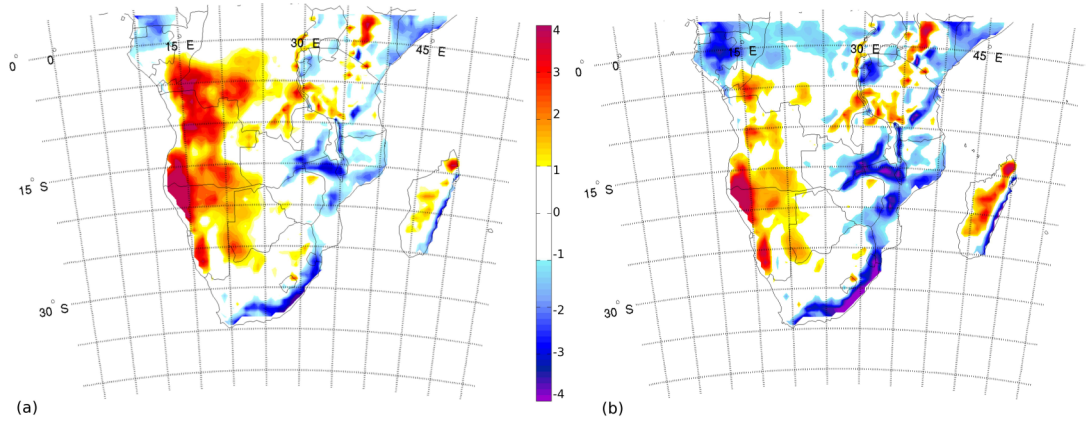

Figure 4.2.1: JJAS temperature bias for (a) the control simulation (CTRL) and (b) the aerosol experiment (AERO) compared to the CRU observations (in °C).

4.2.2 Precipitation and circulation

The accurate representation of precipitation is of vital importance, particularly for the wet deposition of aerosols. Simulated precipitation is compared to two datasets: the enhanced CPC Merged Analysis of Precipitation (CMAP) dataset [*Xie and Arkin,* 1997] as well as the TRMM 3B43 dataset [*Adler et al.,* 2000], both of which cover the entire period of simulation, 2001-2006. The enhanced CMAP dataset has a resolution of 1°x1° and is constructed using precipitation estimates from 5 satellites (GPI, OPI, SSM/I scattering, SSM/I emission and MSU) which are then blended with values from the NCEP-II reanalysis. The TRMM 3B43 product is constructed using a combination of TRMM satellite-retrievals adjusted with gridded rain gauge data from two other ground-based sources (CAMS and GPCC). TRMM data are at 0.25°x0.25° resolution and cover the region from 50°N to 50°S (covering the entire model domain).

Whilst it is the dry season over much of southern Africa the JJAS precipitation is well simulated over most of the region. Compared to both the CMAP (fig. 4.2.2(a)) and TRMM (fig. 4.2.2(b)) observations, both the magnitude and spatial distribution of simulated precipitation (fig. 4.2.2(c)) are well represented. The model bias compared to TRMM is shown in figure 4.2.2(d). The largest region of overestimated precipitation occurs over the northwest Indian Ocean, off the coast of Kenya and Somalia, where precipitation is overestimated by up to 3mm/day. Davis et al. [2009] found a similar positive bias in a study of the East African region, also using RegCM3. They suggested that it was likely that the model is not able to accurately represent the strong monsoon dynamics of this region. However, this region neither influences the climate of more southern regions very strongly, nor is there a high aerosol load over this area, thus the precipitation overestimate is likely of little consequence to the aerosol-climate interactions over southern African during the austral winter season.

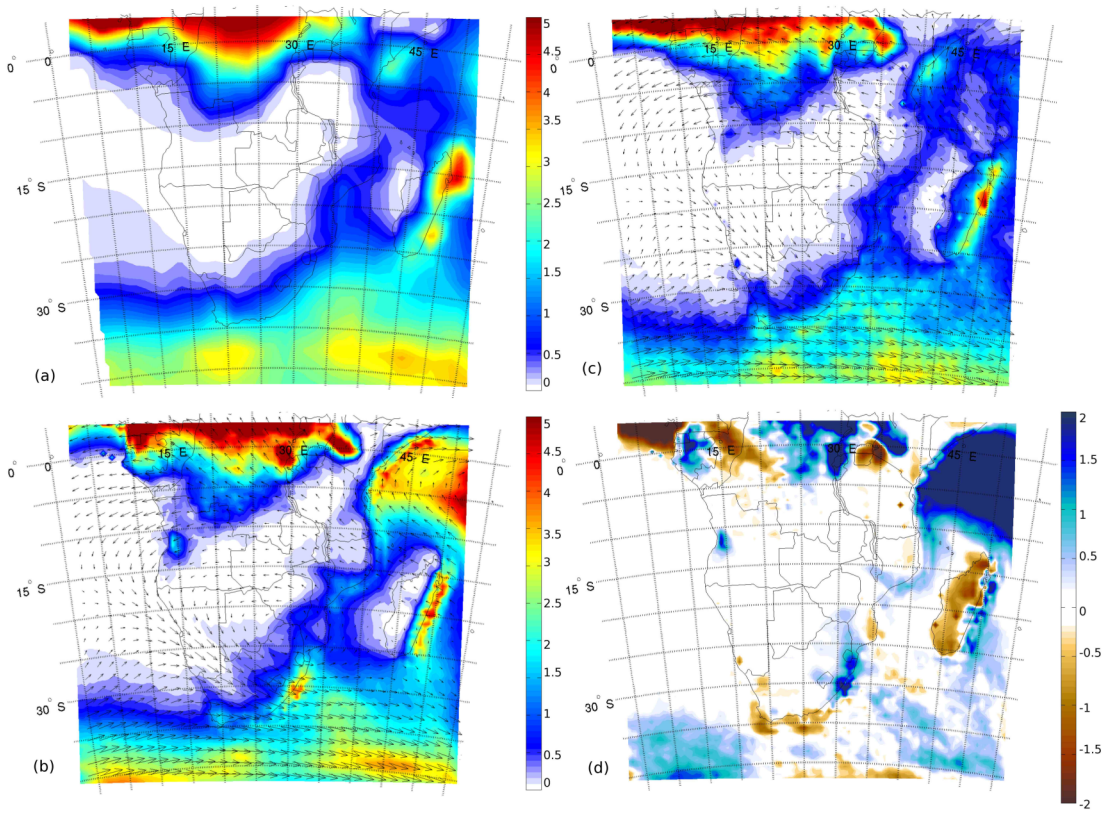

Figure 4.2.2: JJAS precipitation climatology (in mm/d), for (a) CMAP, (b) TRMM with NCEP-II 700hPa winds, (c) RegCM3 with 700hPa winds and (d) JJAS precipitation bias (RegCM3-TRMM).

Perhaps of greater importance in terms of this study is the small region of positive bias just southeast of the South African Drakensberg mountain range (situated near ~30°S, 30°E). The complex topography of this small region (from sea level up to 3000m) likely results in the

overestimation of orographic rainfall in this area. This feature is common to many regional models [e.g. *Christensen et al.,* 1997; *Joubert et al.,* 1999; *Afiesimama et al.,* 2006] and is possibly related to the overestimation of updrafts in mountainous regions. Since this area lies directly in one of the main exit-pathways of aerosol-laden air from the subcontinent [*Tyson et al.,* 1996b], the overestimation of precipitation may possibly result in an overestimation of wet aerosol deposition in this region. Compared to TRMM, simulated precipitation is also overestimated by up to 4mm/day over parts of the equatorial Atlantic Ocean (between 10-15°E as well as 20-35°E), also possibly resulting in an overestimation of wet deposition in this region. Precipitation is underestimated by a similar magnitude over the equatorial oceanic region between 0-5°N, 0-10°E. Again, these biases are likely related to the convective scheme, which is particularly sensitive in the equatorial regions (see appendix A.2).

Since the first absolutely stable layer over much of the interior of the subcontinent preferentially forms at approximately 700hPa [*Tyson et al.,* 1996a] and the moisture flux is maximum at this level [*Freiman and Tyson,* 2000], the NCEP-II and CTRL ensemble JJAS average 700hPa winds are also included in figures 4.2.2(b) and (c), respectively. Overall, the simulated winds show a similar pattern to the NCEP-II reanalysis, both in terms of magnitude and direction. The main features of anticyclonic circulation over the subcontinent south of 10°S are well represented, as is the region of easterly outflow to the Atlantic Ocean between 5-15°S. Likewise, the strong north westerlies and continental outflow from 20-35°S, part of the anticyclonic flow system, are also well simulated, as are the strong mid-latitude westerlies between 30-40°S. The monsoonal flux over the Indian Ocean east of Tanzania (5-10°S, 30-40°E) exhibits mean onshore flow that is slightly too strong, whilst the cross-equatorial winds between 5°S and 5°N present too much of a northerly component. These features again suggest that the model has some difficulty in simulating the monsoon dynamics over the tropical Indian Ocean and in reproducing the convective activity of the equatorial regions.

4.2.3 Aerosol optical depth

Simulated aerosol optical depth (AOD) is compared to AERONET [*Holben et al.,* 1998], MODIS [*Remer et al.,* 2005] and MISR [*Diner et al.*, 1998] observations at Mongu, Zambia and Skukuza, South Africa (the two southern African AERONET sites for which long-term observations are available; see section 2.3.2.1), as well as spatially for the JJAS season.

4.2.3.1 Temporal comparison

The magnitude of AOD is relatively well simulated at both AERONET sites, with the model capturing the seasonal and interannual variability of AOD quite adequately. Two sources of bias are, however, apparent at both sites. Firstly, the RegCM3 simulated AOD peaks one to two months prior to all three observational datasets. At Mongu (fig. 4.2.3(a)) the observed

AOD peaks in September for most years from 2001-2006 (2003 is the only exception with AOD peaking in October according to AERONET, MODIS and MISR). RegCM3, however, consistently shows peak AOD in August (with the exception of 2002, when maximum AOD is simulated in July). A similar feature is evident at Skukuza (fig. 4.2.3(b)), with the model AOD peaking in either July or August, whilst the AERONET and satellite observations generally suggest a later peak in September or October. It is important to note that, as mentioned in chapter three, the observations exhibit some variability in terms of both the magnitude and month of peak AOD, with differences of up to two months between products (e.g. between MISR and AERONET in 2002 at Skukuza). Thus, although there is consistent discrepancy between the model and the observations, there is a similar level of incongruity between the measurements as well.

Secondly, outside of the main biomass burning season (November to May) simulated AOD is significantly underestimated. This feature is particularly evident at Skukuza where the RegCM3 simulated AOD is too low by as much as 0.2 in some months. This is likely related to the fact that no anthropogenic aerosol emissions, which provide a consistent year-round source of aerosol, are included in these simulations. Since Skukuza is situated considerably closer and is thus more strongly influenced by aerosol transport from the main industrial South African Highveld region [*Piketh et al.,* 1999a], this signal is more apparent at this site.

4.2.3.2 Spatial comparison

Figure 4.2.4 presents the spatial distribution of simulated AOD compared to the MODIS-terra version-5 daily AOD product [*Remer et al.,* 2005]. Daily composite averages for 2001-2006 for each of the four months from June through September for MODIS (left column), AERO ensemble mean (middle column, with BB-AMMA emissions contoured) and the GFED sensitivity test (right column, with GFEDv2emissions contoured) are shown. The model AOD average is screened using the satellite observations, taking the average simulated AOD only for the regions and days for which MODIS observations are available. White areas indicate regions where MODIS daily AOD are not available (either because of continuous cloud cover or high surface albedo).

From figure 4.2.4 it is clear that the early bias in simulated AOD is apparent not only at Mongu and Skukuza, but more generally over the entire southern African subcontinent. As at the AERONET sites, the model AOD peaks strongly in July and returns to near background levels by September. In contrast, the MODIS observations indicate that maximum AOD occurs in August and that this signal is maintained into September, particularly over the Atlantic Ocean. Compared to MODIS the simulated AOD is also displaced in space, occurring approximately 5º too far south over land. Over the ocean, where satellite observations are generally more accurate [*Chu et al.,* 2002; *Remer et al.,* 2002], AOD fields appear to agree

better, at least in terms of spatial distribution, with maximum AOD (up to ~1.2) occurring between 5-15°S for both the AERO ensemble and the MODIS observations.

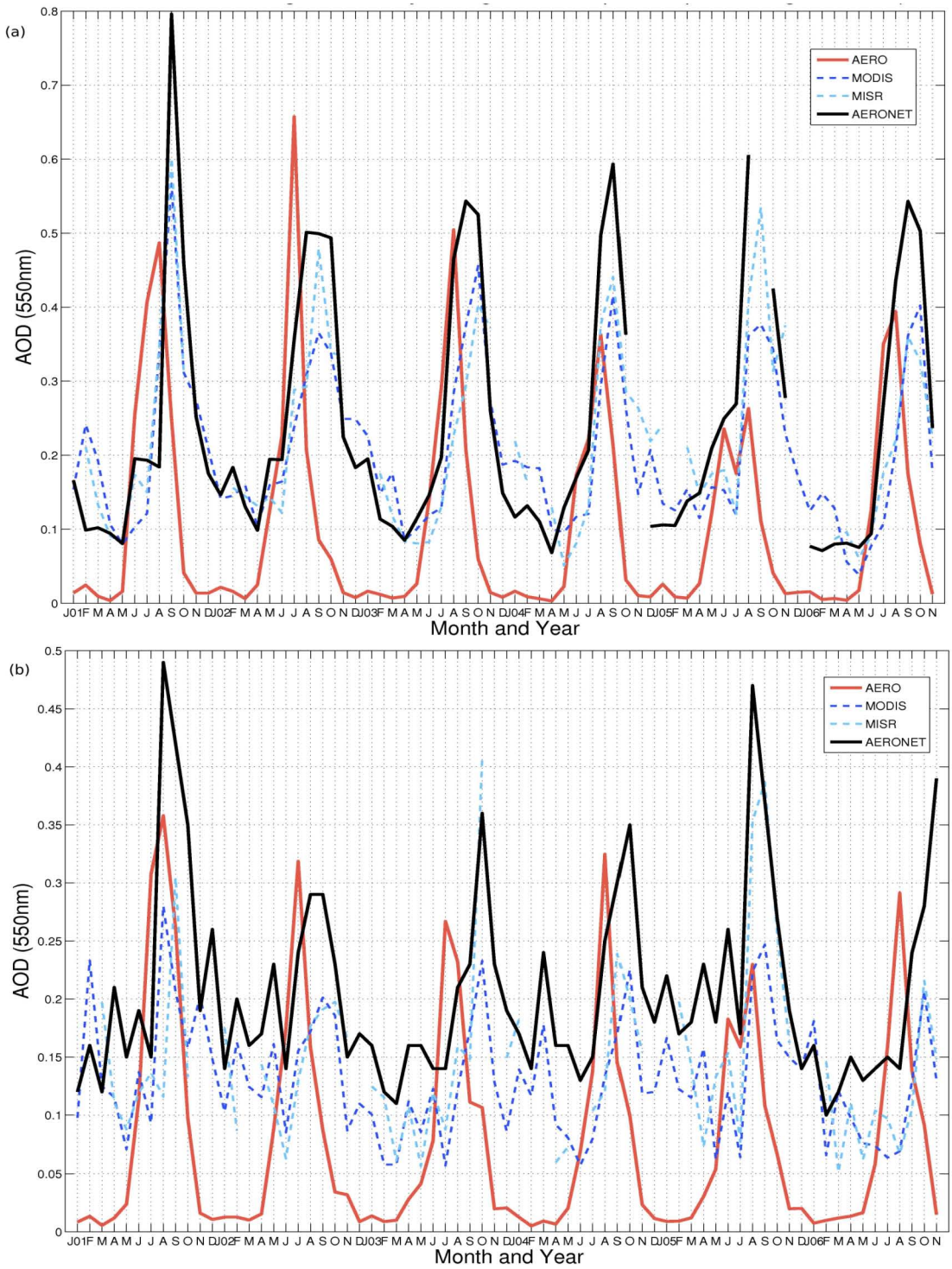

Figure 4.2.3: Monthly average aerosol optical depth (AOD) at (a) Mongu, Zambia and (b) Skukuza, South Africa for RegCM3 (aerosol experiment, AERO), AERONET, MODIS and MISR from January 2001 – November 2006. Note the different y-axis ranges for each site.

Importantly, the simulated spatial and temporal bias appears to be relatively independent of the emissions inventory used. The GFED simulation (right column fig. 4.2.4) exhibits the same early bias and maximum AOD is also similarly situated in space, approximately 5º too far south compared to MODIS. In addition, the AOD in this simulation is significantly underestimated in all months, compared to both the MODIS observations and the AERO ensemble mean. This is a direct consequence of the lower biomass burning emissions of this inventory (see contours fig. 4.2.4 and fig. 4.2.5). The very large difference between the BC and OC emissions estimates of the two inventories is very clear (again see fig. 4.2.5). During the austral winter the GFED estimates are up to 70% lower than the BB-AMMA inventory over southern Africa (domain shown in fig. 4.2.4), while for the rest of the year, there is little difference between the two inventories. The large discrepancy observed during the winter season is likely an accumulation of the different estimates and assumptions used to generate each emissions estimate product. Each inventory was constructed using different satellite products as well as different emission factors and land surface cover maps (see sections 4.1.2.1 and 4.1.2.2). These differences may lead to significant differences in the magnitude, and to a lesser degree, the spatial and temporal location of emissions [*Liousse et al.,* 2010]. The results shown here highlight the large uncertainty still associated with biomass burning emissions estimates over southern Africa.

The disparity between the observed and simulated AOD fields is likely the result of a combination of factors. Firstly, as just described, large uncertainty is still associated with biomass burning estimates. Although the difference in terms of space and timing of emissions is not that large, given the significant range in the magnitude of emissions estimates, there is evidently still considerable uncertainty associated with biomass burning estimates (see above discussion and fig. 4.2.5 below as well) and this very likely contributes to the AOD bias.

Secondly, it is also likely that error in the simulated meteorological fields, which control aerosol transport and deposition processes, affects the model AOD bias. For example, the simulated low-level winds (surface to 850hPa), important for aerosol transport from the source regions, appear to be too weak between 5°N-15°S, 15-30°E (a bias also noted in the sensitivity tests carried out for the previous chapter, see appendix A). The NCEP reanalysis suggests that on average, south-westerly winds of up to 3m/s prevail over the continent in this region. RegCM3, however, simulates winds that come rather from the west, and which are generally weaker (~2m/s), therefore, northward aerosol transport is likely underestimated. This probably contributes to the underestimation of AOD underestimation between 0-5ºS, as previously described. Dynamically, the tropical region is particularly difficult to simulate accurately, and, since a large proportion of biomass burning emissions are released near this region, we cannot exclude the impact that model deficiencies in horizontal and convective transport may have on the simulated AOD distribution.

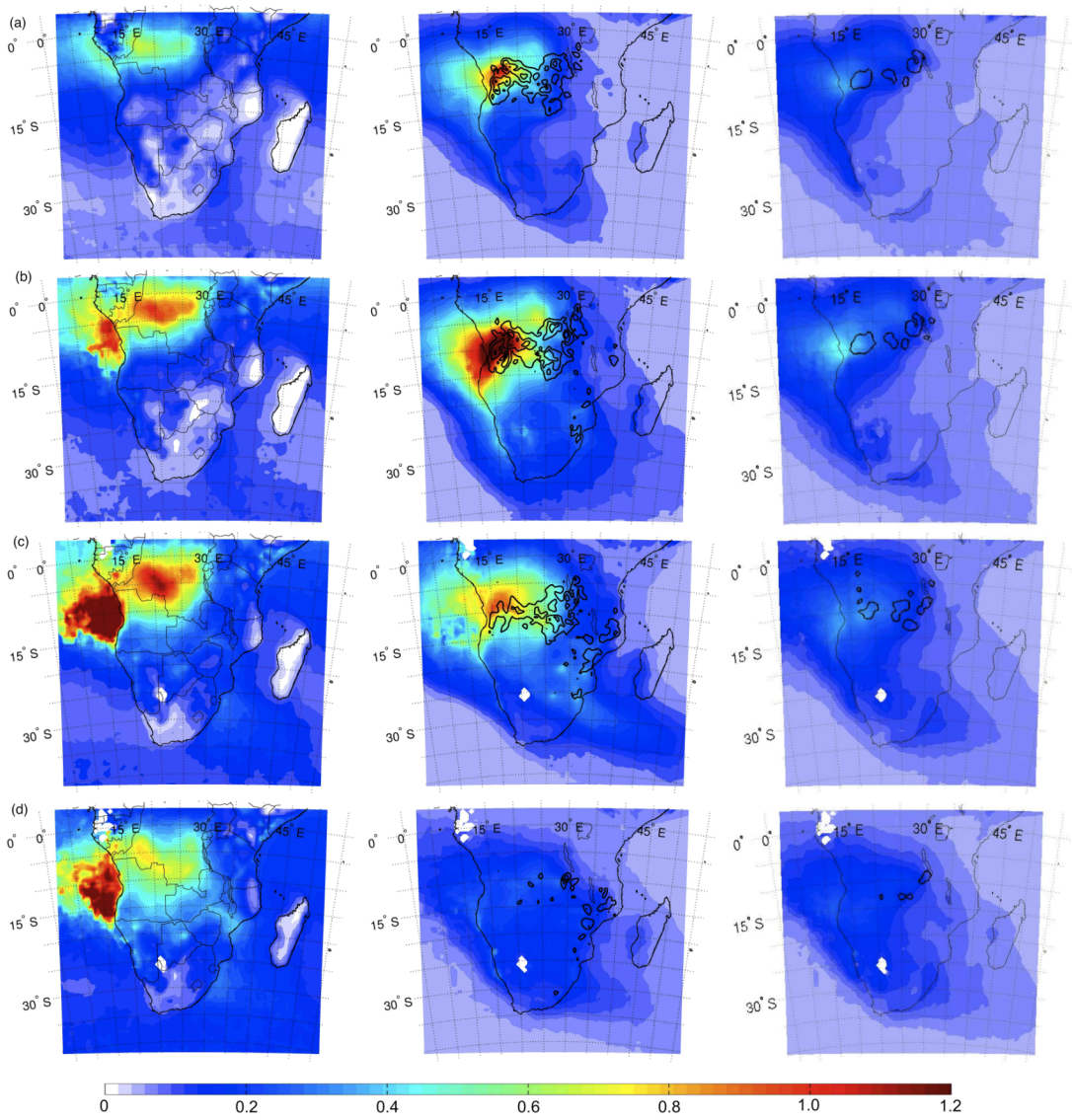

Figure 4.2.4: Daily composite aerosol optical depth (AOD) for (a) June, (b) July, (c) August and (d) September. Left column MODIS, middle column RegCM3 using AMMA emissions (AERO experiment) and right column RegCM3 using GFED emissions (GFED experiment). Biomass burning emissions are contoured over the RegCM3 AOD fields (contours every 20 from 0-120mg/m²/day) for both the AMMA (middle) and GFED (right) inventories.

Thirdly, much of the main biomass burning region is covered by savannah, a surface challenging to observe using remote sensing techniques as a result of the discontinuous canopy structure and associated crown shadowing [*Privette and Roy,* 2005]. Although this error was corrected in later versions of the MODIS product (as used here) [*Remer et al.,* 2005], uncertainty is still associated with satellite observations (as discussed above in sections 4.2.3.1 and 4.2.3.2) and these products are by no means error-free. This error may

at least partly account for the significant difference between observed and simulated AOD between 5 and 15°S.

Finally, these simulations do not include biogenic, industrial or sea-salt aerosol, and AOD is therefore likely to be underestimated, particularly outside of the biomass burning regions and the winter season, when and where other aerosol sources dominate the regional atmospheric loading [*Maenhaut et al.,* 1996, *Piketh et al.,* 1999a, *Tyson and Gatebe,* 2001].

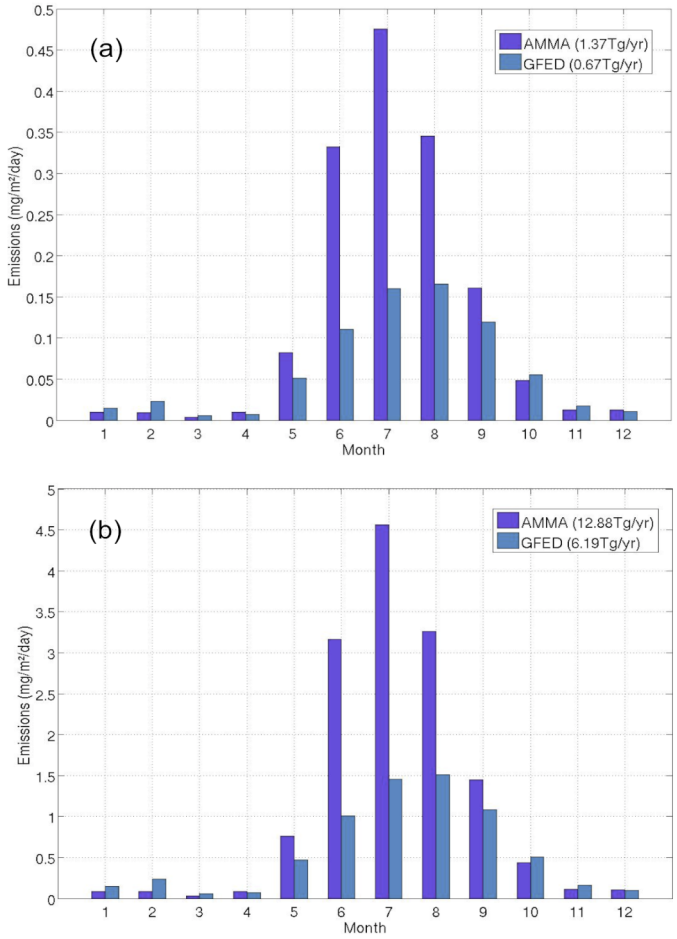

Figure 4.2.5: Climatology of monthly average (a) black carbon (BC) and (b) organic carbon (OC) emissions over southern African for the 2001-2006 period for the BB-AMMA and GFED emissions inventories. The annual totals for each inventory are shown in the upper right-hand corner for each tracer.

In general, RegCM3 reproduces the state of the southern African climate during the austral winter season relatively well. The temporal and spatial distribution of AOD shows some bias compared to the available observations but overall, the model representation of both atmospheric and aerosol properties is considered sufficient as a first step towards estimating

the potential impacts of the direct and semi-direct aerosol radiative effects on the southern African climate.

4.3 Simulated aerosol impacts

This section evaluates the direct and semi-direct radiative effects on the southern African climate for the austral winter season, June through September (JJAS), for the 2001-2006 period.

4.3.1 Surface radiative forcing

The AERO ensemble mean clear-sky RF at the surface, TOA and in the atmosphere is shown in figures 4.3.1(a), (b) and (c), respectively. The surface RF is strongly negative, reaching up to -60W/m² and clearly mirrors the AOD field (see contours on fig. 4.3.1(c)), with maximum surface RF occurring below the region of maximum AOD. Simulated values compare well with estimates obtained during the SAFARI-2000 campaign. For example, Campbell et al. [2003] calculated a surface flux forcing of -50W/m² using lidar measurements over Skukuza, in South Africa, during a smoke haze event in September 2000. Similarly, Bergstrom et al. [2003] used a radiative transfer model and obtained values ranging between -57 to -200W/m² at Inhaca Island, off the coast of Mozambique during a number of high AOD events in August and September 2000. Using a radiative transfer model in combination with GCM-simulated and MODIS-observed aerosol fields, Abel et al. [2005] estimated that monthly average surface radiative forcing ranged between -5.9 to -56.7W/m² for September. Also using RegCM3, Zhang et al. [2008] showed that an AOD of up to 0.6 resulted in a negative surface forcing of greater than -35W/m² over the Amazon biomass burning region. The surface radiative forcing simulated in this study thus appears to fall well within the range of simulated and observed values for the southern African region and for biomass burning regions in general.

Interestingly, the clear-sky surface RF is negative over nearly the entire southern African region. This suggests that despite biomass burning being mostly limited to the savannah regions (see emissions contours fig. 4.2.4, middle column), the impacts of aerosol on the surface radiative balance are observed throughout the region, likely as a result of the extensive recirculation and transport that occurs around the subcontinent. The two main exit pathways of aerosol-laden air, to the Atlantic and Indian Oceans, are also clearly visible in the surface RF. Interestingly, the Indian Ocean plume signal is considerably weaker than that over the Atlantic Ocean, likely as a result of deposition that occurs as aerosol are transported over the subcontinent (which, as presented in section 4.2.2 may be overestimated in some regions where precipitation is overestimated).

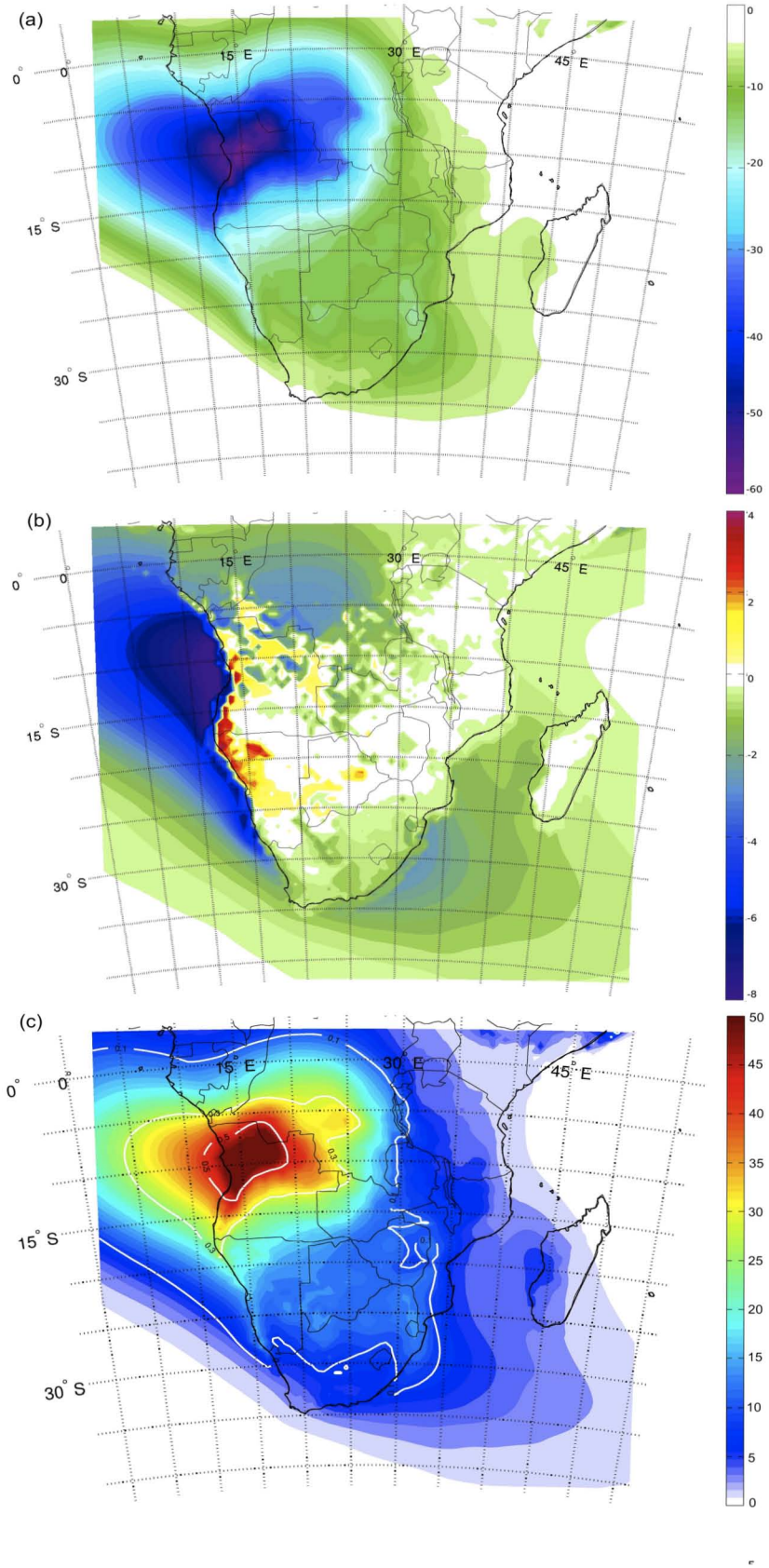

Figure 4.3.1: JJAS average clear-sky (a) surface, (b) top-of-atmosphere (TOA) and (c) atmospheric radiative forcing (RF) attributable to aerosols (in W/m^2). The 2001-2006 average aerosol optical depth (AOD) is contoured over (c), with intervals of 0.2 from 0.1 to 0.5 (AOD is unitless).

4.3.2 Aerosol-induced surface temperature changes

The negative surface radiative forcing results in decreased surface temperatures, as exhibited by the decrease in the positive temperature bias over much of the western half of southern Africa noted previously (compare figures 4.2.1(a) and 4.2.1(b)). This is a direct result of aerosol absorption and scattering decreasing incoming shortwave radiation reaching the surface. Similar positive temperature biases have been found in previous RCM studies (not including aerosol effects) over southern Africa, and it was hypothesised that this was at least partly attributable to an overestimation of incoming solar radiation at the surface [e.g. *Tadross et al.,* 2006]. The inclusion of the aerosol direct and semi-direct radiative effect appears, at least in our case, to improve the simulation of surface temperature, and likely most surface processes, over much of southern Africa.

4.3.3 Top-of-atmosphere radiative forcing

The clear-sky TOA shortwave radiative forcing indicates whether there is a cooling or warming of the surface-troposphere system and is strongly related to aerosol and surface properties [*Liao and Seinfeld,* 1998]. Over land regions the TOA signal varies to a large extent because of the underlying vegetation types, a signal that can clearly be seen in fig. 4.3.1(b). Where absorbing aerosols are simulated over relatively high albedo surfaces (e.g. desert, semi-desert or short-grass covered regions) the planetary albedo is reduced and TOA forcing is positive, indicating an overall warming radiative tendency of the surface-troposphere column. Such a region is clearly evident in a narrow band along the west coast from 10-25°S, where a high absorbing aerosol load over a high albedo surface results in positive TOA forcing of up to 4W/m². Over darker, lower albedo surfaces such as forest (covering the region between 5°S to 5°N) and over the adjacent oceans, the clear-sky TOA forcing is negative, indicating an average radiative cooling tendency of the surface-troposphere column. Negative clear-sky TOA forcing is greatest over the Atlantic Ocean, where it reaches up to -8W/m².

It is important to note, that it is clear-sky TOA radiative forcing that is considered in this case. Several studies carried out over the Atlantic Ocean stratocumulus region have found that the whole-sky TOA forcing in this region is in fact likely to be positive [*Keil and Haywood,* 2003; *Magi et al.* 2003; *Schmid et al.* 2003; *Abel et al.,* 2005]. This is because during the biomass burning season an elevated absorbing aerosol layer lies above the semi-permanent low-level stratocumulus cloud sheet. The aerosol loading therefore potentially has a significant positive TOA forcing in this region, which cannot be diagnosed by the clear-sky TOA forcing. Unfortunately, at present, no diagnostic exists in RegCM3 to visualise the simulated whole-sky TOA forcing due only to aerosols, so we are unable to assess the model's performance of

this feature compared to observations. Further investigation of this region with future versions of RegCM that include this diagnostic will be carried out.

4.3.4 Atmospheric radiative forcing

Figure 4.3.1(c) shows the atmospheric radiative forcing attributable to aerosols (i.e. the difference between the TOA and surface forcing), where positive forcing indicates heating of the atmospheric system. It is clear that the highly absorbing biomass burning aerosol loading results in considerable atmospheric diabatic heating over much of southern Africa, particularly over the main biomass burning region, where atmospheric RF reaches 50W/m^2. The distribution of atmospheric heating clearly mirrors both the surface radiative forcing pattern (fig. 4.3.1(a)) as well as the JJAS average AOD signal (contours fig. 4.3.1(c)). The full implications of this heating are further discussed in sections 4.3.6 and 4.3.7.

4.3.5 Surface energy balance

The large negative surface radiative forcing decreases energy available at the surface, decreasing downward short-wave surface fluxes and modifying the surface energy budget over much of southern Africa. The sensible heat (SH) flux decreases over almost the entire subcontinent, particularly in the main biomass burning regions where decreases of up to 50W/m^2 occur (fig. 4.3.2(a)). The SH flux increases in a narrow band along the east coast of the subcontinent, between 15ºS-5ºN, as well as along the east coast of Madagascar. This appears to be linked to reduction in cloud cover in these regions (not shown) resulting from the aerosol-induced changes in circulation patterns. It is important to note that the surface energy budget does not change in these areas, it is rather the partitioning between SH and latent heat (LH) fluxes that changes (see ensuing paragraph).

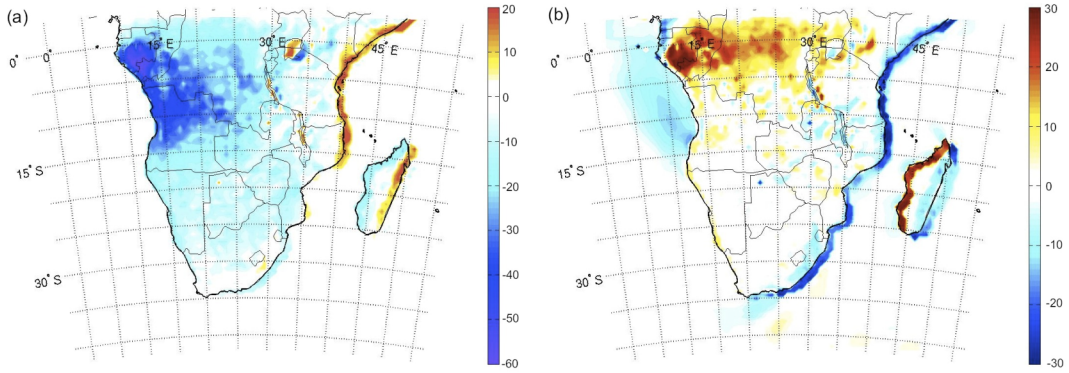

Figure 4.3.2: JJAS seasonal average aerosol-induced (AERO-CTRL) change in (a) sensible heat flux and (b) latent heat flux (in W/m^2).

In contrast, despite the negative surface radiative forcing, the latent heat (LH) flux increases in the equatorial regions between 5°N-5°S as well as along the east coast of Madagascar (fig. 4.3.2(b)). In the tropics, where values of potential evaporation are high, changes in soil moisture can have substantial impact on the latent heat flux [*Delworth and Manabe,* 1989]. Since this region receives more precipitation in the AERO simulation (see ensuing discussions in section 4.3.7 and fig. 4.3.6), the soil moisture increases and this likely increases the LH flux. As already mentioned, the latent heat flux decreases in the Atlantic Ocean aerosol outflow region as well as along the eastern coast of the subcontinent and Madagascar. Aerosol-induced changes in circulation patterns and decreased cloud cover enhance the SH flux but decrease the LH flux in these region. Over the rest of southern Africa there is little change in LH flux because of the predominantly dry conditions.

As a result of the significant negative surface radiative forcing and reduced SH flux over most of the subcontinent, the average planetary boundary layer (PBL) height decreases (fig. 4.3.3(a)). Decreases are largest, up to 30%, along the west coast of the subcontinent between 0-15°S, whilst decreases of approximately 15% occur over much of the main biomass burning region. Small regions of increased PBL height occur over the large East African lakes (Lakes Malawi, Tanganyika and Victoria) as well as off the west coasts of Madagascar, South Africa and southern Namibia. These regions of increased PBL height are likely linked to dynamical feedbacks, cloud cover changes and precipitation anomalies, which are further discussed in sections 4.3.6 and 4.3.7.

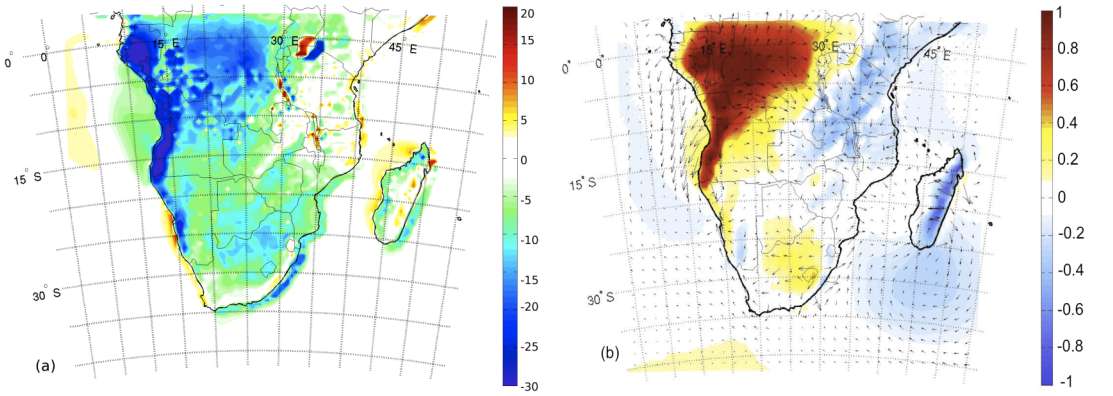

Figure 4.3.3: JJAS anomaly (AERO-CTRL) (a) planetary boundary layer (PBL) height (percentage change) and (b) sea level pressure (SLP) difference (aerosol-control experiment) with 1000hPa anomaly winds. Colours indicate the PBL and SLP differences, while arrows represent the direction and magnitude of the wind anomaly winds.

Figure 4.3.3(b) shows the change in sea level pressure (SLP) induced by the simulated aerosol loading. In the main biomass burning region the decreased surface temperature stabilises the lower atmosphere and results in increased SLP as well as anomalous divergent

circulation. A similar, but weaker signal is also observed over South Africa (between approximately 25-38ºS, 20-30ºE), where again the increase in low-level stability increases SLP slightly and causes anomalous divergence at the surface. In contrast, over much of the eastern half of the subcontinent (effectively east of 30ºE) as well as over a large part of the surrounding ocean regions the SLP decreases, indicative of slight increases in uplift. Over the subcontinent these changes are, again, linked to the aerosol-induced changes in the atmospheric dynamics and vertical structure (see the following section, 4.3.6). Over the ocean the reduction in SLP is largely associated with anomalous uplift induced by aerosol-induced atmospheric warming (since there is no aerosol-SST feedback, effectively only the atmospheric warming impact of aerosol is taken into account over the ocean). Over the Indian Ocean, just south of Madagascar, this uplift is clearly associated with anomalous cyclonic flow (between ~10-30°S, 25-50°E).

4.3.6 Regional dynamical changes

Figure 4.3.4(a) shows the meridional vertical cross-section of the aerosol-induced change (AERO-CTRL) in SW atmospheric heating as well as surface radiative forcing (inset below) averaged over 12-25°E. This SW heating rate difference includes all feedbacks (i.e. from clouds as well as from aerosol), however, the main signal appears to be largely due to aerosol forcing since it is very much consistent with the distribution of aerosol concentrations (contours fig. 4.3.4(a)).

Maximum aerosol-induced heating (up to 1°C/day) and surface forcing (up to -48W/m²) occurs over the main aerosol source region, centred near 12°S. Two characteristic regions emerge: one situated between the equator and approximately 8°S, where there is a vertical extension of aerosol diabatic heating into the upper troposphere as a result of enhanced convective aerosol transport; and a second region south of 8°S, where the aerosol layer and associated SW heating is clearly confined below approximately 500hPa. This latter feature clearly indicates that the model appears to accurately simulate the 500hPa absolutely stable layer, which is an important, semi-permanent feature of the southern African atmosphere during the austral winter season [*Tyson et al.,* 1996; *Swap et al*., 2003]. The simulated heating rate values appear to fall within the range of observed values over the southern African continent. For example, Keil and Haywood [2003] calculated values of similar magnitude (1.77°C/day) using a radiative transfer model and observations of aerosol and cloud properties from SAFARI-2000, whilst instantaneous heating rates of up to 4°C/day over Mongu, in Zambia and 1.5°C/day over Inhaca Island, Mozambique were measured by Pilewskie et al. [2003].

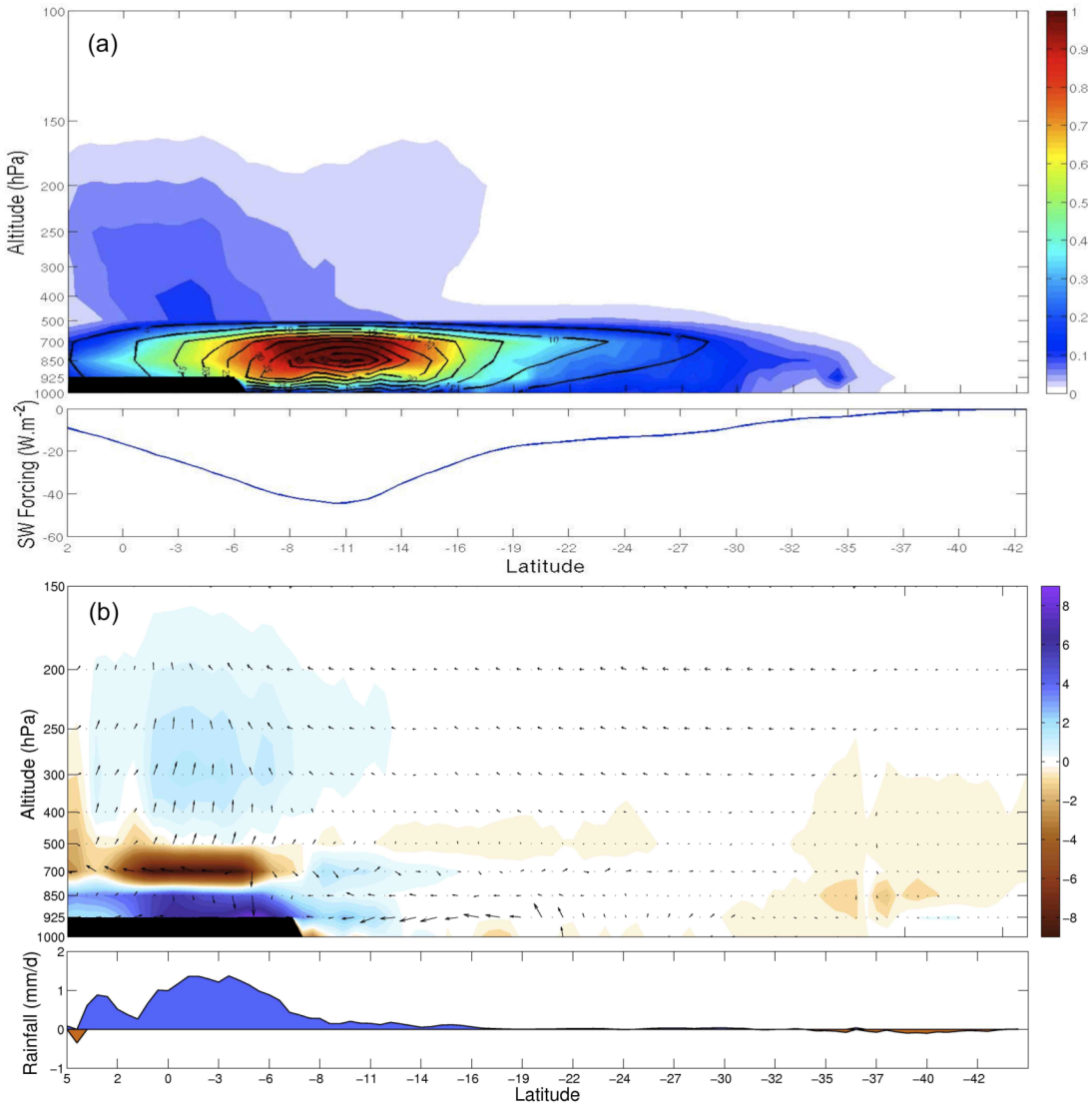

Figure 4.3.4: JJAS latitudinal profiles of (a) heating rate anomaly (AERO-CTRL) in °C/day with carbonaceous aerosol distribution contoured over (vertical profile, top) and surface radiative forcing in W/m^2 (inset bottom); and (b) cloud liquid water path (CLWP, in mg/m^2) and vertical circulation anomalies, as well as precipitation anomaly (inset bottom) averaged over 12-25°E. Only points above the land surface are taken into account in the averages.

Figure 4.3.4(b) shows the meridional average vertical circulation, cloud liquid water path (CLWP) and precipitation anomalies (again the difference between AERO-CTRL ensemble means) averaged over the same region (12-25°E). The distinction between the two regions discussed above is even clearer. In the convective region, north of approximately 8°S, CLWP significantly increases throughout much of the atmosphere except for at the top of the main aerosol layer near 700hPa. The CLWP increase above the aerosol layer is associated with anomalous upward circulation and contributes to divergence in the moisture field at 700hPa. The diabatic warming at the top of the aerosol layer appears to be sufficient to induce enhanced deep convection, which in turn results in increased precipitation (see inset below

fig. 4.3.4(b)). The triggering of convection by aerosol is, however, restricted to the equatorial region where atmospheric conditions are favourable to instability. South of 8ºS there is relatively little change in CLWP, vertical circulation and precipitation, largely as a result of the stability of the atmosphere in this region. As already mentioned, low-level convergence occurs towards the main biomass burning region, and this feature is clearly visible in fig. 4.3.4(b) between 8-19ºS.

Figure 4.3.5 shows the zonal vertical cross-section of CLWP, wind and precipitation anomalies averaged over 5°N-10°S. The significant increase in CLWP in the equatorial regions is again clear, as is the associated increase in precipitation (see inset). In addition, anomalous Walker-like circulation appears to result from the aerosol-induced enhancement of convection. This signal is similar to the 'elevated heat pump' effect described by Lau et al. [2006, 2009]. Using the fvGCM these authors found that the simulated absorbing aerosol burden resulted in anomalous heating at altitude, which in turn increased uplift and convection over the two regions studied (the Himalayas and West Africa). In both cases, these circulation anomalies were reminiscent of Walker-like circulation cells, similar to what is exhibited here.

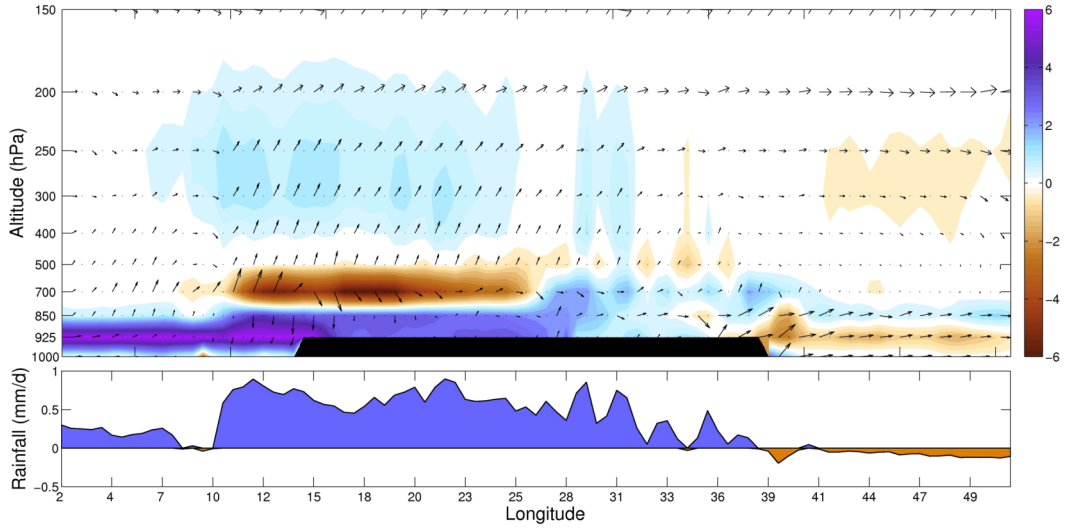

Figure 4.3.5: JJAS longitudinal cloud liquid water path (CLWP) anomaly (AERO-CTRL) (in g/m^2, vertical profile, top) and precipitation anomaly (inset bottom), averaged over 0-15°S latitude. Only points above the land surface are taken into account in the averages.

Below 700hPa subsidence is enhanced through the strong surface radiative cooling and decreases in surface fluxes that occur in the main biomass burning region. Solmon et al. [2008] found similar results over West Africa, where dust aerosol induced surface cooling and a reduction in surface turbulent fluxes. They found that this was generally a drying

mechanism if taken alone. In our case, however, the competing heat pump effect, which increases convective precipitation, is strongest because of the more absorbing nature of biomass burning aerosols that dominate the aerosol loading in the JJAS season.

In the north-eastern part of the domain (between 33-50ºE) small negative CLWP and precipitation anomalies are observed. This relative drying is associated with slight subsidence, corresponding to the descending branch of the Walker-like circulation anomaly (between 23-49°E) triggered by the atmospheric aerosol burden in the main biomass burning regions to the west. In addition, the anomalous offshore westerly flow below 700hPa suggests a reduction in transport of moisture from the Indian Ocean, which also likely contributes to the decreased CLWP and precipitation exhibited in this region.

Over the Atlantic Ocean, between 2-10°E, (again see fig. 4.3.5) the relatively high aerosol loading induces diabatic heating which again results in anomalous uplift. In this region, however, uplift occurs from the very surface, since there is no aerosol feedback on the SST (therefore no low-level stabilisation because of cooler surface temperatures). Despite the reduction in LH flux that occurs in this region (see fig. 4.3.2(b)) the lower atmosphere moistens below 850hPa, partly as a result of this uplift, but also likely as a consequence of increased low-level moisture flux to the region from the north (see fig. 4.2.6). The extent of CLWP increase is, however, vertically limited and appears to remain trapped below the marine boundary layer, likely as a result of the more stable nature of the atmosphere over this part of the ocean [*Tyson and Preston-Whyte*, 2000].

4.3.7 Aerosol-induced precipitation changes

Figure 4.3.6 shows the JJAS average precipitation change induced by the simulated aerosol loading. The increase in precipitation induced by the elevated heat pump effect between 5°N-5°S is clearly evident, with precipitation increasing by up to 2mm/day (or between 10-50% compared to the CTRL simulation). This serves to improve the negative precipitation bias over the western half of the tropics between ~14-20°E, but increases the positive bias exhibited in eastern parts (between 20-40ºE). The small decrease in precipitation along the East African and east Madagascan coasts is also clear, and is of a similar magnitude, up to approximately 50% of the CTRL ensemble mean JJAS seasonal average. The change in surface energy budget partitioning (LH flux increasing but SH flux increasing) that occurs in these regions is likely related to this reduction in precipitation.

Over the southern part of the domain, south of approximately 5°S, little change in precipitation is observed (except for over Madagascar, as just discussed). This is not surprising as little or no precipitation occurs south of approximately 8°S during the austral winter season (see fig.

4.2.2). The only exception is a weak decrease in precipitation (less than approximately 30% compared to the CTRL) over South Africa and the adjacent Indian Ocean (between ~30-35°S, ~20-40°E). This tropospheric drying anomaly is likely associated with the positive surface pressure anomaly over land and decreased onshore moisture flux exhibited in this region (see fig. 4.2.6(a) and 4.3.3(b)). These changes likely lead to reduced moisture convergence and decreased precipitation, which again, serves to decrease the model bias in this region (see fig. 4.2.2(d)).

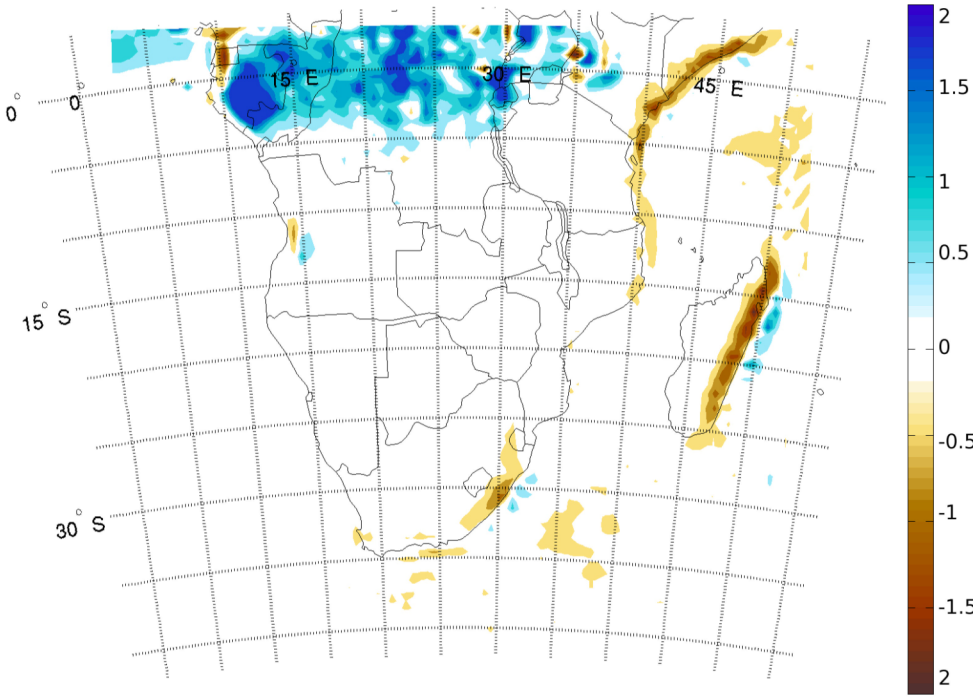

Figure 4.3.6: JJAS average aerosol-induced precipitation anomaly (AERO-CTRL) in mm/day.

4.4 Sensitivity tests

To more quantitatively compare the differences in simulated aerosol impacts between the sensitivity tests (GFED and SST ensemble), the radiative forcing and changes in certain meteorological variables are averaged over the Atlantic Ocean region of 3°N-25°S, 0°-15°E for the JJAS season. This area is chosen since simulated AOD compared best with the MODIS observations here (see fig. 4.2.4) and because this is where aerosol loading is highest over the Ocean so the impact of the SST feedbacks should be greatest.

4.4.1 GFED sensitivity test results

Results indicate that the lower aerosol loading in the GFED simulation induces much weaker surface and top-of-atmosphere (TOA) radiative forcing signals, -9.93W/m^2 and -2.06W/m^2, respectively (approximately half of that of the AERO ensemble in both cases). This in turn results in changes in surface temperature, planetary boundary layer (PBL) height and precipitation that are also only about half as large as that generated in the AERO ensemble (see table 4.4.1). Although the results presented are averaged only over the Atlantic Ocean outflow region, results for the whole domain were similar in magnitude (not shown).

	CTRL	AERO	GFED	SST
Surface RF (W/m²)*	/	-22.76	-9.93 (+56.37%)	-22.77 (-0.06%)
TOA RF (W/m²)*	/	-3.50	-2.06 (+41.05%)	-3.55 (-1.63%)
Surface temperature (°C)	20.86	20.65 (-1.00%)	20.79 (-0.36%)	20.46 (-1.91%)
PBL Height (m)	683.37	648.78 (-4.92%)	677.29 (-0.89%)	639.66 (-6.40%)
Precipitation (mm/day)	0.40	0.55 (+38.37%)	0.48 (+20.08%)	0.57 (+41.82%)

Table 4.4.1: Results of the various experiments (using the BB-AMMA emissions (AERO), using GFEDv2 emissions (GFED) and the sea surface temperature adjustment (SST)) compared to the control (CTRL) ensemble. Results are averaged over the Atlantic Ocean region of 3°N-25°S, 0°-15°E. Values in brackets show the percentage change compared to the CTRL JJAS seasonal mean. *The surface and top-of-atmosphere (TOA) radiative forcing (RF) are compared to the AERO ensemble rather than the CTRL, since in the CTRL simulations the aerosol RF is not taken into account.

4.4.2 Sensitivity to aerosol-SST feedbacks

The sensitivity to the simulated aerosol-induced SST feedback appears to be relatively negligible. The difference between the AERO and SST ensemble mean radiative forcing (RF) signals over the Atlantic Ocean region is considerably smaller than the difference between the AERO and GFED simulations (again see table 4.4.1). The surface and TOA RF are different from the AERO ensemble mean by less than 2%. In contrast the surface and TOA RF of the GFED simulation represent only 56% and 41% of the AERO ensemble mean, respectively.

In terms of the aerosol-induced changes in meteorological variables, the aerosol-SST feedback also appears to have only a small impact. The change in surface temperature is slightly greater compared to the CTRL simulation (-0.40ºC compared to the CTRL), but this is to be expected, since the sea surface cools as a result of the AOD in the SST ensemble, but not in the AERO ensemble (which decreases by 0.21ºC compared to the CTRL). This change

seems to have little impact on the aerosol-induced PBL height change, circulation anomalies or precipitation change over the Atlantic Ocean region (again see table 4.4.1).

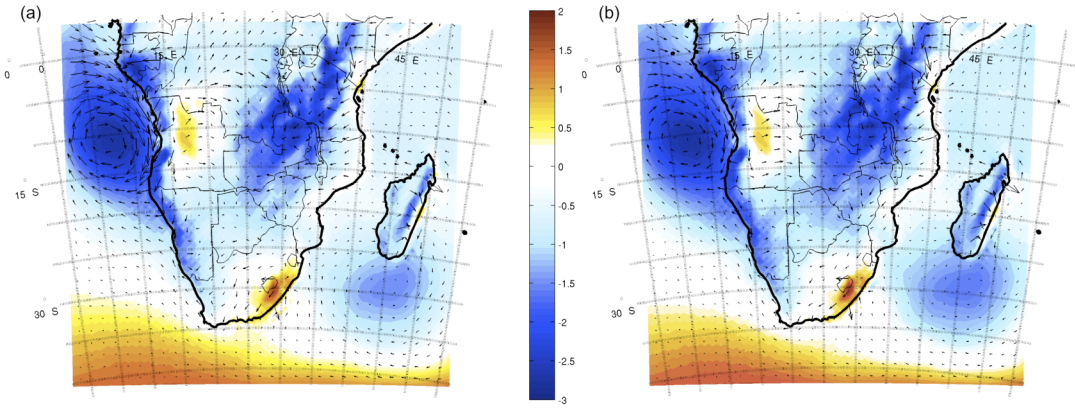

Figure 4.4.1: JJAS average 850hPa geopotential height (in m) and circulation differences between (a) the AERO-CTRL ensemble means and (b) the SST-CTRL ensemble means.

This is indeed the case for the subcontinent in general as well. Changes in 850hPa geopotential height (GPH) and wind anomalies of the AERO and SST ensemble means compared to the CTRL ensemble mean are shown in figures 4.4.1(a) and (b) respectively. It is clear that in both cases the simulated aerosol loading leads to significant changes in the atmospheric dynamics and circulation patterns (as discussed in the previous section 4.3), but there is very little noticeable difference between the two experiments. The dynamical response induced by the ocean surface cooling and reduction of oceanic surface fluxes leads locally to a small increase in atmospheric stability and a possible reduction of moisture advection from the sea to the continent. However, this anomaly does not appear, at least in our case, to be large enough to significantly modify those linked to aerosol-induced changes in diabatic heating and increased convection, which are largest over the continent. It is acknowledged, however, that a fully coupled mixed-layer ocean-atmosphere-aerosol model would be necessary to more realistically simulate and explore the seasonal modification of SST by the aerosols.

4.5 Conclusions

RegCM3 is used to explore the direct and semi-direct aerosol radiative effects of biomass burning aerosol over southern Africa during the austral dry season (JJAS) for six winter seasons from 2001-2006. The simulated aerosol loading results in significant changes to atmospheric stability, circulation patterns, as well as cloud cover and precipitation distributions. The most important results are summarised here.

The regional climatic features of southern Africa during the dry, austral winter are well simulated and both surface temperature and precipitation are consistent with the available observations. AOD is relatively well simulated, particularly over the oceanic regions (where satellite products are more accurate), however, two important biases are exhibited during the main biomass burning season. Firstly, maximum simulated AOD over land occurs approximately 5° further south than the maximum suggested by the MODIS satellite observations. And, secondly, the simulated AOD peaks too early in the season compared to AERONET, MODIS and MISR estimates. Outside of the main biomass burning season AOD is underestimated compared to AERONET, likely since these simulations do not include industrial, biogenic or sea-salt aerosols. Importantly, a sensitivity test using the GFEDv2 biomass burning inventory shows much lower AOD, and neither the temporal nor spatial disparity in simulated AOD is improved.

A strong decrease in clear-sky surface radiative forcing (up to -60W/m^2 in the main biomass burning region) results in decreased SH flux (up to-50W/m^2) and reduced surface temperature (up to 2ºC) over the entire southern African subcontinent (again, maximum over the main biomass burning area). The positive temperature bias over the western half of the southern African subcontinent is thus reduced and, overall, the simulation of surface temperature is improved compared to the CRU observations.

As a result of the strongly absorbing nature of the simulated biomass burning aerosols, diabatic atmospheric warming occurs. This is maximum, up to 1°C/day, near the 700hPa level in the main biomass burning aerosol source region. The simulated surface cooling and heating at altitude stabilises the lower troposphere below the main aerosol layer at 700hPa. In the equatorial regions, the warming near the top of the aerosol layer results in reduced stability above 700hPa and an elevated heat-pump effect is initiated. This enhances deep convection and this leads to an increase in precipitation between 5°N-8°S (by up to 50% compared to the CTRL ensemble mean). Despite significant temperature changes, little precipitation signal is exhibited over the rest of southern Africa, since during the JJAS season dry and stable atmospheric conditions prevail and little or no rainfall occurs over most of the region south of 8°S.

Similar climatic responses are found for the GFED sensitivity test, but the magnitude of these responses is considerably smaller (~50% less in the case of the most atmospheric variables). Interestingly, these results suggest that there is a relatively linear relationship between emissions and simulated climatic changes, since the biomass burning emissions of the GFEDv2 inventory are approximately 50% lower than those of the BB-AMMA inventory.

A third ensemble of four members is carried out using a simple adjustment of SST depending on AOD so as to assess the effect of aerosol-SST feedbacks on the simulated radiative forcing and resultant climatic impacts. The results from these simulations, however, are not significantly different to those without the SST adjustment (AERO ensemble). The sensitivity to the emissions inventory is significantly larger and is likely the largest contributor to uncertainty in terms of the simulated aerosol climatic impacts over southern Africa.

CHAPTER 5

Variability of aerosol-climate impacts at different timescales: Interannual to synoptic variability

5.1 Experiment description, model setup and validation

5.1.1 Model domain and boundary conditions

RegCM3 is used to simulate the southern African climate from 1982-2001. The same domain as all previous experiments is used, covering the region from 18°N-43°S, 3-56°E (see fig. 5.1.1) and, also as before, a horizontal resolution of 60km is used with 18 levels in the vertical. The NOAA OISST weekly average product [*Reynolds et al.,* 2002] is used in

combination with the ERA40 reanalysis [*Uppala et al.,* 2005] as lateral boundary conditions. The ERA40 product is used as an alternative to the NCEP-II reanalysis, which was used as boundary forcing in the previous chapters (3 and 4). Both reanalyses suffer various biases as a result of the different observations and assimilation techniques used [*Betts and Jakob*, 2002; *Troccoli and Kållberg*, 2004; *Uppala et al.,* 2005; *Betts et al., 2006*], however, in the post-satellite era (after 1979) the ERA40 product has been found to be more accurate for certain key variables, such as surface temperature [*Simmons et al.,* 2004]. Short tests carried out comparing simulations using both products showed little significant difference (see Appendix A). Thus, at least over southern Africa, the uncertainty associated with using different boundary conditions in RegCM3 is likely to be negligible in comparison to the uncertainty associated with aerosol emissions inventories, which remains large, particularly in the case of biomass burning aerosol [*Korontzi et al.,* 2004; *Solomon et al., 2007*; *Liousse et al.,* 2010], as was shown in chapter four.

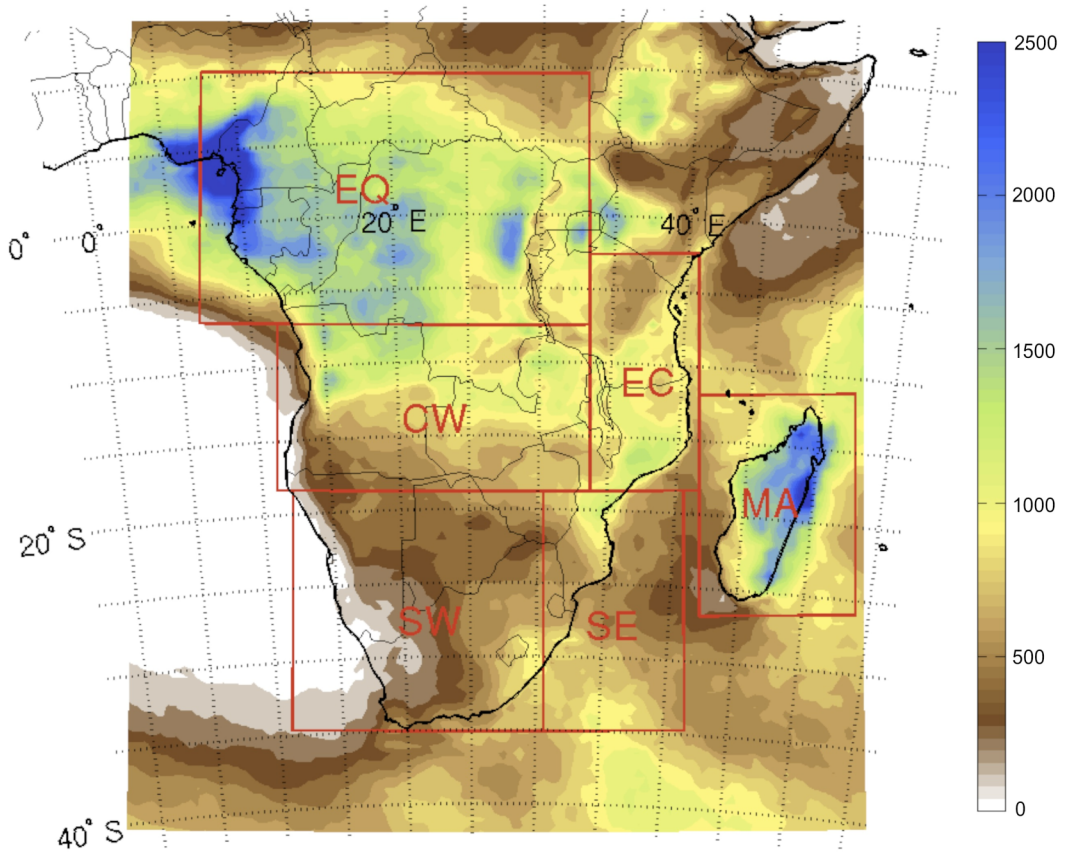

Figure 5.1.1: Annual average precipitation (mm/year) from the TRMM-3B43 product (2001-2006). The six sub-regions discussed are highlighted by the red boxes: EQ (equatorial), CW (Central West), SW (South West), SE (South East), EC (East Coast) and MA (Madagascar).

5.1.2 Aerosol emissions and aerosol module setup

Simulations are run using eight aerosol tracers: hydrophobic and hydrophilic black and organic carbon (BC and OC), two dust tracers (in bins with diameters of 0.1-1.0μm and 1.0-2.5μm, respectively), sulphate aerosol (SO_4) as well as its gaseous phase precursor, sulphur dioxide (SO_2). One simulation including the treatment of all aerosol processes (emission, transport, chemical conversion, deposition) but not their radiative effects (hereafter the CTRL) is compared with a second simulation where aerosol radiative forcing is taken into account in addition to the above-mentioned processes (from here on the AERO simulation). The difference between the two simulations (AERO-CTRL) is used to isolate the direct and semi-direct aerosol effects.

The decadal average biomass burning emissions inventory (i.e. monthly averages for each decade 1981-1990 and 1991-2000) of Mieville et al. [2010] is used to represent biomass burning aerosol sources. This inventory was developed expressly to provide consistent global gridded emissions for the period 1900- 2005. Decadal average emissions for the 20th century (1900-2000) were generated using the global historical reconstruction of burned area of Mouillot and Field [2005]. These estimates were then moderated, by ecosystem, to agree with estimates from a more recent inventory, covering the period 1997-2005, which was constructed using the ATSR fire hotspot product in combination with the GBA2000 burnt area estimates [*Mieville et al.,* 2010].

Simulations also include anthropogenic carbonaceous and sulphur dioxide emissions based on the work of Junker and Liousse [2008]. This database was constructed using country-by-country fossil and bio-fuel consumption and trade statistics from the United Nations Statistical Division (UNSTAT; 1997), in combination with time-varying emissions factors, which take into account the impact of technological development. Emissions estimates are available at 1ºx1º resolution on an annual basis from 1946-2000. Since the period simulated extends to 2001 emissions for the year 2000 are used for 2001 as well.

5.1.3 Validation of simulated aerosol optical depth

As presented in chapter 4, RegCM3 reproduces the southern African climate relatively well. In the interests of brevity, a full validation of the climatological aspects of the 20-year simulations carried out for this study is not presented here (but can be found in Appendix B). The focus of this section is rather on the reproduction of aerosol optical depth, since a different set of emissions inventories is used, and, as previously shown, this can significantly affect the simulated aerosol burden (see section 4.2.3).

Simulated aerosol optical depth (AOD) is compared to TOMS AOD [*Torres et al,* 2002; see section 2.3.2.2 for a full description] from 1982-1992 and 1996-2000, years for which the satellite data are available. It is important to note that TOMS does not detect aerosol in the lowest 500-1000m of the atmosphere [*Torres et al,* 1998], therefore only the model AOD above 900hPa is compared. This feature is a drawback particularly near aerosol sources and in regions where the main aerosol burden remains trapped below a low-level boundary layer.

In order to better assess the simulated aerosol optical depth the domain simulated is divided into six sub-regions (see fig. 5.1.1), named as follows: Equatorial (EQ), Central West (CW), South West (SW), South East (SE), East Coast (EC) and Madagascar (MA). The choice of sub-regions is largely based on the average precipitation climatology [cf. *Nicholson,* 1993] and the known climatic regimes over southern Africa, although the number of grid-points in each sub-region is also accounted for (so as to include enough points for fair averaging).

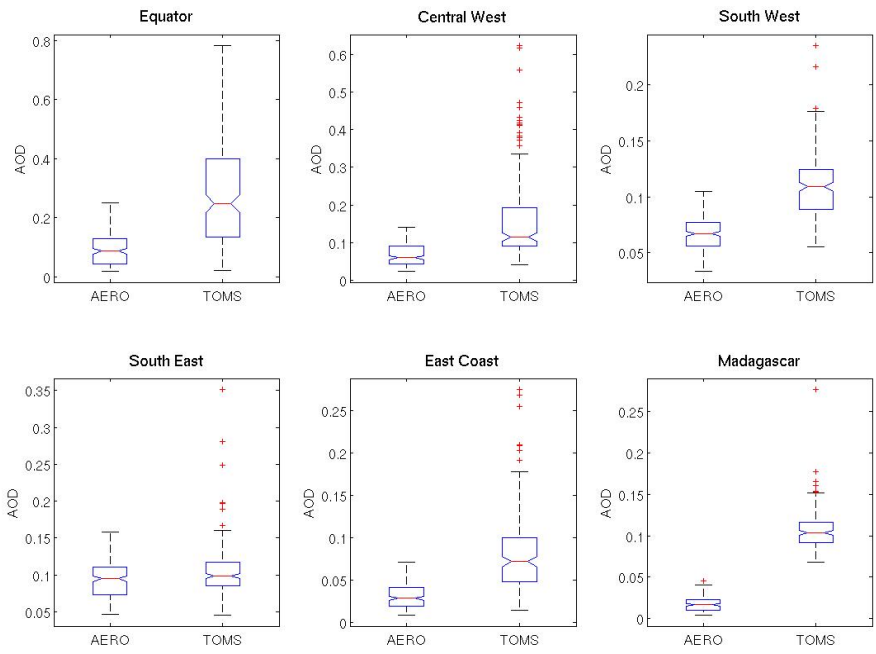

Figure 5.1.2: Box-plot of monthly average aerosol optical depth (AOD) for the RegCM3 AERO simulation and TOMS observations. Blue boxes represent the interquartile range (IQR), the red line the median of each sample and the whiskers extend out to 1.5 times the IQR above and below the median. Notches on the boxes denote the variability of the median between samples and if they do not overlap medians are significantly different at the 5% significance level. Red crosses indicate outliers.

The box-plot of monthly average AOD for the six sub-regions is shown in figure 5.1.2. It is clear that simulated AOD is underestimated over nearly the entire domain with five out of the

six sub-regions being significantly different from the TOMS observations at the 95% level. In addition, the monthly average AOD variability (represented by the extent of the whiskers) is also systematically underestimated in all five of these sub-regions. The only sub-region where the AOD signal agrees relatively well with the TOMS observations is the south east (SE), where both the magnitude and range of variability are well simulated.

The domain-wide underestimation of AOD is perhaps more clearly evident in the seasonal averages (fig. 5.1.2). Simulated AOD is underestimated by as much as 0.6 in the main southern hemisphere biomass burning region (0-10ºS, 10-25ºE) in the core austral winter burning season from June to August (JJA), as well as throughout the year over the two largest southern African dust sources, the Makgadikgadi (22ºS, 24ºE) and Etosha (18ºS, 16ºE) Pan. AOD is also underestimated over the West African Sahel and Gulf of Guinea regions (10ºN-5ºS, 0-20ºE) from September through March.

	BC	OC	BC:OC ratio
Decade 1 (1982-1990)	1.00	6.17	0.162
Decade 2 (1991-2000)	0.98	6.37	0.154
BB-AMMA	1.37	12.90	0.106
GFEDv2	0.68	6.20	0.110

Table 5.1.1: Annual average black and organic carbon (BC and OC respectively) biomass burning emissions estimates (totals in Tg/yr for the domain simulated) of Mieville et al., [2010] for the two decades simulated in this study, as well as the 2001-2006 average for the BB-AMMA inventory [*Liousse et al.,* 2010] and the GFEDv2 inventory [*van der Werf et al.,* 2006] used in chapter 4.

The underestimation of AOD in the main biomass burning regions is very likely related to the emissions inventory used, since the estimates of Mieville et al. [2010] are approximately half (total BC and OC emissions averaged 1980-2000 period of 7.26Tg/year) as large as those of the BB-AMMA inventory (total BC and OC emissions averaged 2001-2006 of 14.27Tg/year) [*Liousse et al.,* 2010] as used in the previous chapter (and which resulted in a relatively accurate reproduction of the magnitude of AOD, see section 4.2.3). The estimates of Mieville et al. [2010] are rather of the same magnitude as the GFEDv2 inventory (total BC and OC emissions averaged 2001-2006 of 6.88Tg/year) [*van der Werf et al.,* 2006; see table 5.1.1], which, as shown in the previous chapter, also resulted in significant underestimation of simulated AOD, but over the 2001-2006 period (see fig. 4.2.4).

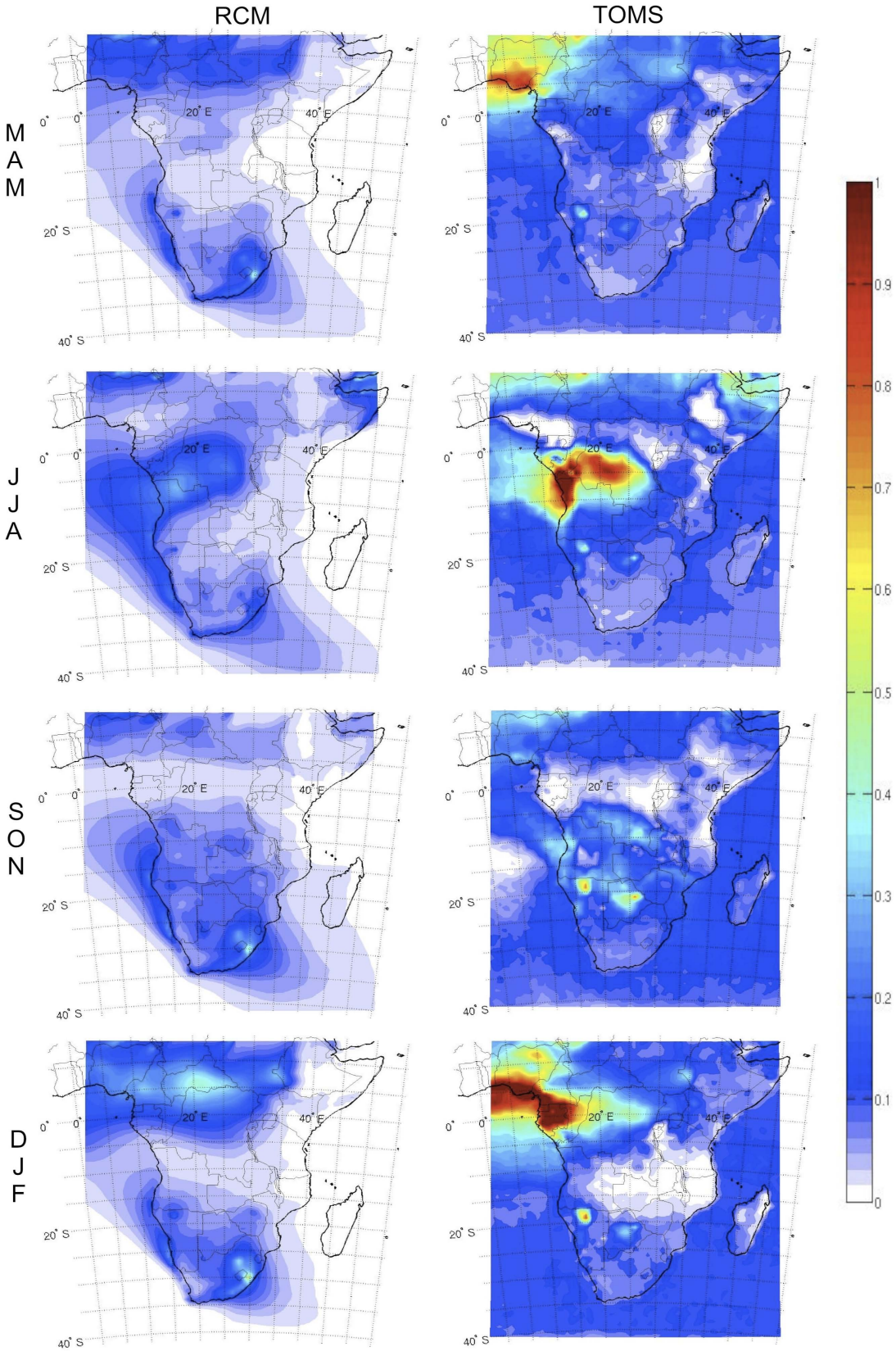

Figure 5.1.3: Seasonal average AOD as simulated by RegCM3 (left column) and as observed by TOMS (right column). Averages are shown for all years for which data are available (1982-1991 and 1996-2001).

The underestimation of AOD over the Makgadikgadi and Etosha Pans is likely the result of too little dust production within RegCM3, which in turn is possibly related to the underestimation of surface wind speeds. Todd et al. [2008a] found a similar result using RegCM3 over the Bodélé Depression in northern Chad, a topographical low and significant dust source not unlike the Makgadikgadi and Etosha Pans of southern Africa. These authors found that RegCM3 was able to reproduce the low-level jet system that contributes most significantly to dust production in the Bodélé, but that the wind strength was significantly underestimated compared to ground-based measurements taken during an experimental campaign. As a result, simulated dust emission was significantly underestimated. In addition, Todd et al. [2008b] found that the NCEP-II reanalysis did not represent the low-level jet feature well, so did not prove useful for model comparison purposes. Given the relative similarity of the nature of the southern African dust sources, it is likely that RegCM3 exhibits similar bias. Unfortunately, however, no surface wind observations are available for either the Makgadikgadi or Etosha Pans to make a more in-depth assessment of this feature and it is unlikely that the ERA40 or NCEP-II reanalyses products accurately represent the local-scale winds responsible for dust production in these two regions. In addition, in the RegCM3 dust module it is assumed that dust is emitted only from desert and semi-desert soils, thus the underlying soil texture type may also contribute to this bias (i.e. in reality dust emissions may be generated in dry grassland areas, but in the model these are nor represented). Also, as mentioned in previous chapters, the underestimation of AOD is also partly related to the fact that RegCM3 does not account for biogenic or sea-salt aerosol emissions.

AOD is overestimated in only two small regions, over the Atlantic Ocean just off the west coast of the southern Africa (between ~22-27ºS, 12-15ºE) as well as over the main Highveld industrial region of South Africa (centred near 27°S, 28°E). The relatively coarse resolution of TOMS (50kmx50km) makes it difficult to avoid cloud contamination, which may have a significant impact on retrieval accuracy [*Kinne et al.,* 2003]. Thus, the model overestimation off the west coast of Namibia and Angola, where a semi-permanent marine stratocumulus cloud layer exists [*Tyson and Preston-Whyte,* 2000; *Keil and Haywood,* 2003], may not be realistic (i.e. the model simulation may be closer to reality than the TOMS observations, which may be the average of only a few measurements). The slight overestimation of AOD over the South African Highveld is possibly related to an overestimation of anthropogenic aerosol emissions from this small region, or again perhaps as a result of error in the TOMS AOD product related to the measurement of more diffusive sulphate aerosol which dominate the atmospheric burden in this region. This overestimation appears to effectively counteract the underestimation of AOD in the rest of the SE sub-region, resulting in the relatively good agreement with TOMS shown in fig. 5.1.1.

The bias in simulated AOD is also, to a certain degree, likely the result of model error. RegCM3 does not reproduce all features of the southern African climate accurately in all

seasons (as discussed in chapter 4 and appendix B). Therefore it is likely that the AOD bias is at least partly a result of this error. However, the consistency of the AOD underestimation between seasons and over most of the domain tends to suggest that it is rather the underestimation of aerosol sources that plays a larger role. In general, despite the magnitude and variability of AOD not being simulated as accurately as previous simulations (see chapters 3 and 4), the spatial representation of AOD is relatively well represented. Unfortunately, besides for the TOMS AOD product no other aerosol measurements (e.g. surface aerosol concentrations) are available over southern Africa for the period simulated, so it is difficult to assess simulated AOD by any other means.

5.2 Long-term austral winter average aerosol-climate impacts

The austral winter average direct and semi-direct aerosol effects are investigated to assess the sensitivity to a third biomass burning aerosol emissions inventory, that of Mieville et al. [2010]. The seasonal average aerosol-climate impacts are presented for the entire simulation period (1982-2001) and, more importantly, compared to results from chapter 4.

5.2.1 JJAS seasonal average radiative forcing

Simulated JJAS average surface radiative forcing (RF) is negative over the entire southern Africa continent, reaching up to -25W/m^2 in the main biomass burning region between 5-10ºS, 15-20ºE (fig. 5.2.1(a)). The surface RF corresponds directly to the AOD signal (see contours fig. 5.2.1(a)) and is very similar to the surface RF signal exhibited using the BB-AMMA emissions (see fig. 4.3.1(a)), although the magnitude of RF is approximately half of that presented in chapter 4. This suggests that despite there still being considerable uncertainty attached to the magnitude of biomass burning emissions estimates, the source regions appear to be relatively well known and seem not to have shifted considerably in location over the past three decades. Perhaps more importantly, however, is the relatively linear nature of the relationship apparent between biomass burning emissions and surface RF. The Mieville et al. [2010] emissions are effectively half of those of the BB-AMMA emissions of Liousse et al. [2010] (see table 5.1.1) and this appears to result in an estimated surface RF which is half as strong (-25W/m^2 simulated here, and up to -60W/m^2 in the 6-year simulations of chapter 4).

In terms of top-of-atmosphere (TOA) RF (see fig. 5.2.1(b)), the signal is again similar to that exhibited in the 6-year simulations using the BB-AMMA emissions inventory (hereafter the BB-AMMA simulations). The signal of mineral dust can clearly be seen over the coastal Atlantic Ocean, adjacent to the main source regions between approximately 15-30ºS, while

the more northern section of this negative TOA RF region is related to biomass burning emissions rather than dust aerosol. The impact of sulphate aerosol can also clearly be seen over south eastern South Africa (near 30ºS, 30ºE) and in the Indian Ocean outflow plume, where the negative TOA RF is in fact stronger than in the BB-AMMA simulations (since they do not include these aerosol).

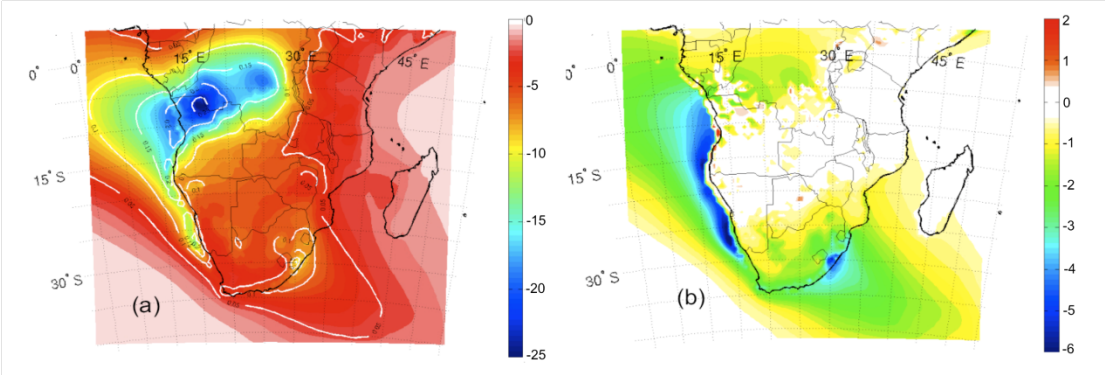

Figure 5.2.1: JJAS seasonal average (1982-2001) aerosol-induced clear-sky SW radiative forcing at (a) the surface and (b) top-of-atmosphere (TOA) in W/m^2. Aerosol optical depth (AOD) is contoured over (a), the surface radiative forcing (contours every 0.05 from 0.05 to 0.25).

The largest difference between the BB-AMMA and 20-year simulations lies in the extent of the region of simulated positive TOA RF, which covers a larger area in the BB-AMMA simulations and is twice as large in magnitude (+4W/m^2 vs. +2W/m^2). As for the BB-AMMA simulations, the simulated atmospheric RF (not shown), mirrors the surface RF and AOD fields, reaching up to 20W/m^2 in the main biomass burning regions. Both the atmospheric and TOA RF again point towards a relatively linear relationship between biomass burning emissions estimates and RF, since the greater the biomass burning emissions the stronger the positive TOA or atmospheric RF.

5.2.2 Surface impacts

Changes in JJAS seasonal average surface temperature mirror the surface RF fields (and hence also the AOD signal), with maximum decreases of up to 1ºC in the main biomass burning regions (fig. 5.2.2). This signal also matches that exhibited in the BB-AMMA experiment, and, as for the RF, the magnitude of surface temperature change simulated here is approximately half as large as that exhibited in the BB-AMMA simulations. These results suggest that the surface temperature response is approximately linear to surface RF, which in turn is almost linearly related to AOD and aerosol emissions (as just described). The two-fold increase in emissions and simulated AOD between the two experiments (6-year BB-AMMA

simulations and 20-year simulations described here) in turn translates into an approximately two-fold increase surface RF and surface temperature (-60W/m^2 and -2ºC respectively, in the BB-AMMA simulations vs. -25W/m^2 and -1ºC simulated here). Therefore, as a very rough estimate, for every ~30W/m^2 forcing at the surface a temperature change of 1ºC can be expected.

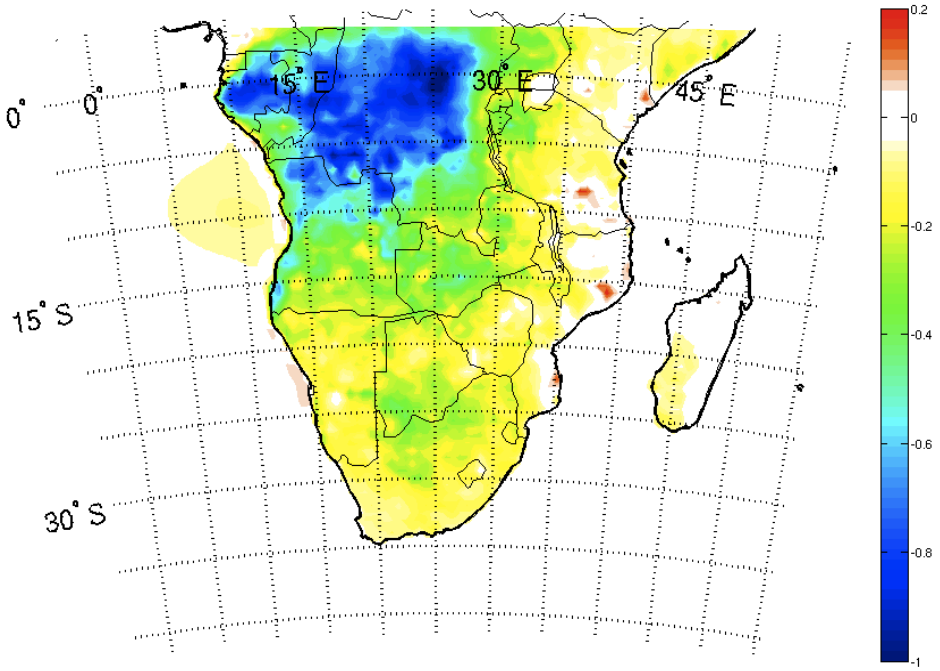

Figure 5.2.2: JJAS seasonal average surface temperature difference (AERO-CTRL) for 1982-2001 (in ºC).

Despite the difference in magnitude between the two experiments (BB-AMMA vs. 20-year), the spatial signal in terms of surface RF and surface temperature change is very similar. The regions of maximum surface RF and surface temperature difference occur below the region of maximum AOD between 5-15ºS, 5-15ºE in both experiments. Therefore, although there is still uncertainty regarding the magnitude of the aerosol impacts, there is much less uncertainty associated with the spatial situation of these impacts, at least as regards surface temperature.

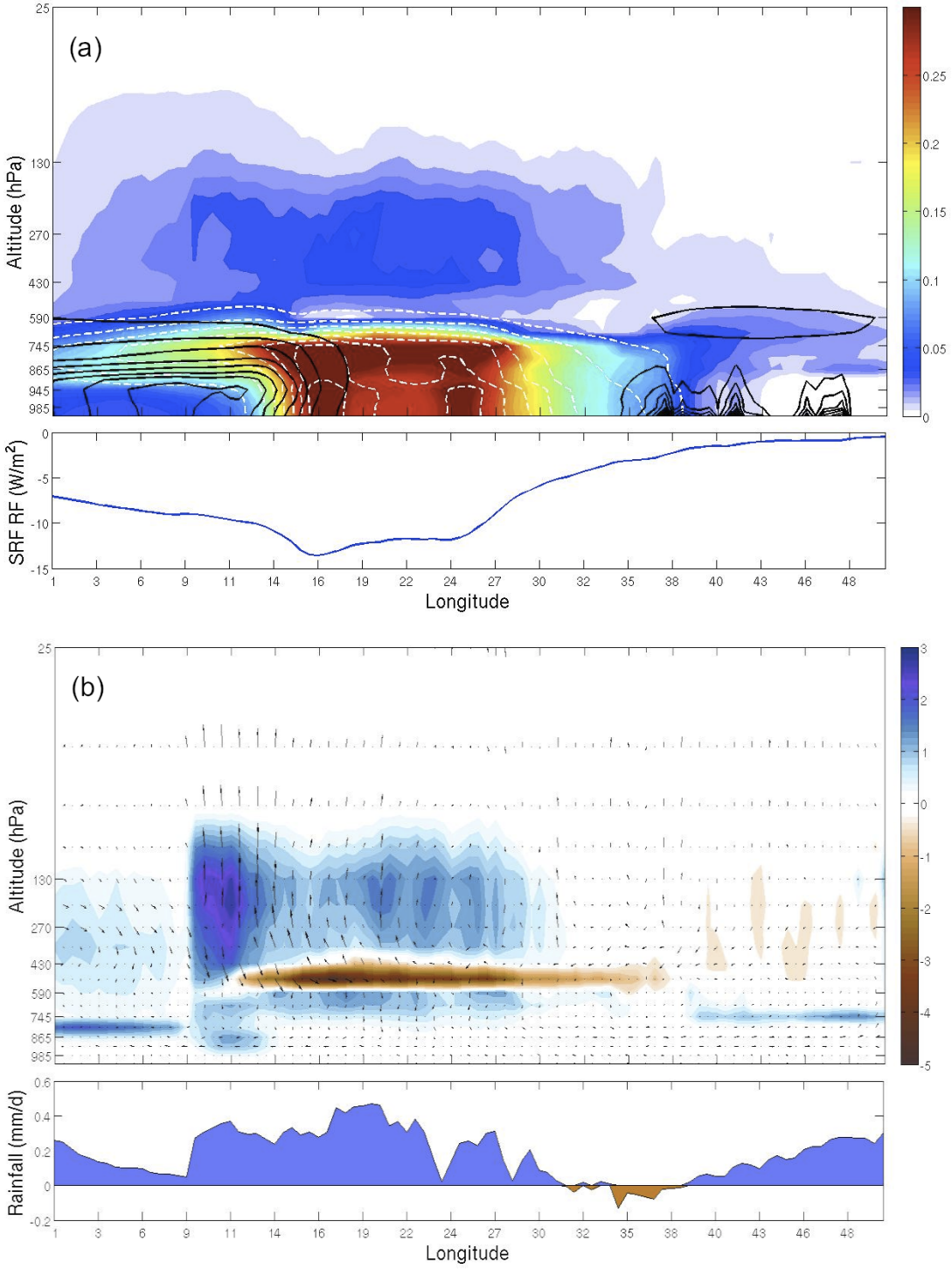

Figure 5.2.3: Latitudinal (5ºN-10ºS) and JJAS seasonal average vertical profile of (a) aerosol-induced atmospheric heating (in ºC/day) with carbonaceous (white dashed contours) and mineral dust (black contours) aerosol concentrations (with average surface radiative forcing inset below) and (b) cloud liquid water path (in g/m^2) and wind anomalies (with average precipitation change inset below).

5.2.3 Regional dynamical changes

Mean dynamical changes in the southern African regional atmosphere during the winter season (JJAS) for the 1982-2001 period reflect a very similar signal to that observed in the 6-year BB-AMMA simulations (2001-2006). As shown in chapter 4, the relatively absorbing biomass burning aerosol that dominate the regional atmospheric burden induce significant atmospheric shortwave (SW) heating below ~500hPa in the main burning regions (fig 5.2.3(a)). This heating is clearly related to the distribution of biomass burning aerosol (white dashed contours) rather than mineral dust aerosol (black contours). The magnitude of heating in the 20-year simulations is considerably smaller (up to just 0.3ºC/day vs. 1ºC/day in the 6-year simulations) and falls somewhat below values (~1.77ºC/day) measured during the SAFARI-2000 campaign [*Keil and Haywood*, 2003]. As expected, maximum surface radiative forcing (inset below, fig. 5.2.2(a)) occurs below the region of maximum heating, where the energy absorbed by the aerosol layer significantly decreases the amount of radiation reaching the surface.

Dynamical changes invoked in the equatorial regions are again very similar but smaller in magnitude to those exhibited in the BB-AMMA simulations. The heating at altitude induces an elevated heat-pump mechanism [cf. *Lau et al.,* 2006, 2009], which in turn results in enhanced convection and moisture convergence aloft of the main aerosol layer where drying occurs (fig. 5.2.2(b)). The increased precipitation (up to approximately 40% compared to the CTRL) in turn enhances soil moisture content and evaporation rates, effectively increasing low-level atmospheric moisture levels and spinning-up the hydrological cycle. Not only are these dynamical changes similar to those presented in chapter four, but Randles and Ramaswamy [2010] also found similar results for the African equatorial regions. Using the GFDL GCM, these authors showed that biomass burning aerosol increased cloud cover, atmospheric moisture and precipitation as a result of surface cooling in combination with enhanced upward motion and low-level convergence in the tropics.

5.3 Interannual variability of seasonal aerosol impacts

This section focuses on the interannual variability of the simulated climatic impacts of aerosol during the austral winter season, an aspect that has had little attention in the literature to date, especially over Africa. The atmospheric aerosol loading varies from year-to-year depending on various meteorological controls and large-scale climatic conditions, which drive natural aerosol emissions (e.g. entrainment of mineral dust) as well as deposition and transport patterns of all aerosol species. Natural aerosol emissions vary in space and magnitude [e.g. *Miller and Tegen*, 1998; *Mahowald et al.,* 2003; *Liousse et al.,* 2010] to a greater extent than anthropogenic aerosol sources, which, in comparison, vary relatively little

in terms of both spatial distribution (cities, towns and industry do not move much, besides for possible expansion) and from season to season. The variability of aerosol sources is reflected in the variability of atmospheric aerosol loading, which in turn affects the variability of climatic impacts in response to the atmospheric aerosol burden. An accurate quantification of the interannual variability of aerosol-climate impacts is essential in order to better estimate the relative contribution of aerosol-climate impacts to interannual climate variability under present climate conditions and to assess whether aerosol have positive or negative feedbacks from year to year. In addition, it is particularly important to have a measure of the range of aerosol-climate impacts so as to provide a better context within which it is possible assess projected aerosol-climate interactions under future climate conditions.

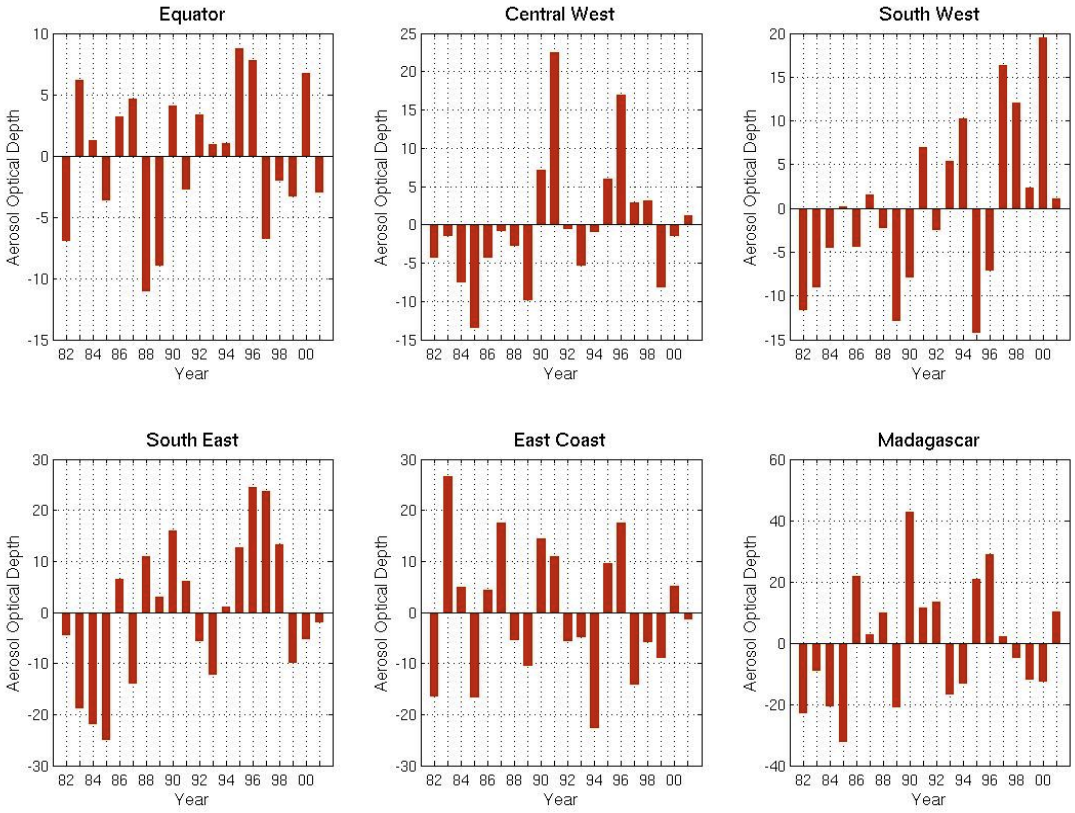

Figure 5.3.1 JJAS seasonal average aerosol optical depth percentage anomaly (percentage difference from the 1982-2001 mean) for each of the six climatological sub-regions.

5.3.1. Interannual variability of aerosol optical depth

To facilitate analysis, the southern African domain is divided into the same six sub-regions as described previously (see fig. 5.1.1). The simulated JJAS seasonal average AOD varies from year to year in all sub-regions, but to different extents, depending largely on the climate variability inherent to each sub-region (fig. 5.3.1). Interannual AOD variability is largest in the

South East (SE), East Coast (EC) and Madagascan (MA) sub-regions, where AOD varies between JJAS seasons by as much as 30-40% of the mean, translating into differences as large as 60% between years (e.g. over the MA sub-region from 1989-1990). Interannual AOD variability is lowest in the equatorial (EQ) sub-region, varying only between ±10% of the 1982-2001 mean. Since climate variability in this area is lowest, the meteorological factors controlling the atmospheric aerosol loading are also less variable.

It is important to note at this point that the prescribed biomass burning emissions do not vary from year to year, but rather only from decade to decade (i.e. from the 1980's to the 1990's), and, the difference between decades is minimal (see table 5.1.1). In addition, the anthropogenic emissions utilised also vary relatively little from year to year over the simulation period (only increasing slightly over the 20 years simulated; not shown). The main source of interannual variability of AOD in the model thus appears to be mostly a consequence of climatological controls (i.e. through large-scale changes of circulation patterns which affect aerosol transport and deposition).

5.3.2 Aerosol-induced surface temperature changes

The interannual variability of the aerosol-induced change in surface temperature in each of the six-sub-regions is shown in figure 5.3.2. The surface temperature decreases in all JJAS seasons from 1982-2001 in the Equatorial (EQ) and Central West (CW) sub-regions, where seasonal average surface temperature decreases vary between -0.16 to -0.5ºC and -0.03 to -0.42ºC, respectively. This corresponds to between 45-150% and 5-120% of the simulated interannual variability in each of these sub-regions (where the standard deviation of the JJAS averages of the CTRL simulation is assumed to give a simple but good indication of the level of interannual variability). This suggests that the simulated aerosol loading results in cooling of the surface that is on occasion as large, or greater in magnitude than, the year-to-year variability in these areas.

Surface cooling in the four other sub-regions (south west (SW), south east (SE), east coast (EC) and Madagascar (MA)) is smaller and less consistent, both in terms of absolute magnitude and in comparison to the simulated interannual variability. The difference between the CTRL and AERO simulations is not significant in any of these sub-regions (see table 5.3.1, last column – 95% significance level, using the Student's T-test) and the relative difference between the two experiments never exceeds more than -0.22ºC, (the equivalent of maximum 65% of interannual variability). Most interestingly perhaps, is the fact that for some years the JJAS average surface temperature difference is in fact positive, indicating that the aerosol loading induces warmer near-surface temperature. There is no increase of incoming solar radiation in any sub-region in any year (not shown), thus the surface temperature

increases do not appear to be the result of increased shortwave radiation at the surface. In addition, the interannual variability of aerosol-induced precipitation (see fig. 5.3.3) and cloud cover (not shown) does not vary concurrently with the year-to-year variability in surface temperature change. Thus, it appears that the induced temperature difference is the result of a combination of different factors, such as surface energy fluxes, soil moisture, circulation patterns, etc, the strengths of which vary from year to year depending on the dominant meteorological conditions.

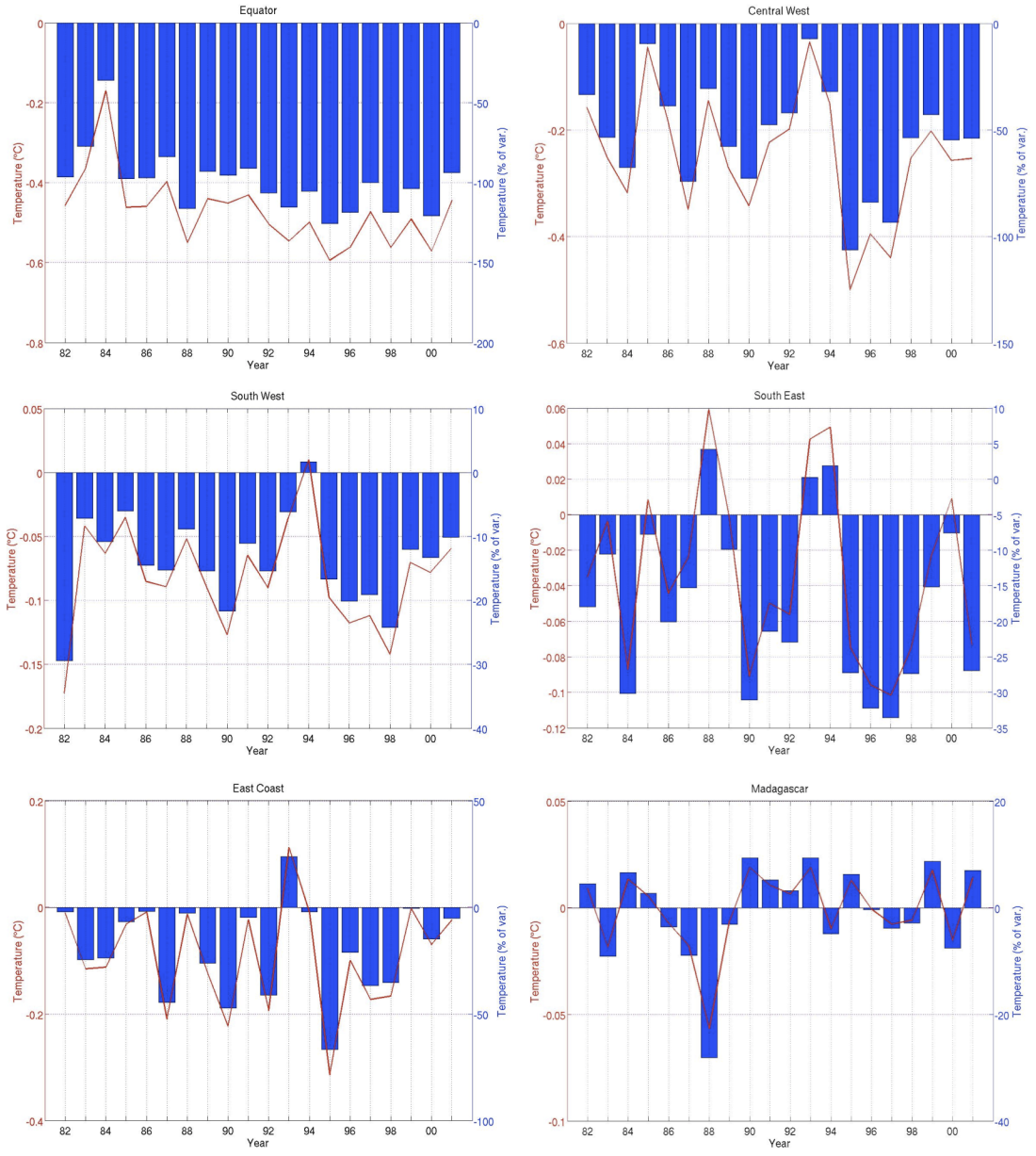

Figure 5.3.2: JJAS seasonal average surface temperature difference (AERO-CTRL) for all six sub-regions for 1982-2001. The red line shows the absolute difference between the two experiments (in ºC), while the blue bars indicate the % of JJAS variability (the standard deviation is assumed to give a good indication of variability) this difference represents.

	Variability (standard deviation)			JJAS mean bias		p-value
	CRU	*CTRL*	*AERO*	*CTRL-CRU*	*AERO-CRU*	
EQ	0.267	0.393	0.440	1.21	0.73	0.001
CW	0.323	0.387	0.337	1.24	0.97	0.042
SW	0.468	0.555	0.549	0.61	0.45	0.614
SE	0.375	0.419	0.423	0.38	0.25	0.678
EC	0.259	0.308	0.219	-0.64	-0.74	0.471
MA	0.299	0.351	0.339	0.15	0.14	0.990

Table 5.3.1: JJAS average surface temperature variability (the standard deviation is assumed to provide a good indication of variability) for each sub-region for the CRU observations, control (CTRL) and experiment (AERO), as well as the average relative bias between observed and simulated surface temperature (in ºC) and the result of a 2-sided Student's t-test comparing the CTRL and AERO simulated surface temperature. P-values are highlighted red if significant (at the 95% level). The sub-regions are: Equator (EQ), Central West (CW), South West (SW), South East (SE), East Coast (EC) and Madagascar (MA).

Over most of southern Africa the simulated interannual surface temperature signal is improved when the direct and semi-direct aerosol radiative effects are taken into account (compare the AERO and CTRL simulations in table 5.3.1). In five out of six of the sub-regions the JJAS average surface temperature bias is reduced, while in four of the six sub-regions (different ones) the estimated interannual variability is also improved. Seasonal average bias increases only slightly in the EC sub-region, becoming more negative (by 0.10ºC) as a result of the simulated aerosol radiative forcing. Surface temperature variability increases only in the EQ and SE sub-regions, although the difference in the SE sub-region is very small (~0.04) and likely within the model noise level. In contrast, the difference in the EQ sub-region (~0.10) is considerably larger. Since convection, which is a relatively stochastic process, is enhanced in this region (see above discussions), this probably contributes to the significant increase of interannual surface temperature variability exhibited in this sub-region.

5.3.3 Precipitation changes

In terms of precipitation, the difference between the AERO and CTRL simulations is more variable than for surface temperature (fig. 5.3.3). Precipitation increases in the main biomass burning sub-regions (EQ and CW), where the absorbing aerosol induces an elevated heat-pump effect, enhancing convection and precipitation (see previous section). In the EQ sub-region where natural interannual variability is relatively low, the seasonal average precipitation increases represent changes of over 50% of the magnitude of variability in most years. In the CW sub-region, where interannual variability is higher, there are fewer years where the differences between the aerosol-induced precipitation changes are of the same magnitude as the interannual variability. For the four other sub-regions, the difference in precipitation is generally much lower than simulated interannual variability (less than 30% for most years). This is also reflected in the results of a significance test which indicate that only

in the EQ region is simulated precipitation significantly different between the AERO and CTRL simulations (see table 5.3.2). This is, however, partly to be expected, since austral winter (JJAS) is the southern African dry season (for most sub-regions except the SW) and, as shown previously, the simulated aerosol loading has little impact on precipitation outside of the equatorial regions (see sections 4.3.7 and 5.2.5).

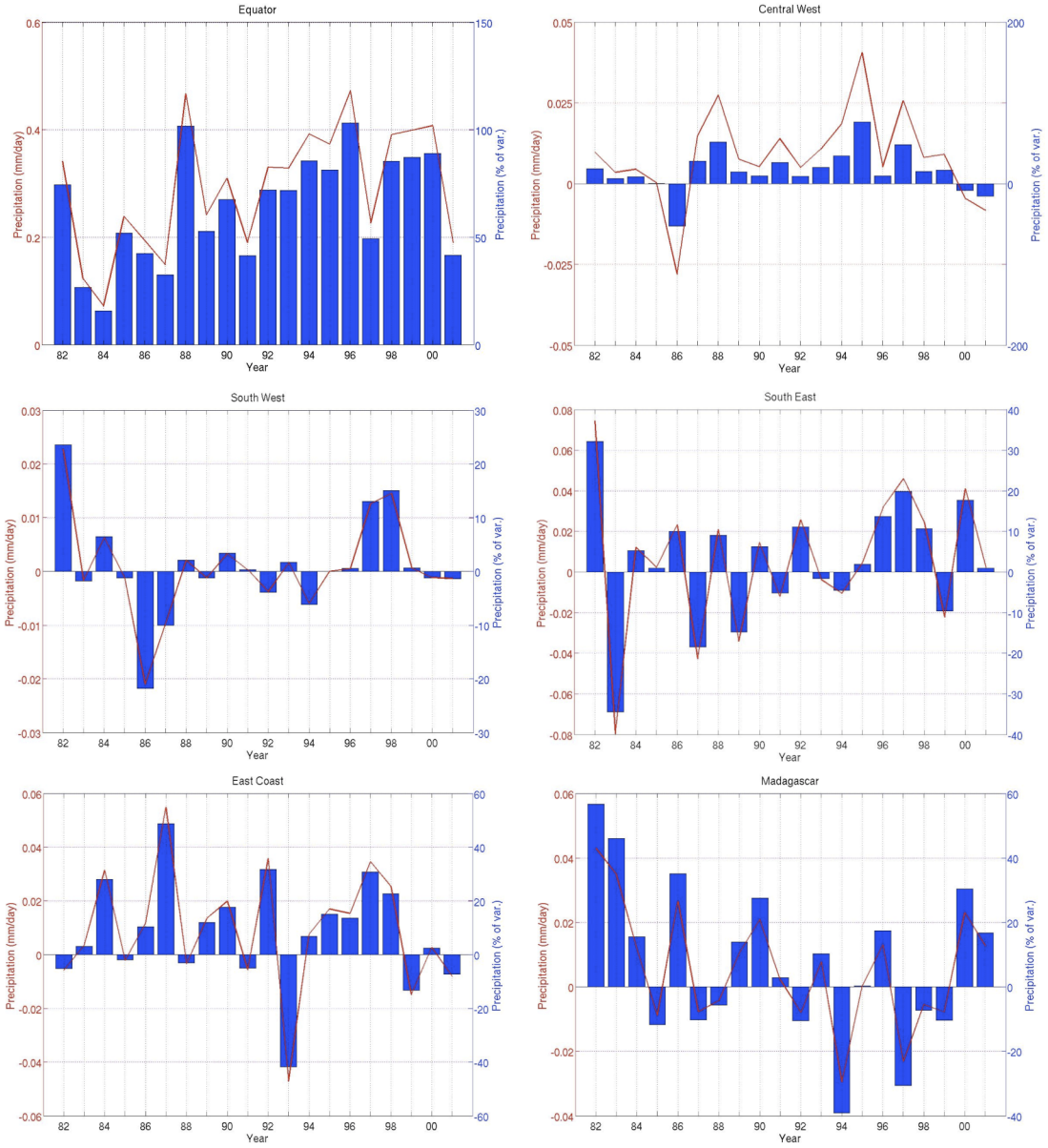

Figure 5.3.3: JJAS seasonal average precipitation difference (AERO-CTRL) for all six sub-regions for 1982-2001. The red line shows the absolute difference between the two experiments (in mm/day), while the blue bars indicate the % JJAS variability (the standard deviation is assumed to give a good indication of variability) this difference represents.

In general, including the direct and semi-direct aerosol radiative effects does not seem to improve the simulation of precipitation. As already mentioned, it is only in the EQ sub-region where a significant difference between the two experiments is exhibited, and the inclusion of the aerosol direct effect in fact appears to result in a slight increase in precipitation bias. Again, this is because convection is enhanced in these regions. These results suggest that outside of the tropics, the simulated aerosol radiative effects are only of second-order importance in terms of model precipitation uncertainty. Since southern Africa experiences a high degree of interannual precipitation variability [*Tyson and Preston-Whyte,* 2000; *Reason et al.,* 2006] and the regional population is still largely dependent on rain-fed agriculture [*Washington et al.,* 2006] it is vital to ascertain which factors most strongly influence interannual precipitation variability. These results seem to suggest that during the austral winter season over most of southern Africa the direct and semi-direct aerosol effects play only a relatively small role in this variability during the austral winter season, at least outside of the tropics.

	Variability (standard deviation)			Relative Bias		p-value
	CRU	*CTRL*	*AERO*	*CTRL-CRU*	*AERO-CRU*	
EQ	0.213	0.324	0.375	-0.08	0.19	0.039
CW	0.096	0.345	0.378	0.22	0.28	0.326
SW	0.103	0.320	0.331	0.19	0.21	0.978
SE	0.253	0.467	0.476	0.62	0.64	0.925
EC	0.080	0.081	0.093	0.12	0.14	0.768
MA	0.228	0.156	0.155	-0.07	-0.06	0.866

Table 5.3.2: JJAS average precipitation variability (the standard deviation is assumed to provide a good indication of variability) for each sub-region for the CRU observations, control (CTRL) and experiment (AERO), as well as the average relative bias between observed and simulated precipitation (in mm/day) and the result of a 2-sided Student's t-test comparing the CTRL and AERO simulated precipitation. P-values are highlighted red if significant (at the 95% level). The sub-regions are: Equator (EQ), Central West (CW), South West (SW), South East (SE), East Coast (EC) and Madagascar (MA).

5.3.4 Association with regional climate drivers

So as to assess which factors potentially play a role in determining the interannual variability of the aerosol-induced surface temperature and precipitation change signal, some relatively simple correlation analyses are carried out comparing the JJAS seasonal mean simulated surface temperature and precipitation changes with four features known to affect interannual variability of the southern African climate: the nino3.4 index of the El-Niño Southern Oscillation (ENSO) and seasonal average SSTs over the South Atlantic Ocean, South Indian Ocean and Tropical Indian Ocean. These features have all been shown to affect southern African climate variability to varying degrees [e.g. *Janowiak*, 1988; *Jury et al.,* 2004; *Reason et al.,* 2006; *Washington and Preston,* 2006; *Jury*, 2009].

The DJF (December-February) mean nino3.4 averages, calculated following Trenberth [1997], are used for comparison purposes since the ENSO signal over southern Africa is strongest during this season [*Reason et al.,* 2006]. The South Atlantic and South Indian Ocean SST regions are specified according to the work of Jury et al. [2004] and cover the areas of 12-32ºS, 45ºW-45ºE and 20-40ºS, 30-120ºE, respectively. The Tropical Indian Ocean SST region covers the area from 0-20ºS, 50-90ºE, following the analyses of Washington and Preston [2006]. Seasonal averages of the preceding austral autumn (MAM) are used in addition to the winter season (JJA) averages, since there is a known lag-time between atmosphere-ocean interactions.

	Nino3.4	S.Atl. (MAM)	S.Ind. (MAM)	T.Ind. (MAM)	S.Atl. (JJA)	S.Ind. (JJA)	T.Ind. (JJA)
EQ	0.04	-0.12	-0.10	-0.14	0.22	0.17	0.44
CW	-0.07	0.02	0.08	-0.14	-0.17	0.23	0
SW	-0.18	0.39	0.24	-0.16	0.12	0.20	-0.25
SE	-0.27	0.23	0.32	-0.02	0.07	0.46	-0.26
EC	-0.15	0.02	0.08	-0.27	-0.15	0.23	0.42
MA	0.17	0.07	-0.42	-0.32	0.02	-0.34	0.36

Table 5.3.3: Correlation coefficients between the JJAS seasonal average surface temperature difference (AERO-CTRL) and the nino3.4 index as well as sea surface temperatures averaged over the South Atlantic (S.Atl.), South Indian (S.Ind.) and Tropical Indian (T.Ind.) sea surface temperatures for the MAM and JJA seasons. Values highlighted in red are significant at the 95% level, while those highlighted in blue are significant at the 90% level.

The aerosol-induced surface temperature response is significantly correlated with the chosen climate indices in five out of the six sub-regions (at either the 90 or 95% levels; see table 5.3.3). Both the EQ and EC sub-regions are significantly positively related to the variability in JJA tropical Indian Ocean SST variability, while JJA south Indian Ocean SST variability appears to be associated with the surface temperature signal in the SE sub-region. The SST averages of the preceding MAM season in this region are also negatively related with the surface temperature changes in the MA sub-region, while the south Atlantic MAM SST averages are positively correlated with those simulated in the SW sub-region. No significant correlation with the DJF nino3.4 index was found in any sub-region.

Significant correlations between the simulated aerosol-induced precipitation changes and the climate drivers investigated are found only in the SW and SE sub-regions, which are significantly correlated with MAM average south Atlantic and JJA average south Indian SSTs, respectively (see table 5.3.4). In both cases the relationships are negative, indicating that warmer SSTs are associated with aerosol-induced decreases in precipitation.

	Nino3.4	S.Atl. (MAM)	S.Ind. (MAM)	T.Ind. (MAM)	S.Atl. (JJA)	S.Ind. (JJA)	T.Ind. (JJA)
EQ	-0.06	0.05	0.05	0.11	-0.20	-0.30	-0.02
CW	0.32	-0.11	0.03	0.28	-0.05	-0.13	0.16
SW	0.12	-0.44	-0.06	0.21	-0.20	-0.02	0.02
SE	-0.23	-0.37	-0.31	-0.13	-0.30	-0.46	0.12
EC	0.28	-0.12	-0.03	0.17	0.15	-0.16	0.11
MA	-0.08	0	-0.34	-0.17	0	0.08	-0.04

Table 5.3.4: Correlation coefficients between the JJAS seasonal average precipitation difference (AERO-CTRL) and the nino3.4 index as well as sea surface temperatures averaged over the South Atlantic (S.Atl.), South Indian (S.Ind.) and Tropical Indian (T.Ind.) for the MAM and JJA seasons. Values highlighted in red are significant at the 95% level, while those highlighted in blue are significant at the 90% level.

Correlations in terms of both simulated surface temperature and precipitation changes are significant only in the SW and SE sub-regions, lending confidence to the idea that there is indeed a real relationship between simulated aerosol-climate impacts and the effect of SST variability in these sub-regions. In the SW sub-region there is a positive (negative) correlation between temperature (precipitation) and MAM South Atlantic SSTs, suggesting that increased SSTs result in greater (smaller) magnitude aerosol-induced temperature (precipitation) changes. In the SE sub-region correlations between JJA average South Indian SSTs and aerosol-induced temperature and precipitation changes are negative.

It is, however, important to bear in mind that significant differences between the AERO and CTRL simulations are found only in the EQ and CW sub-regions in terms of surface temperature, and only in the EQ sub-region in terms of precipitation changes. Thus, the relationships found in all other sub-regions are to be regarded with considerable caution and further exploration of the interannual variability of simulated aerosol-climate impacts would need to be carried out to elucidate the physical mechanisms possibly influencing these patterns. This investigation provides only a very basic analysis of the possible links between aerosol-climate impacts and the interannual variability of these interactions as a consequence of large-scale regional climate variability. It is likely that internal model variability also plays a role in the year-to-year differences exhibited in the aerosol-induced seasonal signal, although this is unlikely to account for all of the interannual variability presented.

5.4 Synoptic variability of aerosol-climate impacts

5.4.1 Self-Organising Maps

During analysis it was noted that the simulated aerosol-climate impacts varied from day to day, depending on the large-scale meteorological conditions. To investigate this further a Self-Organising Map (SOM) [*Kohonen,* 1995] is used. This technique classifies input data into a predefined number of reference patterns or modes using an unsupervised artificial neural network. The patterns produced are essentially generalised states, but the given number of states is fully representative of the input data. The main advantages of the SOM technique are that it can be applied to nonlinear data (such as the continuum of atmospheric conditions) and it does not force orthogonality (as for example in principal component analysis (PCA)). In addition, the results can be directly physically interpreted, unlike, for example the PCA approach which produces patterns of variance rather than direct physical states of the atmosphere.

Although the SOM technique is relatively new to the field of climatology, it has been used successfully in a number of climate studies [e.g. *Crane and Hewitson,* 1998; *Cavazos*, 2000; *Reusch et al.,* 2005a]. In an idealised comparison study, Reusch et al. [2005b] found that SOMs were more robust, isolated predefined patterns and attributed variance more accurately than a rotated principal component analysis (PCA). It is important to note, though, that SOMs are not an "optimal" clustering technique, since they produce clusters of roughly equal size. However, since the SOM approach treats the input data as a continuum, which is more representative of the nature of synoptic conditions, this technique is considered to be most appropriate for our purposes.

5.4.2 Applying the SOM technique over southern Africa

For this study a SOM is applied to the daily average ERA-40 reanalysis data used as lateral boundary conditions. All days from the 20 austral winter (JJA) seasons for the period 1982-2001 are used (a total of 1840 days). Six different meteorological variables are used in order to separate the data into different synoptic types: sea level pressure, potential temperature at the surface, 700hPa relative humidity (RH), 700hPa u-wind, 700hPa v-wind and 500hPa geopotential height. Prior to the application of the SOM, a varimax rotated PCA is carried out in order to reduce dimensionality, using model values for all six variables. Three principal components (PCs) are retained, representing 84.3% of the data variability, and these data are then introduced into the SOM. Since Tyson and Preston-Whyte [2000] categorised South African weather systems into six main "types", it was decided that a 12-node SOM would adequately represent the expected synoptic conditions over the region. Sang et al. [2008] tested various SOM sizes over southern Africa and also deemed a 12-node SOM adequate to represent the large-scale circulation patterns of the region.

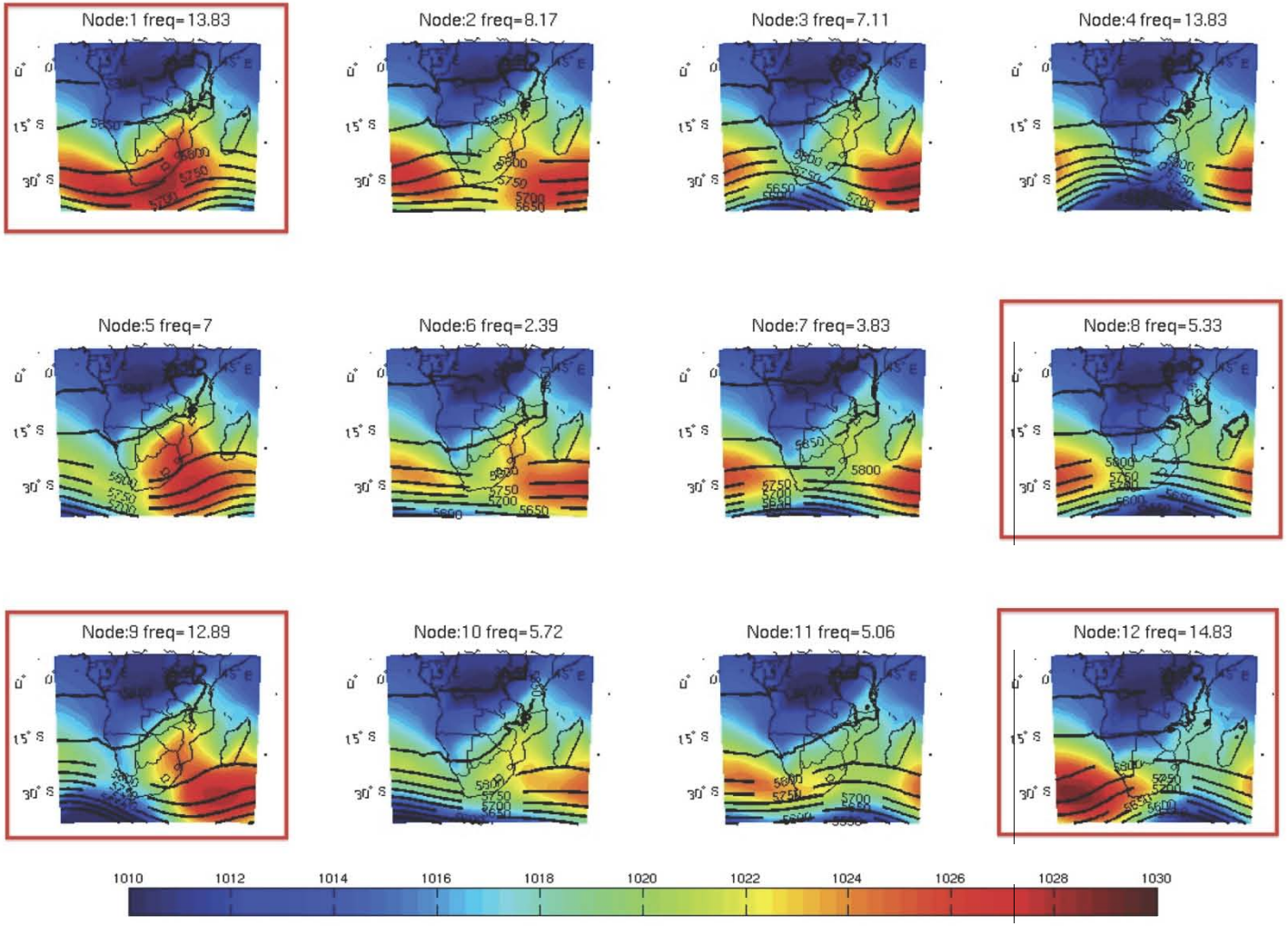

Figure 5.4.1 : JJA average sea level pressure in hPa (colours) and 500hPa geopotential heights (contours) for each of the 12 SOM nodes (CTRL simulation).

The CTRL simulation average sea-level pressure and 500hPa geopotential heights (GPH), and the 700hPa GPH and winds for each of the 12 nodes are shown in figures 5.4.1 and 5.4.2 respectively. The model daily averages for each of the nodes indicates that the SOM analysis was successful, with a clear separation between the different synoptic types evident. According to how a SOM works, the four corner nodes (nodes 1, 4, 9 and 12) are the most different from each other, with the nodes in between representative of the continuum between the corner "extremes". In both figures it is clear that this is the case.

In order to focus the analysis, four of the twelve SOM nodes are chosen, since this provides an overview of the most important results. Three of the four corner nodes are chosen (nodes 1, 9 and 12) as well as node 8 (highlighted by the red boxes in fig. 5.4.1. and 5.4.2). Although node 8 is not a corner node, this node better represents a low-pressure frontal system situated directly over southern Africa than node 4, which depicts such a system slightly to the south west, still approaching the subcontinent. These nodes are also chosen for their importance in terms of the corresponding simulated atmospheric aerosol burdens (see fig. 5.4.3). A brief description of each of the four nodes investigated follows.

Node 1 represents a strong high-pressure system centred over the subcontinent, which is clearly evident in the 700hPa GPH and winds (fig. 5.4.2). Westerly flow occurs in the most southerly latitudes of the domain, but over most of southern Africa anticyclonic conditions prevail with high surface pressure, particularly over South Africa. Over the 20-year period from 1982 to 2001 this node occurs approximately 13.83% of all austral winter days. Node 8 represents quite opposite conditions, with a low-pressure system situated over the southern parts of the subcontinent and high-pressures over the adjacent Atlantic and Indian Oceans. This node occurs less frequently than the other corner nodes, occurring 5.33% of all days. Nodes 9 and 12 essentially represent the 'before' and 'after' conditions of node 8. In node 9 a low pressure is situated to the south-west over the Atlantic Ocean approaching southern Africa, while in node 12 this westerly wave has already passed over the region and is situated to the south-east over the Indian Ocean. These two nodes occur 12.89% and 14.83% of all winter days, respectively. Offshore circulation from the subcontinent towards the south east occurs in the latter three nodes (8, 9 and 12), but to varying degrees depending on the position of the low pressure system relative to the continental land mass.

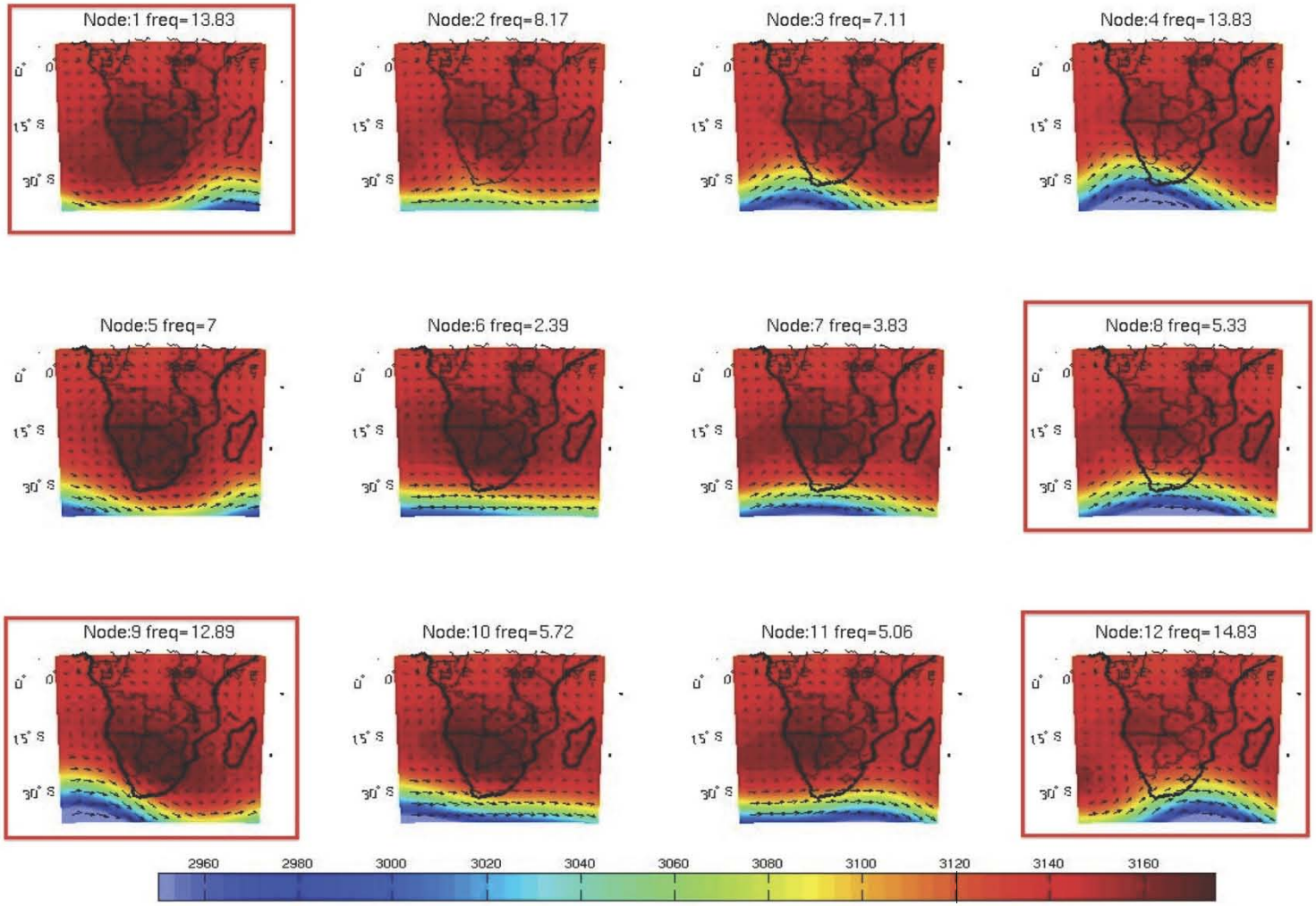

Figure 5.4.2 : JJA average 700hPa geopotential heights (colours) and winds (arrows) for each of the 12 SOM nodes (CTRL simulation).

5.4.3 Synoptic aerosol optical depth variability

The average meteorological conditions strongly influence the atmospheric aerosol loading. This can clearly be seen in figure 5.4.3, which shows the average aerosol optical depth (AOD) for all days allocated to each of the four nodes of interest. High AOD occurs under all synoptic types in the main biomass burning regions between 0-10ºS, 15-30ºE, since emission of these aerosol varies only on a month-by-month basis as specified in the emissions inventory, rather than in association with large-scale synoptic conditions. The offshore transport of these aerosol towards the Atlantic Ocean does, however, vary somewhat under the different synoptic conditions. Highest AOD off the coast of Angola (between approximately 5-15ºS) is associated with the circulation patterns typical of both nodes 1 and 8, since low-level easterly winds are strongest for these two nodes (see fig. 5.4.2). Least offshore transport occurs for node 12 when the high-pressure system over the northern parts of the subcontinent is shifted eastwards and flow tends to result in more southward transport instead.

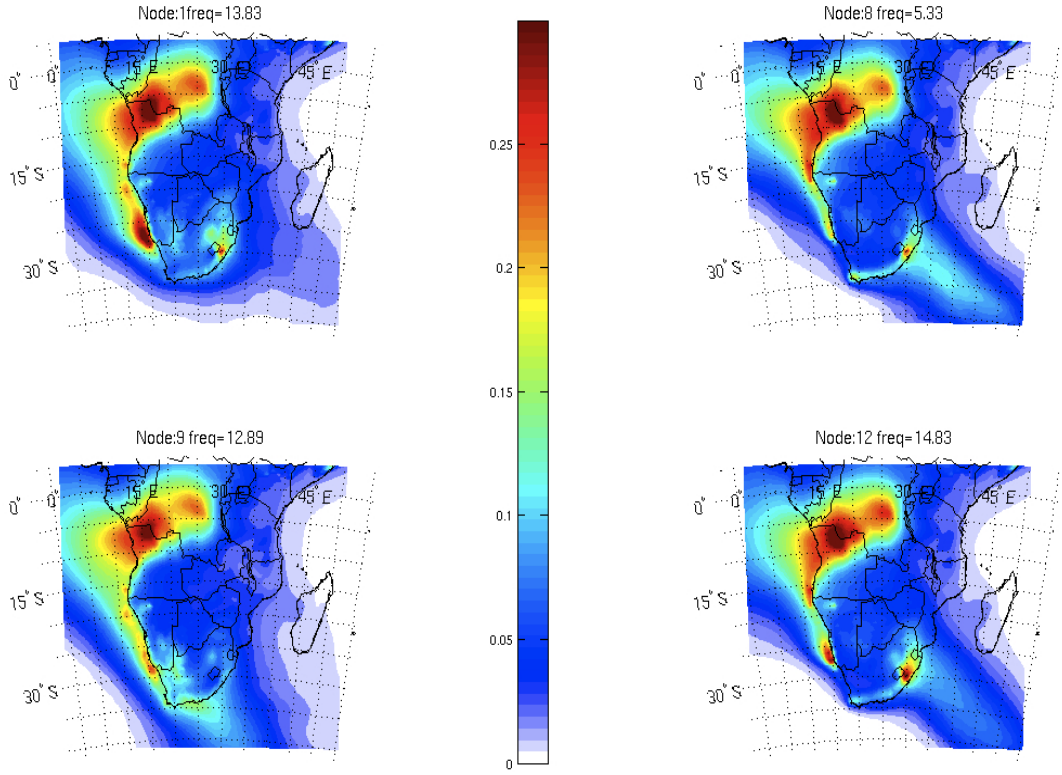

Figure 5.4.3: JJA average Aerosol Optical Depth (AOD) for all days assigned to node 1 (top left), node 8 (top right), node 9 (bottom left) and node 12 (bottom right). The node frequency is shown above each plot.

South of 15ºS simulated AOD varies considerably more between nodes since these regions are more affected by the mid-latitude westerly waves which appear to contribute most to synoptic-scale climate variability over the subcontinent. Largest difference between synoptic types are again most obvious over the oceanic regions, just off the west coast of Namibia (~15-30ºS) as well as in the main Indian Ocean aerosol outflow region (between 25-40ºS, 20-40ºE).

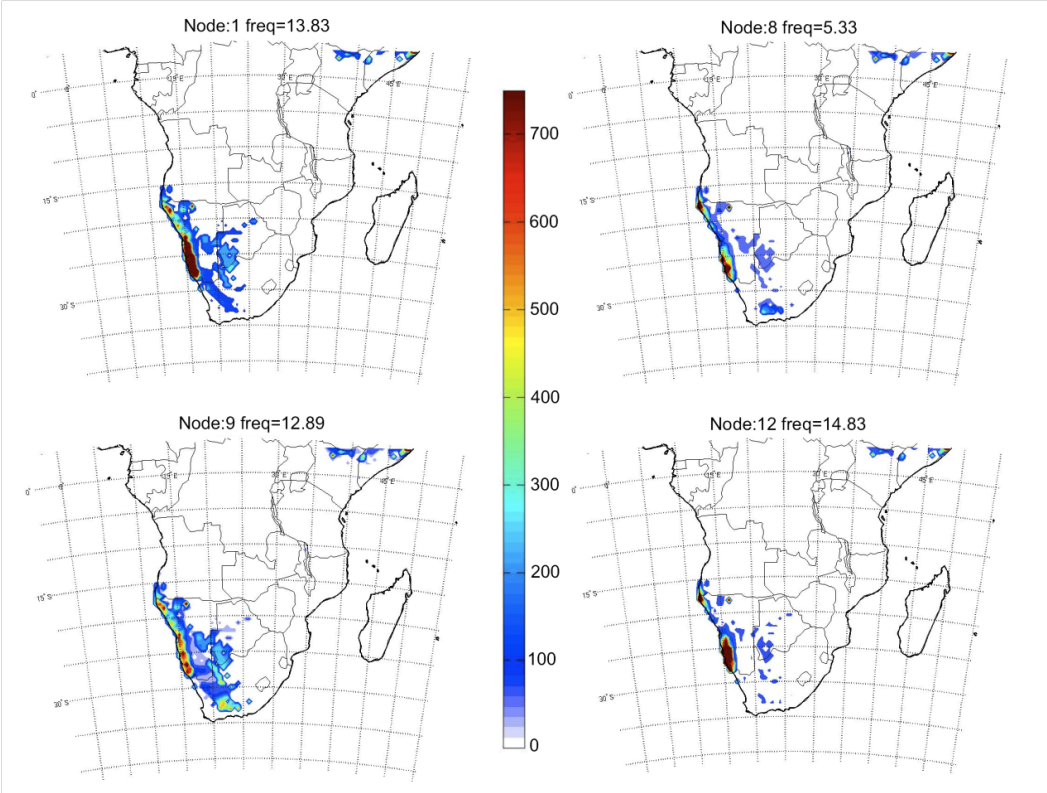

Figure 5.4.4: JJA average dust emissions (in mg/m^2/day) for all days assigned to node 1 (top left), node 8 (top right), node 9 (bottom left) and node 12 (bottom right). The node frequency is shown above each plot.

AOD variability off the coast of Namibia is regulated to a large extent by emission of mineral dust aerosol (fig. 5.4.4), which in turn is largely controlled by surface wind speeds and soil moisture [*Alfaro et al.,* 1998; *Prospero et al.,* 2002]. Highest dust emissions are associated with the dry anticyclonic conditions of node 1, and this is reflected in the high AOD observed along the entire Namibian coast. Dust emissions are also high for nodes 9 and 12, but more of these aerosol are transported to the south east and back over South Africa in the dominant north-westerly winds associated with the passing low-pressure systems. Although the presence of the high-pressure system over the Atlantic Ocean in node 12 favours offshore transport of dust, production of these aerosol is more limited than under the dry anticyclonic conditions dominant for node 1. This is likely a result of the precipitation associated with the

recent passage of the frontal system (which for node 12 is still present over the Indian Ocean), which would serve to increase soil moisture and thus decrease the potential for dust emissions.

Although anthropogenic aerosol emissions from the South African Highveld region (centred near 28ºS, 28ºE) are constant for all days, the AOD variability over this region and in the Indian Ocean outflow plume varies strongly according to synoptic type. Under the anticyclonic conditions of node 1 almost no south-westward transport occurs and instead aerosols from the region accumulate and are recirculated back over the subcontinent. In contrast, under the synoptic conditions typical of nodes 8, 9 and 12 the regional aerosol loading, including the aerosol from the Highveld industrial sources, are clearly transported offshore towards the south west Indian Ocean.

The Indian Ocean outflow plume shifts position depending on the relative position of the low-pressure system. As the front approaches the subcontinent (node 9) the plume exits from the southeastern tip of the subcontinent. Under these conditions, more aerosol from both the Namibian dust and sub-tropical biomass burning source regions appear to be transported southwards in the predominant north-westerly flow, producing relatively high AOD's over much of the western half of South Africa. Formenti et al. [2002] observed similar AOD signals at Sutherland, a remote rural site in western South Africa, where AOD was found to vary from day to day depending on the circulation patterns, but was highest when flow was from the north west.

The Indian Ocean outflow plume is most discrete when the frontal system is situated directly over the subcontinent (node 8), with a very clear and narrow band of high AOD exiting the subcontinent near 30ºS, 30ºE. According to Piketh et al. [1999a] this is effectively the 'climatological' position of this plume. Offshore transport is not as strong once the low-pressure has passed over the subcontinent (node 12) and as a result the AOD within the plume is lower. The ridging anticyclone following the frontal system for node 12 means that more aerosol are recirculated over southern Africa, and only aerosol from the eastern parts of the region are transported offshore to the south-west Indian Ocean.

5.4.4 Simulated radiative forcing variability

The variability of AOD with synoptic type obviously influences the variability of radiative forcing both at the surface and top-of-atmosphere (TOA). As for the seasonal average (fig. 5.2.1(a)), the highest surface RF occurs in the main biomass burning regions of northern Angola and southern DRC, reaching up to -30W/m^2 and varying little between synoptic types (fig. 5.4.5(a)). Surface RF does, however, vary considerably more in the southern parts of the

domain as a result of the variability in AOD (which in turn is a consequence of variability in aerosol transport patterns and dust production, as explained above). Maximum negative surface RF occurs off the West Coast under anticyclonic conditions (node 1), reaching up to -20W/m^2, while it is minimum when a low-pressure westerly wave is situated directly over the south of the subcontinent (node 8). Perhaps more obvious is the variability over the Indian Ocean, where the signal of the main aerosol outflow plume is clear and surface RF in this region reaches up to -10W/m^2 for nodes 8, 9 and 12. In contrast, for node 1 there is no significant surface RF at all over this region.

The simulated TOA RF is, in general, also fairly similar to the seasonal average (see fig. 5.3.1(b)), although there are clear differences between the synoptic types represented by the four nodes (fig. 5.4.5(b)). As for the surface RF, the strong impact of dust can be seen off the west coast of Namibia and Angola, where the region of strongest negative TOA RF occurs. This signal reflects the simulated dust concentrations almost exactly (not shown). Under the anticyclonic conditions of node 1, when dust emission is highest, TOA RF reaches up to -8W/m^2 in a large band between ~20-30ºS. For the other nodes, the TOA RF only reaches up to -6W/m^2 and generally only over a smaller area as well.

As for the JJAS average, biomass burning aerosol appear to have relatively little impact on the TOA RF over the subtropical regions of the subcontinent (between ~5-20ºS), no matter what the dominant circulation type, since the positive TOA forcing of atmospheric absorption effectively cancels out the negative forcing induced by scattering. Over the equatorial regions the TOA RF is slightly negative (up to -2W/m^2), but again does not vary according to circulation patterns since the aerosol loading varies relatively little on the synoptic timescale. As at the surface, the TOA RF signal over the Indian Ocean varies considerably according to synoptic type and is most negative when the plume is clearest (nodes 8 and 12), when TOA RF reaches -4W/m^2.

It is important to note again that no diagnostic for whole-sky radiative forcing is available in the version of RegCM3 used in this study. The consideration of the simulated aerosol radiative impacts under whole-sky conditions would certainly be of interest in terms of this type of synoptic-scale investigation, and this feature will be looked into in future studies.

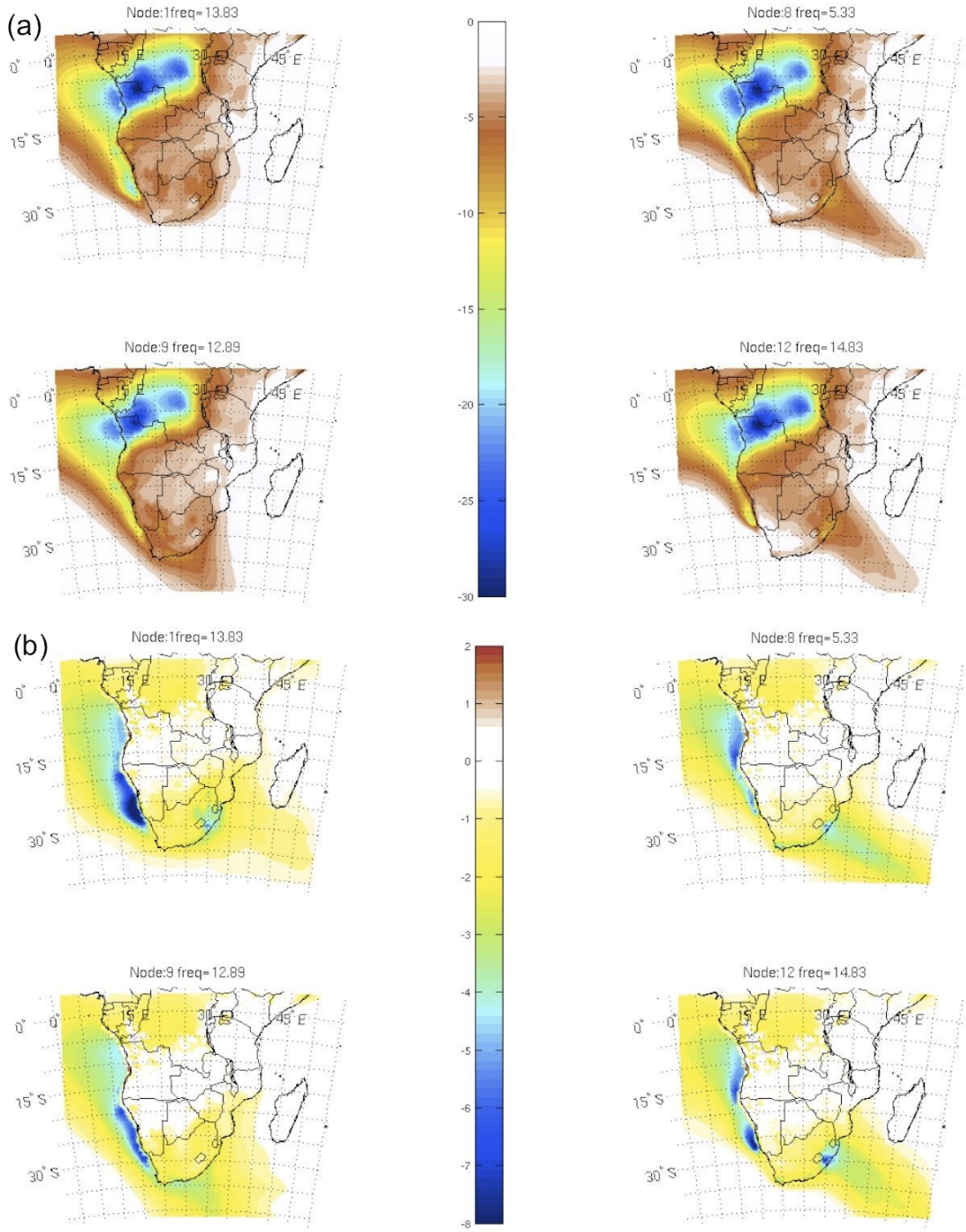

Figure 5.4.5: JJA average radiative forcing at (a) the surface and (b) the top-of-atmosphere for all days assigned to node 1 (top left), node 8 (top right), node 9 (bottom left) and node 12 (bottom right). The node frequency is shown above each plot. Radiative forcing is shown in W/m^2.

5.4.5 Synoptic variability of surface impacts

On the synoptic timescale the strong negative surface RF results in significant decreases in surface temperature (fig. 5.4.6). However, this cooling signal is restricted to the main biomass burning regions and thus varies relatively little with synoptic type (since, as mentioned

previously there is little synoptic variability in terms of surface RF in this area). Interestingly, as was observed in terms of the seasonal average, the region of greatest surface cooling is displaced northwards compared to the regions of maximum AOD and surface RF. This suggests that the surface cooling is also strongly influenced by changes in other factors, such as increased latent heat fluxes which affect the surface energy budget (see the ensuing discussion regarding the simulated changes in precipitation, section 5.4.7).

Significant changes in surface circulation patterns occur mainly only over the Atlantic Ocean between 0-15ºS. As for the seasonal average signal, the biomass burning aerosol loading results in stabilisation of the lower atmosphere (through warming at altitude and surface cooling), which in turn induces increased surface pressure and divergent flow out of the main burning regions. However, at the synoptic timescale this signal varies relatively little between nodes since, as already mentioned, there is comparatively little synoptic variability in simulated AOD and RF in this area.

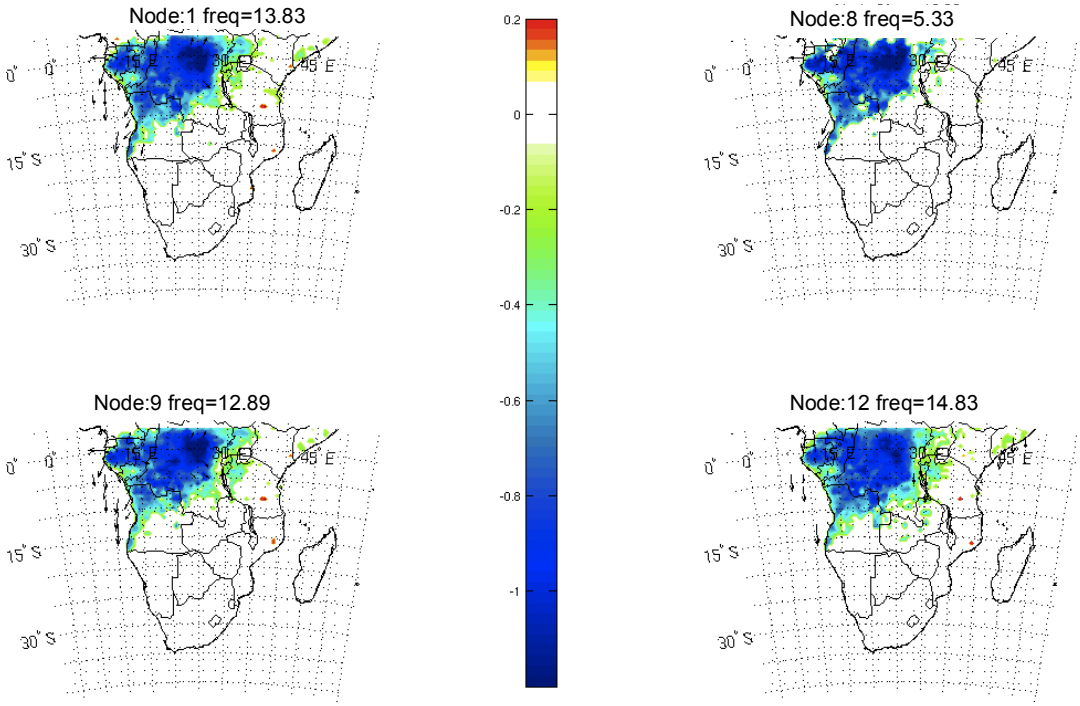

Figure 5.4.6: JJA average aerosol-induced changes in surface temperature (colours) and surface winds (vectors) for all days assigned to node 1 (top left), node 8 (top right), node 9 (bottom left) and node 12 (bottom right). The node frequency is shown above each plot and only the regions where changes are significant (at the 95% level) are shown. Surface temperature difference is expressed in ºC.

5.4.6 Variability of atmospheric dynamics and precipitation changes

As already presented in section 5.2 (and section 4.4), seasonal average aerosol-induced dynamical changes are evident largely only in the equatorial regions. On the synoptic timescale similar results are found, with the simulated aerosol loading affecting cloud liquid water path (CLWP) and precipitation significantly only between 5ºN-5ºS (see fig. 5.4.7 and 5.4.8). Irrespective of the large-scale circulation patterns the elevated heat-pump (EHP) mechanism appears to be induced, resulting in increased CLWP both above and below the main aerosol layer (see section 5.2.3 for a full explanation of these processes) as well as increased precipitation (by up to approximately 40% compared to the CTRL). This is largely to be expected, however, since synoptic variability in the tropical regions is low, and as shown above (fig. 5.4.3) there is little associated variability in AOD in the equatorial latitudes. Although only the cross-section from 12-25ºE is presented here, similar results are apparent in the longitude band between 25-45ºE, indicating that the EHP mechanism is induced throughout the tropics and on all days investigated.

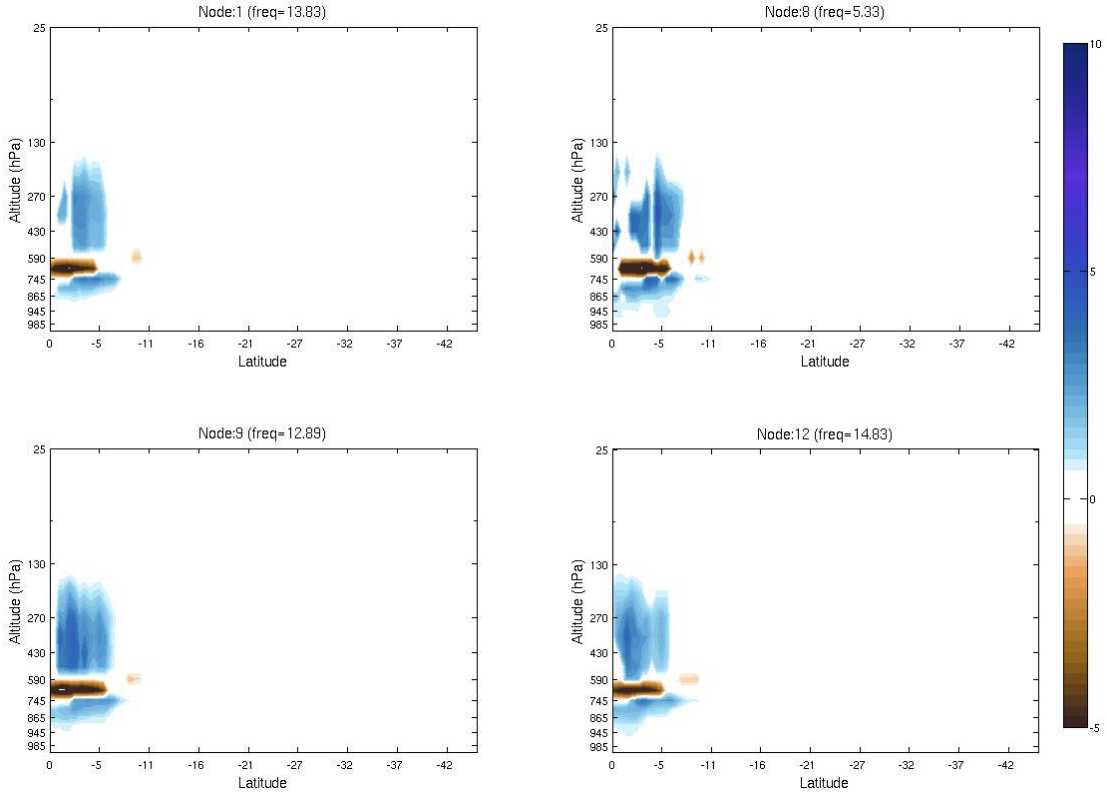

Figure 5.4.7: Latitudinal vertical profile of JJA average aerosol-induced changes in cloud liquid water path (CLWP) averaged over the longitude band 12-25ºE for all days assigned to node 1 (top left), node 8 (top right), node 9 (bottom left) and node 12 (bottom right). The node frequency is shown above each plot and only the regions where changes are significant (at the 95% level) are shown. The change in CLWP is expressed in g/m^2.

South of approximately 5ºS the stable nature of the regional atmosphere means that even on the synoptic-scale there is little significant direct radiative effect on atmospheric dynamical processes and the regional hydrological cycle. Tummon et al. [2010] found that Indian Ocean aerosol outflow events affected the precipitation locally on the synoptic scale by enhancing baroclinicity along the leading edge of passing cold front systems. However, the aerosol loading in these simulations (using the BB-AMMA emissions) was considerably higher than those used here (again see table 5.1.1). Thus, in addition to the atmosphere being stable, it appears that the aerosol loading in the southern parts of the domain is too low to induce any significant effect, even in the main Indian Ocean aerosol outflow region.

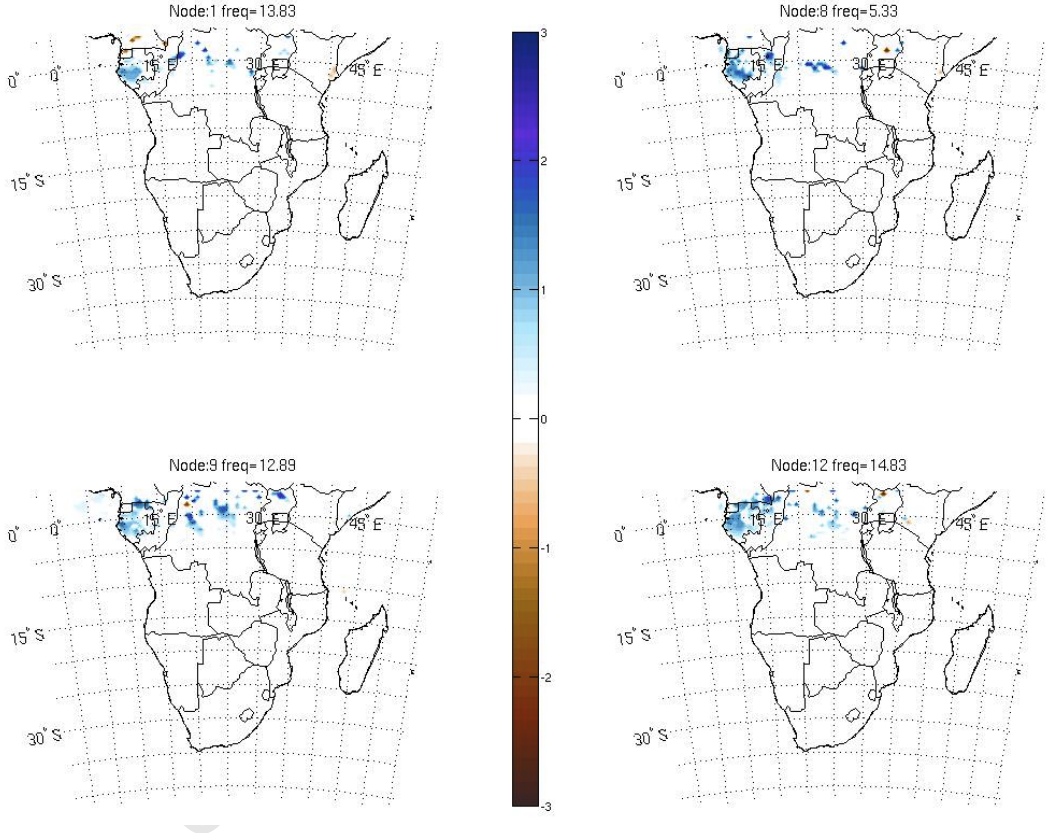

Figure 5.4.8: JJA average aerosol-induced changes in precipitation (in mm/day) for all days assigned to node 1 (top left), node 8 (top right), node 9 (bottom left) and node 12 (bottom right). The node frequency is shown above each plot and only the regions where changes are significant (at the 95% level) are shown.

5.5 Conclusions

RegCM3 is used to simulate twenty years of southern African climate from 1982-2001. The variability of direct and semi-direct aerosol effects are investigated at three different timescales: from the interannual, through seasonal to the synoptic scale.

The inclusion of the direct aerosol effect results in a strong negative surface radiative forcing (RF; up to -30W/m^2) in the main biomass burning regions of northern Angola and southern DRC. This corresponds to approximately half of the value obtained in the 6-year, BB-AMMA simulations of chapter four (up to -60W/m^2). Results suggest that there is a near linear relationship between emissions and simulated aerosol optical depth and surface radiative forcing – the greater the emissions the higher the AOD and greater the surface RF. At the top of the atmosphere (TOA) the relationship is somewhat less clear since the effect of the scattering anthropogenic aerosol included in these 20-year simulations affects the TOA RF significantly, particularly over South Africa.

On the seasonal scale, despite the lower aerosol loading, the simulated atmospheric aerosol burden affects the southern African regional climate is affected in a similar manner to that presented in the BB-AMMA simulations, only the magnitude of aerosol-induced changes is lower. Similar results were observed in the GFED test (see section 4.4.1), in which the lower biomass burning emissions of the GFED inventory resulted in weaker climatic impacts.

An investigation of the interannual variability of the JJAS seasonal average aerosol impacts on surface temperature and precipitation shows that significant differences between the control (CTRL) and aerosol (AERO) experiments are apparent only in the main biomass burning regions, where aerosol loading is high, and in the equatorial latitudes, where the atmosphere is conducive to aerosol-induced enhancement of convective activity. The seasonal average surface temperature decrease varies between -0.16 to -0.50ºC in the equatorial region, the equivalent of up to 150% of the interannual variability in this area. Importantly, accounting for the aerosol radiative effects improves the simulation of both the magnitude of seasonal average temperature and its year-to-year variability. In contrast, the simulation of precipitation is not improved, although no significant difference is apparent between the CTRL and AERO simulations outside of the equatorial region (largely since this is the only area where precipitation occrus during the JJAS season). Simple correlation analyses showed some association between simulated aerosol-climate impacts and regional climate SSTs. There is a potential relationship between simulated aerosol-induced surface temperature and precipitation changes and SSTs in the south west and south east of the domain, while no significant correlation was found between interannual variability of these changes and ENSO. The results of these analyses are, however, to be regarded with considerable caution since correlation does not imply that there is a real relationship between the two factors and further investigation of the mechanisms controlling the interannual variability of the simulated aerosol-climate impacts is required.

A self-organising map (SOM) is applied to daily average data for the twenty austral winter seasons simulated. In terms of simulated AOD and RF, the largest differences between synoptic types is observed in the sub-tropics and mid-latitude regions where synoptic

variability in meteorological conditions affects dust emissions as well as aerosol transport and deposition processes most significantly. AOD and mineral dust production is highest over the subcontinent under high pressure conditions, agreeing with observations that suggest that such conditions result in aerosol recirculation and accumulation over southern Africa [e.g. *Formenti et al.,* 2001; *Swap et al.,* 2003]. With the passage of a mid-latitude westerly wave the regional atmosphere is swept clean and aerosol outflow towards the Indian Ocean occurs. Such outflow is strongest when a low-pressure system is situated directly over the subcontinent but is observed to occur to some extent on most days when no high pressure is present over southern Africa. South of approximately 10ºS, the simulated aerosol loading results in relatively little significant change to either atmospheric circulation patterns or the regional hydrological cycle. This is largely a consequence of the dry and stable nature of the atmosphere in this region during the austral winter season, since atmospheric instability is necessary to amplify the simulated aerosol impacts. In addition, the aerosol loading is relatively weak in these experiments and thus the aerosol-climate impacts outside of the main biomass burning regions are not as strong as in the BB-AMMA simulations. The tropical regions (5ºN-5ºS) appear to be affected more strongly by the magnitude of emissions, which vary largely on a seasonal basis rather than on the synoptic timescale. The elevated heat pump effect appears to be initiated on most days, irrespective of the prevailing synoptic type and as a result convective precipitation increases in this latitude band.

In summary, uncertainty in aerosol emissions estimates appears to have a much larger impact on simulated aerosol-climate impacts than any other factor investigated. Aerosol-induced changes at the surface and within the regional atmosphere are significant only in the equatorial regions, despite variability of AOD and RF being largest in the sub-tropics and mid-latitudes. This does not imply, however, that there are no local aerosol-climate impacts over the southern parts of the region and aerosol may affect urban microclimates or weather systems during intense aerosol events. A higher resolution model and inventory would be necessary to investigate these features in more detail.

CHAPTER 6

Synthesis and perspectives

6.1 Synthesis of results

The main goal of this thesis is to investigate the direct and semi-direct aerosol effects on the southern African regional climate during the austral winter season. This work presents one of the first regional climate modelling studies of these impacts and sets out to address the following objectives:

- to evaluate the internal variability within RegCM3 and determine the model sensitivity to various parameters associated with the online aerosol module;
- to assess the ability of RegCM3 to reproduce southern African regional climate, especially the seasonal atmospheric aerosol characteristics;
- to evaluate the simulated direct and semi-direct aerosol effects on the regional climate during the austral winter and to explore the sensitivity of model simulated aerosol-climate impacts in response to various aerosol emissions inventories and an induced sea surface temperature-feedback; and
- to investigate the aerosol-climate impacts at different time scales, ranging from the interannual to the synoptic scale.

These objectives are addressed within a coupled aerosol-climate modelling framework, making use of the regional climate model RegCM3 in combination with several aerosol

emissions inventories. The model is configured for the southern African domain and run at a horizontal resolution of 60km with 18 levels in the vertical.

6.1.1 Objective One

A comprehensive suite of short-term (two-year) simulations is carried out to assess the sensitivity of RegCM3 to aerosol emission and deposition parameters. Model sensitivity to these parameters is, on average, low, particularly to those used to describe aerosol deposition and biomass burning injection height (which is restricted to within the boundary layer). This is of considerable importance given the relatively large uncertainty still associated with experimental observations of these factors and their parameterisation in the online aerosol module. Internal model variability is also assessed through an ensemble of seven simulations covering the same two-year period. RegCM3 exhibits only a small degree of internal variability, a signal that does not appear to be large enough to either strongly affect or mask the model simulation if perturbed, for example, by aerosol radiative forcing. We attempt to reduce the model 'noise' signal by carrying out ensemble simulations, investigating only the mean of these ensembles.

6.1.2 Objective two

Six-year ensemble simulations are carried out using the biomass burning inventory of Liousse et al. [2010] to assess the ability of RegCM3 to reproduce the southern African climate and atmospheric aerosol characteristics from 2001 to 2006. Results from these simulations are also used to provide an estimate of direct and semi-direct aerosol radiative effects on the regional climate during the austral winter season (JJAS). In addition, a set of ensemble simulations is carried out using a simple adjustment of SST depending on AOD, so as to assess the effect of aerosol-SST feedbacks on the simulated radiative forcing and resultant climatic impacts. Finally, a simulation covering the same period but using the GFEDv2 biomass burning emissions [*van der Werf et al.,* 2006] is also carried out to assess the model sensitivity to a different emissions inventory and to provide an estimate of the range of uncertainty associated with the corresponding simulated aerosol-climate impacts.

The model produced realistic surface temperature, precipitation and cloud cover fields. Bias in terms of these meteorological variables is found to be largely within the limits of uncertainty associated with the available observations as well as within the range of bias shown in other state-of-the-art regional climate models. The RegCM3 representation of the southern African aerosol loading during the austral winter season (JJAS) is found to be very sensitive to the particular choice of biomass burning emission inventory, varying by up to a factor of two in response to the factor of two difference in magnitude between the inventories investigated. Comparison with ground-based AERONET observations as well as MODIS and MISR satellite retrievals indicate that simulations with the BB-AMMA biomass burning inventory

[*Liousse et al.,* 2010] produced the most accurate representation of AOD during the JJAS season. In contrast, AOD was significantly underestimated in simulations incorporating the GFED inventory. Furthermore, a significant discrepancy in terms of the timing of peak AOD is noted. The simulated AOD maximum generally occurs one to two months prior to both ground-based and remote sensing observations. Again, this appears to be strongly, but not exclusively, related to the biomass burning emissions inventories, with peak AOD generally simulated during the month of maximum emission. Importantly, this error is apparent no matter which biomass burning inventory is used.

6.1.3 Objective three

Twenty-year simulations incorporating the historical decadal average biomass burning emissions inventories of Mieville et al. [2010] are carried out covering the period 1982-2001. Results from these simulations are used investigate the aerosol-climate impacts on various time-scales (ranging from the synoptic to the interannual) and also to assess the model sensitivity of the JJAS seasonal average aerosol-climate impacts to a third biomass burning inventory. This latter reason is particularly of importance given the long time period for which these emissions are available (1900-2005) and the possibility this provides for century-long investigations of aerosol-climate interactions on a global scale as well as over southern Africa in particular.

The simulated JJAS atmospheric aerosol loading results in strong negative surface RF, ranging from -25 to -60W/m^2, for the Mieville et al. [2010] and Liousse et al. [2010] inventories respectively. This results in decreased surface temperature (compared to a case with no aerosol radiative forcing) and tends to induce a reduction in surface turbulent fluxes over the southern African subcontinent. Importantly, including the direct and semi-direct aerosol radiative effects significantly reduces the REGCM3 simulated surface temperature bias over the western half of southern Africa. These results suggest that the inclusion of aerosol results in a better representation of climate over southern Africa, and that the aerosol component should be considered in modelling studies of the region. As a consequence of the strongly absorbing nature of biomass burning aerosols, diabatic atmospheric warming is also induced. Heating is maximum at the top of the simulated aerosol layer in the main biomass burning source regions and ranges from 0.3 to 1.2ºC/day, again depending on the emissions inventory utilised.

The simulated surface cooling and heating at altitude stabilises the lower troposphere below approximately 700hPa. In the equatorial regions, where atmospheric conditions are conducive to convection, stability is, however, reduced above the aerosol layer and an elevated heat pump effect [cf. *Lau et al.,* 2006, 2009] is induced. Deep convection is enhanced and precipitation increases by between 0.5-2mm/day (equivalent of up to 40%)

within the tropical latitudes between 5ºN-8ºS. Despite the strong surface and atmospheric forcing, little enhancement of convection or precipitation is apparent over the rest of southern Africa, since, climatologically, the atmosphere in this region is very stable and little or no rainfall occurs during the JJAS season. Consequently, the inclusion of the direct and semi-direct aerosol effects has relatively little impact on precipitation bias over most of the region.

The JJAS seasonal average simulated aerosol optical depth (AOD), radiative forcing (RF) and climatic impacts ranges by approximately a factor of two in direct response to the factor of two difference between the inventories tested. These significant differences highlight the large uncertainty still associated with present biomass burning emissions estimates and, as a consequence, the considerable uncertainty that also remains regarding the climatic impacts of the regional aerosol loading.

6.1.4 Objective four

On the interannual timescale JJAS seasonal average aerosol-induced surface temperature changes vary between -0.5 to +0.1°C depending on the region and year (representing up to 120% of the simulated interannual variability as measured by the standard deviation). In terms of precipitation, JJAS seasonal average aerosol-induced changes vary more significantly from year to year. Rainfall changes ranged from +0.4 to -0.07mm/day, again depending on the region, reflecting changes of up to 100% of the simulated interannual variability.

To further investigate the simulated aerosol-climate impacts, a self-organising map (SOM) is applied to characterise the variability of simulated aerosol-climate impacts according to typical large-scale circulation patterns at the synoptic timescale. Despite significant differences in atmospheric circulation types associated with different synoptic conditions, simulated AOD varies relatively little in the main biomass burning regions since the AOD in these regions is largely controlled by emissions, which are fixed on a monthly basis. It is only in the southern, mid-latitude regions of the domain that simulated AOD is strongly sensitive to the large-scale circulation patterns since the AOD in the southern parts of the subcontinent is mainly controlled by long-range transport. Aerosol outflow towards the Indian Ocean is induced with the passage of a low-pressure system in the westerlies to the south of the domain, while aerosol accumulation and recirculation was observed under high pressure conditions. However, as a result of the low AOD in the southern parts of the region, few significant aerosol-climate impacts are observed. It is only in the equatorial regions where AOD is high enough to induce significant impacts. Since biomass burning, which contributes most of the AOD in the JJAS season, varies relatively little in these areas on the daily scale the simulated aerosol-climate impacts vary relatively little between synoptic types. The simulated radiative

forcing, surface temperature, circulation and precipitation changes are thus relatively similar on all days.

6.1.5 Summary

Considering these results in the context of the main objectives of this work, it can be concluded that:

2 RegCM3 coupled with a relatively simple online aerosol module reproduces the southern African regional climate well, both in terms of meteorological and aerosol characteristics;

3 the simulated direct and semi-direct aerosol effects have a strong impact on regional climate during the austral winter biomass burning season, with the simulated reduction in surface temperature improving model bias;

4 large variability in terms of these impacts is evident in response to different biomass burning inventories, with the magnitude of emissions estimates ranging by up to a factor of two, or greater, resulting in a similar doubling of ranges in the simulated climatic response;

5 although the magnitude of model aerosol-climate response varies depending on the biomass burning emissions inventory used, the sign of change is consistent in all cases;

6 on the interannual time-scale, JJAS seasonal average aerosol-climate impacts vary considerably from year to year, particularly in terms of simulated precipitation changes. In some years the aerosol-induced changes exceed the magnitude of simulated interannual variability, but mainly only in the tropical regions. In contrast, relatively little difference between simulated aerosol-climate impacts is observed at the daily scale;

6.2 Discussion and Perspectives

6.2.1 Caveats and assumptions to be considered

This study provides an initial step towards quantifying the impact of the direct and semi-direct aerosol effects on the southern African regional climate. However, the results need to be considered within the context of the limits, uncertainty and caveats associated with any modelling study, particularly in terms of how they relate to the real environment and climate.

Firstly, the large uncertainty associated with estimates of the magnitude of biomass burning aerosol emissions, which ranges by over a factor of two, will need to be reduced before the radiative impact of the regional aerosol burden can be more accurately assessed. In addition, the discrepancy exhibited between RegCM3 and available observations in terms of the timing

of peak AOD will also need to be eliminated. An accurate representation of the seasonality of aerosol loading is vital particularly for the investigation of aerosol-climate impacts during the transition from dry to wet season in October to November. Studies in other sub-tropical regions have shown that the regional aerosol burden may reinforce the dry season rainfall pattern [e.g. *Zhang et al.,* 2009]. No investigation of the aerosol impacts in these months has been carried out here, but such an analysis would be of considerable importance given that much of the southern African regional population is still largely dependent on rain-fed subsistence agriculture and the timing of the start of these rains. Of particular interest would be the potential role of aerosols affecting soil moisture content, which may lead to differences in rainfall later in the wet season.

No testing of aerosol optical properties is carried out in this work, however, properties such as single scattering albedo can have significant impact on the simulated radiative forcing and associated climatic impacts. Further tests focused on various aerosol optical parameters would allow a better estimation of the range of uncertainty associated with these properties and serve to provide a degree of the range of possible climatic impacts. To this end, additional observational measurements of aerosol optical properties would be very useful as constraints for model simulations.

Also, RegCM3 does not include a detailed cloud-microphysics scheme (e.g. including a proper ice-phase scheme) and thus the indirect aerosol effect cannot be adequately represented. This factor played a large role in the decision to focus on just the dry, austral winter season, when cloud cover and rainfall are minimal over southern Africa and the aerosol indirect effect is likely to provide only a minor contribution to the overall aerosol radiative forcing. However, the inclusion of this effect may affect the RegCM response in the equatorial regions, where the simulated hydrological cycle was found to be sensitive to the direct and semi-direct aerosol radiative effects, particularly in terms of soil moisture and precipitation (see above).

In addition, RegCM3 represents aerosol-chemistry processes very simply. A more complex online aerosol module including other radiatively important species such as ozone and nitrates, internal aerosol mixtures as well as a more refined convective transport and scavenging parameterisation and the inclusion of longwave aerosol effects would certainly serve to provide a more realistic representation of the regional aerosol loading and it's radiative impacts. These developments are ongoing in the RegCM community and some of these features have already been included in the newest version, RegCM4, released in July 2010.

Finally, the biomass burning aerosol emissions are prescribed throughout this work, thus there is no climatic control on the rate of burning and aerosol emissions. Although the

integration of an interactive vegetation-fire-climate module into RegCM would certainly be very complex, simulations with such a model would allow a far more complete assessment of the role played by each component and the interactions between them on various time scales.

6.2.2 Perspectives

The work carried out in this thesis could be complemented by more in-depth investigations of several features. Firstly, the version of RegCM3 used in this study does not include aerosol radiative forcing on the sea surface temperature (SST). Although a sensitivity test carried out using a relatively simple SST adjustment suggests that this aerosol surface cooling effect is relatively minimal, the only way to confirm this premise would be through the application of a coupled regional atmosphere-ocean model. The development of these models has only very recently come to a fore, and RegCM3 has just been coupled to the ROMS ocean model [*Ratham et al.,* 2009]. A study investigating the nature of the aerosol radiative impacts and feedbacks on the regional SSTs would certainly provide some interesting insight into the coupling of the atmosphere-aerosol-ocean system over southern Africa.

Secondly, RegCM3 has also recently been coupled to a new, far more comprehensive land surface scheme [CLM3; *Steiner et al.,* 2009]. Further exploration of the impacts of the regional aerosol loading on vegetation and land surface change, deep soil moisture content as well as the impacts of variability of these features on aerosol emissions and associated radiative forcing (through surface albedo) would also contribute to our understanding of the complex inter-relationships between aerosol-vegetation-land surface interactions over southern Africa.

Thirdly, it would be very informative to evaluate the role of the each type of aerosol (black carbon, organic carbon, mineral dust, sulphates, etc) individually on the southern African regional climate. Also, simulations comparing anthropogenic and natural aerosol emissions would be useful to estimate the contribution of each source to the simulated radiative forcing and climatic impacts. Better estimates of the climate-influence of each species and source may aid policy makers target specific aerosols or sources in terms of developing climate change mitigation strategies for the subcontinent.

Finally, the potential future impacts of aerosol on the southern African climate have been barely investigated in the literature, at least within the context of regional climate modelling studies. Various aerosol emission scenarios are available and it would be of great interest to explore the possible role of aerosols under future climate conditions since they may act either to mitigate or enhance the anthropogenic climate change signal. This is particularly important

over southern Africa given the region's vulnerability to climatic variability and change as well as its relatively limited ability to cope and adapt to such changes.

The chain of responses and feedbacks on climate by atmospheric aerosol is just beginning to be more completely understood. At the regional level, the study of these interactions on the climatic timescale is still in its infancy and a large degree of uncertainty is associated not only with our empirical understanding of these processes, but also particularly in terms of their implementation within climate models. Within this context, this work provides one of the very first estimates of the direct and semi-direct aerosol effects over southern Africa, using a coupled regional aerosol-climate model. Enormous scope for further research over southern Africa exists, particularly pertaining to the seasonality of aerosol-climate interactions as well as aerosol-surface-ocean and vegetation feedbacks.

Appendix A

A.1 RegCM3 domain sensitivity over southern Africa

Regional Climate models (RCMs) tend to be sensitive to both the size and position of the domain simulated [*Seth and Giorgi*, 1998]. Several factors need to be taken into account when choosing the 'best' domain. Firstly, it is important that the major features driving climate in the region of interest are included in the domain. Secondly, the domain needs to be large enough to allow the development of internal model mesoscale circulation. It is advisable, however, not to have too big a domain, since the lateral boundary conditions provide a means to limit the divergence of the RCM solution from the lateral forcing fields [*Giorgi and Bi*, 2000]. This is particularly the case when using reanalysis data as boundary conditions, since these data provide a relatively realistic representation of the atmosphere. Finally, computational restraints also need to be kept in mind, since the larger the domain the more resources required.

A.1.1 Experiment set-up

As regards southern Africa, previous studies have shown that simulations focused on the region should include Madagascar, since the island and the surrounding ocean regions significantly influence the moisture flux from to the subcontinent. The island also appears to affect the migration of cyclonic-like vortices over the region, which are linked to important precipitation events in the region [*Landman et al.*, 2005]. All domains used in this work tested thus include the Madagascan region.

Three different domain sizes are tested: for simplicity's sake termed large, medium and small. The small domain essentially covers only the main area of interest, extending from approximately 4ºN-42ºS and 0-56ºE. This domain does not cover the entire latitude band through which the Inter-Tropical Convergence Zone (ITCZ) ranges, so another somewhat larger domain that does cover this region is tested. The medium domain, covering the region from 18ºN-43ºS, 4ºW-60ºE, is larger in all directions to allow greater internal freedom of the model solution.

Two slight variations of this domain are tested, one using the NCEP-II reanalysis [*Kanamitsu et al.* 2002] and another using the ERA40 Reanalysis [*Uppala et al.,* 2005] as lateral boundary conditions. The reanalyses are produced using different models and data assimilation schemes, and variation between the two datasets reflects a degree of the

uncertainty still associated with our knowledge of the historical state of the atmosphere. Each reanalysis has been shown to have various advantages and biases [*Troccoli and Kallberg*, 2004; *Betts and Jakob*, 2002; *Uppala et al.,* 2005; *Afiesimama et al., 2006*]. For example, although the ERA40 reanalysis was found to represent humidity, surface temperature and precipitation better than the NCEP-II product, in terms of the interannual variability of these variables, the NCEP-II reanalysis compared better to observations [*Betts et al.*, 2006]. Model sensitivity to lateral boundary forcing is particularly important over Africa, where fewer observations exist to restrain the reanalyses and there is greater divergence between the two products.

	Small	**Med-NCEP**	**Med-ERA**	**Large**
Max. latitude	7.22ºN	17.39ºN	19.07ºN	28.53ºN
Min. latitude	43.08ºS	44.34ºS	42.85ºS	55.41ºS
Min. longitude	2.50ºW	6.50ºW	12.44ºW	28.43ºW
Max. longitude	59.14ºE	61.12ºE	61.05ºE	69.07ºE
No. grid points	94x94	118x106	118x118	166x142
L.B. Conditions	NCEP-II	NCEP-II	ERA40	NCEP-II

Table A.1.1: Properties of each domain tested, including maximum and minimum longitudes, number of grid points as well as the reanalysis dataset used for lateral boundary (L.B.) conditions. All domains were run with 60km horizontal resolution.

Finally, a very large domain is tested, covering nearly the entire African continent, from approximately 26ºN-54ºS, 19ºW-67º. This domain is tested largely to investigate whether the extension of the lateral boundaries further away from the region of interest would strongly affect the model solution. In addition, the 'roaring forties' region of the Southern Ocean is included in this domain to test whether the model produces better results over the southernmost areas of the subcontinent, which is affected by cyclonic disturbances generated and transported in the strong westerly winds that occur in this region [*Tyson and Preston-Whyte*, 2000]. The latitudinal and longitudinal extent of each domain as well as the number of grid points and lateral boundary conditions used in each test is presented in table A.1.1. All tests are integrated over a two-year period from January 2001 to December 2002.

Three basic climate variables for which observations are available, surface temperature, precipitation and cloud cover, are used to compare model biases between the various domain sizes. Circulation patterns are compared to the NCEP-II reanalysis dataset since no direct observations of winds are available as a gridded product for the period and region of interest. Averages for the four meteorological seasons starting March-May 2001 (MAM), June-August 2001 (JJA), September-November 2001 (SON) and for December 2001-February 2002 (DJF)

are presented. The following three sections discuss these comparisons. Although certain model biases will be presented, the main aim of these sections is to compare the model solution over different domains rather than to highlight each and every bias observed.

A.1.2 Surface temperature

Seasonal average simulated surface temperatures are compared to the Climate Research Unit (CRU) observational dataset [*Mitchell et al.*, 2004; see section 4.2.1 for a full description]. Over all domains RegCM3 appears to overestimate temperature over the western half of southern Africa, whilst underestimating temperature along the east coast of the subcontinent, a pattern that is apparent for all seasons (fig. A.1.1). The magnitude of positive and negative biases is also similar between seasons, ranging between ±1-4ºC.

In an attempt to more objectively quantify the differences between the domains tested, the bias for each domain is averaged over the region common to all tests, the small domain (effectively the main region of interest in this study). In all seasons and for all tests the model shows consistent negative surface temperature biases compared to the CRU observations (see table A.1.2). Bias ranges from -1.53ºC to -0.11ºC, with the largest bias exhibited in all domains for the austral spring season (MAM). The smallest bias occurs during the austral autumn (SON) for all domains except the large domain, for which the smallest bias is shown in winter (JJA). Over the small domain region, the Med-ERA test performs best, although the bias of the small domain is also very similar. It must be noted that since bias is averaged over a relatively large area, positive and negative bias may cancel out. However, since the spatial patterns of bias are quite similar between domains the comparison between domains still seems valuable. No domain is statistically different from the CRU observations (at the 95% level; table A.1.2).

	Small	Med-NCEP2	Med-ERA40	Large
MAM	-1.07	-0.19	-1.29	-1.75
JJA	-0.24	-0.14	-0.28	-0.28
SON	-0.16	+0.70	-0.11	-0.47
DJF	-0.41	+0.36	-0.18	-0.64
p-value	0.6443	0.3688	0.7292	0.5411

Table A.1.2: Seasonal average surface temperature bias (in ºC) compared to the CRU observations (land area only). Bias for all four domains is averaged over the area of the small domain in order to facilitate comparison between domains. The p-value from a two-tailed Student's t-test is also given (highlighted in red if significant at the 95% level).

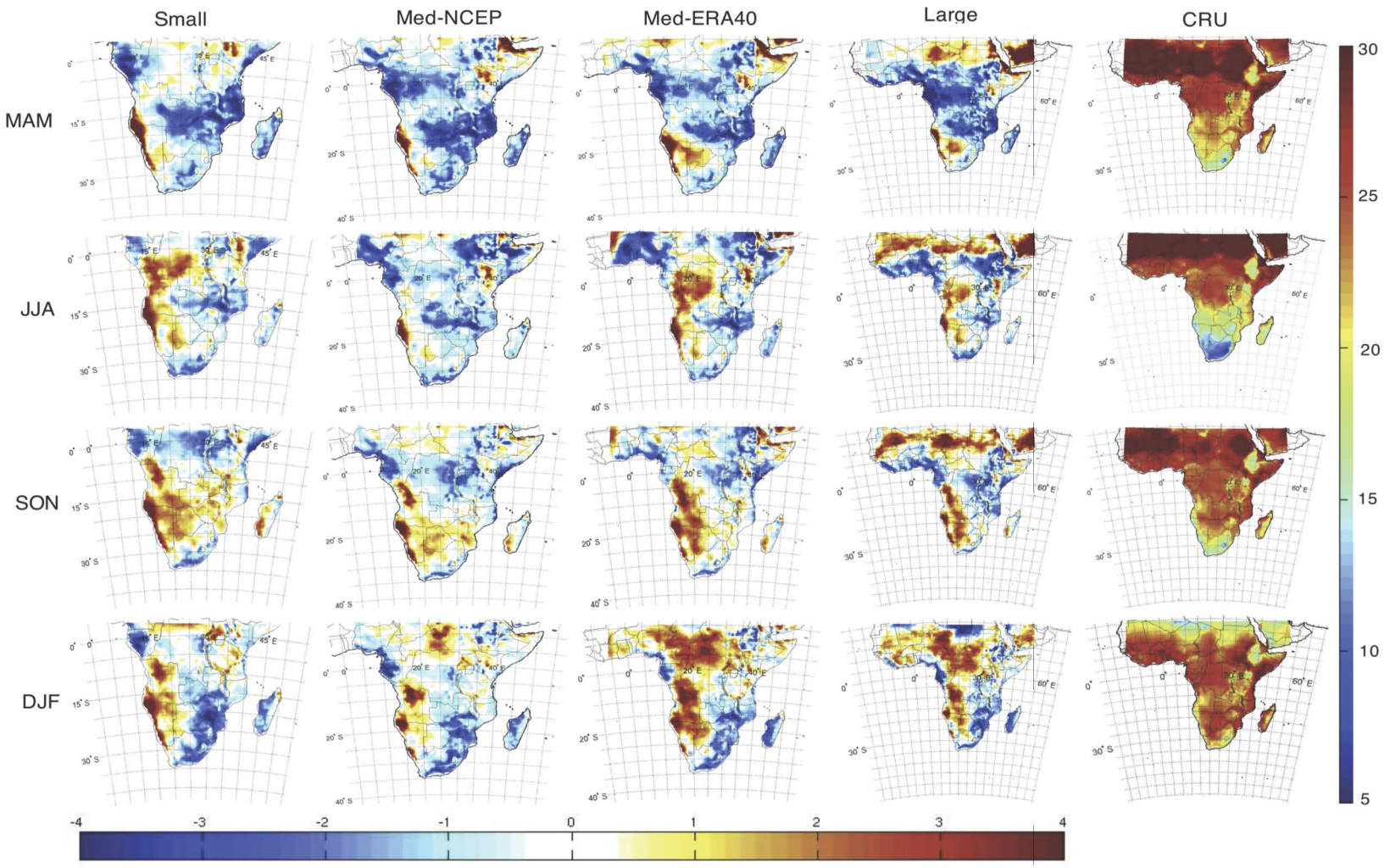

Figure A.1.1: Seasonal average surface temperature bias for all four domain tests (Small, Med-NCEP, Med-ERA40, Large; shown left to right) and the CRU observations from which these biases were calculated. All temperatures are shown in ºC.

In general, comparing the model simulated and CRU surface temperatures for the four seasons, it is clear that the model captures the observed patterns relatively well in all seasons. And, more importantly, bias appears to be relatively independent of the domain size and lateral boundary position. The bias exhibited falls well into the range of bias observed in other state-of-the-art RCMs [e.g. *Giorgi et al.*, 1998; *Hudson and Jones*, 2002b; *Tadross et al.*, 2006].

A.1.2 Precipitation

Simulated precipitation is compared to the TRMM 3B43 product [*Adler et al.,* 2000; as described in section 4.3.2]. Precipitation bias appears to be almost as consistent between domains as surface temperature, although in comparison to the surface temperature signal the spatial precipitation bias varies considerably more between seasons (fig. A.1.2). In general, the model appears to overestimate rainfall in the region of the Inter-Tropical Convergence Zone (ITCZ). This feature is best seen in the large domain, where the seasonal migration of the ITCZ is apparent in the positive precipitation biases shifting from its most northerly position (~5-15ºN) in the northern hemisphere rainy season (JJA) to its most southerly position (~10-20ºS, 20-40ºE) during the peak southern hemisphere rainy season (DJF). Precipitation is also overestimated in regions of high orography, such as the Ethiopian Highlands (if included in the domain) and the South African Drakensberg range, during their respective rainy seasons. As mentioned previously, this seems to be an artefact of most RCMs and is possibly related to the overestimation of vertical velocity in these regions [*Joubert et al.,* 1999].

To a certain extent the simulated precipitation bias corresponds to the model surface temperature bias, since surface temperature is underestimated (overestimated) in regions where precipitation is overestimated (underestimated). This is likely in part due to the bias induced by insufficient (excessive) rates of latent heat flux resulting from underestimated (overestimated) precipitation. Other factors, such as surface albedo and cloud cover may also affect surface temperature, however, and it is likely that the surface temperature bias exhibited is linked to several features. As a general tendency over all domains, the model appears to be too cool, with too much precipitation.

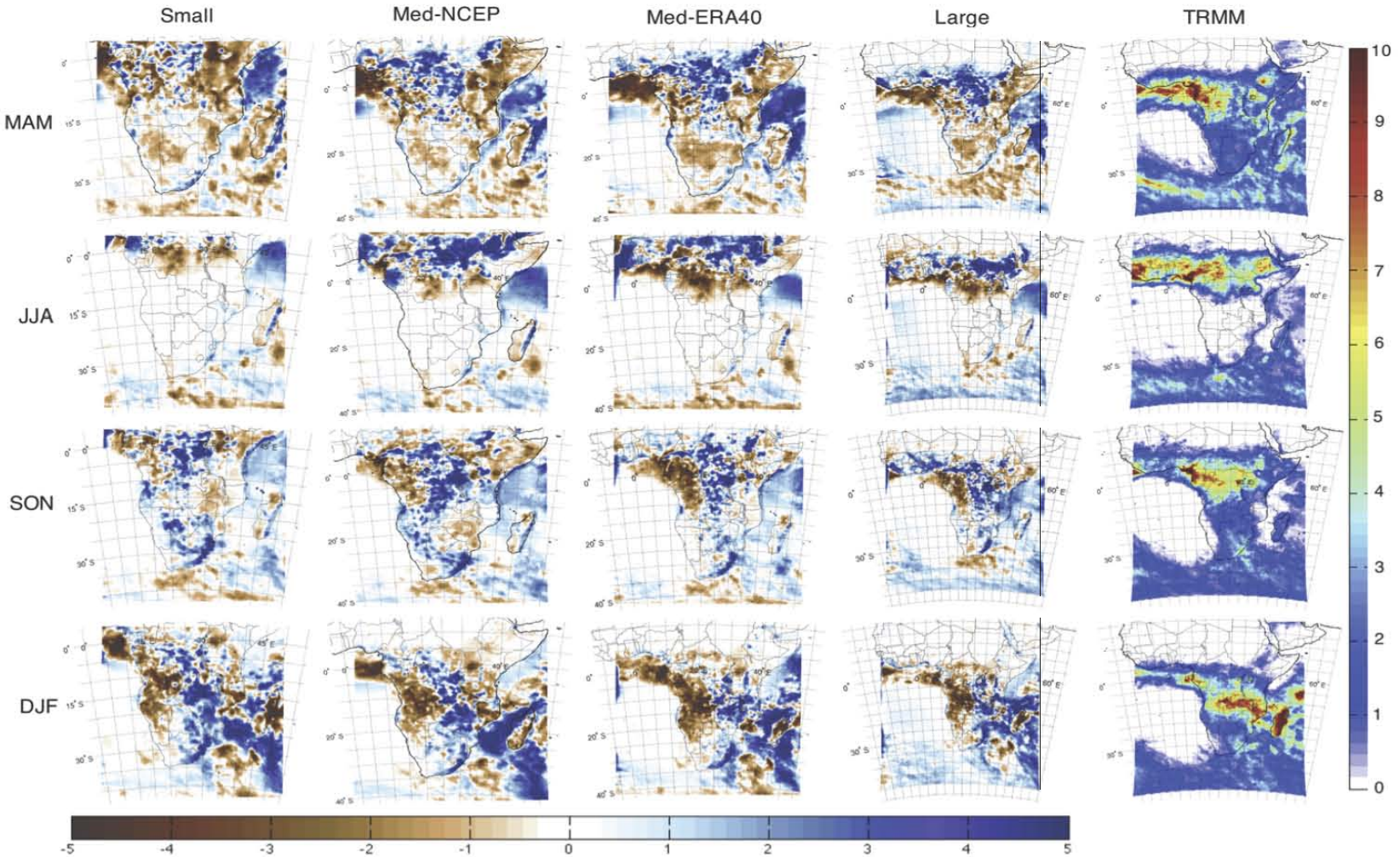

Figure A.1.2: Seasonal average precipitation bias for all four domain tests (Small, Med-NCEP, Med-ERA40, Large; shown left to right) and the TRMM observations from which these biases were calculated. All averages are shown in mm/day.

The seasonal precipitation bias averaged over the small domain region is shown in table A.1.3. Precipitation is overestimated in nearly all tests and all seasons. It is only over the small domain during MAM and in the Med-NCEP2 test during MAM, SON and DJF that precipitation is underestimated (ranging by -3.88% to -44.2% compared to the TRMM observations). The large domain performed best overall, suggesting that the internal model dynamics of RegCM3 are relatively accurate, and also that better results are obtained when the full ITCZ region is included in the domain simulated. The med-ERA domain performs second best, with total annual precipitation bias being only slightly larger than that of the large domain. As discussed above, the ERA40 reanalysis is suspected to improve upon the NCEP-II dataset in some respects [*Betts et al.*, 2006], and this is possibly why the Med-ERA simulation performs somewhat better than the Med-NCEP test in terms of the representation of precipitation.

	Small	**Med-NCEP2**	**Med-ERA40**	**Large**
MAM	-0.1 (-3.9)	-1.14 (-44.2)	+0.36 (+13.9)	0
JJA	+0.23 (+23.2)	+0.06 (+6.0)	0	+0.11 (+11.1)
SON	+0.61 (+33.9)	-0.28 (-15.6)	+0.53 (+29.4)	+0.62 (+34.4)
DJF	+0.54 (+19.6)	-0.74 (-26.9)	+0.71 (+25.8)	+0.54 (+19.6)
p-value	0.3931	0.2046	0.3075	0.3666

Table A.1.3: Seasonal average precipitation bias (in mm/day) compared to the TRMM observations (with % difference given in parentheses). Bias for all four domains is averaged over the area of the small domain (land and ocean) in order to facilitate comparison between domains. The p-value of a two-tailed Student's t-test is also given (highlighted in red if significant at the 95% level).

The seasonal average precipitation bias varies between -44.2% to +34.4% (or by less than ±1mm/day) and the simulated precipitation fields are relatively similar to observed patterns. Again, the observed biases are of similar magnitude to those exhibited in most other GCM and RCM experiments [e.g. *Giorgi et al.*, 1998; *Hudson and Jones*, 2002a,b; *Tadross et al.*, 2006].

A.1.3 Cloud Cover

Seasonal average cloud cover bias compared to the CRU observations is shown in figure A.1.3. Cloud cover tends to be significantly underestimated over much of Africa in all four seasons, except for over the horn of Africa and in the ITCZ region (when included in the domain) where cloud cover is slightly overestimated.

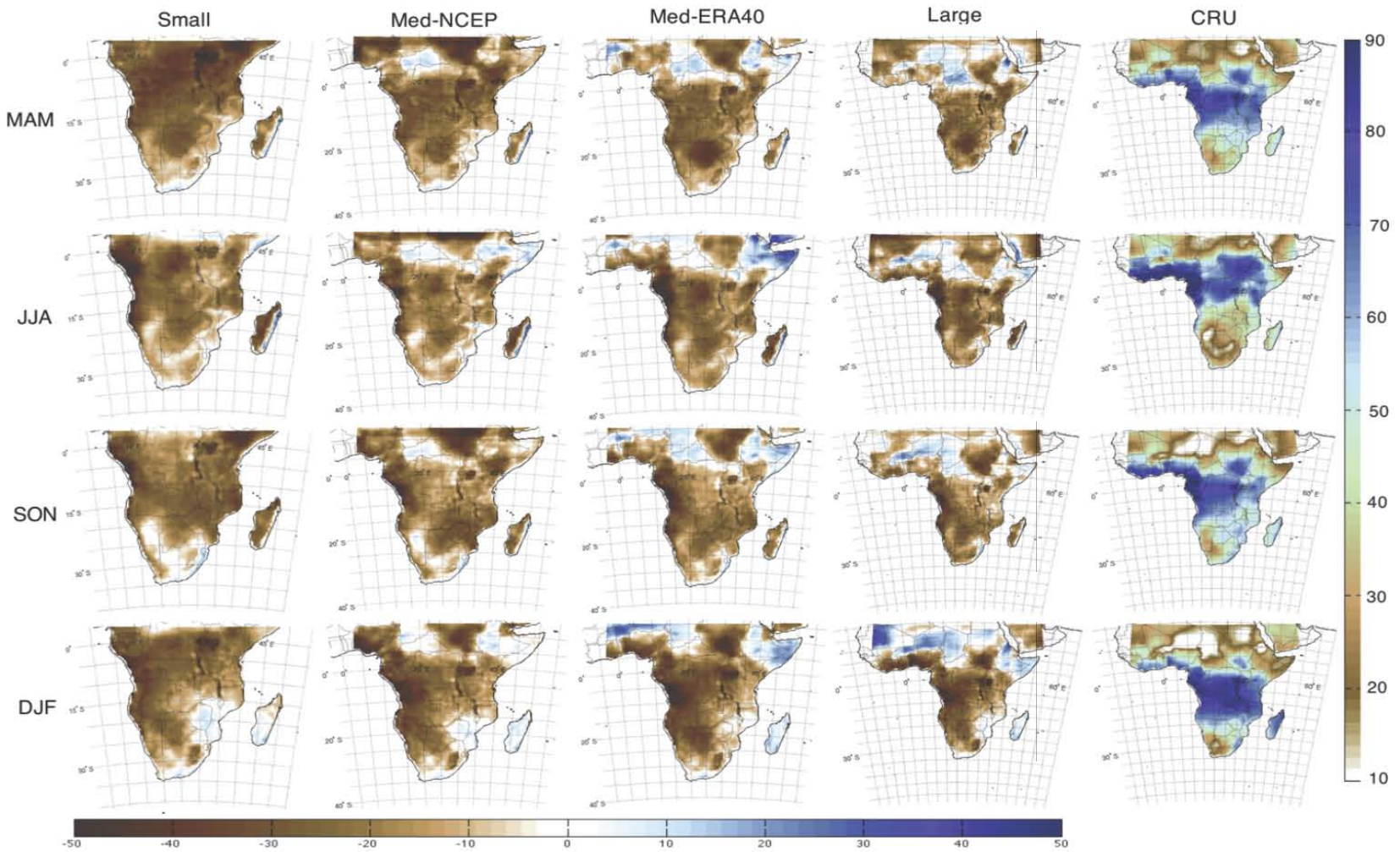

Figure A.1.3: Seasonal average cloud cover bias for all four domain tests (Small, Med-NCEP, Med-ERA40, Large; shown left to right) and the CRU observations from which these biases were calculated. All averages are shown in %.

Interestingly, the cloud cover bias does not correspond well with the simulated precipitation bias, since rainfall is both underestimated and overestimated in regions where there are strong negative cloud cover biases. For example, over southeastern Africa (between 0-15ºS, 20-45ºE), precipitation is overestimated in SON and DJF but mostly underestimated in MAM, while cloud cover biases remain negative in all seasons. This suggests that during the wet season (SON and DJF for this region) conversion of cloud water to precipitation occurs too rapidly (i.e. too much atmospheric moisture is rained out), while during the dry season the negative cloud cover and precipitation biases are more coherent, since not enough atmospheric moisture appears to be produced in the first place.

Seasonal average cloud cover is significantly different from the observations throughout the year and simulated bias is larger in terms of relative magnitude compared to both the surface temperature and precipitation signals (see table A.1.4). It is important to bear in mind that greater uncertainty is associated with the CRU cloud cover observations [*Mitchell et al.,* 2004], thus in reality, the model bias may not be as large as estimated here. However, accurately simulating cloud characteristics is difficult given the complexity of processes associated with these features and most climate models, whether regional or global, are renowned for having very large biases in terms of cloud cover patterns [*Lohmann and Feichter,* 2005; *Solomon et al.,* 2007]. Furthermore, RegCM3 lacks a cloud microphysics module, and this likely contributes to the problem of accurately representing clouds and precipitation processes.

	Small	Med-NCEP2	Med-ERA40	Large
MAM	-23.3	-6.97	-16.02	-16.27
JJA	-17.59	-13.32	-19.89	-20.63
SON	-21.57	-5.91	-18.36	0
DJF	-17.86	-0.29	-17.33	-16.15
p-value	0.0008	0.0037	0.0006	0.0009

Table A.1.4: Seasonal average cloud cover biases (in %) compared to the CRU observations (land area only). Bias for all four domains is averaged over the small domain area in order to facilitate comparison between tests. The p-value of a two-tailed Student's t-test is also given (highlighted in red if significant at the 95% level).

Most important in the context of these tests, is the fact that although simulated cloud cover patterns are significantly different from the observations, the differences between domains are relatively small. Again, it is to be noted, that there is greater uncertainty attached to the cloud cover observations, and this should be kept in mind when considering model performance in terms of the representation of clouds.

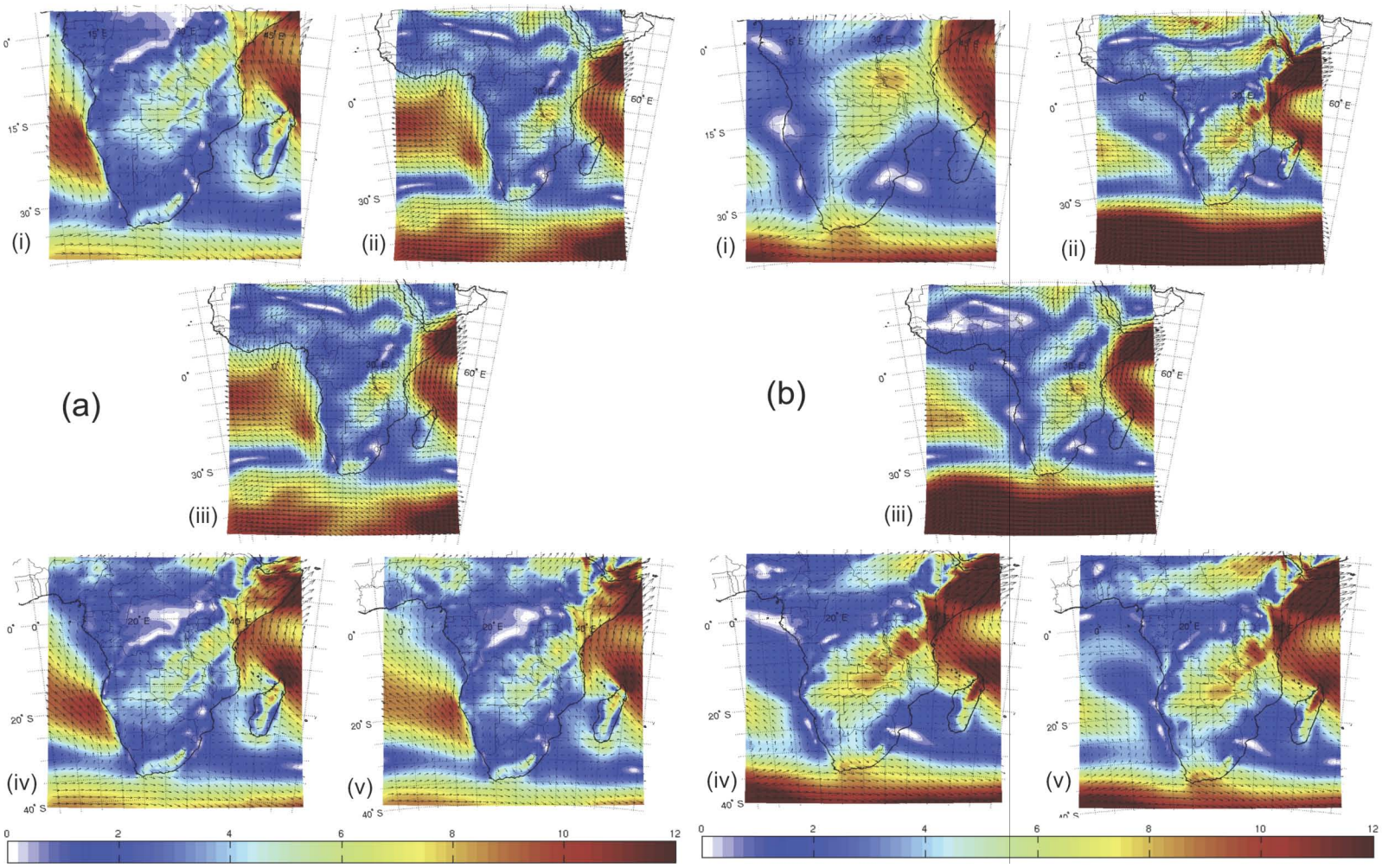

Figure **A.1.4**: JJA Seasonal average winds for the (i) Small, (ii) Large, (iii) NCEP observations, (iv) Med-NCEP and (v) MED-ERA domains at (a) 1000hPa and (b) 850hPa. Colours indicate the wind strength and arrows the wind vectors.

A.1.4 Circulation patterns

Seasonal average circulation patterns for two levels, 1000hPa and 850hPa, are shown for the austral winter (JJA) and summer (DJF) seasons in figures A.1.4 and A.1.5, respectively. These levels are chosen since aerosol concentrations are generally greatest in the lower troposphere and it is therefore essential that the dynamics of this region of the atmosphere, which control aerosol transport, are accurately represented. In addition, the lower troposphere is strongly influenced by land-atmosphere interactions and the representation thereof therefore gives an indirect indication of whether other related processes, such as sensible and latent heat fluxes, are also correctly simulated.

In general, the regional atmospheric circulation patterns are well represented by RegCM3 during both the JJA and DJF seasons. The anticyclonic high pressures systems over the Atlantic and South Indian oceans are well captured, particularly in terms of the position of their respective centres, although the magnitude of wind strength is slightly underestimated at 1000hPa over the Atlantic Ocean (by approximately 1m/s; fig. A.1.4(a) and A.1.5(a)). The strong westerly winds in the southern reaches of the domains are also well simulated in both seasons, as are the monsoonal winds of East Africa (south-westerly in JJA and north-easterly in DJF). During winter, the ITCZ (which only appears in the large domain since it is situated in the northern hemisphere) is well positioned, with converging winds near 16ºN at 1000hPa, similar to the NCEP-II reanalysis (fig. A.1.4(a)). During summer, the ITCZ is relatively well simulated over southern Africa, with convergence extending diagonally south-eastwards from approximately 5ºN, 15ºE to the southern reaches of Madagascar near 20ºS, 45ºE; while over West Africa the simulated ITCZ is situated approximately 2º too far north compared to the NCEP-II reanalysis.

It is mainly only in the equatorial regions that significant model bias is observed. In both seasons the model does not succeed in representing the cross-equatorial winds over central Africa between 5ºS-5ºN, 15-35ºE, where, compared to the NCEP-II reanalysis, the model underestimates wind speed by up to 2m/s in all four tests. These results confirm those of the previous sections (A.1.1-3), which also indicated that largest model bias is apparent in the tropics. This is relatively unsurprising though, since the convective dynamics of this area are highly parameterised in RegCM3.

The most important point to note, however, is that similar circulation pattern bias in the lower troposphere is exhibited over all four domains tested. Sensitivity to domain size and lateral boundary forcing within RegCM3 therefore does not appear to strongly impact the model solution, even in the equatorial regions where mesoscale convective activity is dominant.

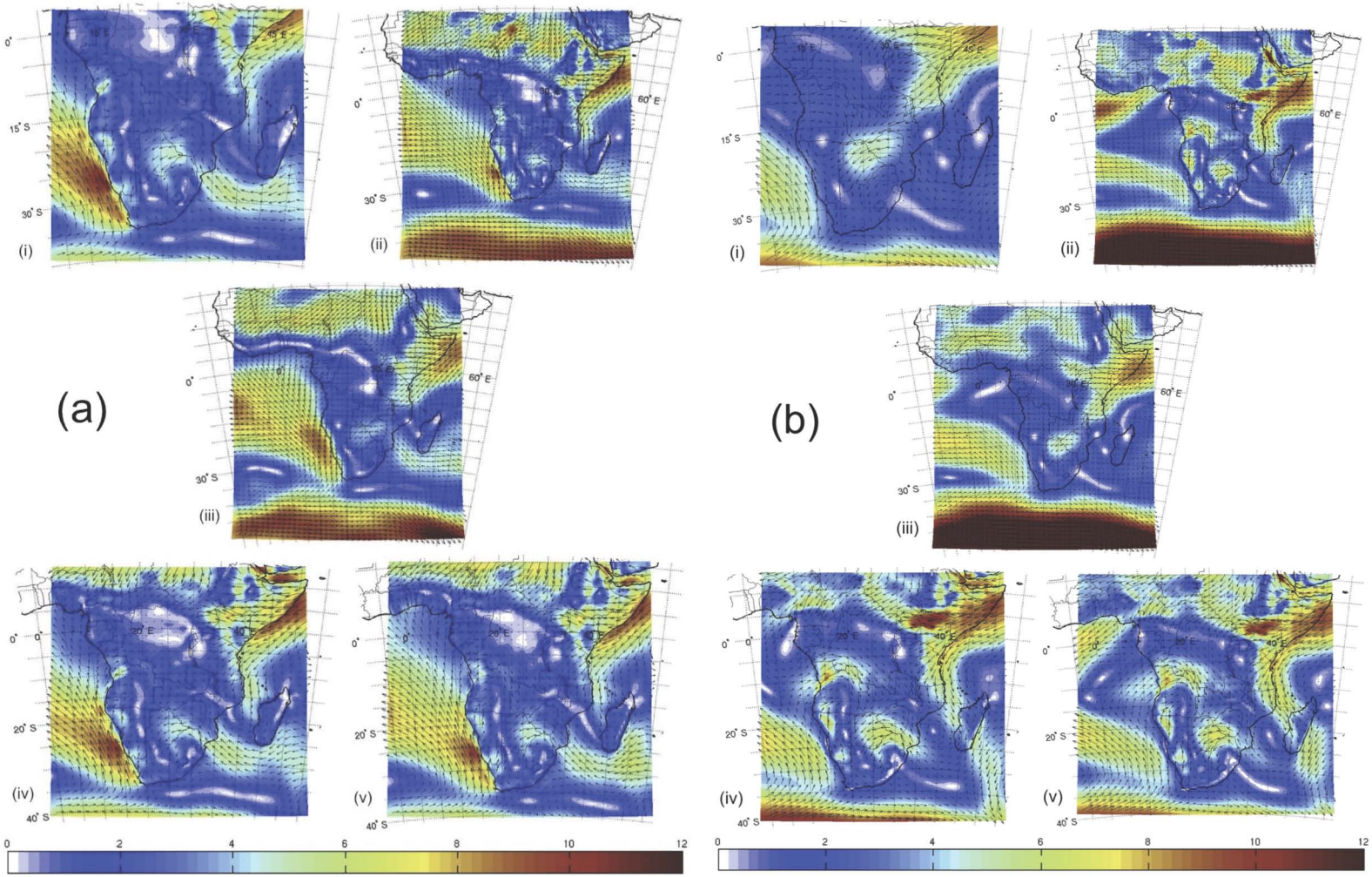

Figure 3.2.5: DJF Seasonal average winds for the (i) Small, (ii) Large, (iii) NCEP observations, (iv) Med-NCEP and (v) Med-ERA domains at (a) 1000hPa and (b) 850hPa. Colours indicate the wind strength and arrows the wind vectors.

A.1.5 Summary

Three different domain sizes are tested (small, medium and large) and two different sets of boundary forcing conditions (NCEP-II and ERA40) are applied. In all four tests carried out, RegCM3 reproduces the southern African climate relatively realistically throughout the year. Largest model error is exhibited in the equatorial regions, somewhat as expected, since the convective dynamics of this area are highly parameterised. Most importantly, very similar bias is observed between all four tests, indicating that RegCM3 appears to be relatively insensitive to domain size and situation, lending confidence to the internal model physics. Furthermore, the similarity between results using the NCEP-II and ERA40 boundary conditions suggests that either reanalysis product can be used with equal confidence to force RegCM3 over southern Africa. A new ERA-interim reanalysis product [*Simmons et al.,* 2007] is currently available, and is the reference dataset of choice for RegCM3 since it has proven more accurate than both ERA-40 and NCEP-II [*Uppalla et al.,* 2008; *Sylla et al.,* 2009]. Unfortunately, however, these data were not available when this work was carried out and therefore have not been used.

A.2 RegCM3 sensitivity to convective parameterisation

Correctly representing the different types of precipitation (convective vs. stratiform) can significantly influence simulated climate because of the difference in vertical structure of latent heat release between these precipitation types [*Davis et al.,* 2009]. For example, Schumacher and Houze [2003] found that incorrect partitioning of convective and stratiform precipitation generated unrealistic circulation feedbacks, especially within the tropics. As hinted at in the previous section, RegCM3 presents largest bias in the equatorial regions thus it is particularly important to test which convective parameterisation scheme best represents precipitation over this region, as well as more generally over the entire domain studied.

A.2.1 Experiment setup

The four convective parameterisation schemes available in RegCM3 are tested over the medium domain region. The four tests are named according to each scheme tested: Anthes (Anthes-Kuo), Emanuel (MIT-Emanuel), Grell-AS (Grell with Arakawa-Schubert closure) and Grell-FC (Grell with Fritsch-Chappell closure). As for the previous set of sensitivity tests (section A.1), all simulations are integrated over a two-year period covering January 2001 to December 2002. The NCEP-II reanalysis product [*Kanamitsu et al.,* 2002] and the National Ocean and Atmosphere Administration (NOAA) Optimum Interpolated sea surface temperature (OISST) product [*Reynolds et al.,* 2002] are used as lateral boundary forcing.

In order to better assess the various convective schemes the domain simulated is divided into six sub-regions as used previously in this work (see fig. 5.1.1), named as follows: Equatorial (EQ), Central West (CW), South West (SW), South East (SE), East Coast (EC) and Madagascar (MA), approximately covering different climatic regimes.

A.2.1 Surface Temperature

Box plots of monthly average surface temperature for each of the four convective tests as well as for the CRU observations (see full description thereof in section 4.2.1) are shown for each of the six sub-regions in figure A.2.1. Average monthly surface temperature varies most between the different tests in the equatorial region, where median values range between 24.4°C to 26°C for the Emanuel and Anthes tests, respectively. This is to be expected, since it is in this highly convective region that the choice of parameterisation scheme has the largest impact on simulated precipitation patterns. Differences between simulated monthly average surface temperatures are small in all other regions, and with the exception of the Anthes test in the CW region, simulated surface temperature is not significantly different from the observations for any test (at the 95% level).

Although convective precipitation is important in all sub-regions, except perhaps the SW, surface temperature does not appear to be very sensitive to the choice of convective parameterisation outside of the equatorial region. Both Grell tests perform equally well over the entire domain (neither are significantly different from the observations in any of the six sub-regions), while the Anthes test appears to reproduce surface temperature least accurately. On the basis of surface temperatures alone it is difficult to make a choice between schemes.

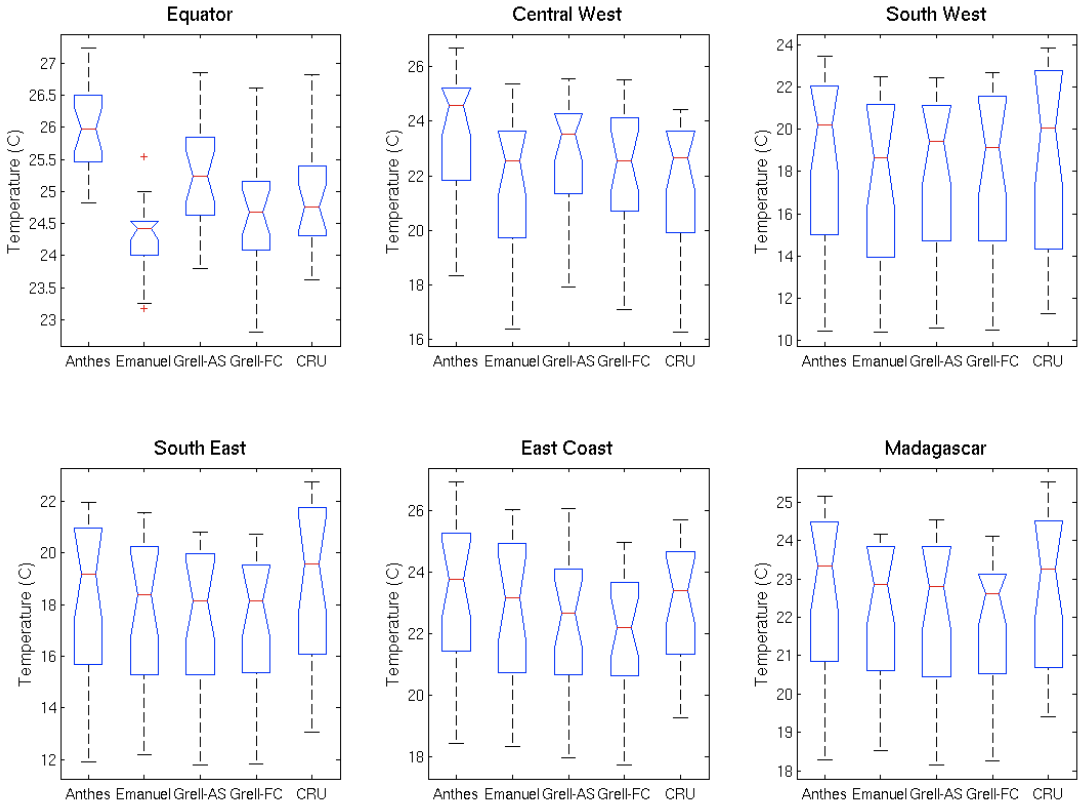

Figure A.2.1: Box plot of monthly average surface temperatures in each sub-region, for the four convective schemes tested as well as for the CRU observations (in ºC). Median values are indicated by the red line, the inter-quartile range (IQR, 25th to 75th quartiles) by the blue box and the range of ±1.5 IQR by the whiskers. Outliers are represented by red crosses (if present). The notches (indents) on the boxes are calculated so as to provide a means to carry out a visual significance test – if notches do not overlap, the samples are significantly different at the 95% level.

A.2.2 Precipitation

Monthly average precipitation is compared to the mixed satellite-gauge observations of the TRMM 3B43 product (see section 4.2.2 for a full description). There is large variability in simulated precipitation between schemes, particularly in the sub-regions where convective rainfall is significant. The Emanuel test clearly overestimates precipitation in all sub-regions during the wet season of each respective sub-region, thus also overestimating the amplitude

of the seasonal cycle (see fig. A.2.2). At the other end of the scale, the Anthes test results in a systematic underestimation of wet season precipitation compared to the TRMM observations. As for surface temperature, the two Grell tests represent intermediate cases, generally producing monthly precipitation totals between those of either the Emanuel or Anthes tests. All tests perform relatively well during the respective dry seasons of each sub-region, however this is relatively unsurprising, given that little precipitation occurs during this period in any case.

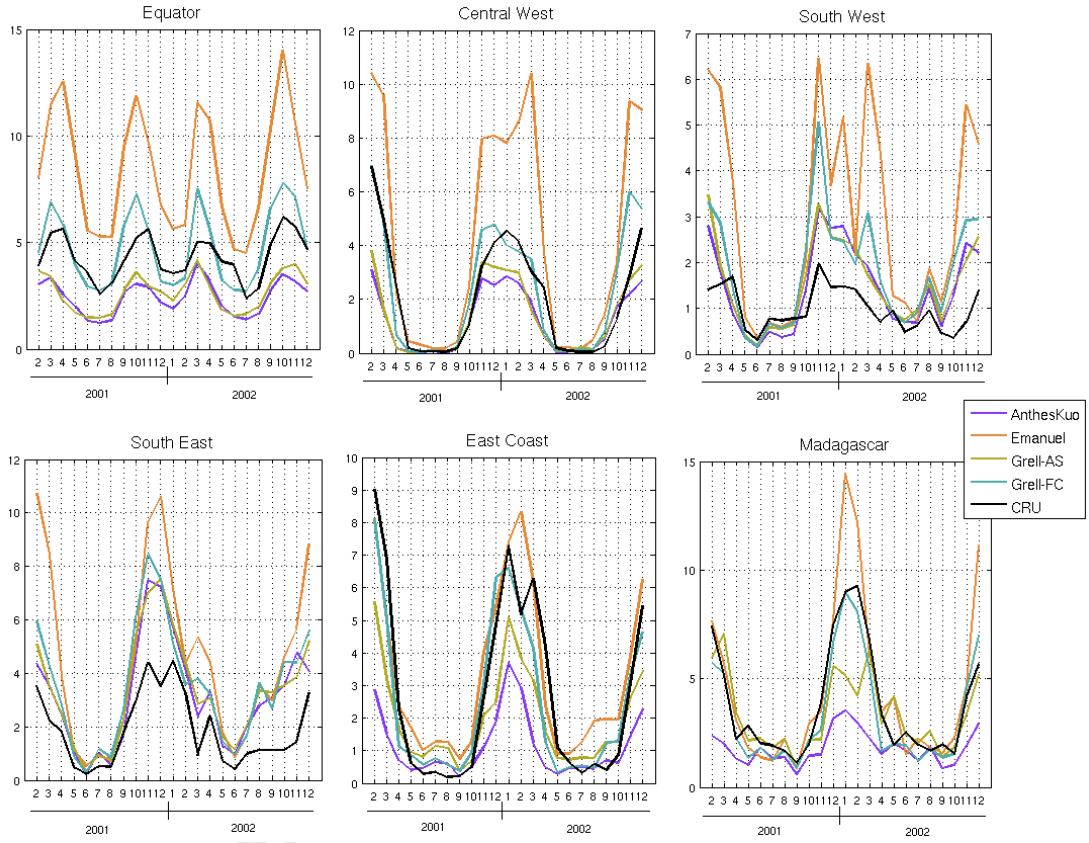

Figure A.2.2: Monthly average precipitation in each sub-region, for the four convective schemes tested as well as for the TRMM observations (in mm/day). Note the different scales for the different sub-regions.

Again, as for surface temperature, the Grell-FC and Grell-AS schemes perform best, with neither of the tests being significantly different from the TRMM observations in five out of the six sub-regions investigated (see table A.2.1). Importantly, the Grell-FC scheme simulates peak rainfall in the right month in all sub-regions. The other schemes either produce too broad a peak (e.g. the Anthes and Grell-AS schemes in the MA sub-region) or with a one-month lag (e.g. the Emanuel scheme peaks one month too late in the EC sub-region).

	Anthes-Kuo	MIT-Emanuel	Grell-AS	Grell-FC
EQ	$9.07e^{-8}$	$1.07e^{-6}$	$6.49e^{-7}$	0.3456
CW	0.1322	0.0243	0.2802	0.5757
SW	0.1452	0.0004	0.0754	0.0088
SE	0.2206	0.0100	0.1964	0.0642
EC	0.0195	0.3093	0.4165	0.7812
MA	0.0086	0.5423	0.2785	0.5091

Table A.2.1: p-values of two-tailed Student's t-tests. p<0.025 indicates that the monthly average precipitation is significantly different from the TRMM observations at the 95% level (highlighted in red if significant).

A.2.3 Cloud Cover

Since cloud cover and precipitation are highly related it is expected that the choice of convective parameterisation will also have a large impact on simulated cloud cover. Monthly average cloud cover for the four convective tests and the CRU observations for each of the sub-regions is presented in figure A.2.3.

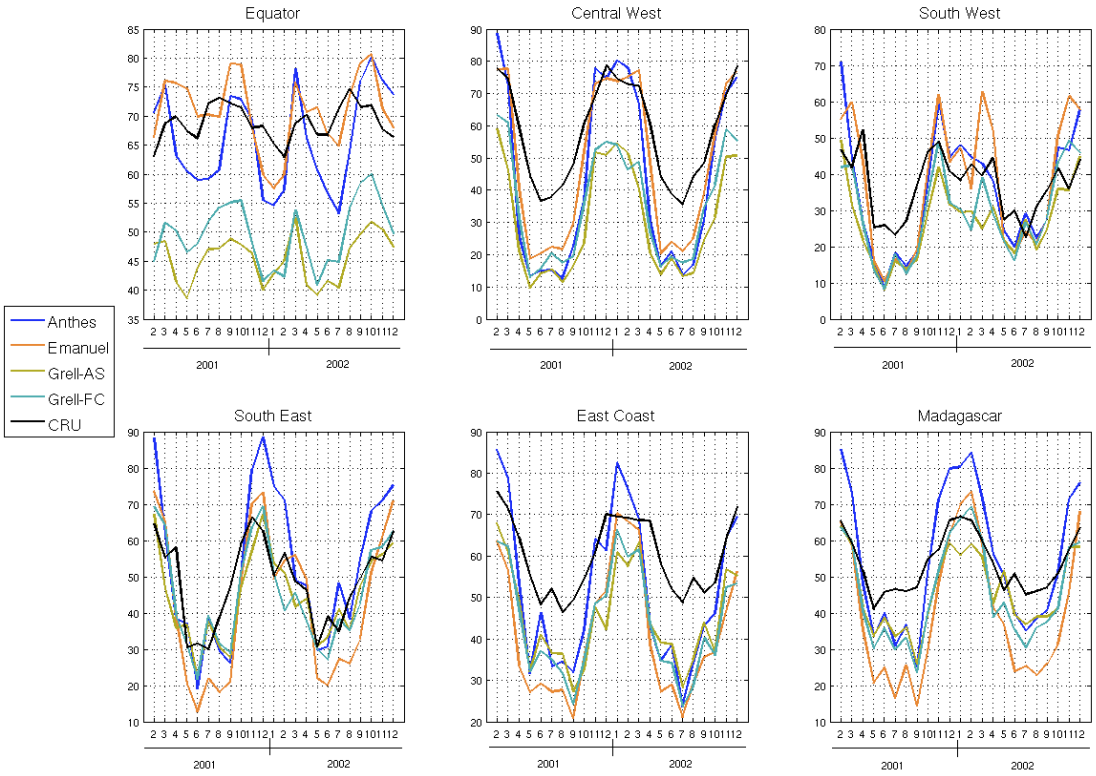

Figure A.2.3: Monthly average cloud cover in each sub-region, for the four convective schemes tested as well as for the CRU observations (in %). Note the different scales used for the different sub-regions.

As for surface temperature and precipitation, the simulated monthly average cloud cover signal varies to a greater extent in the months and sub-regions where convective processes are most active. The Emanuel and Anthes tests reproduce the greatest amounts of cloud cover for most months and also appear to simulate a larger amplitude seasonal cycle (fig. A.2.3). Significance tests show that the Anthes test produces the most accurate results, despite performing relatively poorly in terms of precipitation (see table A.2.2). It appears that this convective scheme results in more cloudy conditions, but less precipitation, resulting in a moister atmosphere. In contrast, the two Grell tests, which both reproduce realistic surface temperature and precipitation fields fare poorly when it comes to the representation of cloud cover. Both of these tests are significantly different from the CRU observations in all sub-regions except for the SE. Nevertheless, no matter which convective regime chosen the model appears to simulate the seasonal cycle of cloud cover relatively well, peaking in concert with the CRU observations in all sub-regions, despite any bias present in terms of magnitude

	Anthes-Kuo	MIT-Emanuel	Grell-AS	Grell-FC
EQ	0.1312	0.2063	$8.06e^{-24}$	$2.11e^{-16}$
CW	0.0457	0.1396	$1.26e^{-6}$	$4.78e^{-5}$
SW	0.6621	0.8988	0.0010	0.0181
SE	0.3936	0.2483	0.2626	0.3724
EC	0.0669	$2.11e^{-5}$	$2.14e^{-5}$	$1.69e^{-5}$
MA	0.7176	0.0037	0.0096	0.0193

Table A.2.2: p-values of two-tailed Student's t-tests, where $p<0.025$ indicates that the monthly average cloud cover is significantly different from the CRU observations (at the 95% level, highlighted in red if significant).

A.2.4 Circulation patterns

The winter and summer seasonal average circulation fields for the four convective tests and the NCEP-II reanalysis are shown in figures A.2.4 and A.2.5, respectively. As in section A.1.4 the seasonal averages for the high sun seasons (JJA and DJF, for the northern and southern hemispheres, respectively) are presented at two model levels, 1000hPa and 850hPa.

At 1000hPa the regional wind fields are relatively well reproduced by RegCM3 in winter and summer, no matter which convective scheme is used. As discussed previously, the most significant model bias is observed in the equatorial regions between 5ºS-5ºN, 15-35ºE, where winds are systematically underestimated in all tests in both seasons. This is particularly the case during summer (DJF), when the ITCZ moves into the southern hemisphere and convective activity over southern Africa is at a maximum. During this season variability

between tests is somewhat greater, specifically in terms of the size and situation of the region where equatorial winds are underrepresented. The Anthes test agrees best with the NCEP-II reanalysis in this region, while the three other tests do not represent the ITCZ convergence region as accurately. Over the Atlantic and tropical Indian Oceans, however, the Anthes test produces stronger south- and north-easterlies, respectively, than the other tests and the NCEP-II reanalysis.

Since very little convective activity occurs over most of southern Africa south of 10ºS during the austral winter (JJA), there is, as expected, very little difference between tests at the 1000hPa level during this season.

The representation of the regional circulation patterns at 850hPa is similar to that at 1000hPa and generally good (see fig. A.2.5(b) and A.2.6(b)). Similar bias patterns are observed, with all four tests under-representing winds in the tropics between 10ºS-5ºN, 15-35ºE. Again, the Anthes test reproduces the equatorial convergence zone best compared to the NCEP-II reanalysis (a factor which likely contributes to the better representation of equatorial cloud cover when using this scheme, as discussed in the previous section, A.2.3). Outside of the tropics, however, this test shows slightly greater bias compared to the three others.

It is important to note that, as mentioned previously as regards the CRU cloud cover observations, greater uncertainty is associated with the NCEP-II reanalysis product in the equatorial regions. Again, this is a result of there being fewer observations available with which to restrain the reanalysis product. In addition, the NCEP-II wind fields fall into the class B output, meaning that they are somewhat less restrained by observations and more strongly determined by the model climatology than class A output, such as mean sea level pressure [*Kidson,* 1999]. As a consequence, a certain degree of caution should be taken when comparing the model and reanalysis, especially in the tropics.

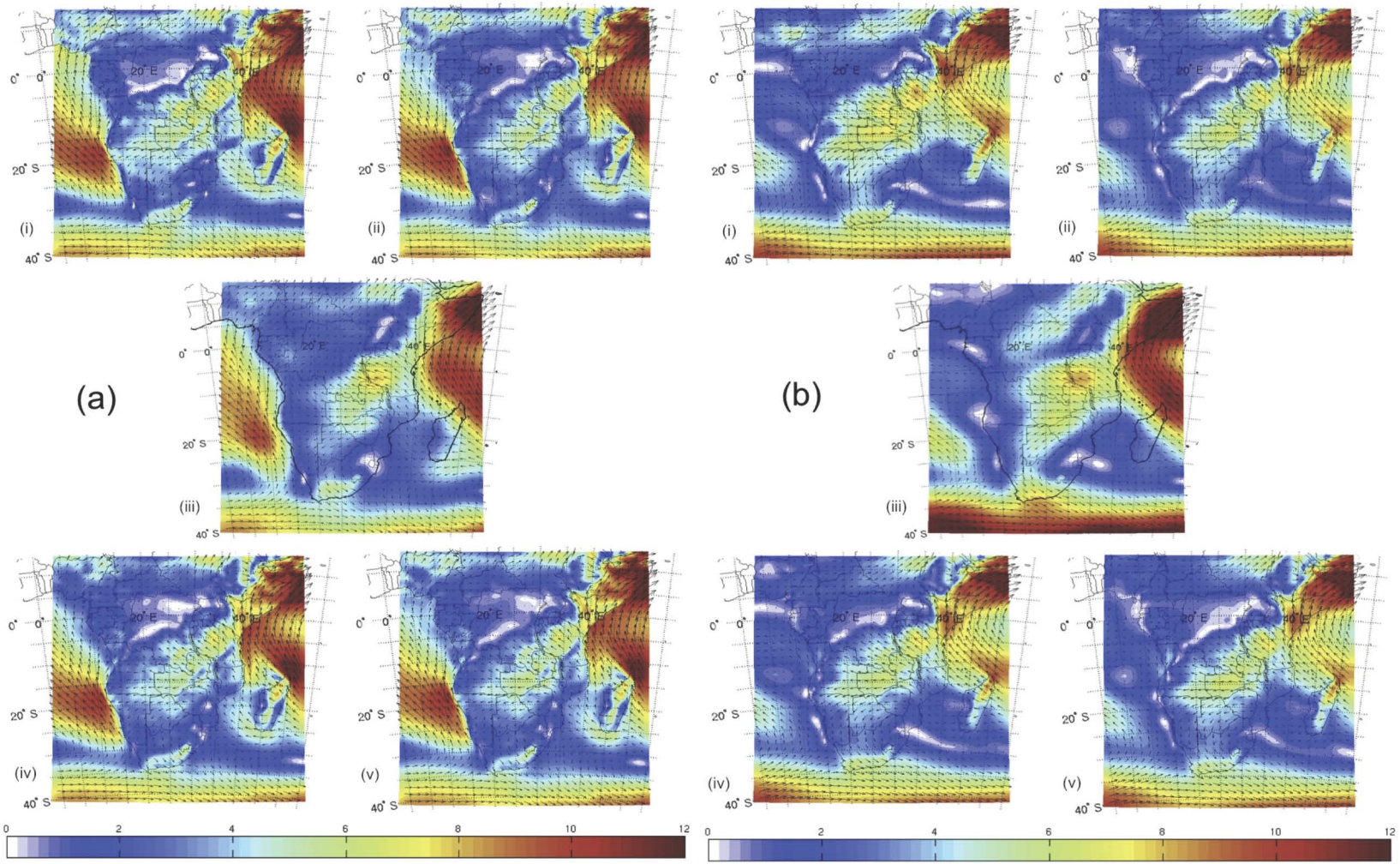

Figure **A.2.4** : JJA Seasonal average winds for the (i) Anthes, (ii) Emanuel, (iii) NCEP observations, (iv) Grell-AS and (v) Grell-FC tests at (a) 1000hPa and (b) 850hPa. Colours indicate the wind strength and arrows the wind vectors.

A.2.5 Summary

Differences between results from the four convective parameterisation tests vary considerably more than for the domain tests (section A.1). Monthly average surface temperature is well simulated in all four tests, and outside of the equatorial regions no test is significantly different from the observations. Based on surface temperature alone it is difficult to assess which scheme appears most accurate, largely because surface temperature is affected by a large number of other factors besides for convective processes.

Unsurprisingly, the largest differences between the four tests are observed in the equatorial regions and during the austral summer, when the ITCZ moves into the southern hemisphere. The different formulation of convective processes in each parameterisation scheme and the inherent stochastic nature of convection in general, mean that wherever these processes dominate greater difference will be exhibited. Where large-scale circulation systems are more dominant, such as the high-pressure system over the Atlantic Ocean there is less divergence between the tests, since the model solution is more controlled by the large-scale circulation patterns initiated through the lateral boundary forcing.

The Grell-FC scheme appears to result in the most accurate representation of precipitation in all six sub-regions in terms of spatial bias and seasonal cycle. Cloud cover is better represented when using the Anthes scheme, particularly in the EQ region. Similarly, the equatorial circulation patterns appear to be better represented when using this scheme. However, this test shows the worst bias in terms of simulated precipitation in almost all sub-regions, and outside of the tropical regions there are greater circulation biases than when using the other three convective schemes.

Taking all factors into account, the Grell-FC convective regime was chosen as the 'optimal' parameterisation scheme. Despite displaying certain errors in terms of cloud cover and circulation patterns, the Grell-FC test represented surface temperature and precipitation best in nearly all sub-regions considered. Also, this scheme has been utilised in various other RegCM3 studies over Africa [e.g. *Davis et al.*, 2009;*Sylla et al.*, 2009; *Afiesimama et al.*, 2006; *Kgatuke,* et al., 2008], thus allowing a better degree of comparison with these studies.

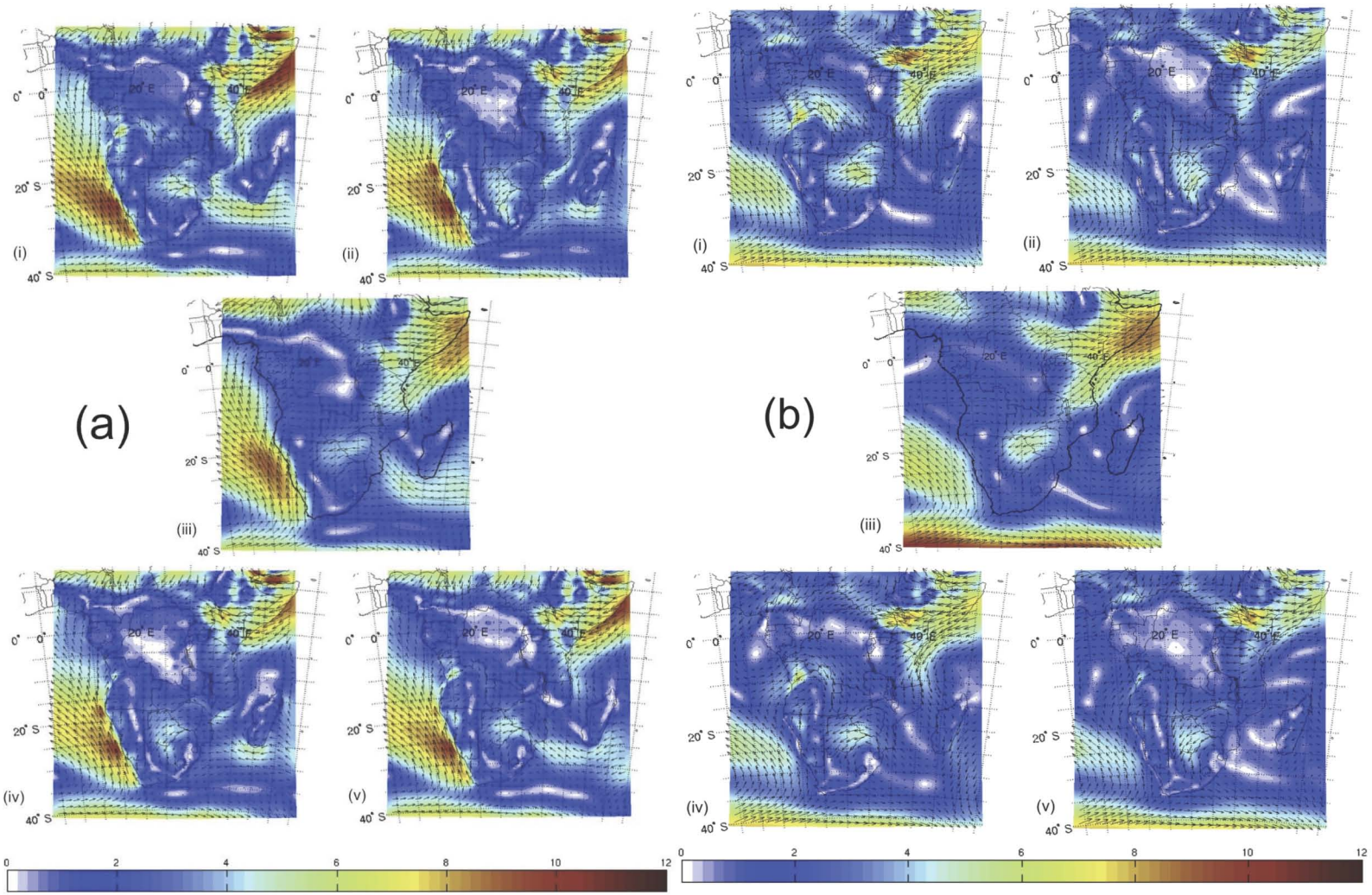

Figure **A.2.5** : DJF Seasonal average winds for the (i) Anthes, (ii) Emanuel, (iii) NCEP observations, (iv) Grell-AS and (v) Grell-FC tests at (a) 1000hPa and (b) 850hPa. Colours indicate the wind strength and arrows the wind vectors.

APPENDIX B

B.1 Validation of southern African climate: 1982-2001

The simulated climate for 1982-2001 is validated mainly with the ground-based CRU observations [*Mitchell et al.*, 2004], which are available for the entire period 1982-2001 (see section 4.2.1 for a full description of this dataset). In order to facilitate comparison and to avoid averaging over large areas (in which model biases may cancel each other out) the domain is divided into the same six sub-domains as already discussed throughout this work (see fig. 5.1.1 for the demarcation of these areas). They essentially correspond to different climatic zones, although the boundaries for each sub-region also depends on the number of model grid-points taken into account for averaging purposes.

B.1.1 Surface Temperature

Simulated monthly mean surface temperature is compared to the CRU observations [*Mitchell et al.*, 2001; see section 4.2.1] as well as with the ERA40 reanalysis [*Uppala et al.,* 2005]. Although the ERA40 data are used as boundary forcing, RegCM3 produces its own surface temperature, and thus was assumed to be largely independent of the lateral forcing conditions provided. Also, as mentioned previously, a considerable degree of uncertainty is associated with the CRU observations, particularly in the tropics [*Mitchell et al.,* 2004; *Jacob et al.,* 2007]. Comparison with two independently derived datasets lends confidence to the analysis, providing a range of the possible real monthly average surface temperatures.

Monthly average surface temperature appears to be relatively well simulated throughout the domain, with the model median temperature not significantly different from the CRU observations in four out of the six sub-regions (fig. B.1.1). Surface temperature is significantly overestimated in the equatorial (EQ) sub-region, compared to both CRU and ERA40, while it is significantly underestimated in the east coast (EC) sub-region, again compared to both datasets. Interestingly, it is only in the (EC) sub-region that the CRU observations and ERA40 reanalysis match, in all five other sub-regions the CRU and ERA40 medians are significantly different at the 95% level, with ERA40 generally tending to reproduce higher surface temperatures than the CRU observations. As a result, when comparing RegCM3 to the ERA40 dataset, the model simulated surface temperature is significantly different in all sub-regions except for the SW area. Nevertheless, the model generally appears to capture the observed spread of values, with similar IQR (as shown by the size of the box and whiskers,

and indicative of the variability) to the CRU observations, and, in most cases to the ERA40 reanalysis as well.

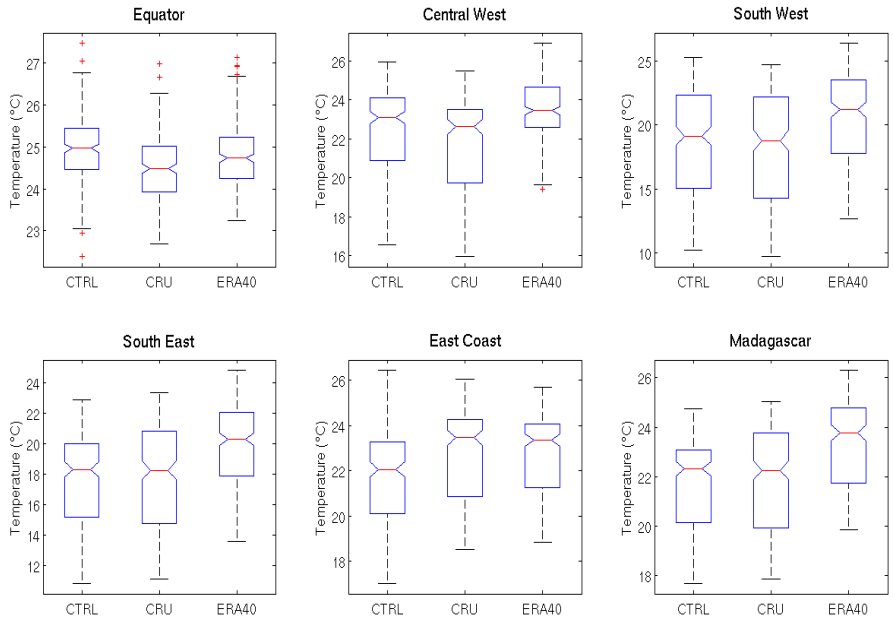

Figure B.1.1: Box plots of monthly average surface temperature for RegCM3, CRU and ERA40 for each of the six sub-domains. Blue boxes represent the interquartile range (IQR), the red line the median of each sample, while the whiskers extend out to 1.5 times the IQR above and below the median. Notches on the boxes denote the variability of the median between samples and if they do not overlap medians are significantly different at the 5% significance level. Red crosses indicate outliers.

The seasonal cycle is also well represented in most sub-regions, with simulated surface temperature following the CRU observations in terms of timing, although slightly underestimating temperature in most months (see fig. B.1.2; the ERA40 data are not included in this figure for clarity's sake). Only in the EQ sub-region does the model simulate minimum surface temperature approximately four months too late compared to the observations, although the model actually simulates the magnitude of temperature best in this region, with all months except for October falling within the bounds of ±1 standard deviation of the mean (as shown by the dashed blue lines).

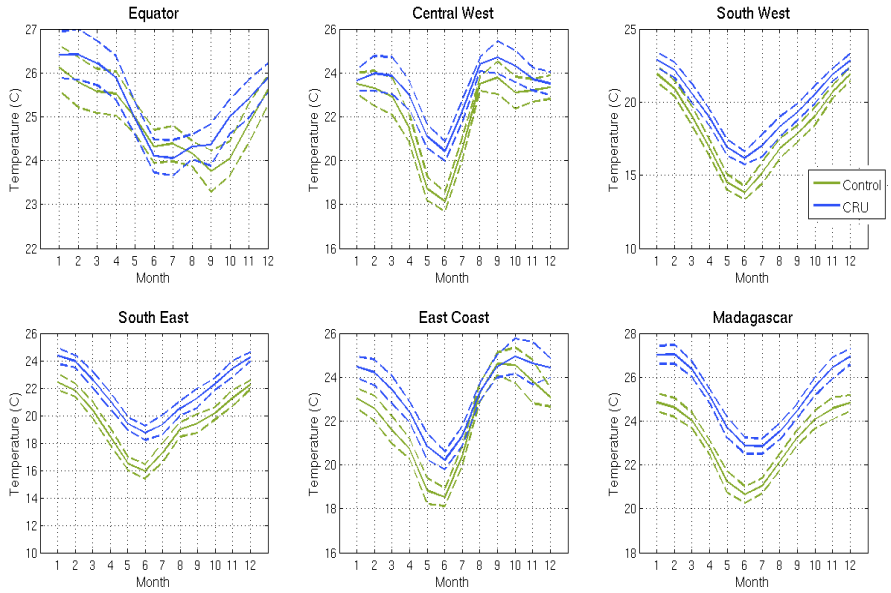

Figure B.1.2: Mean surface temperature climatology (averaged 1982-2001) for the control simulation and CRU observations for each of the six sub-regions. Dashed lines indicate one standard deviation above and below the mean and give an idea of the spread of variability for each month.

B.1.2 Precipitation

Monthly average precipitation is compared to the CRU observations as well as to the CMAP product (see section 4.3.2 for a complete description) and the Global Precipitation Climatology Project (GPCP) version 2 merged dataset [*Adler et al.,* 2003]. The GPCP rainfall estimates are constructed using a combination of four independent satellite products (SSM/I emission, SSM/I scattering, GPI and OPI geostationary estimates, and TOVS) with ground-based rain gauge measurements. Monthly, pentad and daily estimates are available, although in this study just the monthly product is used, so as to provide agreement with the other datasets (which are available at the monthly scale).

Box-whisker plots for all six sub-regions are shown in figure B.1.3. The model compares well to all observations, with monthly median precipitation for the 1982-2001 not significantly different in four of the six sub-regions. Only in the southwest and southeast is precipitation significantly overestimated compared to all three observational datasets, with the model also reproducing more variability (the range of the whiskers) than observed. In general, variability is well captured in the four more northerly regions, except for the equatorial region, where the model tends to overestimate precipitation variability, possibly because simulated convection is too strong. As a general remark, the precipitation distribution in several sub-regions (central west, east coast and Madagascar) is highly skewed, since the median situated well below the centre of each respective box. This indicates that a greater number of months with low

precipitation are observed (or simulated) than months with higher rainfall totals (in both the model and observations).

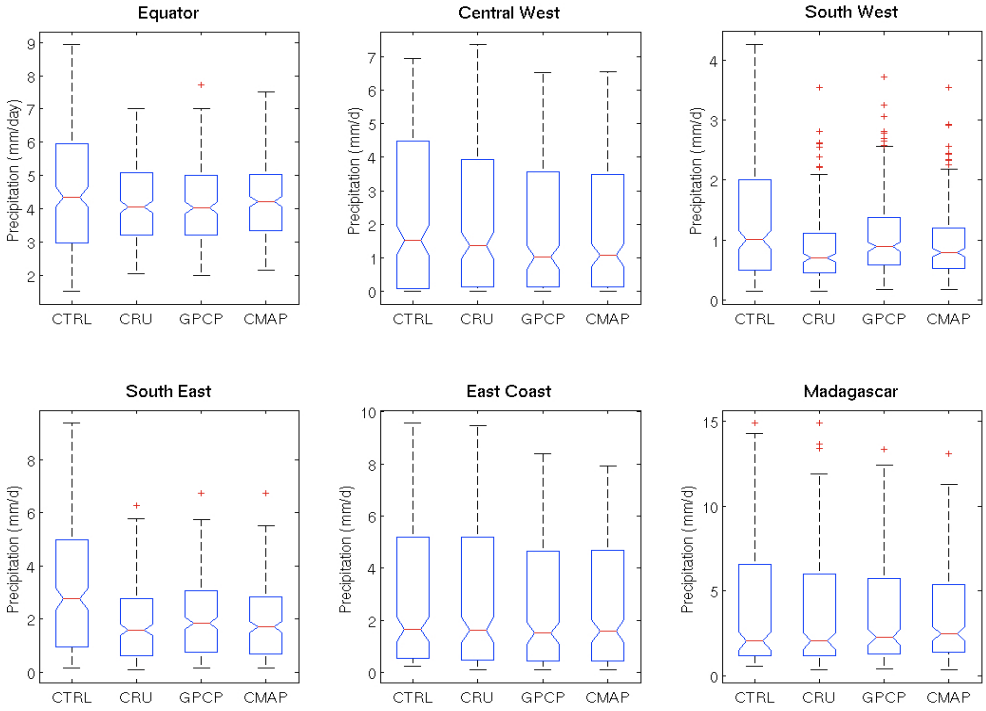

Figure B.1.3: Box-plots of monthly average precipitation (in mm/day) for RegCM3 (control (CTRL) simulation), CRU, GPCP and CMAP observations for each of the six sub-domains. (See fig. B.1.1 for a full description of how to interpret the box-whisker plots).

The spatial patterns of seasonal average precipitation and bias are shown in figure B.1.4. The seasonal shift in precipitation is clearly evident and follows the north-south migration of the ITCZ, with simulated rainfall at a maximum between 5-15°N in the boreal summer season (JJA) and between approximately 5-15°S in the austral summer season (DJF). In the shoulder seasons (MAM and SON) precipitation is maximum in the equatorial region between 5°N-5°S. In general, the model precipitation is overestimated wherever the ITCZ is situated, for example over the entire Sahelian region in JJA (as shown in appendix A). This suggests that the model likely simulates convection that is too intense. During this season precipitation is underestimated south and east of the ITCZ, likely because too much moisture convergence into the ITCZ region occurs, leaving the atmosphere in surrounding regions too dry. This is also clear in the SON and DJF seasons, in a strong west-east, positive-negative dipole. This signal appears to be related to the surface temperature bias, with the model overestimating temperature in the regions with too little precipitation and vice versa, underestimating temperature where too much precipitation occurs (see section B.1.1). This seems to be a general bias apparent in RegCM3 no matter which African domain (see appendix A.1), convective scheme (see appendix A.2) or boundary forcing is used (see chapter 4, for simulations with NCEP-II data as lateral boundary conditions).

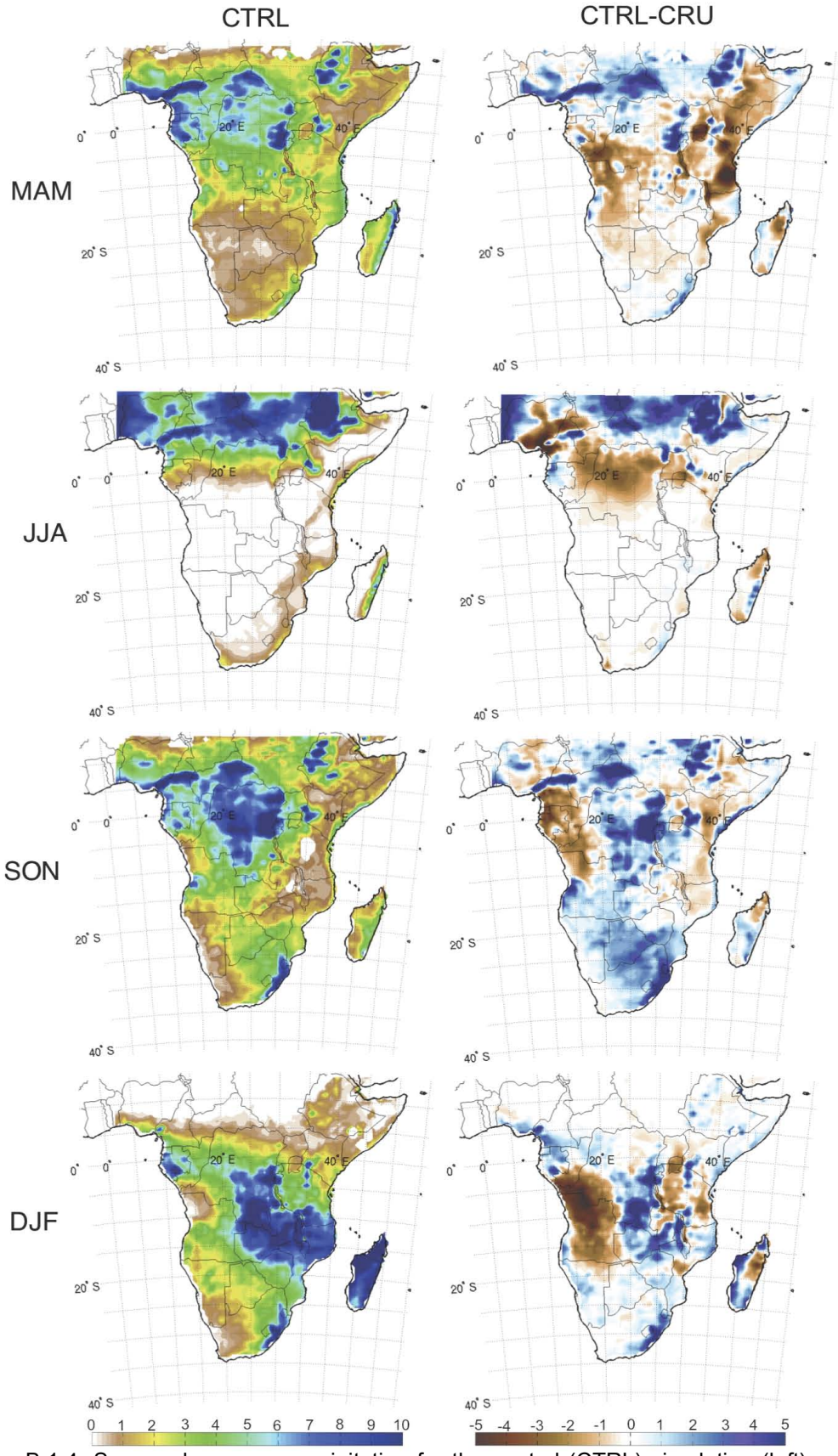

Figure B.1.4: Seasonal average precipitation for the control (CTRL) simulation (left) and the model precipitation bias compared to the CRU observations (right) in mm/day.

B.1.3 Cloud Cover

In comparison to the CRU observations simulated monthly average cloud cover is not as well simulated as either precipitation or surface temperature. Again, as mentioned previously, this is, largely unsurprising since the simulation of clouds, particularly convective clouds, is difficult and remains one of the greatest sources of uncertainty in current climate models [*Solomon et al.,* 2007]. In all sub-regions simulated cloud cover is significantly different from the observed (the notches on boxes do not overlap) and the model generally tends to underestimate cloud cover. This is particularly the case in the equatorial sub-region, where median model cloud cover is approximately 25% lower than the CRU observations. This corresponds with the results in terms of simulated rainfall (see fig. B.1.4), which suggest that convective precipitation is overestimated in the tropics, appearing to result in too much moisture removal from the atmosphere and too little cloud cover. It is, however, again important to bear in mind that greater uncertainty is associated with the CRU cloud cover estimates than those of temperature or precipitation, particularly in the African equatorial regions, where station data is sparse [*New et al.,* 2000, 2002; *Mitchell and Jones*, 2005]. The apparent model discrepancy may thus not be as large as suggested.

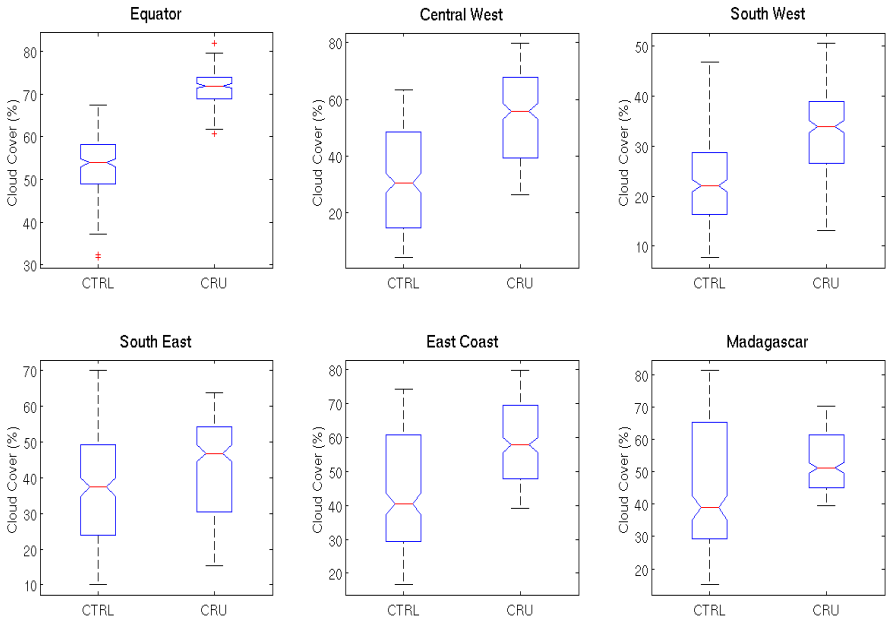

Figure B.1.5: Box plot of monthly average cloud coverage (in %) for the model control (CTRL) simulation and the CRU observations for each of the six sub-regions. (See figure B.1.1 for a full description of how to interpret the box-whisker plots).

The variability of monthly average cloud cover is overestimated in four of the six sub-regions (equator, south east, east coast and Madagascar), while it is relatively well represented in the

central and south west sub-regions. Interestingly, there is little relation between average cloud cover and precipitation biases. On the one hand, the model significantly overestimates precipitation in the south west and south east sub-regions, but significantly underestimates cloud cover in these areas, suggesting that too much of the atmospheric moisture is rained out in these sub-regions. On the other hand, in the four other sub-regions where precipitation bias is fairly low the cloud cover is still significantly underestimated. This, in combination with the fact the cloud cover variability is overestimated in the model suggests that precipitation in these four sub-regions likely occurs too infrequently but in events heavy enough to reproduce the total magnitude of rainfall relatively well.

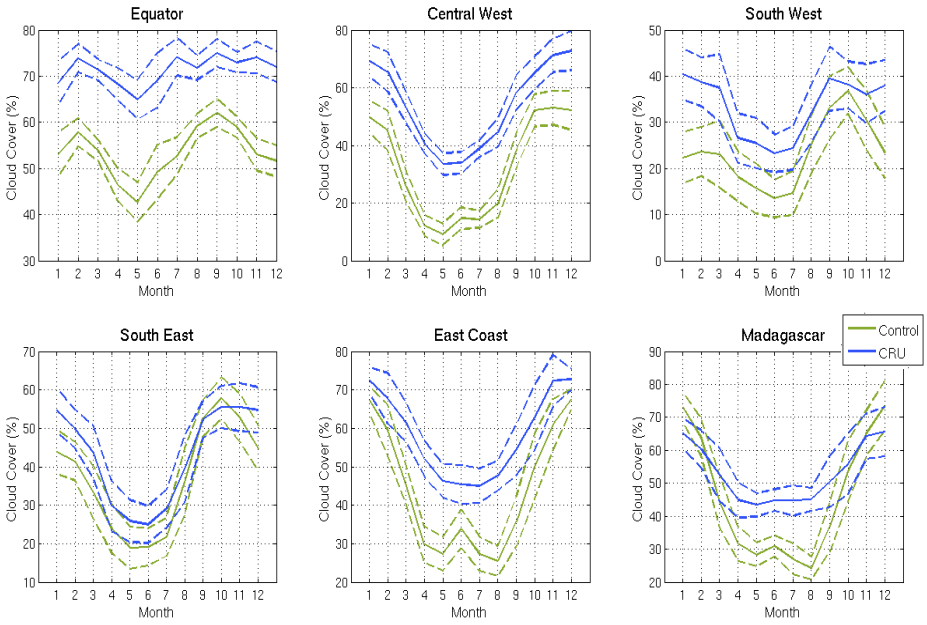

Figure B.1.6: Mean cloud cover climatology (averaged 1982-2001) for the control simulation and CRU observations for each of the six sub-regions. Dashed lines indicate one standard deviation above and below the mean and give an idea of the spread of variability for each month.

Even though monthly average cloud cover is significantly underestimated in all areas the seasonal cycle is relatively well represented in most areas. The timing of peak and minimum cloud cover is well captured in all sub-regions except in the equatorial area. In this sub-region the simulated cloud cover follows the model precipitation pattern, peaking in February and September (precipitation climatology not shown), and, although in terms of the precipitation signal these peaks are accurate, the CRU observations indicate that cloud cover is considerably more consistent throughout the year, varying only by approximately 20% (between ~60-80%). Over the East Coast and Madagascan areas the model also fails to capture the relative consistency of the observed cloud cover, with the model representing a stronger seasonal cycle than observed. Since convective cloud systems and precipitation are

active in these two sub-regions, the model bias again suggests that the convective parameterisation scheme does not accurately represent the cloud structure in these areas, despite reproducing the observed precipitation signal fairly well.

References

Abbott, M.A. and T.G.J. Dyer. 1976. The temporal variation of rainfall and run-off over the summer rainfall region of South Africa. *S. Afr. J. Sci.* **72**. 276-278.

Abel, S.J., J.M. Haywood, E.J. Highwood, J. Li and P.R. Buseck. 2003. Evolution of biomass burning aerosol properties from an agricultural fire in southern Africa. *Geophys. Res. Lett.* **30**(L15,1783). Doi: 10.1029/2003GL017342.

Abel, S.J, E.J. Highwood, J. M. Haywood and M.A. Stringer. 2005. The direct radiative effect of biomass burning aerosols over southern Africa. *Atmos. Chem. Phys. Discuss.* **5**. 1165-1211.

Abiodun B.J., J.S. Pal, E.A. Afiesimama, W.J. Gutowski and A. Adedoyin. 2007. Simulation of West African monsoon using RegCM3 Part II: impacts of deforestation and desertification. *Theor. Appl. Climatol*. **93**. 245–261.

Ackerman, A.S., O.B. Toon, D.E. Stevens, A. J. Heymsfield, V. Ramanathan and E.J. Welton. 2000. Reduction of tropical cloudiness by soot. *Science.* **288**. 1042-1047.

Adler, R.F., J. Huffmann, D.T. Bolvin, S. Curtis and E.J. Nelkin. 2000. Tropical rainfall distributions determined using TRMM combined with other satellite rain gauge information, *J. Appl. Meteor.* **39***.* 2007-2023.

Adler, R.F., G.J. Huffman, A. Chang, R. Ferraro, P. Xie, J. Janowiak, B. Rudolf, U. Schneider, S. Curtis, D. Bolvin, A. Gruber, J. Susskind, P. Arkin. 2003. The Version 2 Global Precipitation Climatology Project (GPCP) Monthly Precipitation Analysis (1979-Present). *J. Hydrometeor***. 4**. 1147-1167.

Afiesimama, E.A., J.S. Pal, B.J. Abiodun, W.J. Gutowski Jr. and A. Adedoyin. 2006. Simulation of West African monsoon using the RegCM3. Part I: Model validation and interannual variability. *Theor. Appl. Climatol.* **86**. 23-37.

Albrecht, B.A. 1989. Aerosol, cloud microphysics and fractional cloudiness. *Science.* **245**. 1227-1230.

Alfaro, S.C., A. gaudichet, L. Gomes and M. Maille. 1998. Mineral aerosol production by wind erosion: aerosol particle sizes and building energies. *Geopys. Res. Lett.* **25**. 991-994.

Alfaro, S.C., L. Gomes, J.L. Rajot and A. Gaudichet. 2000. Modeling mineral aerosol production by wind erosion. Part 1: physical bases. *J. Aerosol Sci.* **31**. S5426-5427.

Alfaro, S.C. and L. Gomes. 2001. Modeling mineral aerosol production by wind erosion: Erosion intensities and aerosol size distribtuions in source areas. *J. Geophys. Res.* **106**(D16). 18,075-18084.

Alleaume, S., C. Hely, J. Le Roux, S. Koronitzi, R.J. Swap, H.H. Shugar and C.O. Justice. 2005. Using MODIS to evaluate heterogeneity of biomass burning in southern African savannahs: a case study in Etosha. *Int. J. Rem. Sens.* **26**. 4219-4237.

Andreae, M.O. 1996. Raising dust in the greenhouse. *Nature.* **380**. 389-390.

Andreae, M.O., J. Fishman and J. Lindesay. 1996. The Southern Tropical Atlantic Region Experiment (STARE): Transport and Atmospheric Chemistry near the Equator-Atlantic (TRACE-A) and Southern African Fire-Atmosphere Research Initiative (SAFARI): An introduction. *J. Geophys. Res.* **101**. 23,519-23,520.

Andreae, M. O., T.W. Andreae, H. Annegarn, J. Beer, H. Cachier, P. Le Canut, W. Elbert, W. Maenhaut, I. Salma, F.G. Wienhold and T. Zenker. 1998. Airborne studies of aerosol emissions from savanna fires in southern Africa: 2. Aerosol chemical composition. *J. Geophys. Res*. **103**. 32119-32128.

Andreae, M.O. and P. Merlet. 2001. Emission of trace gases and aerosols from biomass burning. *Global biogeochem. Cycles*. **15**. 955-966.

Andreae, M.O. and A. Gelencser. 2006. Black carbon or brown carbon? The nature of light-absorbing carbonacoues aerosols. *Atmos. Chem. Phys.* **6**. 3131-3148.

Angstrom, A. 1929. On the atmospheric transmission of sun radiation and dust in the air. *Geogr. Ann.* **11**. 156-166.

Annegarn, H.J., L. Otter, R.J. Swap and R.J. Scholes. 2002. Southern Africa's ecosystem in a test-tube. *S. Afr. J. Sci.* **98**. 111-113.

Anthes, R.A. 1977. A cumulus parameterisation scheme utilising a one-dimensional cloud model. *Mon. Wea. Rev.* **105**. 270-286.

Anthes, R.A. Y.-H. Kuo, E.-Y. Hsie, S. Low-Nam and T.W. Bettge. 1989. Estimation of skill and uncertainty in regional numerical models. *Q. J. R. Meteorol. Soc.* **115**. 763-806.

Anyamba, A., C.J. Tucker and R. Mahoney. 2002. From El Nino to La Nina: Vegetation response patterns over east and southern Africa during the 1997-2000 period. *J. Clim.* **15**. 3096-3103.

Anyamba, A., C.O. Justice, C.J. Tucker and R. Mahoney. 2003. Seasonal to interannual variability of vegetation and fires at SAFARI 2000 site inferred from advanced very high resolution radiometer time series data. *J. Geophys. Res.* **108**(D13,8507). Doi: 10.1029/2002JD002464.

Arimoto, R. 2001. Eolian dust and climate: relationships to sources, tropospheric chemistry, transport and deposition. *Earth-Sci. Rev*. **54**. 29-42.

Assamoi, E.M. and C. Liousse. 2010. A new inventory for two-wheel emissions in West Africa for 2002. *Atmos. Env.* **44**. 3985-3996.

Balling, R.C. Jr. 2005. Interactions of desertification and climate in Africa. In *Climate change and Africa.* Ed. Pak Sum Low. Cambridge University Press.

Bell, G.D., M.S. Halpert,, R.C. Schnell, R. Wayne-Higgins, J. Lawrimore, V.E. Kousky, R. Tinker, W. Thiaw, M. Chelliah, and A. Artusa. 2000. Climate Assessment for 1999. *Bull. Amer. Meteorol. Soc***. 81**. 1328.

Bergstrom, R.W., P.B. Russell and P. Hignett. 2002. Wavelength dependence of the absorption of black carbon particles: Predictions and results from the TARFOX experiment and implications for the aerosol single scattering albedo. *J. Atmos. Sci.* **59**. 567-577.

Bergstrom, R.W., P.Pilewskie, B. Schmid and P.B. Russel. 2003. Estimates of the spectral aerosol single scattering albedo and aerosol radiative effects during SAFARI 2000. *J. Geophys. Res.* **108**(D13,8474). Doi: 10.1029/2002JD002435.

Betts, A. K., and C. Jakob. 2002. Evaluation of the diurnal cycle of precipitation, surface thermodynamics, and surface fluxes in the ECMWF model using LBA data. *J. Geophys. Res*. **107**(D20,8045) . Doi:10.1029/ 2001JD000427.

Betts, A.K., M. Zhao, P.A. Dirmeyer and A.C.M. Beljaars. 2006. Comparison of ERA40 and NCEP/DOE near-surface data sets with other ISLCSP-II data sets. *J. Geophys. Res.* **111**(D22S04). Doi: 10.1029/2006JD007174.

Billmark, K.A., R.A. Swap and S.A. Macko. 2005. Stable isotope and GC/MS characterisation of southern African aerosols. *S. Afr. J. Sci.* **101**. 177-179.

Birkett, C., R. Murtugudde and T. Allan. 1999. Indian Ocean climate events brings flood to East Africa's lakes and the Sudd marsh. *Geophys. Res. Lett.* **26**. 1031-1034.

Bond, T.C., D.G. Streets, K.F. Yarber, S.M. Nelson, J.H. Woo and Z. Klimont. 2004. A technology-based global inventory of black and organic carbon emissions from combustion. *J. Geophys. Res.* **109**(D14203). Doi: 10.1029/2003JD003697.

Bond, T.C. and R.W. Bergstrom. 2006. Light absorption by carbonaceous particles: An investigative review. *Aerosol Sci. Technol.* **40**. 27-67.

Bond, T.C., G. Habib and R.W. Bergstrom. 2006. Limitations in the enhancement of visible light absorption due to mixing state. *J. Geophys. Res.* **111**(D20). D20211.

Brioude, J., O.R. Cooper, G. Feingold, M. Trainer, S.R. Freitas, D. Kowal, J.K. Ayers, E. Prins, P. Minnis, S.A. McKeen, G.J. Frost and E.-Y. Hsie. Effect of biomass burning on marine stratocumulus clouds off the California coast. *Atmos. Chem. Phys*. **9**. 8841–8856.

Bryant, R.G. 2003. Monitoring hydrological controls on dust emissions: preliminary observations from Etosha Pan, Namibia. *Geogr. J.* **169**. 131-141.

Bryant, R.G., G.R. Bigg, N.M. Mahowald, F.D. Eckardt and S.G. Ross. 2007. Dust emission response to climate in southern Africa. *J. Geophys. Res.* **112**(D09207). Doi: 10.1029/2005JD007025.

Cachier, H., C. Liousse, P. Buat-Ménard and A. Gaudichet. 1995. Particulate content of savanna fire emissions. *J. Atmos. Chem.* **22**. 123-148.

Cavazos, T. 2000. Using self-organizing maps to investigate extreme climate events: An application to wintertime precipitation in the Balkans. *J. Clim.* **13**. 1718-1732.

Chameides, W. L., C. Luo, R. Saylor, D. Streets, Y. Huang, M. Bergin, and F. Giorgi. 2002. Correlation between model-calculated anthropogenic aerosols and satellite-derived cloud optical depths: Indication of indirect effect? *J. Geophys. Res.* **107**(D10,4085). Doi:10.1029/2000JD000208.

Campbell, J.R., E.J. Welton, J.D. Spinhirne, Q. Ji, S. Tsay, S.J. Piketh, M. Barenbrug and B.N. Holben. 2003. Micropulse lidar observations of tropospheric aerosols over northeastern South Africa during the ARREX and SAFARI 2000 dry season experiments. *J. Geophys. Res.* **108**(D13,8497). Doi: 10.1029/2002JD002563.

Charlson, R.J., S.E. Schwartz. J.M. Hales, R.D. Cess. J.A. Coakley Jr., J.E. Hansen and D.J. Hoffman. 1992. Climate forcing by anthropogenic aerosols. *Science.* **255**. 423-430.

Chimidza, S. and K. Moloi. 2000. Identification of sources of aerosol particles in three locations in eastern Botswana. *J. Geophys. Res.* **105**. 17,811-17,818.

Christensen, J.H., B. Machenhauer, R.G. Joes, C. Schar, P.M. Ruti and G. Visconti. 1997. Validation of present-day regional climate simulations over Europe: LAM simulations with observed boundary conditions. *Clim. Dyn.* **13**. 489-506.

Christensen, O.B., J.H. Christensen, B. Machenhauer and M. Botzet. 1998. Very high-resolution regional climate simulations over Scandinavia – Present climate. *J. Clim.* **11**. 3204-3229.

Chu, D.A., Y.J. Kaufman, C. Ichoku, L.A. Remer, D. Tanre and B.N. Holben. 2002. Validation of MODIS aerosol optical depth retrieval over land. *J. Geophys. Res.* **29**. Doi: 10.1029/2001GL013205.

Chylek, P. and J.A. Coakley. 1974. Aerosols and climate. *Nature*. **183**. 75-77.

Clarke, A.D. 1989. Aerosol light absorption by soot in remote environments. *Aerosol Sci. Technol.* **10**. 161-171.

Clarke, J.F., E.S. Edgerton and B.E. Martin. 1997. Dry deposition calculations for the clean air status and trends network. *Atmos. Env.* **31**. 3667-3678.

Collins, W.D, P.J. Rasch, B.E. Eaton, D.W. Filmore, J.T. Kiehl, C.T. Beck, C.S. Zender. 2002. Simulation of aerosol distributions and radiative forcing for INDOEX: Regional climate impacts. *J. Geophys. Res.* **107**(D19,8028). Doi: 10.1029/2000JD000032.

Cook, K.H. 2001. A Southern Hemisphere wave response to ENSO with implications for southern African precipitation. *J. Atmos. Sci.* **58**. 2146-2162.

Cooke, W.F., and J.J.N. Wilson. 1996. A global black carbon aerosol model. *J. Geophys. Res.* **101**. 19,395-19,409.

Cooke, W.F., C. Liousse, H. Cachier and J. Feichter. 1999. Construction of a 1x1 fossil fuel emission data set for carbonaceous aerosol and implementation and radiative impact in the ECHAM4 model. *J. Geophys. Res.* **104**. 22137-22162.

Cosijn, C. and P.D. Tyson. 1996. Stable discontinuities in the atmosphere over South Africa. *S. Afr. J. Sci.* **92**. 381-386.

Cowling, E.B. 1982. Acid precipitation in historical perspective. *Environ. Sci. Technol.* **16**. 110A-123A.

Crane, R.G. and B.C. Hewitson. 1998. Doubled CO2 precipitation changes for the Susquehanna basin: Downscaling from the GENESIS general circulation model. *Int. J. Climatol.* **18**. 65-76.

Croft, B., U. Lohmann and L. von Salzen. 2005. Black carbon ageing in the Canadian Centre for Climate modelling and analysis atmospheric general circulation model. *Atmos. Chem. Phys. Discuss.* **5**. 1383-1419.

Crosier, J. J.D. Allan, H. Coe, K.N. Bower and P. Formenti. 2007. Chemical composition of summertime aerosol in the Po valley (Italy), northern Adriatic and Black Sea. *Q. J. R. Meteorol. Soc.* **133**. 61-75.

Crutzen, P.J. and M.O. Andreae. 1990. Biomass burning in the tropics: Impact on atmospheric chemistry and biogeochemical cycles. *Sci.* **250**. 1669-1678.

Cullis, C.F. and M.M. Hirschler. 1980. Atmospheric sulphur: Natural and man-made sources. *Atmos. Env.* **14**. 1263-1278.

D'Almeida, G.A., P. Koepke and E.P. Shettle. 1991. *Atmospheric aerosols: Global climatology and radiative characteristics.* A. Deepak (ed.). Hampton. Vancouver. 561p.

Davis, N., J. Bowden, F. Semazzi and L. Xian (2009), Customization of RegCM3 regional climate model for Eastern Africa and tropical Indian Ocean domain, *J. Clim.* **22**. 3595-3616.

Deardoff, J.W. 1978. Efficient prediction of ground surface temperature and moisture with inclusion of a layer of vegetation. *J. Geophys. Res.* **83**. 1889-1903.

Delmas, R.A., et al., 1999. Experiment for Regional Sinks and Sources of Oxidants (EXPRESSO): An overview. *J. Geophys. Res.* **104**. 30609-30624.

Delworth, T. and S. Manabe. 1989. The influence of soil wetness on near-surface atmospheric variability. *J. Clim.* **2**. 1447-1462.

Diab, R.D., M.Z. Rahman, A. Moorgawa and M.T. Freiman. 2003. First measurements of tropospheric aerosol profiles above Durban using a LIDAR. *S. Afr. J. Sci.* **99**. 168-172.

Dickinson, R.E., R.M. Errico, F. Giorgi and G.T. Bates. 1989. A regional climate model for the western United States. *Climatic Change*. **15**. 383-422.

Dickinson, R.E., A. Henderson-Sellers and P.J. Kennedy. 1993. *Biosphere-Atmosphere Transfer Scheme (BATS) version 1e as coupled to the NCAR Community Climate Model.* Technical Report. Natl. Cent. for Atmos. Res. Boulder, Colorado.

Diner, D.J., J.C. Beckert, T.H. Reilly, C.J. Bruegge, J.E. Conel, R. Kahn, J.V. Martonchik, T.P. Ackerman, R. Davies, S.A.W. Gerstl, H.R. Gordon, J-P. Muller, R. Myneni, R.J. Sellers, B. Pinty, and M.M. Verstraete. 1998. Multi-angle Imaging SpectroRadiometer (MISR) description and experiment overview, *IEEE Trans. Geosci. Rem. Sens.* **36**. 1072-1087.

Diner, D.J., W.A. Abdou, C.J. Brugge, J.E. Conel, K.A. Crean, B.J. Gaitley, M.C. Helmlinger, R.A. Kahn, J.V. Martonchik, S.H. Pilorz and B.N. Holben. 2001. MISR aerosol optical depth retrievals over southern Africa during the SAFARI-2000 dry season campaign. *Geophys. Res. Lett.* **28**. 3127-3130.

Dockery, D.W. and C.A. Pope. 1994. Acute respiratory effects of particulate air pollution. *Ann. Rev. Public Health*. **15**. 107-132.

Dubovik, O., A. Smirnov, B.N. Holben, M.D. King, Y.J. Kaufman, T.F. Eck and I. Slutsker. 2000. Accuracy assessments of aerosol optical properties retrieved from Aerosol Robotic Network (AERONET) Sun and sky radiance measurements. *J. Geophys. Res.* **105**. 9791-9806.

Dubovik, O., B. Holben, T.F. Eck, A. Smirnov, Y.J. Kaufman, M.D. King, D. Tanre and I. Slutsker. 2002. Variability of absorption and optical properties of key aerosol types observed in worldwide locations. *J. Atmos. Sci.* **59**. 590-608.

Duce, R.A., et al., 1991. The atmospheric input of trace species into the world ocean. *Global Biogeochem. Cycles*. **5**. 193-259.

Dufresne, J.-L., C. Gautier, P. Ricchiazzi and Y. Fouquart. 2002. Longwave scattering effects of mineral aerosols. *J. Atmos. Sci.* **59**. 1959–1966.

Eck, T.F, B.N. Holben, D.E. Ward, O. Dubovik, J.S. Reid, A. Smirnov, M.M Mukelabai, N.C. Hsu, N.T. O'Neill and I. Slutsker. 2001. Characterisation of the optical properties of biomass burning aerosols in Zambia during the 1997 ZIBBEE field campaign. *J. Geophys. Res.* **106**. 3425-3448.

Eck, T.F., B.N. Holben, D.E. War, M.M. Mukelabai, O. Dubovik, A. Smirnov, J. S. Schefer, N. C. Hsu, S.J. Piketh, A. Queface, J. Le Roux, R.J. Swap and I. Slutsker. 2003. Variability of biomass burning aerosol optical characteristics in southern Africa during the SAFARI 2000 dry season campaign and a comparison of single scattering albedo estimates from radiometric measurements. *J. Geophys. Res.* **108**(D13,8477). Doi:10.1029/2002JD002321.

Eckardt, F.D. and N. Kuring. 2005. SeaWiFS identifies dust sources in the Namib Desert. *Int. J. Rem. Sens.* **26**. 4159-4167.

Elguindi, N., X. Bi, F. Giorgi, B. Nagarajan, J. Pal, F. Solmon, S. Rauscher and A. Zakey. 2007. *RegCM version 3.1: User's Guide.* Trieste, Italy.

Ellicott, E., E. Vermote, L. Giglio and G. Roberts. 2009. Estimating biomass consumed from fire using MODIS FRE. *Geophys. Res. Lett.* **36**(L13401). Doi: 10.1029/2009GL038581.

Emanuel, K.A. 1991. A scheme for representing cumulus convection in large-scale models. *J. Atmos. Sci.* **48**. 2313-2335.

Emanuel, K.A. and M. Zivkovic-Rothman. 1999. Development and evaluation of a convection scheme for use in climate models. *J. Atmos. Sci.* **56**. 1766-1782.

Entekhabi, D. and S.E. Nicholson. 1988. *ENSO, sea surface temperatures and African rainfall.* Proc. 12th Annual Climate Diagnostics workshop. National Oceanic and Atmospheric Administration, 135-145.

Evan, A.T. 2007. Comment on "How nature foiled the 2006 hurricane forecasts". *EOS, Trans. Amer. Geophys. Union.* **88** 271.

Fishman, J., K. Fakhruzzaman, B. Cros and D. Nganga. 1991. Identification of widespread pollution in the southern hemisphere deduced from satellite analyses. *Science*. **252**. 1693-1696.

Fishman, J., G. Brackett, E. V. Browell, and W. B. Grant. 1996. Tropospheric ozone derived from TOMS/SBU measurements during TRACE-A. *J. Geophys. Res*. **101**(D19). 24,069–24,082.

Foltz, G.R. and M.J., McPhaden. 2008. Impact of Saharan dust on tropical Norht Atlantic SST, *J. Clim.* **21**. 5048-5060.

Formenti, P., H. Winkler, P. Fourie, S. Piketh, B. Makgopa, G. helas and M.O. Andreae. 2002. Aerosol optical depth over a remote semi-arid region of South Africa from spectral measurements of the daytime solar extinction and the nighttime stellar extinction. *Atmos. Res.* **62**. 11-32.

Formenti, P., W. Elbert, W. Maenhaut, J. Haywood, S. Osborne and M.O. Andreae. 2003. Inorganic and carbonanceous aerosol during the Southern African Regional Science Initiative (SAFARI 2000) experiment: Chemical characteristics, physical properties and emission data for smoke from African biomass burning. *J. Geophys. Res.* **108**(D13,8488). Doi:10.1029/2002JD002408.

Forsberg, B. H.-C. Hansson, C. Johansson, H. Areskoug, K. Persson and B. Jarvholm. 2005. Comparative health impact assessment of local and regional particulate air pollutatns in Scandinavia. *Ambio*. **34**. 11-19.

Freiman, M.T. and P.D. Tyson. 2000. The thermodynamic structure of the atmosphere over South Africa: Implications for water vapour transport. *Water S. Afr.* **26**. 153-158.

Freiman, M.T., M.R. Jury and S. Medcalf. 2002. The state of the atmosphere over South Africa during the Southern African Regional Science Inititatve (SAFARI 2000). *S. Afr. J. Sci.* **98**. 91-96.

Freiman, M.T. and S.J. Piketh. 2003. Air transport into and out of the industrial Highveld region of South Africa. *J. Appl. Meteo.* **42**. 994-1002.

Fritsch, J.M. and C.F. Chappell. 1980. Numerical prediction of convectively driven mesoscale pressure systems. Part 1: Convective parameterization. *J. Atmos. Sci.* **37**. 1722-1733.

Frost, P.G.H. 1999. *Fire in southern Africna woodlands: origins, impacts, effects and control*. Proceedings of an FAO meeting on public policies affecting forest fires, FAO forestry paper 138. 181-205.

Fuller, K.A., W.C. Malm and S.M. Kreidenweis. 1999. Effects of mixing on extinction by carbonaceous particles. *J. Geophys. Res.* **104**(D13). 15941-15954.

Ganzeveld, L., J. Lelieveld, and G. J. Roelofs. 1998. A dry deposition parameterization for sulfur oxides in a chemistry and general circulation model. *J. Geophys. Res.* **103**. 5679–5694.

Gao, Y. and J.R. Anderson. 2001. Characteristics of Chinese aerosols determined by individual particle analysis. *J. Geophys. Res.* **106**. 18037-18045.

Garstang, M., P.D. Tyson, R.J. Swap, M. Edwards, P. Kallberg and J.A. Lindesay. 1996. Horizontal and vertical transport of air over southern Africa. *J. Geophys. Res.* **101**. 23,721-23,736.

Garstang, M., W.N. Ellery, T.S. Scholes, M.C. Scholes, R.J. Swap and P.D. Tyson. 1998. The contribution of aerosol- and water-borne nutrients to the functioning of the Okavango Delta, Botswana. *S. Afr. J. Sci.* **94**. 215-222.

Giglio, L. 2007. Characterization of the tropical diurnal fire cycle using VIRS and MODIS observations. *Remote Sens. Environ.* **108**. 407-421.

Gillette, D.A., B. Marticorena and G. Bergametti. 1998. Change in the aerodynamic roughness height by saltating grains: Experimental assessment, test tof theory and operational parameterisation. *J. Geophys. Res.* **103**. 6203-6210.

Giorgi, F. and W.L. Chameides. 1986. Rainout lifetimes of highly soluble aerosols and gases as inferred from simulations with a general circulation model. *J. Geophys. Res.* **91**. 14367-14376.

Giorgi, F. and G. Bates. 1989. The climatological al skill of a regional model over complex terrain. *Mon. Wea. Rev.* **117**. 2325 – 2347.

Giorgi, F. 1990. Simulation of regional climate using a limited area model nested in a general circulation model. *J. Clim*. **3**. 941-963.

Giorgi, F., M.R. Marinucci and G.T. Bates. 1993. Development of a second-generation regional climate model (RegCM2). Part II: Convective processes and assimilation of lateral boundary conditions. *Mon. Weather Rev.* **121**. 2814-2832.

Giorgi, F., L.O. Shields and L. McDaniel. 1998. Regional nested model simulations of present day and 2xCO2 climate over the Central Plains of the US. *Climatic. Change.* **40**. 457-493.

Giorgi, F. and L. O. Mearns. 1999. Introduction to special section: Regional climate modeling revisited. *J. Geophys. Res*. **104**. 6335 – 6352.

Giorgi, F. and X. Bi. 2000. A study of internal variability of a regional climate model. *J. Geophys. Res.* **205**. 29,503-29,521.

Giorgi, F. and R. Francisco. 2000. Evaluating uncertainties in the prediction of regional climate change. *Geophys. Res. Lett.* **27**. 1295-1298.

Giorgi, F., P.H. Whetton, R.G. Jones, J.H. Christensen, L.O . Mearns, B. Hewitson, H. von Storch, R. Francisco and C. Jack. 2001. Emerging patterns of simulated regional climatic

changes for the 21st century due to anthropogenic forcings. *Geophys. Res. Lett.* **28**. 3317-3320.

Giorgi, F., X. Bi and Y. Qian. 2003. Indirect vs. direct effects of anthropogenic sulfate on the climate of east asia as simulated with a regional couple climate-chemistry/aerosol model. *Climatic Change.* **58**. 345-376.

Giorgi, F., Bi, X. and J.S. Pal. 2004. Mean, interannual variability and trends in a regional climate change experiment over Europe. I. Present-day climate (1961-1990). *Clim. Dyn.* **22**. 733-756.

Giorgi, F., J.S. Pal, X. Bi, L. Sloan, N. Elguindi and F. Solmon. 2006. Introduction to the TAC special issue: The RegCNET network. *Theor. Appl. Climatol.* **86**. 1-4.

Gloudemans, A.M.S., M.C. Krol, J.F. Meirink, A.T.J. de Laat, G.R. van der Werf, H. Schrijver, M.M.P. van den Broek and I. Aben. 2006. Evidence for long-range transport of carbon monoxide in the Southern Hemisphere from SCHIAMACHY observations. *Geophys. Res. Lett.* **33**(L16807). Doi: 10.1029/2006GL026804.

Gong, S.L., L.A. Barrie, J.P. Blanchet, K. von Salzen, U. Lohmann, G. Lesins, L. Spacek, L. M. Zhang, E. Girard, H. Lin, R. Leaitch, H. Leighton, P. Chylek and P. Huang. 2003. Canadian Aerosol Module: A size-segregated simulation of atmospheric aerosol processes for climate and air quality models 1. Module development. *J. Geophys. Res.* **108**(D1, 4007). Doi: 10.1029/2001JD002002.

Goudie, A.S. and G.L. Wells. 1995. The nature, distribution and formation of pans in arid zones, *Earth-Sci. Rev.* **38**. 1-69.

Grell, G.A. 1993. Prognostic evaluation of assumptions used by cumulus parameterizations. *Mon. Wea. Rev.* **121**. 764-787.

Grell, G.A., J. Dudhia and D.R. Stauffer. 1994. *A description of the fifth-generation Penn State/NCAR mesoscale model version 5 (MM5).* Technical note TN-398+IA, Technical Report, Natl. Cent. for Atmos. Res. Boulder, Colorado.

Gurjar, B.R. and J. Lelieveld. 2005. New directions: Megacities and global change. *Atmos. Env.* **39**. 391-393.

Hahn, H. 1980. Organic constituents of natural aerosol. *Ann. N.Y. Acad. Sci.* **338**. 359-376.

Hansen, J., M. Sato and R. Reudy. 1997. Radiative forcing and climate response. *J. geophys. Res.* **102**. 6831-6864.

Harrison, M.S.J. 1988. *A synoptic climatology of South African variations*. Ph.D. thesis. 341pp. University of the Witwatersrand, Johannesburg, South Africa.

Hao, W.M., D.E. Ward, R.A. Susott, R.E. Babbitt, B.L. Nordgren, Y.J. Kaufman, B.N. Holben and D. M. Giles. 2005. Comparison of aerosol optical thickness measurements by MODIS, AERONET sun photometers and Forest Service handheld sunphotometers in southern Africa during the SAFARI 2000 campaign. *Int. J. Rem. Sens.* **26**. 4169-4183.

Haywood, J.M., V. Ramaswamy and L.J. Donner. 1997. A limited-area model case study of the effects of sub-grid scale variations in relative humidity and cloud upon the direct radiative forcing of sulphate aerosol. *Geophys. Res. Lett.* **24**. 143-146.

Heinemann, T. and J. Fischer. 2000. Remote sensing of total direct aerosol radiative forcing from MERIS measurements: A comparison of two different retrieval schemes. *Phys. Chem. Earth(B).* **25**. 101-106.

Heitzenberg, J., R.J. Charlson, A.D. Clarke, C. Liousse, V. Ramaswamy, K.P. Shine, M. Wendisch and G. Helas. 1997. Measurements and modelin of aerosol single-scattering albedo: Progress, problems and prospects. *Beitr. Phys. Atmos.* **70**. 249-263.

Helas, G. and J.J. Pienaar. 1996. The influence of vegetation fires on the chemical composition of the atmosphere. *S. Afr. J. Sci.* **92**. 132-136.

Held, G., H. Scheifinger and G.M. Snyman. 1994. Recirculation of pollutants in the atmosphere of the South African Highveld. *S. Afr. J. Sci.* **90**. 91-97.

Hewitson, B.C. and R.G. Crane. 2006. Consensus between GCM climate change projections with empirical downscaling: Precipitation downscaling over South Africa. *Int. J. Clim.* **26**. 1315-1337.

Hobbs, P.V., J.S. reid, R.A. Kotchenruther, R.J. Ferek and R. Weiss. 1997. Direct radiative forcing by smoke from biomass burning. *Science.* **275**. 1776-1778.

Hobbs, P.V., P. Sinha, R.J. Yokelson, T.J. Christian, D.R. Blake, S. Gao, T.W. Kirchstetter, T. Novakov and P. Pilewskie. 2003. Evolution of gases and particles from a savanna fire in South Africa. *J. Geophys. Res.* **108**(D13,8485). Doi: 10.1029/2002JD002352.

Hoffa, E.A., D.E. Ward, W.M. Hao, R.A. Susott and R.H. Wakimoto. 1999. Seasonality of carbon emissions from biomass burning in a Zambian savanna. *J. Geophys. Res.* **104**. 13841-13853.

Holben, B.N., T.F. Eck, I. Slutsker, D. Tanre, J.P. Buis, A. Setzer, E. Vermote, J.A. Reagan, Y.J. Kaufamn, T. Nakajima, F. Lavenu, I, Jankowiak and A. Smirnov. 1998. AERONET – A federated instrument network and data archive for aerosol characterisation. *Rem. Sens. Env.* **66**. 1-16.

Holtslag, A.A.M., E.I.F. DeBruijn and H.L. Pan. 1990. A high-resolution air mass transformation model for short-range weather forecasting. *Mon. Wea. Rev.* **118**. 1561-1575.

Horrel, J.D. and J.M. Wallace. 1981. Planetary-scale atmosphere phenomena associated with the Southern Oscillation. *Mon. Wea. Rev.* **109**. 813-829.

Hsie, E.Y., R.A. Anthes and D. Keyser. 1984. Numerical simulation of frontogenisis in a moist atmosphere. *J. Atmos. Sci.* **41**. 2581-2594.

Huang, Y., W.L. Chameides and R.E. Dickinson. 2007. Direct and indirect effects of anthropogenic aerosol over east Asia. *J. Geophys. Res.* **112**(D03212). Doi:10.1029/2006JD007114.

Hudson, D.A and R.G. Jones. 2002a. *Simulations of present-day and future climate over southern Africa using HadAM3H*. Hadley Centre technical note 38. Hadley Centre for Climate Prediction and Research. Met. Office. Bracknell, U.K.

Hudson, D.A and R.G. Jones. 2002b. *Regional climate model simulations of present-day and future climates of southern Africa*. Hadley Centre technical note 39. Hadley Centre for Climate Prediction and Research. Met. Office. Bracknell, U.K.

Hulme, M., R.M. Doherty, T. Ngara, M.G. New and D. Lister. 2001. African climate change 1900-2100. *Clim. Res.* **17**. 145-168.

Hurrell, J.W. 1995. Decadal trends in the North Atlantic Oscillation: Regional temperatures and precipitation. *Science*. **269**. 676–679.

Husar, R. B., J. M. Prospero, and L. L. Stowe. 1997. Characterization of tropospheric aerosols over the oceans with the NOAA advanced very high-resolution radiometer optical thickness operational product. *J. Geophys. Res*. **102**. 16,889–16,909.

Ichoku, C., L.A. Remer, Y.J. Kaufman, R. Levy, D.A. Chu, D. Tanre and B.N Holben. 2003. MODIS observation of aerosols and estimation of aerosol radiative forcing over southern Africa during SAFARI 2000. *J. Geophys. Res.* **108**(D13,8499). Doi: 10.1029/2002JD002366.

Im, E.S., J.B. Ahn, W.T. Kwon and F. Giorgi. 2008. Multi-decadal scenario simulation over Korea using a one-way double-nested regional climate model system. Part II: future climate projection (2021– 2050). *Clim. Dyn*. **30.** 9–254

Jaenicke, R. 1993. Tropospheric aerosols. *In: Hobbs, P.V. (eds), Aerosol-cloud-climate interactions*. Academic. New York. p1-131.

Jain, A.K. 2007. Global estimation of CO emissions using three sets of satellite data for burned area. *Atmos. Env.* **41**. 6931-6940.

Janowiak, J.E. 1988. An investigation of interannual rainfall variability in Africa. *J. Clim.* **1**. 240-255.

Janowiak, J.E. 1993. Seasonal climate summary: The global climate for September-November 1991: Warm (ENSO) episode conditions strengthen. *J. Clim.* **6**. 1616-1638.

Jayaratne, E.R. and T.S. Verma. 2001. The impact of burning on the environmental aerosol concentration in Gabarone, Botswana. *Atmos. Env.* **35**. 1821-1828.

Jenkins, G. 1997. The 1988 and 1990 summer season simulations for West Africa using a regional climate model. *J. Clim.* **10**. 1255-1272.

Johnson, B.T., K.P. Shine and P.M. Forster. 2004. The semi-direct aerosol effect: Impact of absorbing aerosols on marine stratocumulus. *Q. J. R. Meteorol. Soc.* **130**. 1407-1422.

Jones R.G., J.M. Murphy, and M. Noguer. 1995. Simulation of climate change over Europe using a nested regional climate model I: assessment of control climate, including sensitivity to location of lateral boundary conditions. *Q. J. R. Meteorol. Soc*. **121.** 1413-1449

Joubert, A.M. and M.O. Kohler. 1996. Projected temperature increases over southern Africa due to increasing greenhouse gases and sulphate aerosols. *S. Afr. J. Sci.* **92**. 524-527

Joubert, A.M., J.J. Katzfey, J.L. McGregor and K.C. Nguyen. 1999. Simulating midsummer climate over southern Africa using a nested regional climate model. *J. Geophys. Res.* **104**. 19,015-19,025.

Junker, C. and C. Liousse. 2008. A global emissions inventory of carbonaceous aerosol from historical records of fossil fuel and biofuel consumption for the period 1860-1997. *Atmos. Chem. Phys.* **8**. 1195-1207.

Jury, M.R., C.J. Pathack, W.D. Rautenbach and J.V. Heerden. 1996. Drought over southern African and Indian Ocean SST: statistical correlations and GCM results. *Glob. Ocean. Atmos. Syst.* **4**. 47-63.

Jury, M.R., W.B. White and C.J. Reason. 2004. Modeling the dominant climate signals around southern Africa. *Clim. Dyn.* **23**. 717-726.

Jury, M. 2009. Climate and weather factors modulating river flows in southern Angola. *Int. J. Climatol.* **30**. 901-9008.

Jury, M.R. and K. Whitehall. 2009. Warming of an elevated layer over Africa. *Climatic Change*. **99**. 229-245.

Justice, C.O., J.D. Kendall, P.R. Dowtry and R.J. Scholes. 1996. Satellite remote sensing of fires during the SAFARI campaign using NOAA advanced vary high-resolution radiometer data. *J. Geophys. Res*. **101**. 23851-23863.

Kalashnikova, O.V.K. and I.N. Sokolik. 2004. Modeling the radiative properties of non-spherical soil-derived mineral aerosols. *J. Quan. Spectroscopy Rad. Trans.* **87**. 137-166.

Kanamitsu, M., W. Ebisuzaki, J. Woollen, S.-K. Yang, J.J. Hnilo, M. Fiorino, and G. L. Potter. 2002. NCEP-DEO AMIP-II Reanalysis. *Bul. Atmos. Met. Soc*. 1631-1643.

Kasibhatla, P., W. L. Chameides, and J. St. John. 1997. A three dimensional global model investigation of seasonal variation in the atmospheric burden of anthropogenic sulfate aerosols. *J. Geophys. Res.* **102**. 3737– 3759.

Kasten, F. 1969. Visibility in the prephase of condensation. *Tellus.* **21**, 631–635.

Kaufman, Y.J., R.S. Fraser and R.L. mahoney. 1991. Fossil fuel and biomass burning effect of climate – heating or cooling? *J. Clim.* **4**. 578-588.

Kaufman, Y.J., et al. 1997. Passive remoste sensing of tropospheric aerosol and atmospheric correction for the aerosol effect. *J. Geophys. Res.* **102**. 16815-16830.

Kaufman, Y.J., D. Tanré and O. Boucher. 2002. A satellite view of aerosols in the climate system. *Nature.* **419**. 215-223.

Keen, C.S. 1971. *Rainfall spectra and the delimination of rainfall regimes in South Africa*. M.Sc. report. Climatology Research group. University of the Witwatersrand. Johannesburg, South Africa.

Keil, A. and J.M. Haywood. 2003. Solar radiative forcing by biomass burning aerosol particles during SAFARI 2000: A case study based on measured aerosol and cloud properties. *J. Geophys. Res.* **108**(D13,8467). Doi: 10.1029/2002JD002315.

Kgatuke, M.M., W.A. Landman, A. Beraki and M.P. Mbedzi. 2008. The internal variability of the RegCM3 over South Africa. *Int. J. Climatol.* **28**. 505-520.

Kiehl, J.T. and B.P. Briegleb. 1993. The relative rol of sulfate aerosols and greenhouse gases in climate forcing. *Science.* **260**. 311-314.

Kiehl, J.T., J.J. Hack, G.B. Bonan, B.A. Boville, B.P. Briegleb, D.L. Williamson and P.J. Rasch. 1996. *Description of the NCAR community climate model (CCM3).* NCAR Technical note, NCAR/TN-420+STR. Natl. Cent. for Atmos. Res., Boulder, Colorado. 152pp.

Kiehl, J. T., T. L. Schneider, P. J. Rasch, and M. C. Barth. 2000. Radiative forcing due to sulfate aerosols from simulations with the National Center for Atmospheric Research Community Climate Model version 3. *J. Geophys. Res*. **105**, 1441–2739.

Kiladis, G.N. and H.F. Diaz. 1989. Global climate anomalies associated with extremes in the Southern Oscillation. *J. Clim.* **2**. 1069-1090.

King, M.D., Y.J. Kaufman, D. Tanré and T. Nakajima. 1999. Remote sensing of tropospheric aerosols from space: Past, present and future. *Bull. Amer. Meteor. Soc.* **80**. 2229-2259.

Kinne, S., U. Lohmann, J. Feichter, M. Schulz, C. Timmreck, S. Ghan, R. Easter, M. Chin, P. Ginoux, T. Takemura, I. Tegen, D. Koch, M. Herzog, J. Penner, G. Pitari, B. Holben, T. eck, A. Smirnov, O. Dubovik, I. Slutsker, D. Tanre, O. Torres, M. Mischenko, I. Geogdzhayev, D.A.

Chu and Y. Kaufman. 2003. Monthly averages of aerosol properties: A global comparison models, satellite data and AERONET ground data. *J. Geophys. Res.* **108**(D20,4634). Doi: 10.1029/2001JD001253.

Kinne, S., M. Schulz, C. Textor, S. Guibert, Y. Balkanski, S.E. Bauer, T. Berntsen, T.F. Berglen, O. Boucher, M. Chin, W. Collins, F. Dentener, T. Diehl, R. Easter, J. Feichter, D. Fillmore, S. Ghan, P. Ginoux, S. Gong, A. Grini, J. Hendricks, M. Herzog, L. horowitz, I. Isaksen, T. Iversen, A. Kirkevag, S. Kloster, D. Koch. J.E. Kristjansson, M. Krol, A. Lauer, J.F. Lamarque, G. Lesins, X. Liu, U. Lohmann, V. Montanaro, G. Myhre, J.E. Penner, G. Pitari, S. Reddy, O. Seland, P. Stier, T. Takemura and X. Tie. 2006. An AEROCOM initial assessment – optical properties in aerosol component modules of global models. *Atmos. Chem. Phys.* **6**. 1815-1834.

Kirkman, G.A., S.J. Piketh, G. Helas, H.J. Annegarn and M.O. Andreae. 1998. Seasonal tropospheric aerosol characteristics over southern Africa. *J. Aerosol Sci.* **29**. S555-S556.

Kirkman, G. A., S. J. Piketh, M. O. Andreaea, H. J. Annegarn and G. Helas. 2000. Distribution of aerosols, ozone and cabon monoxide over southern Africa. *S.Afr. J. Sci.* **96**. 423-431.

Kohonen, T. 1995. *Self-Organizing Maps.* Springer series in Information Sciences. **30**. Springer, Berlin.

Konare, A. A.S. Zakey, F. Solmon, F. Giorgi, S. Rauscher, S. Ibrah and X. Bi. 2008. A regional climate modeling study of the effect of desert dust on the West Africa monsoon. *J. Geophys. Res.* **113**(D12206). Doi: 10.1029/2007JD009322.

Koren, I., Y.J. Kaufman, L.A. Remer and J.V. Martins. 2004. Measurement of the effect of Amazon smoke on inhibition of cloud formation. *Science.* **303**. 1342-1345.

Korontzi, S., D.P. Roy, C.O. Justice and D.E. Ward. 2004. Modelling and sensitivity analysis of fire emissions in southern Africa during SAFARI 2000. *Rem. Sens. Env.* **92**. 376-396.

Korontzi, S. 2005. Seasonal patterns of biomass burning emissions from southern Africa vegetation fires for the year 2000. *Glob. Change Biol.* **11**. 1-21.

Kruger, O. and H. Grasl. 2002. The indirect aerosol effect over Europe. *Geophys. Res. Lett.* **29**. Doi: 10.1029/2001GL014081.

Kruger, O., R. Marks and H. Grasl. 2004. Influence of pollution on cloud reflectance. *J. Geophys. Res.* **109**. Doi: 10.1029/2004JD004625.

Labonne, M., F.M. Bréon and F. Chevallier. 2007. Injection height of biomass burning aerosols as seen from a spaceborne lidar. *Geophys. Res. Lett.* **112**(L11806) Doi:10.1029/2007GL029311.

Landman, W.A., A. Seth and S.J. Camargo. 2005. The effect of regional climate model domain choice on the simulation of tropical cyclone-like vortices in the southwestern Indian Ocean. *J. Clim.* **18**. 1263-1274.

Latif, M. and T.P. Barnett. 1995.Interactions of the tropical oceans. *J. Clim.* **8**. 952-964.

Lau, K.M., M.K. Kim and K.M. Kim. 2006. Asian summer monsoon anomalies induced by aerosol direct forcing: the role of the Tibetan Plateau. *Clim. Dyn.* **26**. 855-864.

Lau, K.M. and K.M. Kim. 2007. Reply to comment on "How nature foiled the 2006 hurricane forecasts", *EOS Trans. Amer. Geophys. Union.* **88**. 105-107.

Lau, K.M., M.K. Kim, Y.C. Sud and G.K. Walker. 2009. A GCM study of the response of the atmospheric water cycle of West Africa and the Atlantic to Saharan dust radiative forcing. *Ann. Geophys.* **27**. 4023-4037.

Leahy, L.V., T.L. Anderson, T.F. Eck and R.W. Bergstrom. 2007. A synthesis of single scattering albedo of biomass burning aerosol over southern Africa during SAFARI 2000. *Geophys. Res. Lett.* **34**(L12814). Doi: 10.1029/2007GL029697.

Le Canut, M.O. Andreae, G.W. Harris, F.G. Wienhold and T. Zenker. 1996. Airborne studies of emissions from savanna fires in southern Africa 1. Aerosol emissions measured with a laser optical particle counter. *J. Geophys. Res.* **101**. 23,615-23,650.

Li, J. M. Posfai, P.V. Hobbs and P.R. Buseck. 2003. Individual aerosol particles from biomass burning in southern Africa: 2. Compositions and aging of inorganic particles. *J. Geophys. Res.* **108**. Doi: 10.1029/2002JD002310.

Liao, H., and J. H. Seinfeld. 1998. Radiative forcing by mineral dust aerosols: sensitivity to key variables. *J. Geophys. Res.* **103**(D24). 31,637–31,645.

Lindesay, J.A., M.O. Andreae, J.G. Goldammer, G. Harris, H.J. Annegarn, M. Garsta, R.J. Scholes and B.W. van Wilgen. 1996. International Geosphere-Biosphere Programme/International Global Atmospheric Chemistry SAFARI-92 field experiment: Background and overview. *J. Geophys. Res.* **101**. 23,521-23,530.

Liousse, C., J.E. Penner, C. Chuang, J.J. Walton, H. Eddleman and H. Cachier. 1996. A global three-dimentionsal model study of carbonaceous aerosols. *J. Geophys. Res.* **101**. 19,411-19,432.

Liousse, C., B. Guillaume, J.M. Grégoire, M. Mallet, C. Galy, A. Poirson, F. Solmon, V. Pont, A. Mariscal, L. Dungal, R. Rosset, V. Yoboué, X. Bedou, D. Serça, A. Konaré, C. Granier and A. Mieville. 2010. African Aerosols modeling during the EOP-AMMA campaign with updated biomass burning inventories. *Atmos. Chem. Phys.* **10**. 9631-9646.

Liu, X.D., S.O.Dong, P. Van Espen, F. Adams, J. Cafmeyer and W. Maenhaut. 2000. Size and chemical characterisation of atmospheric aerosol and savanna fire samples in southern Africa. *J. Aerosol. Sci.* **31**. S186-S187.

Liu, J., D.L. Mauzerall and L.W. Horowitz. 2009. Evaluating inter-continental transport of fine aerosols: (2) Global health impact. *Atmos. Env.* **43**. 4339-4347.

Lohmann, J. Feichter, C.C. Chuang and J.E. Penner. 1999. Prediction of the number of cloud droplets in the ECHAM GCM. *J. Geophys. Res.* **104**. 9169-9198.

Lohmann, U. and J. Feichter. 2005. Global indirect aerosol effects: A review. *Atmos. Chem. Phys.* **5**. 715-737.

Loveland, T.R. et al. 2000. Development of a global land cover characteristics database and IGBP DISCover from 1-km AVHRR data. *Int. J. Remote. Sens*. **21**.1303–1330.

Lukacs, H., A. Gelencser, S. Hammer, H. Puxbaum and C. Pio. 2007. Seasonal trends and possible sources of brown carbon based on 2-year aerosol measurements at six sites in Europe. *J. Geophys. Res.* **112**(D23). S18.

Maenhaut, W., I. Salma, J. Cafmeyer, H.J. Annegarn and M.O. Andreae. 1996. Regional atmospheric aerosol compositiona and sources in the eastern Transvaal, South Africa, and impact of biomass burning. *J. Geophys. Res.* **101**. 23631-23650.

Magi, B.I., P.V. Hobbs, B. Schmid and J. Redemann. 2003. Vertical profiles of light scattering, light absorption and single scattering albedo during the dry, biomass burning season in

southern Africa and comparisons of in situ remote sensing measurements of aerosol optical depths. *J. Geophys. Res.* **108**(D13,8504). Doi:10.1029/2002JD002361.

Mahowald, N.M., R.G. Bryant, J. del Corral and L. Steinberger. 2003. Ephemeral lakes and desert dust sources. *Geophys. Res. Lett.* **30**. Doi: 10.1029/2002GL016041.

Marticorena, B and G. Bergametti. 1995. Modeling the atmospheric dust cycle. Part 1: Design of soil-derived dust emission scheme. *J. Geopys. Res.* **100**(D8). 16,415-16,430.

Martin, J.H., R.M. Gordon and S.E. Fitzwater. 1990. Iron in Antarctic waters. *Nature.* **345**. 156-158.

Martins, J.J., R.S. Dhammapala, G. Lachmann, C. Galy-Lacaux and J.J. Pienaar. 2007. Long-term measurements of sulphur dioxide, nitrogen dioxide, ammonia, nitric acid and ozone in southern Africa using passive samplers. *S. Afr. J. Sci.* **103**. 1-7.

Martinez Avellaneda, N. 2010. *The impact of Saharan dust on the North Atlantic circulation*. PhD thesis. 107pp. Univ. Hamburg, Hamburg.

Mason, S.J. 1990. Temporal variability of sea surface temperatures around southern Africa: a possible forcing mechanism for the eighteen-year rainfall oscillation? *S. Afr. J. Sci.* **86**. 243-252.

Mason, S.J. and M.R. Jury. 1997. Climatic variability and change over southern Africa: a reflection on underlying processes. *Prog. In Phys. Geogr.* **21**. 23-50.

Mason, S. J., P. R. Waylen, G. M. Mimmack, B. Rajaratnam, and J. M. Harrison, 1999: Changes in extreme rainfall events in South Africa. *Climatic Change.* **41**. 249-257.

Matzler, C. 2002. *MATLAB functions for Mie scattering and absorption*. IAP Res. Rep. No. 02–08.

McHugh, M.J. and J.C. Rogers. 2001. North Atlantic Oscillation influence on precipitation variability around the southeast African Convergence Zone. *J. Clim.* **14**. 3631-3642.

McMurry, P.H. and X.Q. Zhang. 1989. Size distributions of ambient organic and elemental carbon. *Aerosol Sci. Technol.* **10**. 430-437.

Meadows, M.E. and T.M. Hoffman. 2003. Land degradation and climate change in South Africa. *Geogr. J.* **169**. 168-177.

Mearns, L.O., F. Giorgi, L. McDaniel and C. Shields. 1995. Analysis of daily variability of precipitation in a nested regional climate model: comparison with observations and doubled CO2 results. *Global Planetary Change.* **10**. 55-78.

Menon, S., A.D. Del Genio, D. Koch and G. Tselioudis. 2002. GCM simulations of the aerosol indirect effect: Sensitivity to cloud parameterisation and aerosol burden. *J. Atmos. Sci.* **59**. 692-713.

Mieville, A., C. Granier, C. Liousse, B. Guillaume, F. Mouillot, J.-F. Lamarque, J.-M. Grégoire and G. Pétron. 2010. Emissions of gases and particles from biomass burning during the 20th century using satellite data and an historical reconstruction. *Atmos. Env.* **44**. 1469-1477.

Miller, R.L. and I. Tegen. 1998. Climate response to soil dust aerosols. *J. Clim.* **11**. 3247-3267.

Miller, R.I. and I. Tegen. 1999. Radiative forcing of a tropical direct circulation by soil dust aerosols. *J. Atmos. Sci.* **56**. 2403-2433.

Mishchenko, M.K., I.V. Geogdzhayev, B. Cairns, W.B. Rossow and A.A. Lacis. 1999. Qerosol retrievals over the ocean while using channel 1 qnd 2 AVHRR data: A sensitivity analysis and preliminary results. *Appl. Opt.* **38**. 7325-7341.

Mischenko, M.I., I.V. Geogdzhayev, L. Liu, J.A. Ogren, A.A. Lacis, W. Rossos, JW. Hovenier, H. Volten and O. Munoz. 2003. Aerosol retrievals from AVHRR radiances: effects of particle non-sphericity and absorption and an updated long-term global climatology of aerosol properties. *J. Quan. Spectroscopy Rad. Trans.* **75-80**. 953-972.

Mitchell, T.D., T.R. Carter, P.D. Jones, M. Hulme and M. New. 2004. *A comprehensive set of high-resolution grids of monthly climate for Europe and the globe: the observed record (1901-2000) and 16 scenarios (2001-2100).* Working paper 55, Tyndall Centre for Climate Change Research, Norwich.

Molina, M.J. and L.T. Molina. 2005. UNEP Sasakawa environment prize 20th anniversary. Panel discussion: Air.

Moody, J.L., A.A.P. Pszenny, A. Grandy, W.C. Keene. J.N. Galloway and G. Polian. 1991. Precipitation composition and its variability in the southern Indian Ocean: Amsterdam Island, 1980-1987. *J. Geophys. Res.* **96**. 20,769-20,786.

Moosmuller, H., S.M. Kreidenweis, J.L. Collett, Jr., and W.C. Malm. 2007. Characterisation of particle emissions from laboratory combustion of wildland fuels. *iLEAPS Newsletter*. **4**. 22-23.

Mouillot, F. and C.B. Field. 2005. Fire history and the global carbon budget: a 1ºx1º fire history reconstruction for the 20th century. *Glob. Change Biol.* **11**. 398-420.

Mphepya, J.N., J.J. Pienaar, C. Galy-Lacaux, G. Held and C.R. Turner. 2004. Precipitation chemistry in semi-arid areas of southern Africa: A case stuy of a rural and an industrial site. *J. Atmos. Chem.* **47**. 1-24.

Muller, J.F. 1992. Geographical distribution and seasonal vairation of surface emissions and deposition velocities of atmospheric gases. *J. Geophys. Res.* **97**. 3787-3804.

Myhre, G., T.K. Berntsen, J.M. Haywood, J.K. Sundet, B.N. Holben, M. Johnsrud and F. Stordal. 2003. Modeling the solar radiative impact of aerosols from biomass burning during the Southern African Regional Science Initiative (SAFARI 2000) experiment. *J. Geophys. Res.* **108**(D13,8501). Doi:10.1029/2002JD002313.

Myhre, G., F. Stordal, M. Johnsrud, D.J. Diner and I.V. Geogdzhayev. 2004. Intercomparison of satellite retrieved aerosol optical depth over ocean during the period September 1997 to December 2000. *Atmos. Chem. Phys.* **5**. 1697-1719.

Myhre, G., T.F. Berglen, M. Johnsrud, C.R. Hoyle, T.K. Berntsen, S.A. Christopher, D.W. Fahey, I.S.A. Isaksen, T.A. Jones, R. A. Kahn, N. Loeb, P. Quinn, L. Remer, J.P. Schwarz and K.E. Yrttri. 2008. Radiative forcing of the direct aerosol effect using a multi-observation approach. *Atmos. Chem. Phys. Discuss.* **8**. 12823-12886.

Myhre, G. 2009. Consistency between satellite-derived and modeled estimates of the direct aerosol effect. *Science*. **325**. 187-190.

New M, M. Hulme and P. Jones. 2000. Representing twentieth- century space-time climate variability. Part II: development of 1901–1996 monthly grids of terrestrial surface climate. *J. Clim*. **13**. 2217–2238

Nicholson, S.E. 1986. The nature of rainfall variability in Africa south of the equator. *J. Climatol.* **6**. 515-530.

Nicholson, S.E. 1996. A review of climate dynamics and climate variability in eastern Africa. *The limnology, climatology and paleoclimatology of the East African Lakes.* (T.C. Johnson and E.O. Odada, Eds.). Gordon and Breach. p25-56.

Nicholson, S.E. and J. Kim. 1997. The relationship of the El Niño-Southern Oscillation to African rainfall. *Int. J. Clim.* **17**. 117-135.

Nicholson, S.E. and J.P. Grist. 2003. The seasonal evolution of the atmospheric circulation over West Africa and Equatorial Africa. *J. Clim*. **16**. 1013-1030.

Noone, K. 2001. The indirect radiative effect of aerosols. *IGACtivities newsletter*. **23**. 16-17.

Nyanganyura, D., W. Maehaut, M. Mathuthu, A. Makarau and F. X. Meixner. 2007. The chemical composition of tropospheric aerosols and their contributing sources to a continental background site in northern Zimbabwe from 1994 to 2000. *Atmos. Env.* **41**. 2644-2659.

Organization for Economic Cooperation and Development (OECD). 1977. *The OECD program on long range transports of pollutants*. Summary report for the Organization for Economic Cooperation and Development. Paris.

Ogallo, L.J. 1988. Relationships between seasonal rainfall in east Africa and the Southern Oscillation. *J. Climatol.* **8**. 31-43.

Otter, L.B., R.J. Scholes, P. Dowty, J. Privette, K. Caylor, S. Ringrose, M. Mukelabai, P. Frost, N. Hanan, O. Totolo and E.M. Veenendaal. 2002. The Southern African Regional Science Initiative (SAFARI 2000): wet season campaigns. *S. Afr. J. Sci.* **98**. 131-137.

Pak, B.C. 2000. *Vertical structure of atmospheric trace gases over southeast Australia*. PhD. Thesis. Univ. of Melbourne, Australia (available at hhttp://adtl.lib.unimelb.edu.u/adt-root/public/).

Pak, B.C., R.L. Langenfelds, S.A. young, R.J. Francey, C.P. Meyer, L.M. Kivlighon, L.N. Cooper, B.L. Dunse, C.E. Allison, L.P. Steele, I.E. Galbally and I.A. Weeks. 2003. Measurements of biomass burning influences in the troposphere over southeast Australia during the SAFARI 2000 dry season campaign. *J. Geophys. Res.* **108**(D13,8480). Doi: 10.1029/2002JD002343.

Pal, J.S., E.E. Small and E.A.B. Eltahir. 2000. Simulation of regional-scale water and energy budgets: representation of subgrid cloud and precipitation processes within RegCM. *J. Geophys. Res.* **105**(D24). 29,579-29,594.

Pal, J.S. NS E.A.B. Eltahir. 2003. A feedback mechanism between soil moisture distribution and storm tracks. *Q. J. R. Meteorol. Soc*. **129**. 2279–2297.

Pal, J.S., F. Giorgi, X. Bi, N. Elguindi, F. Solmon, X. Gao, S.A. Rauscher, R. Francisco, A. Zakey, J. Winter, M. Ashfaq, F.S. Syed, J.L. Bell, N.S. Diffenbaugh, J. Karmaharya, A. Konare, D. Martinez, R.P. da Rocha, L.C. Sloan and A.L. Steiner. 2007. Regional climate modeling for the developing world: The ICTP RegCM3 and RegCNET. *Bull. Amer. Met. Soc.* **88**. 1395-1409.

Pan, Z., E.S. Takle, and F. Otieno. 2001. Evaluation of uncertainties in regional climate change simulations. *J. Geophys. Res*. **106**(D16). 17735–17752.

Penner, J.E., R.E. Dickinson and C.A. O'Neill. 1992. Effects of aerosol from biomass burning on the global radation budget. *Sci.* **256**. 1432-1434.

Penner, J.E., H. Eddleman and T. Novakov. 1993. Towaards the development of a global inventory for black carbon emissions. *Atmos. Env.* **27A**. 1277-1295.

Penner, J.E., C.C. Chuang and K. Grant. 1998. Climate forcing by carbonaceous and sulfate aerosols. *Clim. Dyn.* **14**. 839-851.

Penner, J.E., Zhang, S.Y., M. Chin, C.C. Chuang, J. Feichter, Y. Feng, I.V. Geogdzhayev, P. Ginoux, M. Herzog, A. Higurashi, D. Koch, C. Land, U. Lohmann, M. Mishchenko, T. Nakajima, G. Pitari, B. Soden, I. Tegen and L. Stowe. 2002. A comparison of model- and satellite-derived aerosol optical depth and reflectivity. *J. Atmos. Sci.* **59**. 441-460.

Perlwitz, J. and R.L. Miller. 2010. Cloud cover increase with increasing aerosol absorptivity: A counterexample to te conventional semidirect aerosol effect. *J. Geophys. Res.* **115**(D08203). Doi: 10.1029/2009JD012637.

Pham, M., J.F. Muller, G.P. Brasseur, C. Granier and G. Megie. 1995. A three-dimensional study of the tropospheric sulfur cycle. *J. Geophys. Res.* **100**. 26,061-26,092.

Pilewskie, P., J. Pommier, R. Bergstrom, W. Gore, S. Howard, M. Rabbette, B. Schmid, P.V. Hobbs and S.C. Tsay. 2003. Solar spectral radiative forcing during the Southern African Regional Science Initiative. *J. Geophys. Res.* **108**(D13,8486). Doi: 10.1029/2002JD002411.

Piketh, S.J., H.J. Annegarn and P.D. Tyson. 1999a. Lower tropospheric aerosol loadings over South Africa: The relative contribution of aerolian dust, industrial emissions and biomass burning. *J. Geophys. Res.* **104**. 1597-1607.

Piketh, S.J., R.J. Swap, C.A. Anderson, M. T. Freiman, M. Zunckel and G. Held. 1999. The Ben MacDhui high altitude trace gas and aerosol transport experiment. *S. Afr. J. Sci.* **95**. 35-43.

Piketh, S.J., P.D. Tyson and W. Steffen. 2000. Aeolian transport from southern Africa and iron fertilistation of marine biota in the South Indian Ocean. *S. Afr. J. Sci.* **98**. 244-246.

Pilewskie, P., J. Pommier, R. Bergstrom, W. Gore, S. Howard, M. Rabbette, B. Schmid, P.V. Hobbs and S.C. Tsay. 2003. Solar spectral radiative forcing during the Southern African Regional Science Initiative. *J. Geophys. Res.* Vol. **108**(D13,8486). Doi: 10.1029/2002JD002411.

Pilinis, C.,S.N. Pandis and J.H. Seinfeld. 1995. Sensitivity of direct climate forcing by atmospheric aerosols to aerosol size and composition. *J. Geophys. Res.* **100**. 18739-18754.

Pincus, R. and M. Baker. 1994. Precipitation, solar absorption and albedo susceptibility in marine boundary layer clouds. *Nature*. **372**. 250 – 252.

Posfai, M., R. Simonics, J. Li, P.V. Hobbs and P.R. Buseck. 2003. Individual aerosol particles from biomass burning in southern Africa: 1. Compositions and size distributions of carbonaceous particles. *J. Geophys. Res.* **108**(D13,8483). Doi:10.1029/2002JD002291.

Privette, J.L., Y. Tian, G. Roberts, R.J. Schole, Y. Wang, K.K. Caylor, P. Frost and M. Mukelabai. 2004. Vegetation structure characteristics and relationships of Kalahari woodlands and savannas. *Glob. Change. Bio.* **10**. 281-291.

Privette, J.L. and D.P. Roy. 2005. Southern Africa as a remote sensing test bed: the SAFARI 2000 Special Issue overview. *Int. J. Rem. Sens.* **26**. 4141-4158.

93. Prospero, J.M., P. Ginoux, O. Torres, S.E. Nicholson and T.E. Gill. 2002. Environmental characterisation of global sources of atmospheric soil dust identified with the Nimbus 7 Total Ozone Mapping Spectrometer (TOMS) absorbing aerosol product. *Rev. Geophys.* **40**. 1-31.

Pye, K. *Aeolian dust and dust deposits.* Academic. San Diego. California. 334pp.

Qian, Y., F. Giorgi, Y. Huang, W. Chameides and C. Luo. 2001. Regional simulation of anthropogenic sulfur over East Asia and its sensitivity to model parameters. *Tellus*. **53B**. 171-191.

Queface, A.J., S.J. Piketh, H.J. Annegarn, B.N. Holben and R.J. Uthui. 2003. Retrieval of aerosol optical thickness and size distribution from the CIMEL Sun photometer over Inhaca Island, Mozambique. *J. Geophys. Res.* **108**(D13,8509). Doi: 10.1029/2002JD002374.

Quijano, A.L., I.N. Sokolik and O.B. Toon. 2000. Influence of the aerosol vertical distribution on the retrievals of aerosol optical depth from satellite radiance measurements. *Geophys. Res. Lett.* **27**. 3457-3460.

Ramanathan, V. and G. Carmichael. 2008. Global and regional climate changes due to black carbon. *Nature Geosci*. **1**. 221-227.

Randles, C.A. and V. Ramaswamy. 2010. Direct and semi-direct impacts of absorbing biomass burning aerosol on the climate of southern Africa: a GeophysicalFluid Dynamics Laboratory GCM sensitivity study. *Atmos. Chem. Phys.* **10**. 9819-9831.

Ratham, J.V., F. Giorgi, A Kaginalkar and S. Cozzini. 2009. Simulation of the Indian monsoon using the RegCM3-ROMS regional coupled model. *Clim. Dyn. **33***. 119-139.

Reason, C.J.C. 2002. Sensitivity of the southern African circulation to dipole sea-surface temperature patterns in the south Indian ocean. *Int. J. Climatol.* **22**. 377-393.

Reason, C.J.C. and M. Roualt. 2005. Links between the Antarctic Oscillation and winter rainfall over western South Africa. *Geophys. Res. Lett.* **32**(L07705). Doi: 10.1029/2005GL022419.

Reason, C.J.C., F. Engelbrecht, W.A. Landman, J.R.E. Lutjeharms, S. Piketh, W. Rautenbach and B.C. Hewitson. 2006. A review of South Africa research in atmospheric science and physical oceanography during 2000-2005. *S. Afr. J. Sci.* **102**. 35-45.

Reid, J.S., P.V. Hobbs, R.J. Ferek, D.R. Blake, J Venderlei Martins, M.R. Dunlap and C. Liousse. 1998. Physical, chemical and optical properties of regional hazes dominated by smoke in Brazil. *J. Geophys. Res.* **103**(D24). 32,059-32,080.

Reissell, A. 2007. Editorial. *iLEAPS Newsletter 4*. p2.

Remer, L.A., Y.J. Kaufman, Z. Levin and S. Ghan. 2002. Model assessment of the ability of MODIS to measure top of atmosphere direct radiative forcing form smoke aerosols. *J. Atmos. Sci.* **59**. 657-667.

Remer, L.A., Y.J. Kaufman, D. Tanré, S. Mattoo, D.A. Chu, J.V. Martins, R.-R. Li, C. Ichoku, R.C. Levy, R.G. Kleidman, T.F. Eck, E. Vermote and B.N. Holben. 2005. The MODIS aerosol algorithm, products and validation, *J. Atmos. Sci.* **62**. 947-973.

Reusch, D. B., B. C. Hewitson, and R. B. Alley. 2005a. Towards ice core- based synoptic reconstructions of West Antarctic climate with artificial neural networks. Int. *J. Climatol.* **25**. 581-610.

Reusch, D.B., R.B. Alley and B.C. Hewitson. 2005b. Relative performance of self-organizing maps and principal component analysis in pattern extraction from synthetic climatological data. *Polar Geogr*. **29**. 188-212.

Reynolds, R.W., N.A. Rayner, T.M. Smith, D.C. Stokes, and W. Wang. 2002. An improved in situ and satellite SST analysis for climate. *J. Clim*. **15**. 1609-1625.

Richard, Y., S. Trzaska, P. Roucou and M. Roualt. 2000. Modification of the southern African rainfall variability/ENSO relationship since the late 1960s. *Clim. Dyn.* **16**. 883-895.

Richard, Y., N. Fauchereau, I. Poccard, M. Roualt and S. Trzaska. 2001. 20th century droughts in southern Africa: Spatial and temporal variability, teleconnections with oceanic and atmospheric conditions. *Int. J. Clim.* **21**. 873-885.

Roberts, G., M.J. Wooster and E. Lagoudakis. 2008. Annual and diurnal African biomass burning temporal dynamics. *Biogeosciences. Discuss.* **5**. 3623-3663.

Robertson, A.W., U. Lali, S.E. Zebaik and L. Goddard. 2004. Improved combination of multiple atmospheric AGCM ensembles for seasonal prediction. *Mon. Wea. Rev.* **132**. 2732–2744.

Rocha, A., and I. Simmonds. 1997a. Interannual variability of southeastern African summer rainfall. Part 1: relationships with air-sea interaction processes. *Int. J. Climatol.* **17**. 235-265.

Rocha, A., and I. Simmonds. 1997b. Interannual variability of southeastern African summer rainfall. Part 2: modelling the impact of sea surface temperatures on rainfall and circulation. *Int. J. Climatol.* **17**. 267-290.

Rogers, J.C. 1984. The association between the North Atlantic oscillation and the Southern oscillation in the Northern Hemisphere. *Mon. Weath. Rev.* **112**. 1999-2015.

Rogger, W.F, L.M. Hildemann, M.A. Mazurek, G.R. Cass and B.R.T. Simoneit. 1993. Cources of fine organic aerosol, 3. Road dust, tire debris and organometallic brake lining dust. *Environ. Sci. Technol.* **27**. 2700-2711.

Ropelewski, C.F. and M.S. Halpert. 1996. Quantifying Southern Oscillation-precipitation relationships. *J. Clim.* **9**. 1043-1059.

Ross, K.E., S.J. Piketh, R.T. Bruintjies, R.P. Burger, R.J. Swap and H.J. Annegarn. 2003. Spatial and seasonal variations in CCN distribution and the aerosol-CCN relationship over southern Africa. *J. Geophys. Res.* **108**(D13,8481). Doi: 10.1029/2002JD002384.

Roy, D.P., P.G.H. Frost, C.O. Justice, T. Landman, J.L. Le Roux, K. Gumbo, S. Makungwa, K. Dunham, R. Du Toit, K. Mhwandagara, A. Zacarias, B. Tacheba, O.P. Dube, J.M.C. Pereira, P. Mushove, J.T. Morisette, S.K. Santhanan Vannan and D. Davies. 2005. The Southern African Fire Network (SAFNet) regional burned-area product-validation protocol. *Int. J. Rem. Sens.* **26**. 4265-4295.

Salma, I., W. Maenhaut, H.J. Annegarn, M.O. Andreae, F.X. Meixner and M. Garstang. 1997. Combined application of INAA and PIXE for studying the regional aerosol composition in southern Africa. *J. Radioanal. Nucl. Chem.* **216**. 143–148.

Sang, B.H., A.E. Gelfand, C. Lennard, G. Hegerl and B. Hewitson. 2008. Interpreting self-organising maps through space-time data models. *Ann. Appl. Stat.* **4**. 1194-1216.

Satheesh, S.K. and K.K. Moorthy. 2005. Radiative effects of natural aerosols: A review. *Atmos. Env.* **39**. 2089-2110.

Schmid, B., J. Redemann, P.B. Russell, P.V. Hobbs, D.L. Hlavka, M.J. McGill, B.N. Holben, E.J. Welton, J.R. Campbell, O. Torres, R.A. Kahn, D.J. Diner, M.C. Helmlinger, D.A. Chu, C. Robles-Gonzalez and G. de Leeuw. 2003. Coordinated airborne, spaceborne and ground-based measurements of massive thick aerosol layers during the dry season in southern Africa. *J. Geophys. Res.* **108**(D13,8496). Doi: 10.1029/2002JD002297.

Scholes, R.J., J. Kendall and C.O. Justice. 1996. The quantity of biomass burned in southern Africa. *J. Geophys. Res.* **101**. 23,667-23,676.

Scholes, R.J. 1997. Savanna. In *Vegetation of southern Africa*. R.M Cowling, D.M. Richardson and S.M. Pierce (eds.). Cambridge Univeristy Press.Cambridge. p258-277.

Scholes, M. and M.O. Andeae. 2000. Biogenic and pyrogenic emissions from Africa and their impact on the global atmosphere. *Ambio.* **29**. 23-29.

Schutz, L. 1980. Long-range transport of desert dust with special emphasis on the Sahara. *Ann. N.Y. Acad. Sci.* **388**. 515-532.

Seinfeld, J.H. and S.N. Pandis. 2006. *Atmospheric chemistry and physics: from air pollution to climate*. Wiley. New York.

Seth, A, and F. Giorgi. 1998. The effects of domain choice on summer precipitation simulation and sensitivity in a regional climate model. *J. Clim.* **11**. 2698-2712.

Shugart, H.H., S.A. Macko, P. Lesolle, T.A.Szuba, M.M. Mukelabai, P. Dowty and R.J. Swap. 2004. The SAFARI-2000 Kalahari transect wet season campaign of year 2000. *Glob. Change. Biol.* **10**. 273-280.

Shukla, J. 1998. Predictability in the midst of chaos: a scientific basis for climate forecasting. *Science.* **282**. 728–731.

Sinclair, M.R., J.A. Renwick and J.W. Kidson. 1997. Low-frequency variability of Southern Hemisphere sea level pressure and weather system activity. *Mon. Wea. Rev.* **125**. 2531-2543.

Simmons, A.J., V. da Costa Bechtold, A.C.M. Beljaars, P.W. Kallberg, S. Saarinen, S.M. Uppala, P. Viterbo and N. Wedi. 2004. Comparison of trends and low-frequency variability in CRU, ERA-40 and NCEP/NCAR analyses of surface air temperature. *J. Geophys. Res.* **109**(D24115). Doi: 10.1029/2004JD005306.

Sinha, P., P.V. Hobbs, R.J. Yokelson, I.T. Bertschi, D.R. Blake, I.J. Simpson, S. Gao, T.W. Kirchstetter and T. Novakov. 2003. Emissions of trace gases and particles from savanna fires in southern Africa. *J. Geophys. Res.* **108**(D13,8487). Doi: 10.1029/2002JD002325.

Slingo, J.M. 1989. A GCM parameterization for shortwave radiative properties of water clouds. *J. Atmos. Sci.* **46**. 1419-1427.

Slingo, A., T.P. Ackerman, R.P. Allan, et al. 2006. Observations of the impact of a major Saharan dust storm on the atmospheric radiation balance. *Geophys. Res. Lett.* **33**(L24817). Doi:10.1029/2006GL027869.

Smirnov, A., B.N. Holben, T.F. Eck, I. Slutsker, B. Chatenet and R.T. Pinker. 2002. Diurnal variability of aerosol optical depth observed ar AERONET (Aerosol Robotic Netweork) sites. *Geophys. Res. Lett.* **29**(D23,2115). Doi: 10.1029/2002GL016305.

Solmon, F., F. Giorgi and C. Liousse. 2006. Aerosol modelling for regional climate studies: application to anthropogenic particles and evaluation over a European/African domain. *Tellus.* **58B**. 51-72.

Solmon, F., M. Mallet, N. Elguindi, F. Giorgi, A. Zakey, and A. Konare. 2008. Dust aerosol impact on regional precipitation over western Africa, mechanisms and sensitivity to absorption properties. *Geophys. Res. Lett.* **35**(L24705). Doi:10.1029/2008GL035900.

Solomon, S., D. Qin, M. Manning, Z. Chen, M. Marquis, K.B. Averyt, M. Tignor and H.L. Miller (eds.). 2007. *Contribution of Working Group I to the Fourth Assessment Report of the Intergovernmental Panel on Climate Change*. Cambridge University Press. Cambridge, United Kingdom and New York, NY, USA.

Spiro, P.A., D.J. Jacob and J.A. Logan. 1992. Global inventory of sulfur emissions with 1°x1° resolution. *J. Geophys. Res.* **97**. 6023-6036.

Stein, D.C., R.J. Swap, S. Greco, S.J. Piketh, S.A. Macko, B.G. Doddridge, T. Elias and R.T. Bruintjies. 2003. Haze layer characterisation and associated meteorological controls along the eastern coastal region of southern Africa. *J. Geophys. Res.* **108**(D13,8506). Doi: 10.1029/2002JD003237.

Steiner, A.L., J.S. Pal, S.A. Rauscher, J.L. Bell, N.S. Diffenbaugh, A. Boone, L.C. Sloan and F. Giorgi. 2009. Land surface coupling in regional climate simulations of the West African monsoon. *Clim. Dyn.* **33**. 869-829.

Stevens, R.K., T.G. Dzubay, C.W. Lewis and R.W. Shaw, Jr. 1984. Source apportionment methods applied to the determination of the origin of ambient aerosols that affect visibility in forested areas. *Atmos. Env.* **29**. 939-947.

Stroppiana, D., P.A. Brivio, , J-M. Gre´goire, C. Liousse, B. Guillaume, C. Granier, A. Mieville and M. Chin. 2010. Comparison of global monthly CO emission maps derived from remotely sensed burned area datasets. *Atmos. Chem. Phys*. *Discuss.* **10**. 17.657-17,697.

Sturman, A.P., P.D. Tyson and P.C. D'Abreton. 1997. A preliminary study of the transport of air from Africa and Australia to New Zealand. *J. R. Soc. New Zealand.* **27**. 485-498.

Sud, Y.C., E. Wilcox, W.K-M. Lau, G.K. Walker, X.H. Liu, A. Nenes, D. Lees, K.-M. Kim, Y. Zhou and P.S. Bhattacharjee. 2009. Sensitivity of boreal-summer circulation and precipitation to atmospheric aerosols in selected regions – Part 1: Africa and India. *Ann. Geophys.* **27**. 3989-4007.

Swap, R., M. Garstang, S.A. Macko, P.D. Tyson, W. Maenhaut, P. Artaxo, P. Kallberg and R. Talbot. 1996. The long-range transport of southern African aerosol to the tropical South Atlantic. *J. Geophys. Res.* **101**. 23,777-23,791.

Swap, R.J. and P.D. Tyson. 1999. Stable discontinuities as determinants of the vertical distribution of aerosols and trace gases in the atmosphere. *S. Afr. J. Sci.* **95**. 63-71.

Swap, R.J., H.J. Annegarn, J.T. Suttles, J. Haywood, M.C. Helmlinger, C. Hely, P.V. Hobbs, B.N. Holben, J. Ji, M.D. King, T. Landmann, W. Maenhaut, L. Otter, B. Pak, S. J. Piketh, S. Platnick, J. Privette, D. Roy, A.M. Thompson, D. Ward ad R. Yokelson. 2002a. The Southern African Regional Science Inititatve (SAFARI 2000): overview of the dry season field campaign. *S. Afr. J. Sci.* **98**. 125-130.

Swap, R.J., H.J. Annegarn and L.Otter. 2002b. Southern Afrian Regional Science Initiative (SAFARI 2000): Summary of science plan. *S. Afr. J. Sci.* **98**. 119-124.

Swap, R.J., H.J. Annegarn, J.T. Suttles, M.D. King, S. Platnick, J.L. Privette and R.J. Scholes. 2003. Africa burning: A thematic analysis of the Southern African Regional Science Initiative (SAFARI 2000). *J. Geophys. Res.* **108**(D13,8465). Doi: 10.1029/2003JD003747.

Sylla, M.B., E. Coppola, L. Mariotti, F. Giorgi, P.M. Rutti, A. Dell'Aquila and X. Bi. 2009. Multiyear simulation of the African climate using a regional climate model (RegCM3) with the high resolution ERA-interim reanalysis. *Clim. Dyn.* **35**. 231-247.

Tadross, M., C. Jack and B. Hewitson. 2005. On RCM-based projections of change in southern African summer climate. *Geophys. Res. Lett.* **32**(L23713). Doi: 10.1029/2005GL024460.

Tadross, M.A., W.J. Gutowski Jr., B.C. Hewitson, C. Jack and M. New. 2006. MM5 simulations of interannual change and the diurnal cycle of southern African regional climate. *Theor. Appl. Climatol.* **86**. 63-80.

Takemura, T., T. Nakajima, O. Dubovik, B.N. Holben and S. Kinne. 2002. Single-scattering albedo and radiative forcing of various aerosols species with a global three-dimensional model. *J. Clim.* **15**. 333-352.

Tan, Q., Y. Huang, and W. L. Chameides. 2002. Budget and export of anthropogenic SOx from east Asia during continental outflow conditions. *J. Geophys. Res*. **107**(D13,4167). Doi:10.1029/2001JD000769.

Tansey, K., J.M. Grégroire, P. Defoumy, R. Leigh, J.F. Pekel, E. von Bogaert and E. Bartholomé. 2008. A new, global, multi-annual (2000-2007) burnt area product at 1km resolution. *Geophys. Res. Lett.* **35**(L01401). Doi: 10.1029/2007GL031567.

Tanré, D., J. Haywood, J. Pelon, J.F. Léon, B. Chatenet, P. Formenti, P. Francis, P. Goloub, E.J. Highwood and G. Myhre. 2003. Measurement and modeling of the Saharan dust radiative impact: Overview of the Saharan Dust Experiment (SHADE). *J. Geophys. Res.* **108**(D18,8574). Doi: 10.1029/2002JD003273.

Taylor, K.E. and J.E. Penner. 1994. Response of the climate system to atmospheric aerosols and greenhouse gases. *Nature.* **369**. 734-737.

Tegen, I. and I. Fung. 1994. Modeling of mineral dust in the atmosphere: sources, transport and optical thickness. *J. Geophys. Res.* **99**. 22,897-22,914.

Tegen, I. and I. Fung. 1995. Contribution to the atmospheric mineral aerosol load from land surface modification. *J. Geophys. Res.* **100**. 18,707-18,729.

Tegen, I., A.A. Lacis and I. Fung. 1996. The influence of climate forcing of mineral aerosols from disturbed soils. *Nature*. **380**. 419-422.

Tegen, I., S.P. Harrison, K. Kohfeld, I.C. Prentice, M. Coe and M. Heimann. 2002. Impact of vegetation and preferential source areas on global dust aerosol: results from a model study. *J. Geophys. Res.* **107**. Doi: 10.1029/2001JD000963.

Terblanche, D.E., M.P. Mittermaier, S.J. Piketh, R.T. Bruintjies and R.P. Burger. 2000. The Aerosol Recirculation and Rainfall Experiment (ARREX): and initial study on aerosol-cloud interactions over South Africa. *S. Afr. J. Sci.* **96**. 15-21.

Thompson, D.W.J. and J.M. Wallace. 2000. Annular modes in the extra-tropical circulation. Part 1: Month-to-month variability. *J. Clim.* **13.** 1000-1016.

Thompson, D.W.J. and S. Solomon. 2002. Interpretation of recent Southern Hemisphere climate change. *Science.* **296**. 895-899.

Todd, M.C. and R. Washington. 2004. Climate variability in central equatorial Africa: Influence from the Atlantic sector. *Geophys. Res. Lett.* **31**(L23202). Doi:10.1029/2004GL020975.

Todd, M.C., et al. 2008a. Quantifying uncertainty in estimates of mineral dust flux: An intercomparison of model performance over the Bodélé Depression, northern Chad. *J. Geophys. Res.* **113**(D24107). Doi:10.1029/2008JD010476.

Todd, M.C., R. Washington, S. Raghavan, G. Lizcano and P. Knippertz. 2008b. Regional Model Simulations of the Bodélé Low-Level Jet of Northern Chad during the Bodélé Dust Experiment (BoDEx 2005). *J. Clim.* **21**. 995–1012.

Torrance, J.D. 1972. Malawi, Rhodesia and Zimbabwe. *World Survey of Climatology*: *Climates of Africa (J.F. Griffiths, Ed.).* Elsevier. p409-460.

Torres, O., P.K. Bhartia, J. R. Herman, Z. Ahmad, and J. Gleason. 1998. Deri- vation of aerosol properties from satellite measurements of back- scattered ultraviolet radiation: Theoretical basis. *J. Geophys. Res.* **103.** 17,099-17,110.

Torres, O., P.K. Bhartia, J.R.Herman, A.Sinyuk, P.Ginoux and B. Holben. 2002. A long-term record of aerosol optical depth from TOMS observations and comparison to AERONET measurements. *J. Atmos. Sci.* **59**. 398-413.

Trenberth, K. 1997. The definition of El Nino. *Bull. Amer. Meteorol. Soc.* **12**. 2771-2777.

Troccoli, A., and P. Kallberg. 2004. *Precipitation correction in the ERA-40 reanalyses*. ERA-40 Proj. Rep. 13. Eur. Cent. for Med.-Range Weather Forecasts. Reading. U.K. (Available at http://www.ecmwf.int/publications/library/ecpublications/_pdf/era40/ERA40_PRS13.pdf).

F. Tummon, F. Solmon, M. Tadross and C. Liousse. 2010. Simulation of the climatic impacts of the natural aerosol loading over southern Africa during the biomass burning season using RegCM3. *J. Geophys. Res*. **115**(D19206). Doi: 10.1029/2009JD013738.

Turn, S.Q., B.M. Jenkins, J.M. Chow, L.C. Pritchett, D. Campbell, T. Cahill and S.A. Whalen. 1997. Elemental characterisation of particulate matter emitted from biomass burning: wind tunnel derived source profiles for herbaceous and wood fuels. *J. Geophys. Res.* **102**. 3683-3699.

Twomey, S. 1974. Pollution and planetary albedo. *Atmos. Env.* **8**. 1251-1256.

Tyson, P.D. 1978. Rainfall changes over South Africa during the period of meteorological record. In *Biogeography and ecology of southern Africa, (ed. M.J.A. Werger*). W. Junk. The Hague. p53-69.

Tyson, P.D., M. Garstang, R. Swap, P. Kallberg and M. Edwards. 1996a. An air transport climatology for subtropical southern Africa. *Int. J. Clim.* **16**. 265-391.

Tyson, P.D., M. Garstang and R. Swap. 1996b. Large-scale recirculation of air over Southern Africa. *J. Appl. Meteor.* **35**. 2218-2236.

Tyson, P.D. and P.C. D'Abreton. 1998. Transport and recirculation of aerosols off southern Africa – Macroscale plume structure. *Atmos. Env.* **32**. 1511-1524.

Tyson, P.D., S.J. Mason, M.Q.W Jones and G.R.J. Cooper. 1998. Global warming in South Africa: evidence from geothermal profiles. *Geophys. Res. Lett.* **25**. 2711-2713.

Tyson, P.D. and R.A. Preston-Whyte. 2000. *The weather and climate of southern Africa.* Oxford University Press. Cape Town.

Tyson, P.D. and C.K. Gatebe. 2001. The atmosphere, aerosols, trace gases and biogeochemical change in southern Africa: a regional integration. *S. Afr. J. Sci.* **97**. 106-118.

UNSTAT: *The United Nations energy statistics database*. 1997. Tech. rep., Stat. Div., New York.

Uppala, S.M., P.W. Kallberg, A.J. Simmons, U. Andrae, V. da Costa Bechtold, and co-authors. 2005. The ERA-40 re-analysis. *Q. J. R. Meteorol. Soc.* **131**. 2961–3012.

Usman, M.T. and C.J.C. Reason. 2004. Dry spell frequencies and their variability over southern Africa. *Clim. Res.* **26**. 577-597.

Van der Werf, G.R., J.T. Randerson, L. Giglio, G.J. Collatz, P.S. Kasibhatla and A.F. Arellano Jr. 2006. Interannual variability of global biomass burning emissions from 1997 to 2004. *Atmos. Chem. Phys.* **6**. 3175-3226.

Van der Werf, G.R., J.T. Randerson, L. Giglio, G.J. Collatz, M. Mu, P.S. Kasibhatla, D.C. Morton, R.S. DeFries, Y. Jin and T.T. van Leeuwen. 2010. Global fire emissions and the contribution of deforestation, savanna, forest, agricultural and peat fires (1997-2009). *Atmos. Phys. Chem. Discuss.* **10**. 16153-16230.

Vannitsem, S. and F. Chome. 2005. One-way nested regional climate simulations and domain size. *J. Clim.* Vol. **18**. 229-233.

Ward, D.E., W.M. Hao, R.A. Susott, R.E. Babbitt, R.W. Shea, J.B. Kaufman and C.O. Justice. 1996. Effect of fuel composition on combustion efficiency and emission factors for African savanna ecosystems. *J. Geophys. Res.* **101**. 23569-23576.

Washington, R. and M. Todd. 1999. Tropical-temperate links in southern Africa and southwest Indian Ocean satellite derived daily rainfall. *Int. J. Climatol.* **19**. 1601-1616.

Washington, R., M. Todd, N.J. Middleton and A.S. Goudie. 2003. Dust-storm source areas determined by the Total Ozone Monitoring Spectrometer and surface observations. *Ann. Assoc. Amer. Geogr.* **93**. 297-313.

Washington, R. and A. Preston. 2006. Extreme wet years over southern Africa: Role of Indian Ocean sea surface temperatures. *J. Geophys. Res.* **111**(D15104) Doi: 10.1029/2005JD006724.

Washington, R., M. Harrison, D. Conway, E. Black, A. Challinor, D. Grimes, R. Jones, A. Morse, G. Kay and M. Todd. 2006. African climate change: taking the shorter route. *Bull. Amer. Meteor. Soc.* **87**. 1355-1366.

Winter, B. and P. Chylek. 1997. contribution of sea salt aerosol to the planetary clear-sky albedo. *Tellus-B*. **49**. 72-79.

Wolff, G.T, M.S. Ruthkosky, D.P. Stroup and P.E. Korsog. 1991. A characterization of the principal PM-10 species in Claremont (summer) and Long Beach (fall) during SCAQS. *Atmos. Env.* **25A**. 2173-2186.

Woodward, S. and D.L. Roberts. 2000. Modelling mineral dust aerosol in a climate model: sensitivity to parameterisation. *J. Aerosol. Sci.* **31**. S430.

Xie, P. and P.A. Arkin. 1997. Global precipitation: A 17-year monthly analysis based on gauge observations, satellite estimates and numerical model outputs. *Bull. Amer. Meteor. Soc.* **78**. 2539-2558.

Yang, P., K.N. Liou, M.I. Mischenko and B.C. Gao. 2000. An efficient finite-difference time domain scheme for light scattering by dielectric particles: application to aerosol. *Appl. Optics.* **39**. 3727-3737.

Yang, P., Q. Feng, G. Hong, G.W. Kattawar, W.J. Wiscombe, M. I. Mishchenko, O. Dubovik, I. Laszlo and I.N. Sokolik. 2007. Modeling of the scattering and radiative properties of nonspherical dust-like aerosols. *J. Aerosol Sci.* **38**. 995-1014.

Yokelson, R.J., I.T. Bertschi, T.J. Christian, P.V. Hobbs, D.E. Ward and W.M. Hao. 2003. Trace Gas Measurements in Nascent, Aged and Cloud-processed Smoke from Africa Savanna Fires by Airborne Fourier Transform Infrared Spectroscopy (AFTIR). *J. Geophys. Res.* **108**(D13,8478). Doi:10.1029/2002JD002322

Yoshioka, M., N.M. Mahowald, A.J. Conley, W.D. Collins, D.W. Fillmore, C.S. Zender and D.B. Coleman. 2007. Impact of desert dust radiative forcing on Sahel Precipitation: Relative importance of dust compared to sea surface temperature variations, vegetation changes and greenhouse gas warming. *J. Clim.* **20**. 1445-1467.

Zakey, A., F. Solmon and F. Girogi. 2006. Development and testing of a desert dust module in a regional climate model. *Atmos. Chem. Phys*. **6**. 4687-4704.

Zender, C.S, R.L. Miller and I. Tegen. 2004. Quantifying mineral dust mass budgets: Terminology, constraints and current estimates. *EOS*. **85**. 509.

Zeng, X. M. Zhao and R.E. Dickinson. 1998. Intercomparison of bulk aerodynamic algorithms for the computation of sea surface fluxes using TOGA COARE and TAO data. *J. Clim.* **11**. 2628-2644.

Zhang, Y., R. Fu, H. Yu, R.E. Dickinson, R.N. Juarez, L. Chin and H. Wang. 2008. A regional climate model study of how biomass burning aerosol impacts land-atmosphere interactions over the Amazon. *J. Geophys. Res.* **113**(D14S15). Doi:10.1029/2007JD009449.

Zhang, Y., R.Fu,. H. Yu, R. Dickinson, M. Assunçao, F. Silva Dias, P.L. de Silva Dias and K. Fernandes. 2009a. Impact of biomass burning aerosol on the monsoon circulation transition over Amazonia. *Geophys. Res. Lett.* **36**(L10814). Doi:10.1029/2009GL037180.

Zhang, D.F., A.S. Zakey, X.J. Gao, F. Giorgi and F. Solmon. 2009b. Simulation of dust aerosol and its regional feedbacks over East Asia using a regional climate model. *Atmos. Phys. Chem.* **9**. 1095-1110.

Zhao, T.L., S.L. Gong, X.Y. Zhang and I.G. McKendry. 2003. Model size segregated wet and dry deposition budgets of soil dust aerosol during ACE-Asia 2001: Implications for trans-Pacific transport. *J. Geophys. Res.* **108**(D23,8665). Doi: 10.1029/2002JD003363.

Zunckel M., C.R. Turner and R.B. Wells. 1996. Dry deposition of sulphur on the Mpumalanga highveld: In a pilot study using the inferential method. *S. A. J. Sci*. **92**. 485-491.

Zunckel, M. 1999. Dry deposition of sulphur over eastern South Africa. *Atmos. Env.* **33**. 3515-3529.

Zunckel, M., S. Piketh and T. Freiman. 1999. Dry deposition of sulphur at a high-altitude background station in South Africa. *Water, Air & Soil Poll.* **115**. 445-463.

Zunckel, M., L. Robertson, P.D. Tyson and H. Rodhe. 2000. Modelled transport and deposition of sulphur over Southern Africa. *Atmos. Env.* **34**. 2797-2808.